

INFORMATION TO USERS

This manuscript has been reproduced from the microfilm master. UMI films the text directly from the original or copy submitted. Thus, some thesis and dissertation copies are in typewriter face, while others may be from any type of computer printer.

The quality of this reproduction is dependent upon the quality of the copy submitted. Broken or indistinct print, colored or poor quality illustrations and photographs, print bleedthrough, substandard margins, and improper alignment can adversely affect reproduction.

In the unlikely event that the author did not send UMI a complete manuscript and there are missing pages, these will be noted. Also, if unauthorized copyright material had to be removed, a note will indicate the deletion.

Oversize materials (e.g., maps, drawings, charts) are reproduced by sectioning the original, beginning at the upper left-hand corner and continuing from left to right in equal sections with small overlaps.

Photographs included in the original manuscript have been reproduced xerographically in this copy. Higher quality 6" x 9" black and white photographic prints are available for any photographs or illustrations appearing in this copy for an additional charge. Contact UMI directly to order.

ProQuest Information and Learning
300 North Zeeb Road, Ann Arbor, MI 48106-1346 USA
800-521-0600

UMI[®]

SEYFERT AND STARBURST ACTIVITY IN GALAXIES:
MODELING AND ANALYSIS

by

Valentin Dimitrov Ivanov

A Dissertation Submitted to the Faculty of the
DEPARTMENT OF ASTRONOMY
In Partial Fulfillment of the Requirements
For the Degree of
DOCTOR OF PHILOSOPHY
In the Graduate College
THE UNIVERSITY OF ARIZONA

2 0 0 1

UMI Number: 3010245

UMI[®]

UMI Microform 3010245

Copyright 2001 by Bell & Howell Information and Learning Company.

All rights reserved. This microform edition is protected against
unauthorized copying under Title 17, United States Code.

Bell & Howell Information and Learning Company
300 North Zeeb Road
P.O. Box 1346
Ann Arbor, MI 48106-1346

THE UNIVERSITY OF ARIZONA ©
GRADUATE COLLEGE

As members of the Final Examination Committee, we certify that we have
read the dissertation prepared by Valentin Dimitrov Ivanov
entitled Seyfert and Starburst Activity in Galaxies:
Modeling and Analysis

and recommend that it be accepted as fulfilling the dissertation
requirement for the Degree of Doctor of Philosophy

Marcia J. Rieke
Dr. Marcia J. Rieke

4/20/01
Date

Laird Close
Dr. Laird Close

3/27/01
Date

Michael P. Meyer
Dr. Michael Meyer

3-27-01
Date

Dennis Zaritsky
Dr. Dennis Zaritsky

3/27/01
Date

Date

Final approval and acceptance of this dissertation is contingent upon
the candidate's submission of the final copy of the dissertation to the
Graduate College.

I hereby certify that I have read this dissertation prepared under my
direction and recommend that it be accepted as fulfilling the dissertation
requirement.

Marcia J. Rieke
Dissertation Director Dr. Marcia J. Rieke

4/20/01
Date

STATEMENT BY AUTHOR

This dissertation has been submitted in partial fulfillment of requirements for an advanced degree at The University of Arizona and is deposited in the University Library to be made available to borrowers under rules of the Library.

Brief quotations from this dissertation are allowable without special permission, provided that accurate acknowledgment of source is made. Requests for permission for extended quotation from or reproduction of this manuscript in whole or in part may be granted by the head of the major department or the Dean of the Graduate College when in his or her judgment the proposed use of the material is in the interests of scholarship. In all other instances, however, permission must be obtained from the author.

SIGNED: Valentin Dimitrov Ivanov

ACKNOWLEDGMENTS

This work and my participation in the Ph.D. program at the University of Arizona would have been impossible without the help and encouragement of my thesis adviser Dr. Marcia J. Rieke, Dr. George H. Rieke, and Fr. George V. Coyne, S.J. They generously provided me with funding, advice, and wisdom, in and outside of science. I am happy to thank my friends and collaborators - Almudena Alonso-Herrero, Charles "Chad" Engelbracht, Mario Hamuy, Christopher Groppi, Philip Pinto, Petko Nedialkov, Jura Borissova, Leonardo Vanzì, - and the fellow graduate students who had the patience to bear with me. Very special thanks to my friends Amaya Moro-Martin and Ive Kohnenkamp, who helped a lot on the final stage, and to all my friends scattered across the world. Finally, I would like to express my gratitude to my loving parents for the trust, support, and patience.

DEDICATION

Dedicated to E.A.G.

TABLE OF CONTENTS

	LIST OF FIGURES	10
	LIST OF TABLES	13
	ABSTRACT	15
1	INTRODUCTION	16
1.1	Seyfert Galaxies	16
1.1.1	Motivation	16
1.1.2	Technique	18
1.1.3	Application	19
1.2	Starburst Galaxies	19
1.2.1	Motivation	19
1.2.2	Technique	21
1.2.3	Application	22
1.3	Contents of the Thesis	23
2	TESTING THE AGN-STARBURST CONNECTION	24
2.1	Introduction	24
2.2	Observations and Data Reduction	28
2.2.1	Infrared Spectroscopy	28
2.2.2	Infrared Line Measurements	30
2.2.3	CO Band Measurements	31
2.2.4	Aperture Photometry	32
2.2.5	K-band Imaging	33
2.3	Analysis	33
2.3.1	The CO Band Strength and Circumnuclear Starbursts	33
2.3.2	Infrared Colors	42

2.3.3	Comparison with Other Work	43
2.4	Summary	44
3	NEAR INFRARED EMISSION PROPERTIES OF THE CFA SEYFERTS . . .	80
3.1	Introduction	80
3.2	Previous Work	81
3.3	Data Reduction and Line Measurements	86
3.3.1	Observations and Data Reduction	86
3.3.2	Continuum Subtraction	86
3.3.3	Infrared Line Measurements	88
3.4	Results	89
3.4.1	$\text{Br}\gamma$ and $\text{H}_2 v = 1 - 0 S(1)$ $2.12 \mu\text{m}$	89
3.4.2	Separating Seyfert and Starburst Activity	91
3.4.3	Power Sources in the Ultraluminous Infrared Galaxies	92
3.5	Summary	94
4	AN INFRARED STELLAR LIBRARY FOR SPECTRAL SYNTHESIS OF STARBURST GALAXIES	110
4.1	Introduction	110
4.2	Infrared Libraries and Population Synthesis	113
4.3	Observations and Data reduction	115
4.4	Sample Selection and Stellar Parameters	119
4.5	Index Definitions	121
4.6	Fitting Functions	122
4.7	Behavior of the Infrared Features	124
4.7.1	MgI	124
4.7.2	NaI and CaI	127
4.7.3	SiI	128
4.7.4	FeI and Other Weak Atomic Lines	129

4.7.5	CO Bands	130
4.8	Two-Dimensional Spectral Classification	132
4.9	Disentangling Flat Continuum Contamination	135
4.10	Elemental Abundance Ratios	137
4.11	Summary	137
5	NEAR-INFRARED EVOLUTIONARY POPULATION SYNTHESIS	241
5.1	Introduction	241
5.2	Short Description of Starburst99	244
5.3	Modifying Starburst99	247
5.4	Spectral Measurements	249
5.5	Results	250
5.5.1	Evolution of the Stellar Absorption Features	250
5.5.2	Dilution by Featureless Continuum	253
5.6	Discussion	254
5.7	Summary	255
6	METAL ABUNDANCES OF STARBURST GALAXIES	282
6.1	Introduction	282
6.2	Sample	284
6.2.1	Stars	284
6.2.2	Galaxies	284
6.3	Metallicity Indicators	285
6.4	MgI 1.50 μm	286
6.4.1	Empirical Calibration	286
6.4.2	Theoretical Calibration	288
6.4.3	Magnesium-based Metallicities of the Sample Galaxies	290
6.5	CO 1.62 μm	291

6.6	Infrared Metallicities of the Sample Galaxies and Iron Abundance . .	292
6.7	Metallicity and Parameters of the Sample Starburst Galaxies	293
6.8	Magnesium and the Iron Abundance in Starbursts	295
6.8.1	Chemical Enrichment Toy-Model	296
6.8.2	Discussion	298
6.9	Summary	300
7	CONCLUDING REMARKS	317
7.1	Summary of the Main Results	317
7.1.1	Seyfert Galaxies	317
7.1.2	Starburst	318
7.2	Future Work	320
A	APPENDIX CALIBRATIONS FOR THE INFRARED SPECTRAL INDICES - FIGURES	321
	REFERENCES	340

LIST OF FIGURES

2.1	Infrared spectra of the CfA Seyfert sample	68
2.2	Distributions of CO indices of star forming galaxies	74
2.3	Histograms of the observed and corrected values of the CO index . . .	75
2.4	CO index versus $K - L$ diagram	78
2.5	Infrared color-color diagrams for Seyfert galaxies	79
3.1	Comparison of our measurements with data from the literature	106
3.2	Comparison of the strengths of H_2 2.12 μm and $Br\gamma$ emission	107
3.3	Optical and infrared emission line ratios	108
3.4	Histograms of the equivalent widths and full widths at half maximum for $Br\gamma$ and H_2 2.12 μm	109
4.1	Difference between the spectra of two K3 III stars	225
4.2	Example of the data	226
4.3	Metallicity distribution of stars in the library	227
4.4	Definitions of the spectral indices	228
4.5	Metallicities of library stars	229
4.6	A subset of H and K spectra of supergiants	230
4.7	A subset of H and K spectra of giants	231
4.8	A subset of H and K spectra of dwarfs	232
4.9	A selection of H and K spectra of K giants spanning a range of metallicities	233
4.10	Line ratios as temperature indicators	234
4.11	New line ratios as temperature indicators	235
4.12	Spectral and luminosity class diagnostics	236
4.13	New spectral and luminosity class diagnostics	237

4.14	Dilution estimate technique	238
4.15	MgI line ratios	239
4.16	CO-to-metal line ratios	240
5.1	Parameters of the library stars	264
5.2	Synthetic spectra	265
5.3	Time evolution of magnesium stellar absorption features	268
5.4	Time evolution of sodium and calcium stellar absorption features . .	269
5.5	Time evolution of 2.29 μm CO bands	270
5.6	Time evolution of other indices	271
5.7	Time evolution of infrared line ratios	272
5.8	Magnesium lines and CO 1.62 μm versus CO 2.29 μm	273
5.9	Magnesium lines versus CO 1.62 μm	274
5.10	Sodium, calcium, silicon and iron lines versus CO 2.29 μm	275
5.11	Sodium, calcium, silicon and iron lines versus CO 1.62 μm	276
5.12	Iron, silicon, sodium and calcium versus magnesium 1.50 μm	277
5.13	Metal-to-metal line relations	278
5.14	Metal-to-metal line relations	279
5.15	Dilution by featureless continuum spectrum: CO bands diagnostics .	280
5.16	Dilution by featureless continuum spectrum: CO bands and magnesium diagnostics	281
6.1	Tree-dimensional fit for MgI 1.50 μm equivalent width	308
6.2	One-dimensional fit for MgI 1.50 μm equivalent width	309
6.3	Theoretical calibration of MgI 1.50 μm equivalent width	310
6.4	Histograms of the derived metallicities	311
6.5	Magnesium-based iron abundance versus optical metal indices	312
6.6	Magnesium-based iron abundance versus parameters of the starburst host galaxies	313

6.7	Magnesium-based iron abundance versus properties of the starbursts .	314
6.8	Magnesium-based iron abundance versus mid-infrared <i>IRAS</i> colors .	315
6.9	Chemical evolution	316
A.1	Calibration of MgI 1.50 μ m index (this work)	322
A.2	Calibration of MgI 1.71 μ m index (this work)	323
A.3	Calibration of MgI 2.11 μ m index (this work)	324
A.4	Calibration of MgI 2.28 μ m index (this work)	325
A.5	Calibration of MgI 2.28 μ m index (Ramírez et al. 1997)	326
A.6	Calibration of NaI 2.21 μ m index (Ramírez et al. 1997)	327
A.7	Calibration of NaI 2.21 μ m index (Kleinmann & Hall 1986)	328
A.8	Calibration of CaI 2.26 μ m index (Ramírez et al. 1997)	329
A.9	Calibration of CaI 2.26 μ m index (Kleinmann & Hall 1986)	330
A.10	Calibration of SiI 1.59 μ m index (Origlia, Moorwood & Oliva 1993) .	331
A.11	Calibration of FeI 1.58 μ m index (this work)	332
A.12	Calibration of CO 1.62 μ m index (Origlia, Moorwood & Oliva 1993) .	333
A.13	Calibration of CO 2.29 μ m index (Origlia, Moorwood & Oliva 1993) .	334
A.14	Calibration of $^{12}\text{CO}(2,0)$ 2.29 μ m index (Kleinmann & Hall 1986) .	335
A.15	Calibration of CO 2.29 μ m index (Ivanov et al. 2000)	336
A.16	Calibration of $^{12}\text{CO}(3,1)$ 2.29 μ m index (Kleinmann & Hall 1986) .	337
A.17	Calibration of $^{13}\text{CO}(2,0)$ 2.29 μ m index (Kleinmann & Hall 1986) .	338
A.18	Calibration of CO 2.29 μ m index (Doyon, Joseph & Wright 1994) .	339

LIST OF TABLES

2.1	Log of spectroscopic observations.	46
2.2	Equivalent widths for H-band spectral features $W_\lambda(\text{\AA})$	52
2.3	Equivalent line widths $W_\lambda(\text{\AA})$, and CO index for K-band absorption features for the CfA Seyfert sample.	53
2.4	Infrared aperture photometry.	56
2.5	Corrected CO indices for Seyfert galaxies.	61
2.6	Photometric data for the control sample of starburst galaxies.	63
2.7	Observed and corrected CO indices for the control sample of starburst galaxies.	65
2.8	Aperture photometry of Seyfert galaxies from the literature.	67
3.1	Estimated non-stellar fraction F_K of the total K-band flux.	96
3.2	Effective widths and line fluxes of narrow $\text{Br}\gamma$ ($2.16\ \mu\text{m}$) and H_2 ($2.12\ \mu\text{m}$) for the CfA Seyfert sample.	98
3.3	Measurements of some additional emission lines.	104
3.4	Results from the Kolmogorov-Smirnov test.	105
4.1	Properties of previous infrared spectral libraries.	140
4.2	Log of spectroscopic observations.	141
4.3	Adopted atmospheric parameters of the stars.	162
4.4	Definitions of spectral bands.	181
4.5	Spectral indices of features of interest.	183
4.6	Calibrations for the spectral indices.	206
5.1	Metallicity bins.	257
5.2	Velocity dispersion corrections.	258
5.3	Equivalent widths for $\sigma = 200\ \text{km s}^{-1}$ models.	259

6.1	Properties of the galaxy sample.	302
6.2	Magnesium line ($1.50\ \mu\text{m}$) measurements and derived metallicities of the galaxies.	304
6.3	Measurements and derived parameters of the galaxies.	306

ABSTRACT

We carried out an extensive infrared study of galaxies with Seyfert and starburst activity, to constrain the impact of these phenomena on the host galaxy evolution in a local galaxy sample. We developed new tools for stellar population analysis in the infrared, using stellar absorption features. These tools are ideally suited for studies of dusty galaxies and obscured stars in the Milky Way.

We used the CO band at $2.3\mu\text{m}$ to estimate the contribution from red supergiants to the total K-band flux in the central regions of 46 Seyferts from the CfA redshift survey, based on new infrared spectroscopy ($R \sim 700$). We removed the non-stellar contribution for 16 Seyferts, and found no evidence for strong starbursts in the majority of them. A comparison to starbursts suggests that the $[\text{FeII}]^{1.26\mu\text{m}}/\text{Pa}\beta^{1.28\mu\text{m}}$ versus $\text{H}_2^{2.121\mu\text{m}}/\text{Br}\gamma^{2.16\mu\text{m}}$ diagram is the best available Seyfert-starburst separator.

We created a unique infrared evolutionary population synthesis model for starbursts based on empirical spectral library ($R \approx 2000\text{--}3000$) of HK spectra of 218 red stars, spanning a range of $[\text{Fe}/\text{H}]$ from -2.2 to $+0.3$. We analyzed the behavior of 19 indices, and developed diagnostics for the stellar parameters. Finally, we incorporated the library into Starburst99 (Leitherer et al. 1999), and compared the synthetic spectra with observational data, to constrain the metallicity of starburst and "normal" galaxies. Our new infrared magnesium-based $[\text{Fe}/\text{H}]$ indicator is in excellent agreement with the strength of the optical iron lines. The correlation between α -element and iron-peak element suggests multiple bursts of star formation in the galaxies of our sample.

1. INTRODUCTION

During recent years there has been a growing interest in active galactic nuclei and starburst galaxies. These two spectacular phenomena can dominate completely the total spectrum of their host galaxies, and they are present in a significant fraction of the local galaxy population. There is a growing evidence that they might play an important part in the galaxy evolution at high redshift (e.g. Dey et al. 1999, Cimatti et al. 1999, Barger et al. 2001), prompting us to carry out a detailed study of nearby galaxies with active nuclei and starbursts, to take advantage of the more detailed analysis that can be carried out in the local Universe.

1.1. Seyfert Galaxies

1.1.1. Motivation

It is commonly accepted that Seyfert galaxies are a class of galaxies with active nuclei, characterized with strong high-ionization emission lines, usually hosted in spirals and S0s. They are divided in two types, according to the morphology of their spectra. Broad ($\gtrsim 10^3$ km s $^{-1}$) permitted hydrogen and helium recombination, together with narrow (500-700 km s $^{-1}$, Koski 1978) forbidden lines occur in Type 1 Seyferts. Both permitted and forbidden lines are narrow in Type 2 Seyferts. In addition, there are intermediate objects, classified as Types 1.5, 1.8, and 1.9

Seyferts, which exhibit broad and narrow components of their permitted lines.

The most widely adopted model for the Seyfert activity involves a central black hole, surrounded by a dusty torus. The two types of lines are produced respectively in Broad Line Regions (BLR) and Narrow Line Regions (NLR). While the NLRs occupy spatially larger volume, and can not be obscured by the torus, the BLRs are located near the black hole, and their visibility depends strongly on the torus inclination. Therefore, this so-called Unified model, postulates that the two types of Seyferts differ only superficially as a result of the different inclination angle with respect to the line of sight.

However, there has been some evidence in the literature that there might be different physical processes taking place in Type 1s and Type 2s. Maiolino et al. (1995a) found that Type 2 Seyferts tend to occur in galaxies with enhanced star formation based on 10 μm photometry. Absorption lines, originating in the atmospheres of young stars have been detected in optical, ultraviolet, and infrared spectra of Type 2 Seyferts (Heckman et al. 1997, Nelson & Whittle 1998, Kunth & Contini 1999), suggesting that they show more active star formation than Type 1s.

Circumnuclear starbursts, along with bars, tidal interactions, and minor mergers, could account for driving the gas toward the centers of Seyfert galaxies, to fuel their central engines. New quantitative constraints on star formation in Seyfert galaxies are needed to confirm or reject the Seyfert-starburst connection. If confirmed, such a connection will require a revision of the Unified model. If the starburst do not appear in most of the Seyferts, some other fueling mechanisms will have to be considered.

1.1.2. Technique

We address the question whether the starburst is related to the nuclear activity, based on the most complete sample of Seyfert galaxies available to date - the CfA Seyfert sample. Our goal was to develop a technique, that is able to distinguish between young and old stellar populations. Although this is a trivial problem in the optical and ultraviolet (e.g. via stellar absorption lines, see Gonzalez-Delgado et al. 1998), the high extinction in the circumnuclear regions of Seyferts precludes such a straightforward test. The infrared wavelengths, where the extinction is reduced tenfold, offer the only feasible alternative. Fortunately, the CO bands and 1.62 and 2.29 μm are sensitive to the surface gravity of the stars, and therefore to the stellar mass and age. The K-band CO is the stronger of the two, and has a weaker metallicity dependence because it is saturated. A comparison between the distribution of the CO indices of Seyfert and starburst galaxies will yield information about the dominant stellar populations in these galaxies.

In most cases, the observed CO indices appear diluted (filled in by a featureless component), compared to pure red stellar population dominated spectra, by the presence of a non-stellar component (most likely, warm dust surrounding the active nucleus). We used JHKL aperture photometry to estimate the non-stellar contribution at 2.3 μm , and successfully corrected the CO band for the dilution for 16 Seyferts which were not dominated by the non-stellar component. Comparing with CO indices measured in elliptical and purely starbursting galaxies, we find no evidence for strong starbursts in the majority of these galaxies.

The relative strength of the infrared emission lines offers an additional constraint to the stellar populations of the galaxies (e.g. Alonso-Herrero 1997, Hill et al. 1999). A comparison of the emission line properties of Seyferts and the

ultraluminous infrared galaxies (ULIRG) can yield information about their energy sources. ULIRGs are defined as galaxies with strong mid infrared emission (see Strauss et al. 1990), indicating presence of dust.

Both methods critically rely on using a complete sample of Seyfert galaxies for the comparisons, and our observations provided such a sample for the first time.

1.1.3. Application

We applied our new technique on the most complete sample of Seyfert galaxies, available up to date - the CfA Seyfert Sample (Huchra & Burg 1992). This is a magnitude limited sample, which includes galaxies with broad optical emission lines as far as ~ 130 Mpc. The sample completeness was confirmed by means of a V/V_m test (Huchra & Sargent 1973). Undoubtedly the optical wavelength selection introduces a bias toward galaxies with relatively less extinction. The sample may also be biased against the low luminosity Seyferts, discussed in Ho et al. (1997). Therefore, we constrained our conclusions to the "classical" Seyfert galaxies, which are well represented by the CfA sample.

Our correction procedure was applied on a subset of 16 Seyferts that were not dominated completely by this non-stellar component. We concluded that the K-band flux in the majority of these galaxies is produced by old stellar populations, and not by strong circumnuclear starbursts in red supergiant phase.

1.2. Starburst Galaxies

1.2.1. Motivation

Although starbursts are relatively short events compared to the age of the galaxies, they strongly affect their hosts. At the beginning of the burst they deplete the gas

reservoir, converting it into stars. The newly formed blue stars heat the interstellar material up. The bursts continue to dominate the infrared total light as these stars turn into red supergiants. The effect of the starburst is noticeable even later, when the asymptotic giant branch stars are the brightest in the near infrared. Furthermore, the dust formed in the atmospheres of the cool stars and the metals produced during the burst irrevocably change the composition of the interstellar material in the host.

The mechanism that triggers starbursts is still unclear (e.g. Conselice, Bershadsky, & Gallagher 2000, Mihos & Hernquist 1994). Many of them occur in merging, barred and tidally disrupted galaxies, but some isolated galaxies also demonstrate elevated star formation. Starbursts-like events might take place at high redshift, perhaps when present day ellipticals were formed in mergers.

Many diagnostic tools have been developed for the optical and ultraviolet wavelengths. However, the near infrared wavelengths that have to be used in a severely obscured environments - such as those in starburst galaxies - seem largely neglected, compared to the massive efforts in the optical and ultraviolet (e.g. Leitherer & Heckman 1995, Gonzalez-Delgado et al. 1998). The need for a comprehensive near infrared spectral atlas that provides a basis for stellar studies, and for building an evolutionary stellar population model, is obvious.

Metal lines in the infrared seldom have been used to constrain the stellar populations. Yet, they potentially offer the same diagnostic power as their optical counterparts. Stellar population models predict the time evolution of these features for a given abundance, and comparisons of the synthetic and observed line strength can yield a metallicity estimate.

1.2.2. Technique

The spectral evolutionary population synthesis is a powerful tool for stellar population analysis of unresolved galaxies. The first step of this method assumes an initial mass function, and a star formation history (most often a short single burst or a constant star formation over some time interval), which are coupled with theoretical stellar evolutionary tracks to produce a synthetic Hertzsprung-Russell diagram (HRD) for a given age and metallicity. Then this HRD is convoluted with a set of stellar observables (broad band fluxes, spectra, or both) to produce the total observables of the stellar system.

The efforts of many groups (e.g. Brusual & Charlot 1993, Worthey 1994, Lançon & Rocca-Volmerange, 1996, Vazdekis 1999, Leitherer et al. 1999) have helped to advance the technique to great detail. However, the evolutionary population synthesis is not an answer to all problems in stellar populations. In fact, Charlot, Worthey, & Bressan (1996) and Vazdekis et al. (2001) have shown that this method has to be used with caution, and only to answer very specific and well defined questions.

One of the main goals of this project is to derive a reliable metallicity indicator in the infrared. Therefore, we investigated the behavior of various features in spectra of stars with well known parameters, before carrying out a sophisticated population synthesis analysis to estimate their sensitivity to the metal abundance. Next, we incorporated these stellar spectra into a population synthesis model, to estimate the metallicity of a sample of local galaxies.

1.2.3. Application

We assembled the largest near infrared spectral library to date. It contains H and K spectra of 218 red stars, mostly supergiants and giants, covering spectral types from G to M. Stars of these types dominate the infrared emission in galaxies. Our library includes mainly field stars, but to span a broader range of metallicities ($[\text{Fe}/\text{H}] = -2.2$ to $+0.3$), we added stars from the Galactic globular clusters and from the Galactic Bulge, near Baade’s window. Each spectrum requires 10-12 grating settings, to cover completely the entire H and K atmospheric windows. The spectra are taken at resolution $R \sim 2000 - 3000$, necessary to measure reliably somewhat weaker metal lines. The signal-to-noise ratio varies across the spectra but is typically in the 50-100 range.

We report the equivalent widths and line indices of 19 spectral indices, and investigate how good the individual lines and line ratios are for spectral classification, diagnostics of individual stellar parameters, and stellar population studies - namely metallicity determination, abundance ratios, and disentangling of composite stellar populations.

The library was incorporated into Starburst99, an evolutionary stellar population model developed by Leitherer et al. (1999). We calculated a set of synthesis spectra over the 1-30 Myr age range. The evolutionary tracks quickly become unreliable after that, mainly because of the uncertain lifetime and effective temperature of the thermally pulsating asymptotic giant branch stars. Velocity dispersion corrections were derived for each index.

We developed for the first time a magnesium-based near infrared metallicity scale. It is consistent with optical abundance indicators, and is ideally suited for highly obscured objects. The models and metallicity calibrations were applied

to a sample of starbursts and "normal" (mostly giant ellipticals) galaxies. Not surprisingly, the giant elliptical galaxies appear to be super metal rich, while most of the starbursts exhibit near solar abundances.

We developed a simple chemical enrichment model, and explored the sensitivity of our magnesium-based metallicity indicator to the star formation history before the last burst. We conclude that using a variety of α and iron-peak metallicity indicators allows us to constrain the prior star formation history better than just using a single species. Large uncertainties in the current state-of-the-art chemical yields prevent us from making more than just a qualitative statement for the presence of previous bursts.

1.3. Contents of the Thesis

The material in this work is arranged in a combination of chronological and logical order, with later chapters using the data and results described in the preceding ones. Chapter 2 presents a purely empirical analyses of the starburst-Seyfert connection. Chapter 3 uses the emission lines to determine the nature of the power source in ULIRGs. Chapter 4 describes the spectral library, and Chapter 5 describes the population synthesis model. The metal abundances of starburst galaxies are reported in Chapter 5, and the results are summarized in Chapter 6.

2. TESTING THE AGN-STARBURST CONNECTION

2.1. Introduction

One of the most basic problems of galaxies with active nuclei - what fuels the central engine - remains open, despite the massive multiwavelength effort. Tidal interactions, minor mergers, bars and starbursts have been considered as possible answers. There are many observational examples of starbursts occurring in active galaxies (e.g. Mauder et al. 1994; Maiolino, Rieke & Keller 1995; Heckman et al., 1997; Gonzalez-Delgado et al., 1998; Nelson & Whittle, 1998; Kunth & Contini, 1999). As a result, possible connections between active galaxies and circumnuclear starbursts are the subject of extensive speculation.

Such associations might arise just because circumnuclear starbursts have a common cause with AGNs. For example, mergers, interactions between galaxies, and bars (Shlosman, Frank & Begelman, 1989; Shlosman, Begelman & Frank, 1990; Maiolino et al., 1997; Knapen, Shlosman & Peletier, 1999) have all been invoked as a means to distort the gravitational potential of the host galaxy, allowing the gas to lose angular momentum to the stars, so it can fall inward toward the AGN. All of these phenomena appear also to be associated with nuclear starbursting.

A more direct connection has been proposed by von Linden et al. (1993), who suggest that starburst-induced turbulence in the ISM is responsible for the

final stages of infall of gas into the nuclear engine. Weedman (1983) pioneered an AGN model involving a large number of small accretors - the remnants of the massive stars in a compact circumnuclear starburst, preceding the AGN stage. Bailey (1980), David (1987a, 1987b), and Norman & Scoville (1988) refined this idea, pointing out that a compact star cluster can form a super massive black hole. More sophisticated models were developed by Perry & Dyson (1985), Perry (1992), and more recently, of Williams, Baker & Perry (1999).

It has also been proposed that a starburst can mimic an AGN (Terlevich & Melnick, 1985). Terlevich et al. (1992) showed that at least low luminosity Seyfert 2's can be explained via active circumnuclear star formation alone. However, this model has difficulties explaining the rapid X-ray variability, the polarization properties, and the broad iron emission lines of more luminous active galaxies. Cid Fernandes (1997) summarized the current status of the model and suggested a dichotomy among AGNs, in which some are powered by a black hole and others by a nuclear starburst.

Still another possibility is that circumnuclear starbursts strongly alter the observed properties of AGNs. For example, Ohsuga & Umemura (1999) consider a model in which the wind from the circumnuclear starburst forms an obscuring dust wall. The alternative process, in which an AGN disturbs the galactic ISM and triggers a starburst was reported by van Breugel et al. (1985), van Breugel & Dey (1993), and Dey et al. (1997). This behavior is usually related to the expansion of a radio source into the ambient medium. Once formed, by whatever means, the black hole and the associated jet can disturb and compress the ambient interstellar gas, triggering a circumnuclear starburst.

A better understanding of the frequency of AGN and starburst coincidences

is required to probe the connection between the two phenomena. A conventional method to search for young starbursts is to look for stellar absorption features in the ultraviolet (e.g. Heckman et al., 1997; Gonzalez-Delgado et al., 1998). Current instrumentation allows this approach to be applied in just a few cases; Heckman (1999) found only four Seyfert 2 nuclei bright enough to obtain UV spectra with sufficiently high signal-to-noise to identify young stars. It is possible that they show starburst signatures because of the selection bias toward galaxies with high surface brightness, which could be a result of the active star formation. The application of this technique to AGNs is restricted by the extinction. Because the ISM lies around the AGN in a complex three-dimensional distribution, a significant component of the observed UV flux may come from the stellar population in front of the active nucleus and not be associated closely with it.

In the optical, Kunth & Contini (1999) detected emission signatures of Wolf-Rayet stars in the spectra of two Seyfert 2 galaxies out of five observed. CaII triplet absorption at 8555\AA is strong in the spectra of red supergiants and can also indicate the presence of starbursts (Terlevich, Diaz & Terlevich, 1989; Terlevich, Diaz & Terlevich, 1990; Forbes, Boisson & Ward, 1992; Nelson & Whittle, 1998). However, studies of this line in Seyfert galaxies were not conclusive because for a fraction of these galaxies the CaII index values were inconsistent with a normal galaxy spectrum diluted by a featureless power law continuum. This feature even appears in emission in some Seyferts (see also Persson, 1988; Diaz, Terlevich & Terlevich, 1989).

The infrared range has an advantage in probing AGN environments because of the lower extinction. Also, the spectral energy distributions of cool stars peak there. Henceforth, the stellar-to-AGN emission ratio is optimal in the infrared

for studying the underlying red stellar populations. Because the strengths of the CO bands at $1.6\ \mu\text{m}$ and $2.3\ \mu\text{m}$ are sensitive to the stellar surface gravity, they can indicate the presence of young red supergiants. The CO band strength is also a function of metallicity. However, in the bulges of large spirals (usually with nearly solar metallicity), the typical haunt of a Seyfert nucleus, the surface gravity dependence - related to the stellar population type - dominates. Empirically, quiescent spirals have a very narrow range of $2.3\ \mu\text{m}$ band strengths (Frogel et al., 1978; Frogel, 1985) and most starburst galaxies have bands substantially deeper than this value (Ridgway, Wynn-Williams & Becklin 1994; Goldader et al. 1995; Engelbracht 1997)

Although the $2.3\ \mu\text{m}$ strength has proven useful in identifying and studying starbursts, in applying similar techniques to Seyfert galaxies one must contend with the possibility that the band can be diluted by radiation from the warm dust surrounding the central engine in the AGN. Oliva et al. (1995) therefore used the second overtone at $1.6\ \mu\text{m}$ to probe the environments of AGNs. Unfortunately, this band is weak, and since it is not saturated, its dependence on metallicity is strong comparable to $2.3\ \mu\text{m}$ CO band. To avoid these issues, Oliva et al. (1999) derived the mass to luminosity of the nuclear region and identified starburst/Seyfert combinations where this ratio was low, rather than relying on the CO band strengths. Both of these approaches require high signal to noise spectra of moderately high resolution. Thus, they can only be applied to AGNs that are bright in the near infrared, which may result in a selection bias toward examples with strong circumnuclear starbursts.

To address the Seyfert-starburst connection more thoroughly, we obtained K-band spectra of 46 Seyfert galaxies in the CfA sample (Huchra & Burg, 1990) at

the $2.3\ \mu\text{m}$ CO bandhead. In addition, we obtained spectra of 5 ellipticals, and used 19 starburst galaxy spectra from Engelbracht (1997) for comparison. With this sample, we hope to alleviate the typical small number statistics of previous studies, and to overcome the bias toward galaxies with high surface brightness. We apply a technique based on JHKL aperture photometry and imaging to correct for the dilution of the CO band from dust heated by the AGN. We then compare the corrected CO band strengths with those of the ellipticals and starbursts.

2.2. Observations and Data Reduction

2.2.1. Infrared Spectroscopy

The infrared spectra were taken over a period of four years at three different telescopes with FSpec (Williams et al., 1993), a cryogenic long slit near infrared spectrometer utilizing a NICMOS3 256x256 array. We used $R \approx 700$, $R \approx 1200$, and $R \approx 3000$ resolution modes, corresponding to gratings of 75, 300, and 600 lines/mm. The slit width was 1.2 arcsec at the MMT (Multiple Mirror Telescope), 2.4 and 3.6 arcsec at Steward Observatory 2.3m and 1.55m telescopes. The plate scales were 0.4, 1.2 and 1.8 arcsec/pixel respectively. The observing log is presented in Table 2.1. The galaxies are sorted in order of right ascension.

The spectra were reduced using *IRAF*¹ tasks written specifically for FSpec (Engelbracht, 1999). An average of sky background images taken immediately before and after each object image was subtracted to remove the sky emission

¹*IRAF* is distributed by the National Optical Astronomy Observatories, which are operated by the Association of Universities for Research in Astronomy, Inc., under cooperative agreement with the National Science Foundation.

lines, and simultaneously, the dark current and offset level. Dark-subtracted dome flats were used to correct for pixel-to-pixel sensitivity variations. Then the two-dimensional images of each object were corrected for distortion, shifted along the spatial axis (to account for the nodding the telescope along the slit), and combined to produce a single two-dimensional spectrum. Known bad pixels were masked out. The large number of object images allowed us to exclude any remaining bad pixels and cosmic rays. The one-dimensional spectrum was extracted by fitting a 3-5 order polynomial to the continuum in the two-dimensional image. The angular sizes of the extraction apertures are given in Table 2.1.

The object spectra were divided by spectra of stars close to solar type (usually F7-G3; so-called telluric standards), observed at the same airmass and grating position, to remove the effects of the atmospheric absorption (Maiolino, Rieke & Rieke, 1996). Next, we multiplied by a solar spectrum to correct for the artificial emission features due to the absorption lines in the spectra of the telluric standards themselves. The true shape of the continuum was restored by multiplying the spectra by the ratio of black bodies with standard star and solar effective temperatures. We used the OH airglow lines (Oliva & Origlia, 1992), complemented when necessary with Ne-Kr comparison lamp spectra, for wavelength calibration.

Special attention was paid to determining the signal-to-noise of our data. The main sources of uncertainty are the photon statistics for faint objects, the strong sky emission lines, and sky variation. First, we calculated the photon statistics, taking into account the object, the sky emission and the contribution from the standard star used for atmospheric correction. This is an optimistic estimate because it neglects the sky variations. Second, we calculated the noise from a relatively featureless part of the spectrum, which gives a pessimistic estimate

because weak absorption lines were included as noise. Finally, for a few galaxies we calculated the signal-to-noise in the process of combining one-dimensional spectra extracted from each individual two-dimensional image. This is the most robust method and it accounts for all possible sources of error. The last two determinations gave virtually the same answers. To obtain the noise level at the lines and bands of interest, we rescaled the photon statistics noise spectrum to match the noise determined from the clear part of the spectra. This allowed us to obtain signal-to-noise estimates for the spectral region under the CO band, where the atmospheric transmission quickly deteriorated, and there was no clear continuum. The corresponding averaged signal-to-noise ratio is shown in Table 2.1.

2.2.2. Infrared Line Measurements

The equivalent widths, indices and line flux measurements used Gaussian fitting. Broadband K images, kindly provided by McLeod & Rieke (1995), were used to flux calibrate the spectra using the absolute calibration of Campins, Rieke & Lebofsky (1985). In turn, most of the images were re-calibrated using our aperture photometry (discussed below). The spectra in Figure 2.1 are divided by a low-order polynomial fit to the continuum, and shifted vertically, for display purposes. The individual absorption feature measurements are listed in Tables 2.2, and 2.3. Emission lines will be discussed in another chapter. One $-\sigma$ errors for the flux measurements include uncertainties both in the spectra (sky variation, continuum placement, shot noise) and in the flux calibration. One $-\sigma$ errors for the equivalent line widths include only the uncertainties in the spectra which are dominated by the continuum placement error. The latter was estimated by taking measurements at different continuum positions. Empty items in the tables denote a lack of spectral coverage, and zero equivalent widths stand for a non-detection.

In the latter case, the 1σ error has the meaning of a 1σ upper limit.

2.2.3. CO Band Measurements

Our high resolution spectra lack the wavelength coverage to measure the photometric CO index of Frogel et al. (1978) or the spectroscopic CO index of Doyon, Joseph & Wright (1994a). We defined a narrower CO index to utilize the complete set of data. Our spectral index has the advantage of being insensitive to extinction. It follows the recipe of Doyon, Joseph & Wright (1994a), but the measured regions are narrower and closer:

$$\text{CO} = -2.5 \times \log_{10}(F_{22980\text{\AA}}^{\circ}/F_{22850\text{\AA}}^{\circ}) \quad (2.1)$$

where $F_{22980\text{\AA}}^{\circ}$ is flux averaged within a 100\AA wide window centered at 22980\AA , and $F_{22850\text{\AA}}^{\circ}$ is flux averaged on nearby continuum within a 100\AA wide window centered at 22850\AA , in the rest frame of the object.

A narrow index that does not encompass totally the spectral feature is sensitive to velocity dispersion variations. To alleviate this problem, we left out NGC 5990 and NGC 6240 from the comparison starburst sample, because they have exceptionally large velocity dispersions. NGC 6240 is also not a typical starburst galaxy, because its faint $Br\gamma$ emission is indicative of a relatively old burst of star formation.

An additional incentive to use narrower bandpasses is related to possible uncertainties in the continuum shape of the infrared spectra. The CO feature is close to the edge of an atmospheric window and we cannot measure the continuum level on both sides of the spectral feature. Although during the data reduction the original continuum shape was restored after the spectra were multiplied by the solar spectrum, we could not exclude some small deviations in the continuum

shape. The narrow CO index minimizes the effect of the continuum shape on our analysis. To quantify this effect we used our JK aperture photometry to calculate the continuum slope at $2.3 \mu\text{m}$ via simple linear interpolation. We imposed this slope on continuum divided spectrum and measured the CO index again, generally modifying the CO indices by 0.005–0.01 mag.

To determine the true uncertainties, we took advantage of the multiple spectra of some galaxies, taken on different nights, and with different spectral resolution. We found the typical total uncertainty in the CO index to be 0.02 mag. The statistical errors in the CO index ($\sigma_{CO} = 0.01$ mag for a spectrum with $S/N=30$ per pixel) account for almost half of that. The rest is due to the uncertain continuum slope and sky background variations.

Finally, we compared our CO index with that of Doyon, Joseph & Wright (1994a) calculating both indices for the set of stellar spectra by Kleinmann & Hall (1986). For 26 stars, the linear conversion is:

$$\text{CO}(\text{this work}) = (0.97 \pm 0.03) \times \text{CO}(\text{Doyon}) + (0.002 \pm 0.006) \quad (2.2)$$

with standard deviation of residuals of 0.02. That is, within the errors the two indices are equivalent. Our CO index is related to other systems of CO indices via transformations derived by Doyon, Joseph & Wright (1994a).

2.2.4. Aperture Photometry

The aperture photometry was carried out at the original MMT using the facility single pixel InSb aperture photometer. Aperture diameters, fluxes and observed colors with 1σ errors are shown in Table 2.4. The calibration is based on the standard star network of Elias et al. (1982) with zero points based on Campins, Rieke & Lebofsky (1985). With data already available in the literature, a full set

(JHKLN) of ground-based photometry is now available for the entire CfA sample. Throughout this work we neglected the difference between various photometric systems (e.g. CIT versus Arizona, etc.) because they are usually small (1-5%) than the other sources of errors like the uncertain slit orientations (5-10%).

2.2.5. K-band Imaging

The K-band imaging was taken from the survey of McLeod & Rieke (1995). All images were calibrated using our aperture photometry. Many of them had independent calibrations from McLeod & Rieke (1995), and a comparison between the two showed good agreement. The calibration was transferred to the spectra by extracting fluxes with a rectangular aperture that matched the slit size for the corresponding spectrum. To obtain an upper limit to the uncertainties imposed by field rotation at the MMT, we placed this pseudo slit in 4 orientations rotated by 45 degrees on the nucleus of each galaxy. In most cases, the errors due to slit rotation were the dominant source of uncertainty. These uncertainties and the statistical ones were propagated through our CO band correction procedure (see the next Section) to obtain a final error on the CO correction.

2.3. Analysis

2.3.1. The CO Band Strength and Circumnuclear Starbursts

CO Band Strength and Starbursts

The goal of this study is to probe the presence of circumnuclear starbursts in the Seyfert galaxies by measuring their $2.3\ \mu\text{m}$ first overtone CO bandhead strength. The strength of this band depends on stellar temperature, metallicity, and surface gravity/luminosity. These multiple dependencies suggest that interpretation of the

band would be difficult. However, in the case of nuclear starbursts in luminous galaxies, the behavior is dominated by the stellar luminosity.

The best evidence for this conclusion is empirical. From the work of Ridgway, Wynn-Williams & Becklin (1994), we compute that 23 "normal" galaxies recalibrated to the spectroscopic scale have a CO index of 0.20 ± 0.02 (measured over $2.7''$ apertures). Because of the tight distribution, this value is very well determined. In comparison, from this same work we find that the average CO band absorption index in 14 nuclear starbursts is more widely distributed, but with an average value of 0.27 ± 0.05 (as suggested by Ridgway et al., we include only starbursts with $0.4 < H - K < 0.9$, to minimize extinction effects, and to exclude any blue star dominated galaxies and hidden weak AGNs). Goldader et al. (1995) reports includes for 31 luminous infrared galaxies, dominated by star formation, with an average spectroscopic CO index of 0.26 ± 0.05 . The average photometric CO index of the higher quality spectra of Engelbracht (1997) is 0.30 ± 0.07 . The data of Oliva et al. (1995) show a similar behavior.

For four low metallicity starbursting galaxies with well developed CO bands, the band strengths fall close to the average for normal galaxies ($\text{CO}_{\text{spec}} = 0.13 \pm 0.03$; Vanzi & Rieke, 1997). The metallicities of these galaxies are typically 3 to 5 times lower than solar. Thus, the metal abundance does have the expected effect on starburst CO band strengths. However, the host of Seyfert nuclei are generally massive and metal rich galaxies, reducing the metallicity effect only to a modest one. Because of this modest dependence, it is unlikely that the strong CO bands in starbursts could arise from high metallicity, particularly because there is little evidence for higher than solar metallicities in starbursts.

The starburst CO band strengths measured by Ridgway, Winn-Williams &

Becklin (1994) and Goldader et al. (1995) do show a range that overlaps with the average value for normal galaxies (Figure 2.2), so it would be hazardous to conclude that any given galaxy with a normal CO band depth could not harbor a starburst. However, there are few if any normal galaxies with bands as deep as the average for the starbursts, so deep bands are a relatively reliable indication of a recent starburst in red supergiant phase (6-12 Myr). This conclusion becomes even stronger in comparing samples of galaxies, because a few outliers in the distributions will have little effect on average values of the CO index.

In principle, the CO bands will be weak if the starburst is so young that hot stars make a significant contribution to the K-band light. This may emphasize the few starbursts with weak CO. However, this phase is short-lived; the red supergiants start to dominate the near infrared after only a few million years, and continue to do so, until the burst is 50-100 Myr old.

Measuring CO Band Strengths in Seyfert Galaxies

AGNs often have spectral energy distributions peaking in the mid infrared due to emission by hot dust, and this component could fill in the $2.3\ \mu\text{m}$ absorption and weaken it. To use our spectra to estimate intrinsic CO band strengths requires that we correct for this emission. The hot dust emission rises steeply between the K and L ($3.5\ \mu\text{m}$) bands (e.g., McAlary & Rieke 1988). In most Sy1s, where the hot dust dominates the emission in L, the estimates of hot dust emission at $2.3\ \mu\text{m}$ are too uncertain to allow an accurate correction to the CO band strength. In Sy2s, the excess emission above the stellar contribution at L is still present but relatively weak compared to Sy1s, so even approximate corrections can yield a useful determination of the intrinsic CO band strength.

The distribution of observed CO indices is shown on the top panel in Figure 2.3. We assume that the observed fluxes at $2.3 \mu\text{m}$ are the sums of similar stellar and non-stellar contributions. We have developed a procedure to disentangle the two based on a priori knowledge of their typical infrared colors.

(i) Our first step is to assume that the K-band emission is totally of stellar origin. As we shall see, this assumption is usually not accurate but by repeating the procedure iterative we can correct for the remaining non-stellar contribution.

(ii) Next we estimate the stellar component in L-band using the typical $K - L$ color for red stars. The infrared colors of normal galaxy nuclei are well known and are not a strong function of the stellar population, as shown by Aaronson (1977). We adopted his typical colors of ellipticals as representative of old stellar populations: $J - H = 0.73$, $H - K = 0.21$, and from Impey, Wynn-Williams & Becklin (1986): $K - L = 0.26$. However, the infrared colors at the centers of spirals are virtually identical (Aaronson 1977). Here we neglected the extinction. Indeed, the average observed $J - H$ of the corrected galaxies is 0.78 ± 0.10 mag. This corresponds to a color excesses $E(J - H) = 0.06 \pm 0.10$ and $E(J - H) = 0.03 \pm 0.05$ mag (assuming Rieke & Lebofsky 1985 extinction law).

(iii) Then we subtract the stellar contribution at L from the observed flux, and obtain the non-stellar L-band flux. This step is facilitated by the equal diameter of K and L band apertures.

(iv) The next step is to use the typical $K - L$ color for the non-stellar component to estimate the non-stellar contribution in the K-band. Typical colors of the non-stellar component were inferred from Seyferts which show no or very weak CO absorption, hence excluding galaxies with a significant stellar contribution. We selected eight galaxies with observed CO index ≤ 0.05 and obtained an average

observed nuclear color $(K - L)_{\text{nuc}} = 2.79 \pm 0.40$ mag, as a difference between the K flux measured within the slit aperture and the L-band flux within the circular aperture. Here we assume that the non-stellar component is concentrated in a point-source (e.g. Alonso-Herrero et al. 1998), and is fully encompassed by both the circular apertures and the slit.

(v) We then subtract a featureless spectrum, normalized to the non-stellar K-band flux, from the flux-normalized K-band spectrum. The resulting spectrum is corrected for dilution.

The procedure has to be repeated to correct for the inaccurate initial assumption but it converges after only one or two iterations. The correction can be applied in other ways, such as starting at J, or H rather than K-band. The final results converge closely to the similar values, independently of which band the procedure begins with (see Table 2.5, columns 4 and 7).

An underlying assumption in this approach is that the nuclear sources in the sample galaxies all have similar $K - L$ colors. It appears that the near infrared nuclear emission is characterized approximately by a blackbody at the typical destruction temperature of dust grains (Rieke & Lebofsky, 1981; McAlary & Rieke, 1988; Alonso-Herrero et al., 1998). As a test, we combined in various fractions a spectrum of an elliptical galaxy, representing the dominant old stellar population, with a diluting black body spectrum, and measured the colors and the CO index of the composite spectra. Most of our galaxies are consistent with $T_{\text{Black Body}} = 1000 - 1200\text{K}$ (Figure 2.4), supporting our assumption for the universal nature of the diluting spectra in Seyfert galaxies.

We also assume that the non-stellar nuclear flux at L-band flux comes from a source smaller than our slit width; that is, that there is no significant level of

extended featureless emission. Typical scale sizes for the hot dust source component are ≤ 10 pc, judged from variability time scales (Rieke & Lebofsky, 1979; Glass, 1992; Glass, 1997; Glass, 1998; Quillen et al., 2000). The central engine is not expected to heat up the dust at 0.5-1 kpc from the center or further, which is the typical linear size of the slit at the distance of most of our targets. The dust can also be heated by an extended starburst in the disk. In that case, the L-band nuclear component will be overestimated, leading to an overcorrection of the CO band, and deduction of a stronger starburst. This effect would only strengthen our conclusions if we do not detect excess starburst activity.

We minimized the effect of reddening by starting our correction procedure from the K-band. However, we can put limits on the reddening by comparing the observed $J - H$ colors of the Seyferts with those of a typical stellar population. This comparison is not exact because of both the likely variations in the reddening within our photometric aperture and the emission associated with the central engine. However, the derived $J - H$ color excesses are small, so these potential difficulties are relatively unimportant. We derive that $K - L$ color excesses for the stars are only a couple of percent, smaller than or comparable to the observational uncertainties. This is not a surprise because the CfA Seyfert sample is selected base on optical spectroscopy. Hence, in our analysis we neglected the effects of reddening in $K - L$. We will discuss in more detail the colors of some of the galaxies in the next section.

The procedure described above cannot be applied to all of our targets. In many Type 1 Seyferts the non-stellar component is dominant. We adopted the criterion for attempting a correction that the L-to-K aperture flux ratio has to be smaller or equal to 1.0, equivalent to $K - L \leq 0.91$ mag. At this limit the fraction of

the non-stellar contribution is about half of the total K-band flux (see for example NGC 5033), and the correction approaches the corrected value, rendering our procedure unreliable. Table 2.5 includes all Seyferts with corrected CO indices. We excluded from further analysis 2237+07 because of the insufficient signal-to-noise ratio at the long wavelength edge of the K-band. We also discarded four fainter galaxies with corrections larger than 25 % in flux at K to keep lower the additional uncertainty added by the photon statistics. This constrains our maximum CO index correction to 0.05 mag.

For comparison purposes we carried out the same procedure on a sample of starburst galaxies from Engelbracht (1997). The photometric data for these galaxies were collected mostly from the literature (Table 2.6). Unlike the Seyferts, starburst galaxies display significant reddening. For most of the targets Engelbracht (1997) inferred $A_V = 3 - 10$ mag, from infrared spectroscopy (hydrogen and iron line ratios). We also used the infrared colors to supplement the reddening estimates. We carried out the CO correction for the starburst galaxies twice. First, we neglected the extinction and carried the correction for the non-stellar contribution using the observed colors. Second, we dereddened the photometry before correcting the CO band. The reddening accounts for part of the K – L color excess. Since the CO correction relies on that color excess, the reddening correction leads to smaller CO corrections (typically by 0.02 mag). This strengthens our conclusion for the absence of strong starbursts in Seyferts.

Results

The results of the CO correction procedure starting at K, as described in the previous section, are shown in Table 2.5 for Seyferts and Table 2.7 for starburst

galaxies. The histograms of the CO indices are plotted in Figure 2.3. The top panel shows the observed CO indices, the middle panel shows the corrected CO indices neglecting the reddening ($A_V = 0$ mag) in starbursts, and the bottom panel shows again the corrected CO indices but the colors of the starbursts were dereddened prior to the CO correction. Ticks on the horizontal axis show the bin borders.

The CO absorption strength in luminous ellipticals is narrowly distributed within the 0.18-0.22 bin. We excluded Abell 770 as a double nucleus galaxy, and M 87 because of its mildly active nucleus (see also Ridgway et al. 1994). As shown in Figure 2.3, our corrections to the CO index in the type 2 Seyfert galaxies usually recovered the CO indices of an underlying old stellar population, similar to that of the elliptical galaxies. We do not find evidence for a significant contribution from young red stars, except in a few of the active galaxies.

To determine the significance of this result we ran a Monte-Carlo simulation. We fitted a Gaussian to the distribution of the corrected CO indices of starburst galaxies, with reddening taken into account. Next, we drew random realizations, and counted the cases that match or have an excess of shallower CO indices compared with the corrected distribution of the CO indices of Type 1.8-2 Seyfert galaxies. Based on 10^5 realizations, there is a probability of only 0.2% that the two distributions are drawn from the same parent distribution.

We quantified the role of starbursts in our sample by constructing a set of composite spectra. We added a fiducial starburst spectrum and an average spectrum of an elliptical galaxy, in different ratios, and ran the same Monte-Carlo simulation described above. We took an elliptical galaxy CO strength distribution and added the distribution typical of starbursts until there was less than a 5% probability that the CO strengths in the synthetic spectra were drawn from the

same distribution as the observed distribution of CO strengths in the Seyfert galaxies. We excluded Mkn 993 from the fitting because its extremely strong CO index may partially result from the relatively low signal-to-noise ratio of that spectrum. The simulation suggests that it is still possible to draw matching CO index distributions in about 5 % of the cases, if the starburst contributes up to 1/3 of the K-band flux. Increasing the starburst component in the composite spectrum quickly lowers that probability.

Let us assume that the starburst and the old population are represented by single bursts of ages 10^7 and 10^9 years, respectively. Then, the upper limit on the K luminosity implies that the starburst would contribute no more than 31% of the bolometric luminosity, 8% of the flux in the V-band and 11% of the flux in the B-band. That is, the blue continuum of a typical type 1.8-2 Seyfert galaxy in our sample may have a weak contribution from young blue stars, but is unlikely to be dominated by such stars. The starburst masses cannot typically exceed 10^7 , or in the most extreme cases, $10^8 M_{\odot}$. The corresponding limits on the starburst luminosities are similar to or lower than those of the AGNs in these galaxies.

According to the predictions of the same model, the CO strength reaches the typical value of an old stellar population about 50-100 Myr after the beginning of the starburst. Thus, our technique is not sensitive to very old (and very young - 1-5 Myr - and featureless in the infrared) starbursts. However, after 100 Myr, the starburst absolute K – band flux decreases by 3-4 mag, and its contribution to the total K – band flux from the galaxy nucleus would become negligible.

2.3.2. Infrared Colors

Color-color diagrams ($J - H$ versus $H - K$ and $H - K$ versus $K - L$) from our sample of Seyfert galaxies are shown in Figure 2.5, with 1σ errors along both axes. Solid dots represent Seyfert types 1.8 and later, and open circles represent earlier Seyferts. Crosses and stars are elliptical (Frogel et al., 1978) and starburst (Engelbracht, 1997) galaxies, respectively. The oval loci represent the adopted colors of elliptical galaxies and their uncertainties. Giants lie along the solid lines and supergiants along the dashed lines. Stellar colors are from Johnson (1966) and Frogel et al. (1978). Although the photometric systems used by various authors may not be exactly the same, particularly the L-band, they are sufficiently close to our system for qualitative comparison. The giants span the range between G5 and M8 on left panel and between G5 and M5 on the right. The supergiants span the range between B0 and M5 on both panels. Reddening vectors according to the Rieke & Lebofsky (1985) reddening law are also shown.

Most of our targets are redder than a typical old, red giant dominated stellar population as represented by the elliptical galaxy locus. The spread of colors in Seyferts cannot be explained just by reddening, as in pure starburst galaxies which are distributed along a line parallel to the reddening line. Indeed, the $K - L$ colors of Seyferts are redder than the predicted from the $H - K$ excess and a standard reddening law. Type 1 Seyferts show an extreme excess even on $J - H$ versus $H - K$ diagram. Therefore, there is an additional component in the K-L color of Seyferts, showing non-stellar nuclear contribution. It is present more strongly in $(K - L)$ (Glass & Moorwood, 1985; Spinoglio et al., 1995; Alonso-Herrero, Ward & Kotilainen, 1996; Alonso-Herrero et al., 1998).

A number of galaxies show peculiar blue colors. In these cases, we have

searched the literature for additional measurements, shown in Table 2.8. Although comparisons are undermined to some extent by possible variability, from them we can get a feeling for the external accuracy of our measurements. In the case of NGC 1144, we believe the best measurement is $K - L = 0.73$ from Carico et al. (1988), because it is consistent with other colors. 1058+45 is a faint source and given the observational uncertainties, we attributed the peculiar $K - L$ color to a statistical error. Our literature search for Mkn 270 and NGC 7682 yielded measurements consistent with ours. The blue colors ($H - K$ and $K - L$) of NGC 7682 can be partially explained if it has a relatively weak non-stellar component, presence of hot stars, or scattered light from the torus. This explanation is consistent with the observed CO index of 0.18, which is close to the typical purely stellar value. Still, the colors are bluer than expected from a giant dominated stellar population, suggesting perhaps the presence of blue young stars of early spectral types. In contrast, Mkn 270 has peculiar $J - H$ and $K - L$ colors, while $H - K$ is close to the typical values of other target galaxies. It has a CO index of 0.11, suggesting some dilution. The observed colors can be produced by a heavily reddened ($A_V \approx 6$ mag) blue population, even younger than in NGC 7682.

2.3.3. Comparison with Other Work

Oliva et al. (1999) have used the near infrared stellar absorption bands to determine velocity dispersions and mass to luminosity ratios, M/L_H , for active galaxies. Eleven "obscured" Seyferts (types 1.8-2) have a distribution of M/L_H that is consistent with a combination of those for normal spirals and starbursts. In this comparison, we exclude NGC 1052 and M87 because their nuclear properties are rather different from the other objects in their sample. Five of these eleven have sufficiently low M/L_H to suggest recent circumnuclear starbursts. By comparison,

in 14 type 1.8-2 Seyferts, we find two (Mkn 993 and Mkn 461) with deep CO indicative of starbursts. Because of the broad distribution of CO band strength in starbursts, we cannot exclude other members of the sample from this group. However, from the distributions in Figure 2.3, we can conclude that such events are present in only a minority of the galaxies we have observed.

The Oliva et al. (1999) sample favors galaxies with bright nuclei; our study is less biased in this direction. Nonetheless, the results are consistent in indicating that the near infrared stellar luminosities in the majority of type 1.8-2 Seyfert galaxies are NOT dominated by red supergiants from starbursts.

Oliva et al. show that the M/L_H distribution for eight Seyfert 1 galaxies is indistinguishable from that of normal spirals. It therefore appears that the near infrared luminosities of type 1 Seyfert nuclei are seldom dominated by starburst-generated supergiants. Because of the relatively strong nuclear emission of type 1 Seyfert galaxies, we have been able to measure CO band strengths for only two, but neither is strong.

2.4. Summary

We obtained K band spectroscopy of a set of Seyfert galaxies, to measure their stellar first overtone CO band strengths at $2.3 \mu\text{m}$. We used JHKL aperture photometry to estimate the non-stellar contribution at this wavelength. We successfully corrected the CO band for the dilution for 16 galaxies which were not dominated by the non-stellar component. The comparison to CO indices measured in elliptical and purely starbursting galaxies yielded no evidence for strong starbursts in the majority of Seyfert 1.8-2 galaxies. This result suggests the nuclear activity in many Seyfert 2 galaxies arises independently of any strong

circumnuclear starbursts. We do not extend our conclusions to Type 1 Seyferts, which are completely dominated by the nuclear emission. We used an evolutionary starburst model to place an upper limit of $\sim 11\%$ on the contribution to the B band light from hot, young stars in a typical type 1.8-2 Seyfert.

Table 2.1 Log of spectroscopic observations.

NGC	Mkn	R.A. Dec.	Galaxy	Sy ^a	V_{rad}^b	Date	Site	Int.	λ_c^c	Gr. ^d S/N ^e	Slit ^f
(other)	(other)	(1950)	Type ^a		km/s			T.,s	μm		Size,"
-	334	00:00:35 +21:40:54	Pec	1.8	6582±2	951009	2.3	1440	2.25	75	80 2.4x4.8
(0048+29)	(U524)	00:48:53 +29:07:46	(R')SB(s)b	1	10770	951010	2.3	720	2.25	75	30 2.4x4.8
-	993	01:22:43 +31:52:36	SAB0/a	2	4658±6	971012	MMT	960	2.33	300	15 1.2x1.6
-	573	01:41:23 +02:05:56	(R)SAB(rs)0+	2	5174±23	951009	2.3	720	1.60	75	30 2.4x4.8
						951009	2.3	720	2.25	75	50 2.4x4.8
						971012	MMT	2160	2.33	300	30 1.2x1.6
(0152+06)	(U1395)	01:52:45 +06:22:02	SA(rs)b	1.9	5208	951009	2.3	1440	2.25	75	25 2.4x4.8
863	590	02:12:00 -00:59:58	SA(s)a:	1.2	7910±12	951009	2.3	720	2.25	75	90 2.4x4.8
1144	-	02:52:39 -00:23:08	RingB	2	8648±14	971018	MMT	5520	2.33	300	45 1.2x1.6
-	3	06:09:48 +71:03:11	S0:	2	4050±5	950313	MMT	4320	2.34	600	40 1.2x1.6
2273	620	06:45:38 +60:54:13	SB(r)a:	2	1849	950314	MMT	5760	2.32	600	30 1.2x2.0
3081	-	09:57:10 -22:35:10	(R ₁)SAB(r)0/a	2	2358±7	950314	MMT	1920	2.34	600	20 1.2x1.6
3080	1243	09:57:14 +13:17:03	Sa	1	10608	960206	MMT	1920	2.25	75	35 1.2x2.0

NGC	Mkn	R.A. Dec.	Galaxy	Sy ^a	V_{rad}^b	Date	Site	Int.	λ_c^c	Gr. ^d	S/N ^e	Slit ^f
(other)	(other)	(1950)	Type ^a		km/s			T.,s	μm			Size,"
3227	-	10:20:47 +20:07:06	SAB(s) pec	1.5	1157 \pm 3	960207	MMT	480	2.20	75	70	1.2x2.4
						940323	2.3	960	2.31	600	25	2.4x6.0
						950313	MMT	1440	2.32	600	40	1.2x2.0
(1058+45)	(U6100)	10:58:43 +45:55:22	Sa?	2	8778	960406	MMT	480	2.20	75	15	1.2x2.0
3516	-	11:03:23 +72:50:20	(R)SB(s)00:	1.5	2649 \pm 7	931125	MMT	2880	2.34	600	50	1.2x1.6
3786	744	11:37:05 +32:11:11	SAB(rs)a pec	1.8	2678 \pm 6	960205	MMT	960	2.25	75	80	1.2x2.0
3982	-	11:53:52 +55:24:18	SAB(r)b:	2	1109 \pm 6	960210	MMT	1920	2.20	75	35	1.2x2.4
4051	-	12:00:36 +44:48:35	SAB(rs)bc	1.5	0725 \pm 5	960210	MMT	1440	2.20	75	80	1.2x2.0
						950313	MMT	2880	2.32	600	40	1.2x1.6
4151	-	12:08:01 +39:41:02	(R')SAB(rs)ab:	1.5	0995 \pm 3	960210	MMT	1440	2.20	75	140	1.2x2.0
4235	-	12:14:37 +07:28:09	SA(s)a	1	2410 \pm 10	960210	MMT	1440	2.20	75	60	1.2x2.0
						950314	MMT	12960	2.34	600	30	1.2x1.6
4253	766	12:15:56 +30:05:26	(R')SB(s)a:	1.5	3876 \pm 16	960210	MMT	960	2.20	75	70	1.2x2.0

NGC	Mkn	R.A. Dec.	Galaxy	Sy ^a	V_{rad}^b	Date	Site	Int.	λ_c^c	Gr. ^d S/N ^e	Slit ^f
(other)	(other)	(1950)	Type ^a		km/s			T.,s	μm		Size,"
4258	-	12:16:29 +47:34:53	SAB(s)bc	1.9	0448±3	950313	MMT	1440	2.31	600	40 1.2x1.6
4388	-	12:23:15 +12:56:17	SA(s)b: sp	2	2524±1	960206	MMT	480	2.25	75	30 1.2x2.4
-	231	12:54:05 +57:08:38	SA(rs)c? pec	1	12651±6	940402	1.55	360	1.60	75	110 3.6x7.2
						940402	1.55	1080	2.21	75	90 3.6x7.2
5033	-	13:11:09 +36:51:31	SA(s)c	1.9	0875±1	960206	MMT	240	2.25	75	60 1.2x2.4
						950313	MMT	2880	2.32	600	30 1.2x1.6
-	789	13:29:55 +11:21:44	-	1	9476±22	960329	MMT	2400	2.20	75	30 1.2x2.0
(1335+39) (U8621)		13:35:28 +39:24:31	S?	1.8	6023	960329	MMT	2880	2.20	75	25 1.2x2.0
5252	-	13:35:44 +04:47:47	S0	1.9	6926	960329	MMT	1440	2.20	75	45 1.2x2.0
5256	266	13:36:15 +48:31:48	Compact pec	2	8360±81	960327	MMT	1800	2.20	75	35 1.2x1.6
						960328	MMT	1440	2.20	75	40 1.2x2.0
5283	270	13:39:41 +67:55:28	S0?	2	2700±77	960329	MMT	960	2.20	75	70 1.2x2.0
						950313	MMT	5280	2.31	600	30 1.2x1.6

GC (other)	Mkn (other)	R.A. Dec. (1950)	Galaxy Type ^a	Sy ^a	V_{rad}^b km/s	Date	Site	Int. T.,s	λ_c^c μm	Gr. ^d S/N ^e	Slit ^f Size,"
5273	-	13:39:55 +35:54:21	SA(s)00	1.9	1089	960209	MMT	1440	2.20	75 50	1.2x2.4
-	461	13:45:04 +34:23:52	S	2	4856 \pm 32	960329	MMT	2880	2.20	75 40	1.2x2.0
-	279	13:51:54 +69:33:13	S0	1.5	8814 \pm 90	960209	MMT	480	2.20	75 75	1.2x2.0
5427	-	14:00:48 -05:47:19	SA(s)c pec	2	2730 \pm 4	950314	MMT	960	2.33	600 5	1.2x1.6
5548	1509	14:15:44 +25:22:01	(R')SA(s)0/a	1.5	5149 \pm 7	960207	MMT	960	2.20	75 80	1.2x1.6
5674	-	14:31:22 +05:40:38	SABc	1.9	7442	960328	MMT	3360	2.20	75 65	1.2x2.4
						950314	MMT	3840	2.37	600 20	1.2x1.6
5695	686	14:35:20 +36:47:02	SBb	2	4225 \pm 9	960329	MMT	1440	2.20	75 40	1.2x2.0
						950314	MMT	1920	2.34	600 20	1.2x1.6
-	841	15:01:36 +10:37:56	E	1.5	10860 \pm 90	960329	MMT	480	2.20	75 70	1.2x2.0
5929	-	15:24:19 +41:50:41	Sab: pec	2	2492 \pm 8	960329	MMT	960	2.20	75 45	1.2x2.0
5940	1511	15:28:51 +07:37:38	SBab	1	10122	960206	MMT	1440	2.20	75 25	1.2x2.4
6104	(1614+35)	16:14:40 +35:49:50	-	1.5	8382 \pm 50	951010	2.3	2880	2.25	75 30	2.4x4.8

NGC	Mkn	R.A. Dec.	Galaxy	Sy ^a	V_{rad}^b	Date	Site	Int.	λ_c^c	Gr. ^d S/N ^e	Slit ^f
(other)	(other)	(1950)	Type ^a		km/s			T.,s	μm		Size,"
(IIZw136)	1513	21:30:01 +09:55:01	-	1	18630±90	951010	2.3	4320	2.25	75 100	2.4x4.8
(2237+07)	(U12138)	22:37:46 +07:47:34	SBa	1.8	7375±90	951007	2.3	1440	2.20	75 70	2.4x6.0
						951010	2.3	720	2.25	75 50	2.4x4.8
7469	1514	23:00:44 +08:36:16	(R')SAB(rs)a	1.2	4892±2	941119	MMT	720	2.35	600 40	1.2x1.6
7603	530	23:16:23 -00:01:47	SA(rs)b: pec	1.5	8851±22	951007	2.3	720	2.20	75 60	2.4x6.0
						951010	2.3	720	2.25	75 90	2.4x4.8
7674	533	23:25:24 +08:30:13	SA(r)bc pec	2	8713±10	951010	2.3	720	2.25	75 70	2.4x4.8
7682	-	23:26:31 +03:15:28	SB(r)ab	2	5107	951009	2.3	1440	1.60	75 30	2.4x4.8
						951009	2.3	2160	2.25	75 30	2.4x4.8
(Abell770A)		09:14:12 +60:38:00	E	-	-	940404	1.55	1860	2.21	75 90	3.6x7.2
(Abell770B)		09:14:12 +60:38:00	E	-	-	940404	1.55	1860	2.21	75 50	3.6x5.4
3379	(M105)	10:45:11 +12:50:48	E1	-	0920±10	940402	1.55	5520	2.21	75 90	3.6x7.2
4472	(M49)	12:27:14 +08:16:36	E2/S0	-	0868±8	940402	1.55	4860	2.21	75 70	3.6x7.2

NGC (other)	Mkn (other)	R.A. Dec. (1950)	Galaxy Type ^a	Sy ^a	V_{rad} ^b km/s	Date	Site	Int. T.,s	λ_c ^c μ m	Gr. ^d S/N ^e	Slit ^f Size,"
4486	(M87)	12:28:18 +12:39:58	E+0-1 pec	Sy	1282 \pm 9	940404	1.55	3060	2.21	75 110	3.6x7.2

^a From N.E.D.

^b From N.E.D.

^c Central wavelength.

^d Grating, in lines/mm.

^e Signal-to-noise ratio per pixel; averaged over the entire spectral range.

^f Angular size of the spectral aperture, i.e. the width of the slit x the width of the extracted one-dimensional spectrum.

NOTE: Uxxxx = UGCxxxx

Table 2.2 Equivalent widths for H-band spectral features $W_{\lambda}(\text{\AA})$.

Galaxy	MgI	FeI	SiI	CO Ind
Name	1.504 ^a	1.583	1.590	1.620
Mkn573	4.2 ± 0.3	2.1 ± 0.2	3.4 ± 0.2	6.2 ± 0.4
Mkn231	1.1 ± 0.1	0.0 ± 0.2	0.7 ± 0.1	0.9 ± 0.2
NGC7682	4.6 ± 0.3	0.5 ± 0.3	3.3 ± 0.3	9.0 ± 1.0
NOTE: Equivalent line widths are given in \AA .				
For index definitions see Chapter 4.				

Table 2.3 Equivalent line widths $W_\lambda(\text{\AA})$, and CO index for K-band absorption features for the CfA Seyfert sample.

Galaxy	MgI	NaI	CaI	MgI	CO Ind
Name	2.107 ^a	2.207	2.264	2.281	2.230
Seyfert Galaxies					
Mkn334	0.6 ± 0.1	3.0 ± 0.4	2.4 ± 0.2	0.0 ± 0.1	0.07
0048+29		3.4 ± 0.2	4.5 ± 0.4		0.18
Mkn993		7.3 ± 0.6	3.9 ± 0.7	1.9 ± 0.3	0.26
Mkn573	0.7 ± 0.3	3.1 ± 0.3	1.3 ± 0.4	1.0 ± 0.3	0.15
0152+06		3.3 ± 0.4	3.4 ± 0.3		0.16
Mkn590	0.7 ± 0.3	2.4 ± 0.1	2.2 ± 0.2	0.0 ± 0.1	0.06
NGC1144		4.0 ± 0.3	3.2 ± 0.1	0.0 ± 0.1	0.15
Mkn3				0.3 ± 0.1	0.20
NGC2273				0.8 ± 0.1	0.13
NGC3081					0.20
Mkn1243	1.5 ± 0.5	3.5 ± 0.2	6.7 ± 0.2	1.5 ± 0.2	0.04
NGC3227	0.0 ± 0.1	3.2 ± 0.3	0.7 ± 0.2	0.0 ± 0.1	0.10
1058+45	0.3 ± 0.1	4.6 ± 0.4	10.0 ± 5.0	0.0 ± 0.2	0.22
NGC3516					0.06
Mkn744	0.5 ± 0.2	3.2 ± 0.2	0.7 ± 0.2	0.0 ± 0.1	0.09
NGC3982	0.0 ± 0.1	6.4 ± 0.6	5.3 ± 0.2	0.0 ± 0.2	0.17
NGC4051	0.5 ± 0.2	1.9 ± 0.2	2.8 ± 0.3	0.0 ± 0.1	0.06
NGC4151	0.3 ± 0.1	0.9 ± 0.1	0.4 ± 0.2	0.0 ± 0.1	0.01
NGC4235	0.9 ± 0.4	3.3 ± 0.3	2.4 ± 0.2	0.8 ± 0.2	0.09

Galaxy	MgI	NaI	CaI	MgI	CO Ind
Name	2.107 ^a	2.207	2.264	2.281	2.230
Mkn766	0.0 ± 0.1	0.9 ± 0.1	1.9 ± 0.2	0.0 ± 0.4	0.02
NGC4258				0.4 ± 0.1	0.18
NGC4388	1.6 ± 0.3	2.3 ± 0.2	5.8 ± 0.7	0.0 ± 0.2	0.09
Mkn231	0.0 ± 0.2	0.0 ± 0.1	3.9 ± 0.3	0.0 ± 0.2	0.01
NGC5033	0.0 ± 0.2	4.4 ± 0.3	0.7 ± 0.1	0.9 ± 0.2	0.14
Mkn789	0.0 ± 0.5	4.1 ± 0.3	12.6 ± 1.0	0.0 ± 0.5	0.13
1335+39	0.0 ± 1.0	4.7 ± 0.3	3.7 ± 0.6	0.0 ± 0.5	0.04
NGC5252	0.9 ± 0.5	2.0 ± 0.4	3.3 ± 1.0	1.0 ± 0.5	0.10
Mkn266	0.6 ± 0.6	5.3 ± 0.4	15.3 ± 1.5	1.0 ± 0.3	0.17
Mkn270	0.6 ± 0.4	5.2 ± 0.3	2.3 ± 0.5	0.8 ± 0.2	0.11
NGC5273	0.9 ± 0.1	5.0 ± 0.4	4.8 ± 0.8	2.0 ± 0.4	0.25
Mkn461	0.5 ± 0.3	5.6 ± 0.4	0.0 ± 0.2	2.3 ± 0.7	0.19
Mkn279	0.0 ± 0.3	0.3 ± 0.2	0.8 ± 0.2	0.6 ± 0.2	0.03
NGC5427					0.05
NGC5548	0.4 ± 0.3	2.7 ± 0.1	0.0 ± 0.1	0.0 ± 0.1	0.03
NGC5674	0.0 ± 0.3	4.8 ± 0.2	4.7 ± 0.3	0.0 ± 0.2	0.14
Mkn686	1.1 ± 0.5	3.4 ± 0.1	5.8 ± 0.2	0.0 ± 0.2	0.16
Mkn841	0.9 ± 0.1	2.1 ± 0.2	0.0 ± 0.2	0.0 ± 0.2	0.02
NGC5929	0.5 ± 0.2	6.1 ± 0.4	3.2 ± 0.3	0.0 ± 0.2	0.17
NGC5940	0.0 ± 0.3	0.0 ± 0.3	3.1 ± 0.6	0.0 ± 0.2	0.03

Galaxy	MgI	NaI	CaI	MgI	CO Ind
Name	2.107 ^a	2.207	2.264	2.281	2.230
1614+35	0.0 ± 0.5	5.4 ± 0.5	5.7 ± 0.8	0.0 ± 0.3	0.05
IIZw136	0.0 ± 0.1	0.4 ± 0.2	0.0 ± 0.2	0.0 ± 0.1	0.01
2237+07	0.4 ± 0.3	3.6 ± 0.3	2.3 ± 0.4	1.9 ± 0.5	0.06
NGC7469					0.25
Mkn530	0.8 ± 0.1	3.4 ± 0.5	0.9 ± 0.4	0.0 ± 0.1	0.06
Mkn533	0.0 ± 0.3	1.0 ± 0.1	0.9 ± 0.2	0.0 ± 0.2	0.03
NGC7682	2.1 ± 0.2	6.8 ± 0.3	4.5 ± 0.3	1.0 ± 0.3	0.18
Template Elliptical Galaxies					
A770A	0.9 ± 0.1	6.9 ± 0.3	1.7 ± 0.3	0.0 ± 0.2	0.16
A770B	0.0 ± 0.2	6.7 ± 0.3	14.1 ± 0.5	3.3 ± 0.5	0.23
NGC3379	0.8 ± 0.1	5.7 ± 0.3	3.2 ± 0.2	0.9 ± 0.2	0.20
NGC4472	0.9 ± 0.1	5.7 ± 0.3	2.7 ± 0.3	0.8 ± 0.2	0.20
M87	0.9 ± 0.1	4.2 ± 0.2	2.4 ± 0.1	1.0 ± 0.2	0.16

^a Central wavelengths in μm .

NOTE: Equivalent line widths are given in \AA . Some galaxies have been observed a few times, and the unweighted averages from different spectra are given. The second number in each column is 1σ uncertainty except for the CO index, where the typical uncertainty for the entire sample is 0.02 mag (see section 2.3). Missing equivalent line widths indicate lack of spectral coverage.

Table 2.4 Infrared aperture photometry.

Galaxy	Ap ^a	F_J^{ap}	F_H^{ap}	F_K^{ap}	F_L^{ap}	F_K^{sl}	(J – H) ^{ap}	(H – K) ^{ap}	(K – L) ^{ap}	Note ^b
Name	"	mJy	mJy	mJy	mJy	mJy	mag	mag	mag	
Mkn334	8.6	13.5 ± 0.7	21.1 ± 1.1	29.0 ± 1.5	41.0 ± 2.0	21.5 ± 1.5	0.92 ± 0.08	0.85 ± 0.08	1.30 ± 0.08	
0048+29	5.4	10.4 ± 0.5	13.9 ± 0.7	13.1 ± 0.7	10.0 ± 1.0	7.9 ± 0.7	0.75 ± 0.08	0.44 ± 0.08	0.63 ± 0.12	
Mkn993	8.6	13.8 ± 0.7	19.0 ± 0.9	16.0 ± 0.8	10.0 ± 1.0	2.3 ± 0.8	0.78 ± 0.08	0.32 ± 0.08	0.42 ± 0.12	
Mkn573	8.6	22.0 ± 1.1	29.5 ± 1.5	26.3 ± 1.3	23.0 ± 1.1	14.1 ± 1.3	0.75 ± 0.08	0.38 ± 0.08	0.78 ± 0.08	2.4x4.8
						4.9 ± 1.3				1.2x1.6
0152+06	5.4	5.2 ± 0.5	7.0 ± 0.7	8.0 ± 0.8	6.0 ± 0.6	5.4 ± 0.8	0.76 ± 0.15	0.65 ± 0.15	0.62 ± 0.15	
Mkn590	5.4	20.0 ± 1.0	25.0 ± 1.2	40.0 ± 2.0	64.0 ± 3.2	29.9 ± 2.0	0.68 ± 0.08	1.01 ± 0.08	1.44 ± 0.08	
NGC1144	5.4	12.0 ± 0.6	16.5 ± 0.8	14.6 ± 0.7	7.0 ± 0.7	1.8 ± 0.7	0.78 ± 0.08	0.37 ± 0.08	0.13 ± 0.12	
Mkn1243	5.4	5.5 ± 0.6	7.9 ± 0.8	9.5 ± 0.9	14.5 ± 0.7	2.3 ± 1.0	0.83 ± 0.15	0.70 ± 0.15	1.39 ± 0.12	
NGC3227	8.6	63.0 ± 3.2	78.0 ± 3.9	78.0 ± 3.9	71.0 ± 3.5	16.3 ± 3.9	0.67 ± 0.08	0.50 ± 0.08	0.83 ± 0.08	1.2x2.0
						12.9 ± 3.9				1.2x1.6
						45.9 ± 3.9				2.4x6.0

Galaxy	Ap ^a	F_J^{ap}	F_H^{ap}	F_K^{ap}	F_L^{ap}	F_K^{sl}	(J – H) ^{ap}	(H – K) ^{ap}	(K – L) ^{ap}	Note ^b
Name	"	mJy	mJy	mJy	mJy	mJy	mag	mag	mag	
NGC3362	5.4	4.2 ± 0.4	5.4 ± 0.5	4.5 ± 0.5	4.0 ± 1.0		0.71 ± 0.15	0.32 ± 0.15	0.78 ± 0.16	
1058+45	5.4	7.2 ± 0.7	9.7 ± 1.0	8.2 ± 0.8	3.3 ± 0.3	2.2 ± 0.8	0.76 ± 0.15	0.32 ± 0.15	-0.06 ± 0.15	
Mkn744	8.6	19.8 ± 1.0	25.9 ± 1.3	27.8 ± 1.4	31.0 ± 1.5	8.4 ± 1.4	0.73 ± 0.08	0.58 ± 0.08	1.05 ± 0.08	
NGC3982	5.4	11.2 ± 0.6	12.2 ± 0.6	10.2 ± 0.5	7.1 ± 0.9		0.53 ± 0.08	0.32 ± 0.08	0.52 ± 0.12	
NGC4051	8.6	40.0 ± 2.0	49.0 ± 2.5	65.0 ± 3.2	77.0 ± 3.8	14.9 ± 3.3	0.65 ± 0.08	0.81 ± 0.08	1.11 ± 0.08	1.2x1.6
						17.7 ± 3.3				1.2x2.0
NGC4151	8.6	105.0 ± 5.2	130.0 ± 6.5	194.0 ± 9.7	344 ± 17.2	35.3 ± 9.8	0.67 ± 0.08	0.94 ± 0.08	1.55 ± 0.08	
NGC4235	5.4	23.0 ± 1.1	35.4 ± 1.8	29.9 ± 1.5	22.0 ± 1.1	4.8 ± 1.5	0.90 ± 0.08	0.32 ± 0.08	0.59 ± 0.08	1.2x1.6
						5.7 ± 1.5				1.2x2.0
Mkn766	5.4	16.3 ± 0.8	26.7 ± 1.3	43.2 ± 2.2	86.0 ± 4.3	11.8 ± 2.2	0.97 ± 0.08	1.02 ± 0.08	1.68 ± 0.08	
Mkn231	5.8	43.0 ± 2.2	77.0 ± 3.8	175.0 ± 8.8	360 ± 18	73.5 ± 8.8	1.07 ± 0.08	1.39 ± 0.08	1.71 ± 0.08	

Galaxy	Ap ^a	F_J^{ap}	F_H^{ap}	F_K^{ap}	F_L^{ap}	F_K^{sl}	(J – H) ^{ap}	(H – K) ^{ap}	(K – L) ^{ap}	Note ^b
Name	"	mJy	mJy	mJy	mJy	mJy	mag	mag	mag	
NGC5033	8.6	44.1 ± 2.2	61.6 ± 3.1	47.8 ± 2.4	43.0 ± 2.2	6.0 ± 2.4	0.80 ± 0.08	0.23 ± 0.08	0.81 ± 0.08	1.2x1.6
						7.4 ± 2.4				1.2x2.0
						8.1 ± 2.4				1.2x2.4
1335+39	5.4	4.5 ± 0.4	6.7 ± 0.7	7.2 ± 0.7	10.2 ± 0.5	2.0 ± 0.7	0.87 ± 0.15	0.58 ± 0.15	1.31 ± 0.12	
NGC5252	5.4	10.6 ± 0.5	14.9 ± 0.7	14.9 ± 0.7	19.3 ± 1.0	4.2 ± 0.8	0.80 ± 0.08	0.50 ± 0.08	1.21 ± 0.08	
Mkn266	8.6	6.0 ± 0.6	8.8 ± 0.9	8.7 ± 0.9	7.0 ± 0.7	2.6 ± 0.9	0.85 ± 0.15	0.49 ± 0.15	0.69 ± 0.15	1.2x1.6
						3.3 ± 1.0				1.2x2.0
Mkn270	5.8	16.0 ± 0.8	18.0 ± 0.9	17.0 ± 0.9	7.0 ± 0.7	5.3 ± 0.9	0.56 ± 0.08	0.44 ± 0.08	–0.04 ± 0.12	1.2x2.0
						4.6 ± 0.9				1.2x1.6
Mkn461	5.4	8.5 ± 0.9	10.8 ± 0.5	9.1 ± 0.9	8.5 ± 0.9	2.6 ± 0.9	0.69 ± 0.12	0.32 ± 0.12	0.85 ± 0.15	
Mkn279	8.6	18.0 ± 0.9	24.0 ± 1.2	23.0 ± 1.1	32.0 ± 1.6	7.2 ± 1.2	0.75 ± 0.08	0.46 ± 0.08	1.29 ± 0.08	
IC4397	5.4	4.7 ± 0.5	6.5 ± 0.7	5.4 ± 0.5	5.8 ± 1.4		0.79 ± 0.15	0.32 ± 0.15	0.99 ± 0.16	

Galaxy	Ap ^a	F_J^{ap}	F_H^{ap}	F_K^{ap}	F_L^{ap}	F_K^{sl}	(J – H) ^{ap}	(H – K) ^{ap}	(K – L) ^{ap}	Note ^b
Name	"	mJy	mJy	mJy	mJy	mJy	mag	mag	mag	
NGC5548	8.6	27.0 ± 1.4	36.0 ± 1.8	52.0 ± 2.6	91.0 ± 4.6	12.9 ± 2.6	0.75 ± 0.08	0.90 ± 0.08	1.54 ± 0.08	
NGC5674	5.4	11.1 ± 0.6	15.2 ± 0.8	15.1 ± 0.8	15.5 ± 0.8	4.9 ± 0.8	0.78 ± 0.08	0.49 ± 0.08	0.96 ± 0.08	1.2x1.6
						5.9 ± 0.8				1.2x2.4
Mkn686	5.4	13.3 ± 0.7	17.2 ± 0.9	13.9 ± 0.7	8.9 ± 0.9	3.0 ± 0.7	0.71 ± 0.08	0.27 ± 0.08	0.44 ± 0.12	1.2x1.6
						3.5 ± 0.7				1.2x2.0
NGC5929	5.4	14.6 ± 0.7	20.2 ± 1.0	17.2 ± 0.9	13.7 ± 0.7	4.1 ± 0.9	0.79 ± 0.08	0.33 ± 0.08	0.68 ± 0.08	
NGC5940	5.4	4.7 ± 0.5	7.0 ± 0.7	8.3 ± 0.8	10.7 ± 0.8		0.87 ± 0.15	0.70 ± 0.15	1.19 ± 0.16	
1614+35	5.4	3.6 ± 0.4	5.6 ± 0.6	5.6 ± 0.6	6.4 ± 1.0		0.91 ± 0.15	0.52 ± 0.15	1.06 ± 0.16	
2237+07	8.6	12.0 ± 0.6	17.8 ± 0.9	19.4 ± 1.0	16.0 ± 0.8	12.3 ± 1.0	0.86 ± 0.08	0.60 ± 0.08	0.72 ± 0.08	2.4x6.0
						11.9 ± 1.0				2.4x4.8
NGC7469	8.6	57.0 ± 2.8	74.0 ± 3.7	123.0 ± 6.2	163 ± 8.1	18.5 ± 6.2	0.72 ± 0.08	1.05 ± 0.08	1.23 ± 0.08	

Galaxy	Ap ^a	F_J^{ap}	F_H^{ap}	F_K^{ap}	F_L^{ap}	F_K^{sl}	(J – H) ^{ap}	(H – K) ^{ap}	(K – L) ^{ap}	Note ^b
Name	"	mJy	mJy	mJy	mJy	mJy	mag	mag	mag	
Mkn530	8.6	17.0 ± 0.9	25.0 ± 1.2	25.0 ± 1.2	25.0 ± 1.2	16.1 ± 1.3	0.85 ± 0.08	0.50 ± 0.08	0.93 ± 0.08	2.4x6.0
						15.4 ± 1.3				2.4x4.8
Mkn533	8.6	10.1 ± 0.5	15.6 ± 0.8	24.2 ± 1.2	46.0 ± 2.3	16.1 ± 1.2	0.91 ± 0.08	0.98 ± 0.08	1.63 ± 0.08	
NGC7682	8.6	10.5 ± 0.5	14.9 ± 0.7	9.5 ± 0.9	4.6 ± 0.5	5.7 ± 1.0	0.81 ± 0.08	0.01 ± 0.12	0.14 ± 0.15	

^a Aperture diameter, arcsec.

^b Slit size in arcsec, if more than one spectra were taken

NOTE: The table contains: JHKL fluxes within the given aperture diameter, centered at the nucleus, K flux within the slit, used to calibrate the spectra, and the colors derived from the aperture fluxes, using the absolute calibration of Campins, Rieke & Lebofsky (1985): $F_J^0 = 1603 \pm 34$, $F_H^0 = 1075 \pm 32$, $F_K^0 = 667 \pm 14$, $F_J^0 = 288 \pm 6$ Jy. The second number in each column is 1σ uncertainty.

Table 2.5 Corrected CO indices for Seyfert galaxies.

Name	$(L/K)_{ap}$	CO _{obs}	CO _{cor} ^H	% _{nst} ^H	Iter.	CO _{cor} ^K	% _{nst} ^{K_s}	Iter.
1	2	3	4	5	6	7	8	9
0048+29	0.76	0.18	0.21	10	1	0.20	6	2
Mkn993	0.62	0.26	0.33	18	1	0.29	10	1
Mkn573	0.87	0.15	0.21	29	1	0.19	21	1
0152+06	0.75	0.16	0.18	11	1	0.18	5	2
NGC1144	0.48	0.15	0.15	2	1	0.15	0	0
NGC3227	0.91	0.10	0.15	40	1	0.13	28	1
1058+45 ^a	0.40	0.22	0.22	0	0	0.22	0	0
NGC4235	0.74	0.09	0.11	27	1	0.10	19	1
NGC5033	0.90	0.14	0.23	48	1	0.22	42	1
Mkn266	0.80	0.17	0.22	22	1	0.20	14	1
Mkn270 ^a	0.41	0.11	0.11	0	0	0.11	0	0
Mkn461	0.93	0.19	0.26	29	1	0.24	23	1
Mkn686	0.64	0.16	0.18	11	1	0.18	7	1
NGC5929	0.80	0.17	0.23	25	1	0.21	18	1
2237+07	0.82	0.06	0.08	14	1	0.08	8	2

Name	$(L/K)_{ap}$	CO _{obs}	CO _{cor} ^H	% _{nst} ^H	Iter.	CO _{cor} ^K	% _{nst} ^{K_s}	Iter.
1	2	3	4	5	6	7	8	9
NGC7682 ^a	0.48	0.18	0.18	0	0	0.18	0	0

^a $L - K < (L - K)_{Sy1}$

Column 2 gives the L-to-K band flux ratio.

Columns 4 and 7 contain the corrected CO indices with correction procedure started from H and K respectively.

Columns 5 and 8 show the non-stellar part of the K flux.

The number of iterations are presented in columns 6 and 9.

Zero iterations indicates that the galaxy has $K - L$ bluer than the adopted pure non-stellar color $(K - L)_{Sy1} = 2.79$, and we assumed negligible non-stellar flux at K.

Table 2.6 Photometric data for the control sample of starburst galaxies.

Name	Slit Size	Eff ^a	Ph.	F_J^{ap}	F_H^{ap}	F_K^{ap}	F_K^{sl}	F_L^{ap}	A _V	Ref
	"	Ap''	Ap''	mJy	mJy	mJy	mJy	mJy	Mag	
NGC253	2.4x12.0	6.1	6.0	115.0	226.7	280.6	278.1	390.3	7.4	1,8 ^b
NGC660	2.4x9.6	5.4	5.0	27.9	40.9	36.7	69.2	34.7	6.4	6
Maffei2	2.4x6.0	4.3	slit	16.6	45.6	55.5	55.5	-	8.5	1
IC342	2.4x6.0	4.3	3.8	49.0	74.0	71.0	87.1	44.0	5.1	9
NGC1614	2.4x6.0	4.3	6.0	32.3	52.4	51.5	27.6	55.9	3.5	11
NGC2146	2.4x6.0	4.3	17.0	132.1	253.2	270.5	94.3	285.7	6.4	2
NGC2782	2.4x6.0	4.3	17.0	55.1	73.7	62.5	22.1	65.6	2.9	2
M82	2.4x26.4	8.9	7.8	161.0	350.0	475.0	-	436.0	10.2	10
NGC3079	2.4x6.0	4.3	6.0	29.2	66.6	82.4	34.7	63.9	7.8	4
NGC3628	2.4x6.0	4.3	slit	06.2	14.8	19.4	19.4	-	9.7	1
NGC4102	2.4x6.0	4.3	3.8	80.5	118.0	117.0	87.1	89.0	5.7	5
NGC4194	2.4x6.0	4.3	13.0	73.3	78.6	67.3	24.9	69.0	3.5	3
NGC4339	2.4x6.0	4.3	slit	15.0	21.6	17.2	17.2	-	1.0	1
NGC5990	2.4x6.0	4.3	slit	16.6	23.7	27.6	27.6	-	7.7	1
NGC6000	2.4x6.0	4.3	slit	30.3	37.3	37.3	37.3	-	5.1	1
NGC6240	2.4x6.0	4.3	9.0	27.9	50.5	53.5	31.3	43.2	9.9	3

Name	Slit Size	Eff ^a	Ph.	F_J^{ap}	F_H^{ap}	F_K^{ap}	F_K^{sl}	F_L^{ap}	A _V	Ref
	"	Ap"	Ap"	mJy	mJy	mJy	mJy	mJy	Mag	
NGC6946	2.4x7.2	4.7	3.0	23.8	35.3	36.3	-	-	4.3	1
NGC7714	2.4x6.0	4.3	5.0	20.4	25.6	21.5	18.5	22.4	4.3	4
Mkn331	2.4x6.0	4.3	5.0	26.0	36.4	34.9	23.8	29.1	4.8	7

^a The effective aperture is a circle with the same area as the slit aperture.

^b 1 for JHK, 8 for K – L

NOTE: References are for the aperture photometry only. The flux within the slit is from Engelbracht (1997), who gives K_s, instead of K, unlike the other sources. The difference between the two filters is of order of 0.01 mag, insignificant compared to the typical uncertainties of 0.05-0.10 mag.

REFERENCES: (1) Engelbracht (1997); (2) Hunt & Giovanardi (1992); (3) Allen (1976); (4) Lawrence et al. (1985); (5) Roche et al. (1991); (6) Brindle et al. (1991); (7) Carico et al. (1988); (8) Rieke & Low (1975); (9) Becklin et al. (1980); (10) Rieke et al. (1980); (11) Glass & Moorwood (1985)

Table 2.7 Observed and corrected CO indices for the control sample of starburst galaxies.

Name	CO _{obs}	$A_V = 0$			$A_V \neq 0$			
		CO _{cor} ^H	CO _{cor} ^K	Iter.	A_V	CO _{cor} ^H	CO _{cor} ^K	Iter.
1	2	3	4	5	6	7	8	9
NGC253	0.24	0.31	0.29	1	7.4	0.27	0.26	1
NGC660	0.22	0.23	0.23	1	6.4	0.22	0.22	1
Maffei2	0.22	0.22	0.22	0	8.5	0.22	0.22	0
IC342	0.26	0.27	0.26	1	5.1	0.25	0.27	2
NGC1614	0.28	0.28	0.28	0	3.5	0.28	0.28	0
NGC2146	0.18	0.27	0.24	1	6.4	0.21	0.20	1
NGC2782	0.14	0.19	0.18	1	2.9	0.17	0.17	1
M82	0.27	0.27	0.27	0	10.2	0.27	0.27	0
NGC3079	0.17	0.22	0.19	1	7.8	0.17	0.17	1
NGC3628	0.24	0.24	0.24	0	9.7	0.24	0.24	0
NGC4102	0.19	0.21	0.22	1	5.7	0.19	0.20	2
NGC4194	0.15	0.21	0.20	1	3.5	0.18	0.18	1
NGC4339	0.25	0.25	0.25	0	1.0	0.25	0.25	0
NGC5990	0.12	0.12	0.12	0	7.7	0.12	0.12	1
NGC6000	0.25	0.25	0.25	0	5.1	0.25	0.25	0

Name	CO _{obs}	A _V = 0			A _V	A _V ≠ 0		
		CO _{cor} ^H	CO _{cor} ^K	Iter.		CO _{cor} ^H	CO _{cor} ^K	Iter.
1	2	3	4	5	6	7	8	9
NGC6240	0.18	0.22	0.21	2	9.9	0.17	0.18	1
NGC6946	0.26	0.26	0.26	0	4.3	0.26	0.26	0
NGC7714	0.26	0.30	0.29	1	4.3	0.27	0.28	1
Mkn331	0.22	0.25	0.26	2	4.8	0.23	0.23	2

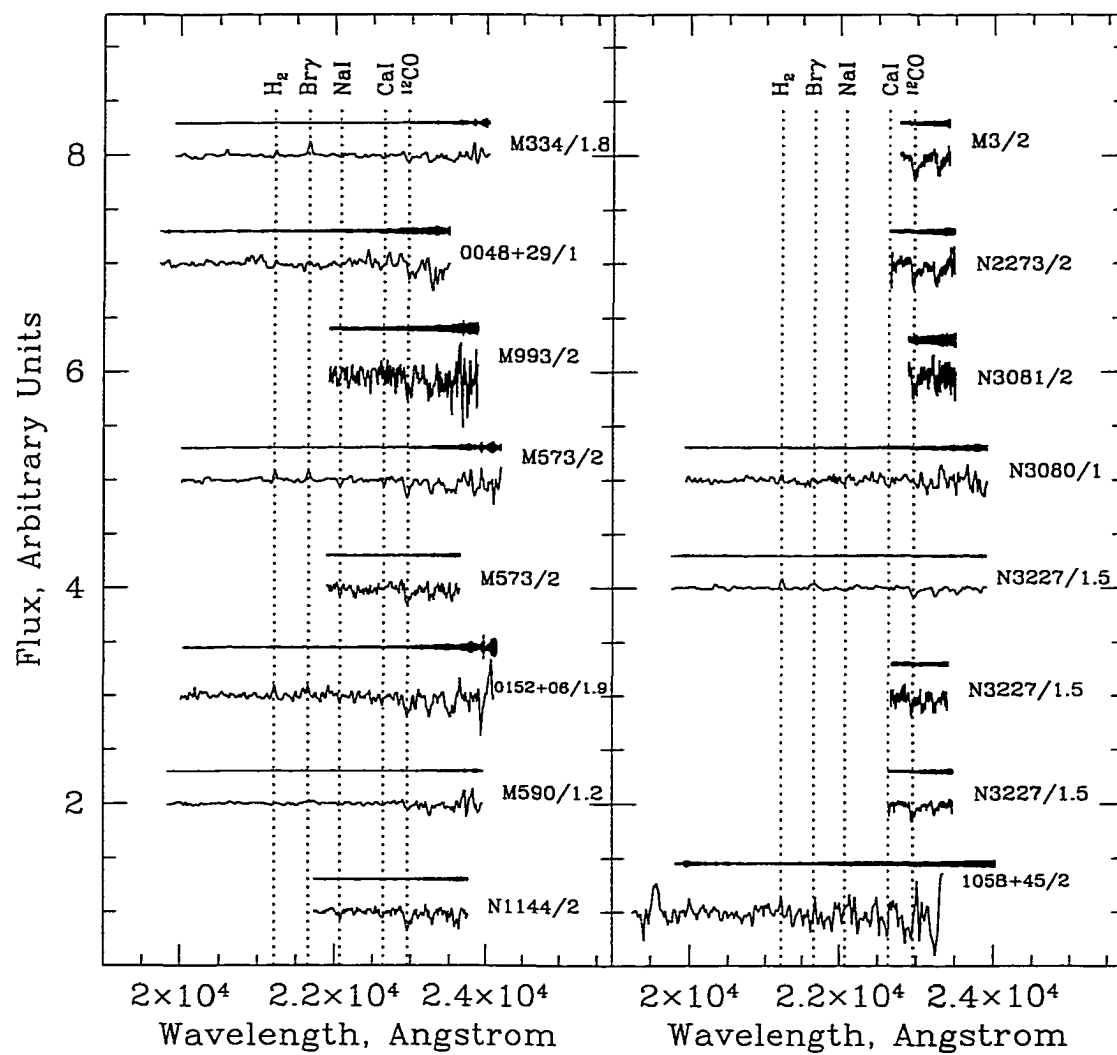
NOTE: The notation is the same as in Table 2.6.

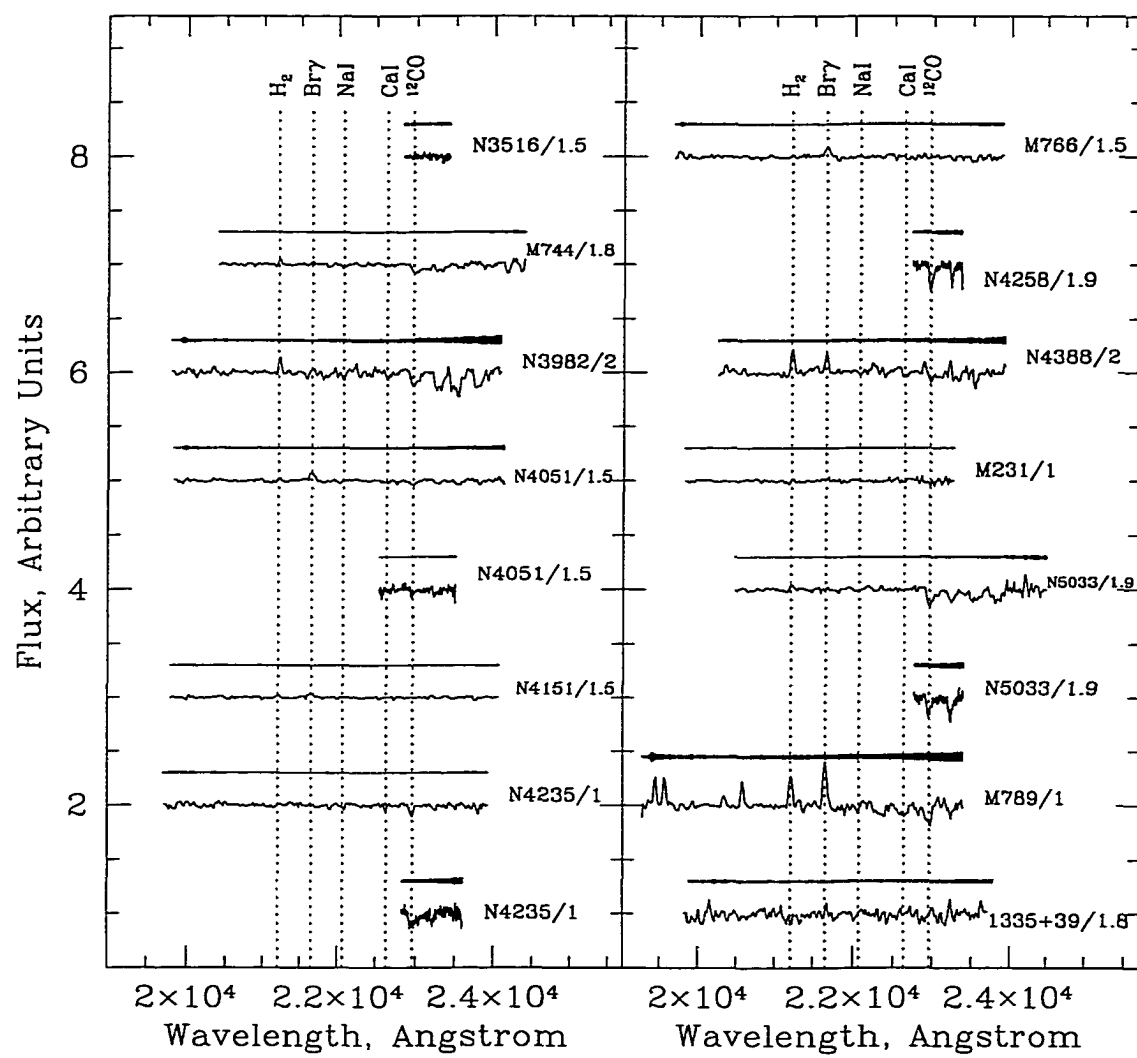
Table 2.8 Aperture photometry of Seyfert galaxies from the literature.

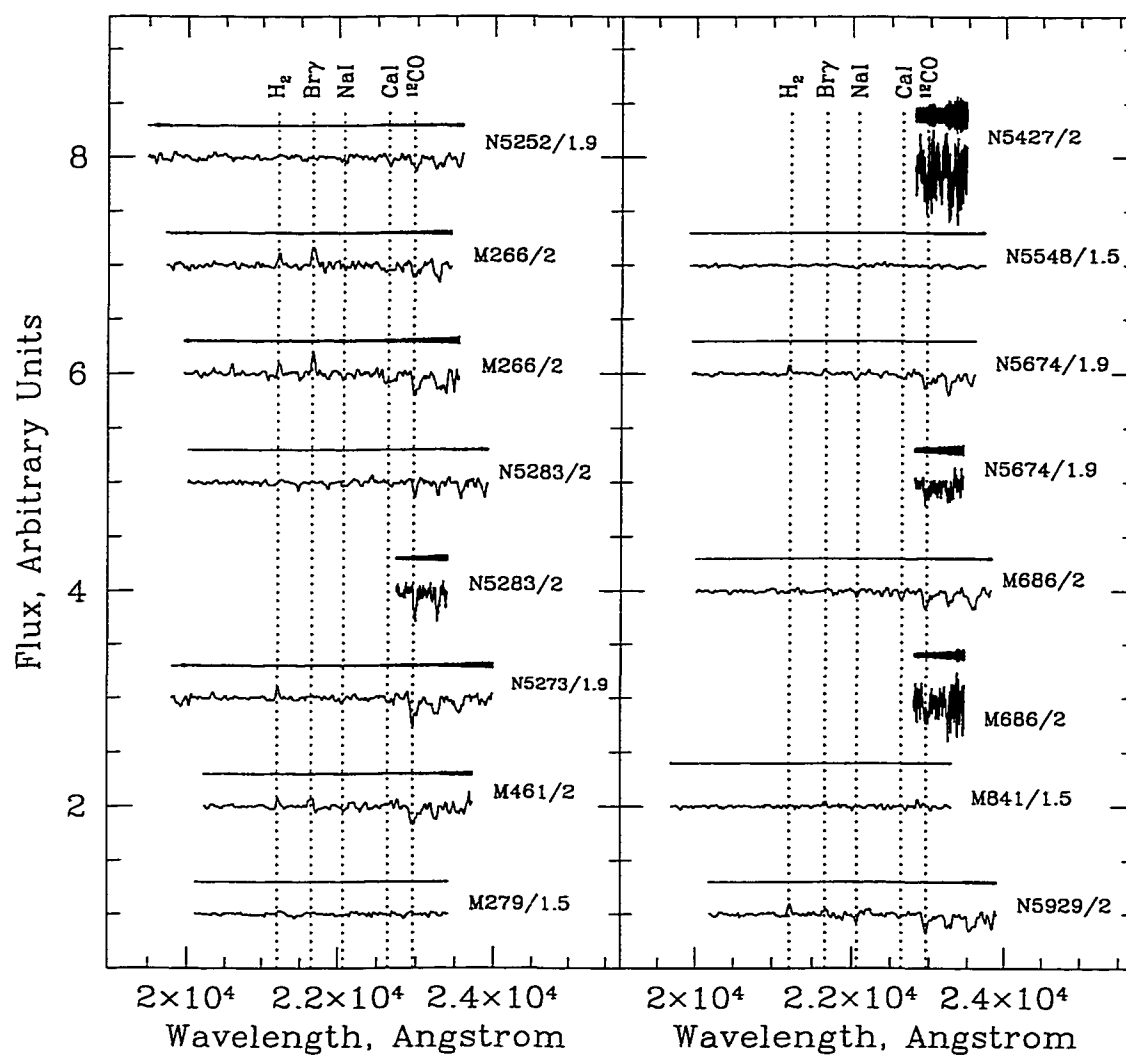
Name	Ap.,''	J – H	H – K	K – L	Ref.
NGC1144	4.0	0.89	0.38	0.55	1
	5.0	0.72	0.44	0.73	2
	5.4	1.01	0.47		3
	8.5	1.43	0.58		4
	12.0	0.75	0.41		5
	30.0	0.75	0.21		6
Mkn270	5.9	0.50	0.46	-0.07	7
	15.0	0.50	0.35	≤ 0.84	8
NGC7682	8.5	0.80	0.02		4

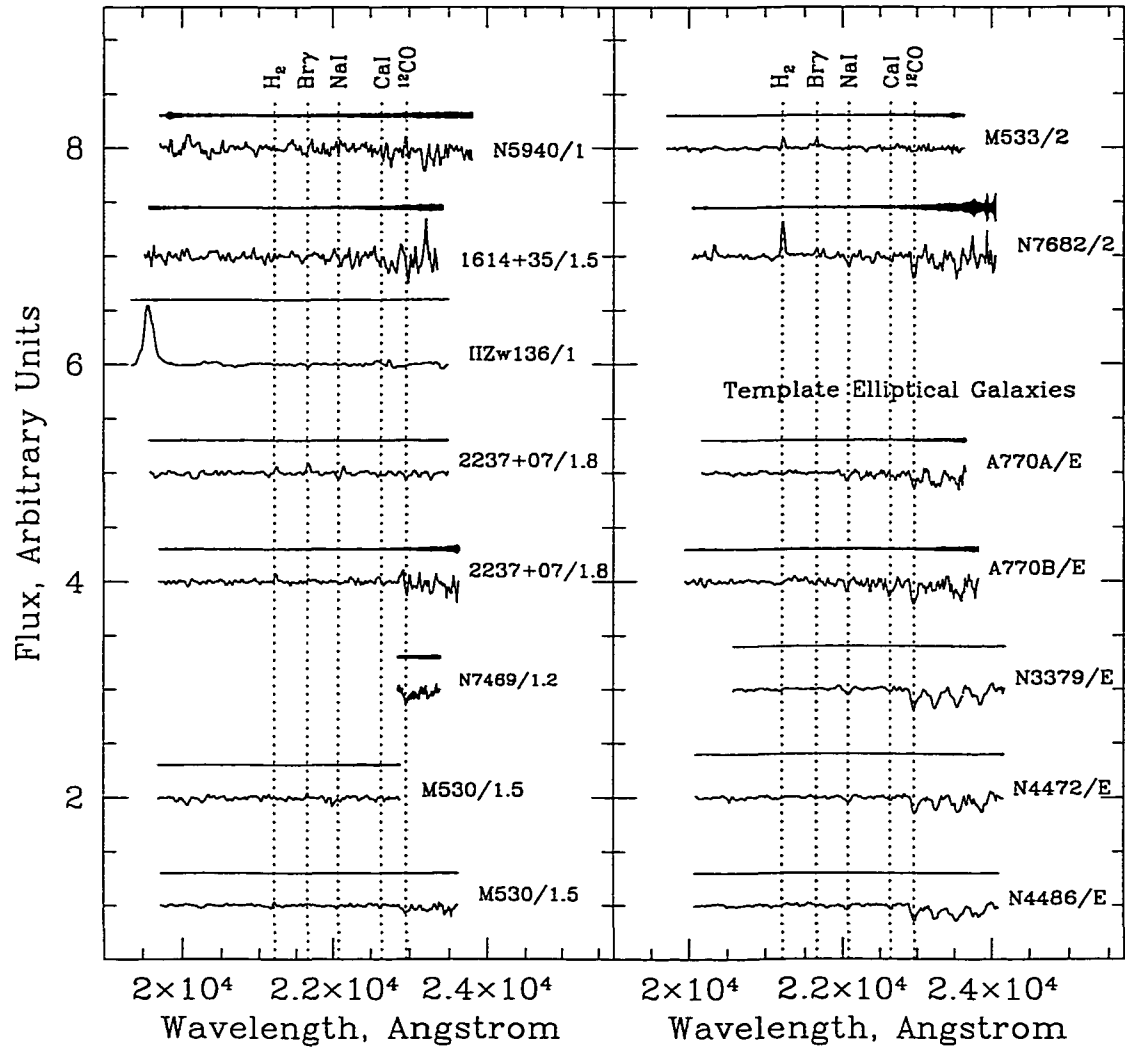
REFERENCES: (1) Joy & Ghigo (1988); (2) Carico et al. (1988); (3) Bushouse & Stanford (1985); (4) Edelson, Malkan & Rieke (1987); (5) Cutri & McAlary (1985); (6) Spinoglio et al. (1995); (7) Rieke (1978); (8) McAlary, McLaren & Crabtree (1979)

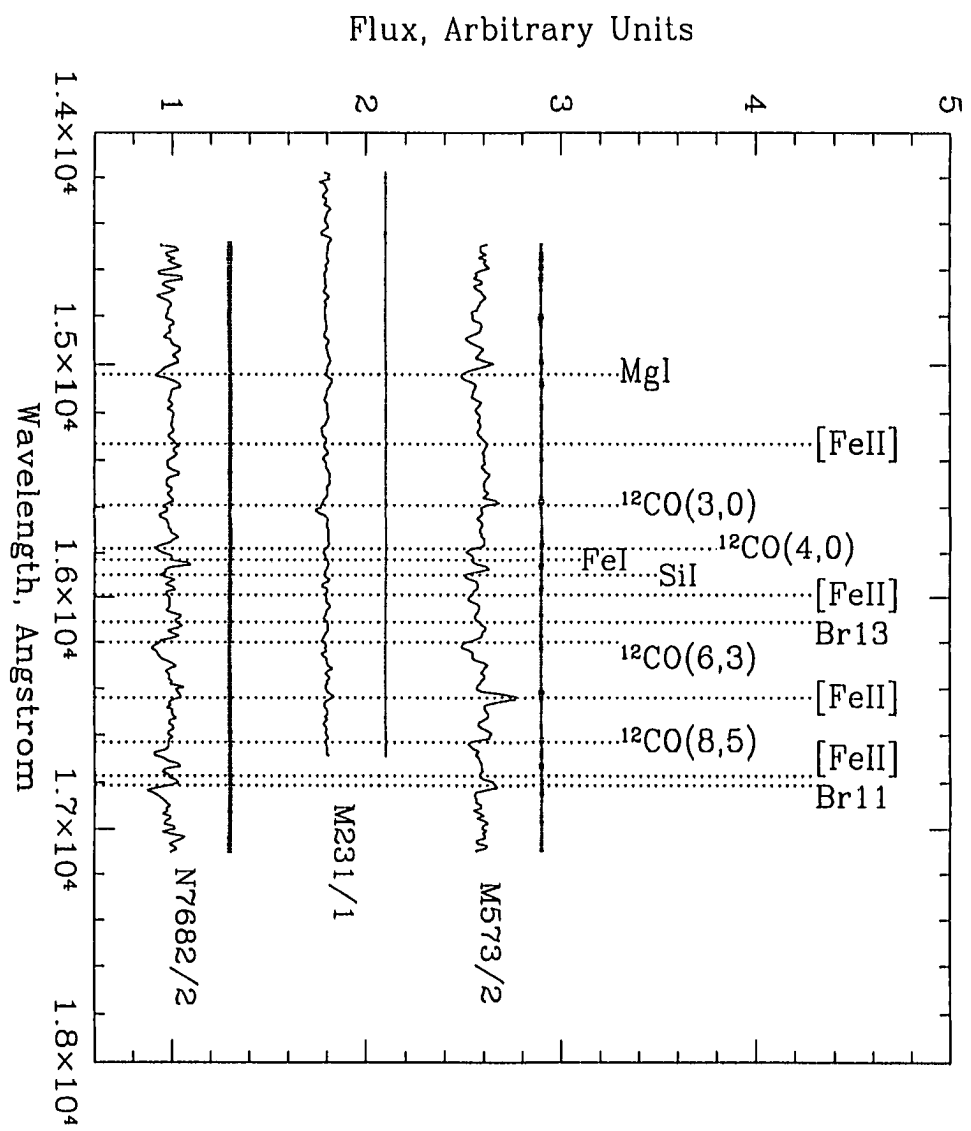
Figure 2.1 Spectra of the sample galaxies, continuum-divided and shifted vertically for display purposes, in order of increasing R.A. 1σ noise spectrum (see section 2.1) is shown above each spectrum. The galaxy names and Seyfert types are indicated. Vertical dot lines show some features of interest. (a)-(d) K-band spectra. (e) H-band spectra.











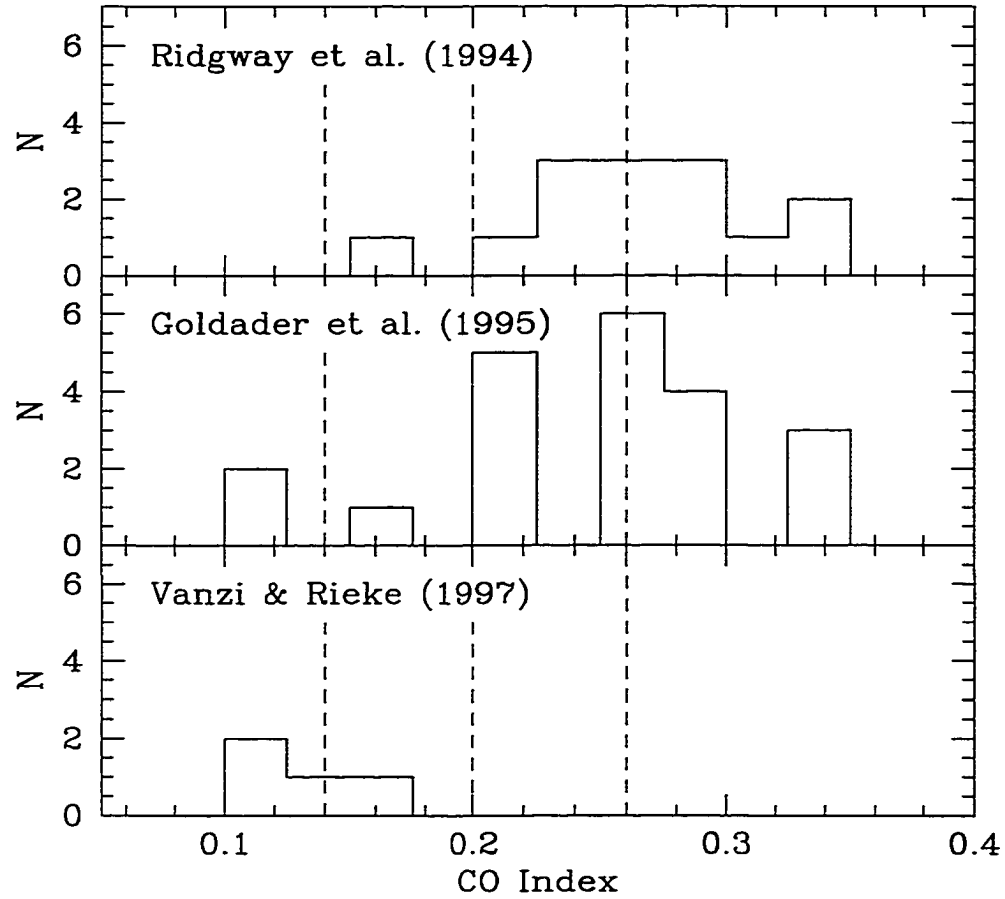
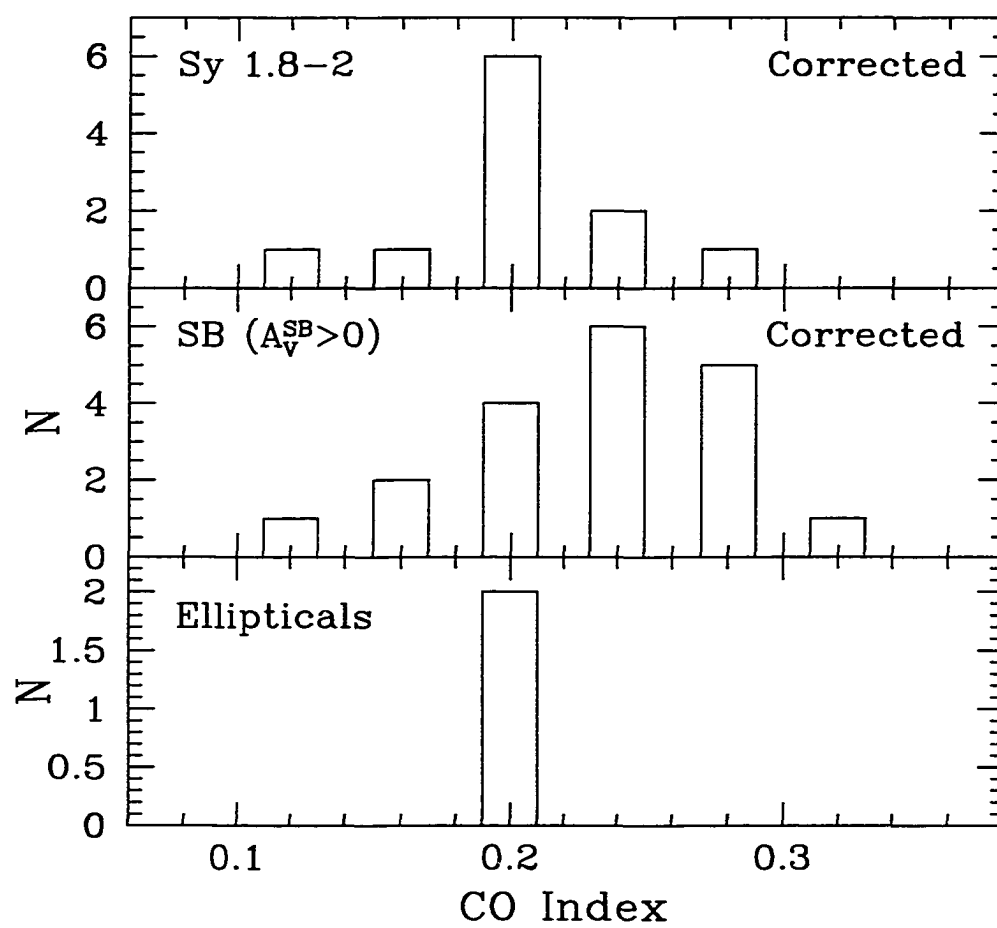


Figure 2.2 Distributions of the spectroscopic CO indices of star forming galaxies from Ridgway et al. (1994) in the top panel, Goldader et al. (1995) in the middle panel, and Vanzi & Rieke (1997) in the bottom panel. The vertical dashed lines indicate the average CO index for *normal* galaxies from Ridgway et al. (1994), and the corresponding 3σ limits.

Figure 2.3 Histograms of the observed and corrected values of the CO index. (a) Type 1-1.5 Seyferts - dotted line, Type 1.8-2 Seyferts - solid line, starbursts - dashed line. The top panel shows the observed CO indices in all classes of galaxies. The middle panel shows the CO indices corrected for dilution - starting from K-band neglecting the reddening ($A_V = 0$) in starbursts. The bottom panel shows again the corrected CO indices but the colors of starburst have been dereddened prior to the CO correction. Ticks on the horizontal axis show the bin borders. The ellipticals fall into 0.18-0.22 bin. See section 3.1 for details. (b) Distributions of CO indices used for the comparison analysis and simulations. The top panel shows the dilution corrected CO indices of Seyferts. The middle panel shows the same for starbursts (with reddening taken into account). The bottom panel shows the location occupied by the ellipticals, which represent a typical red giant dominated stellar population.



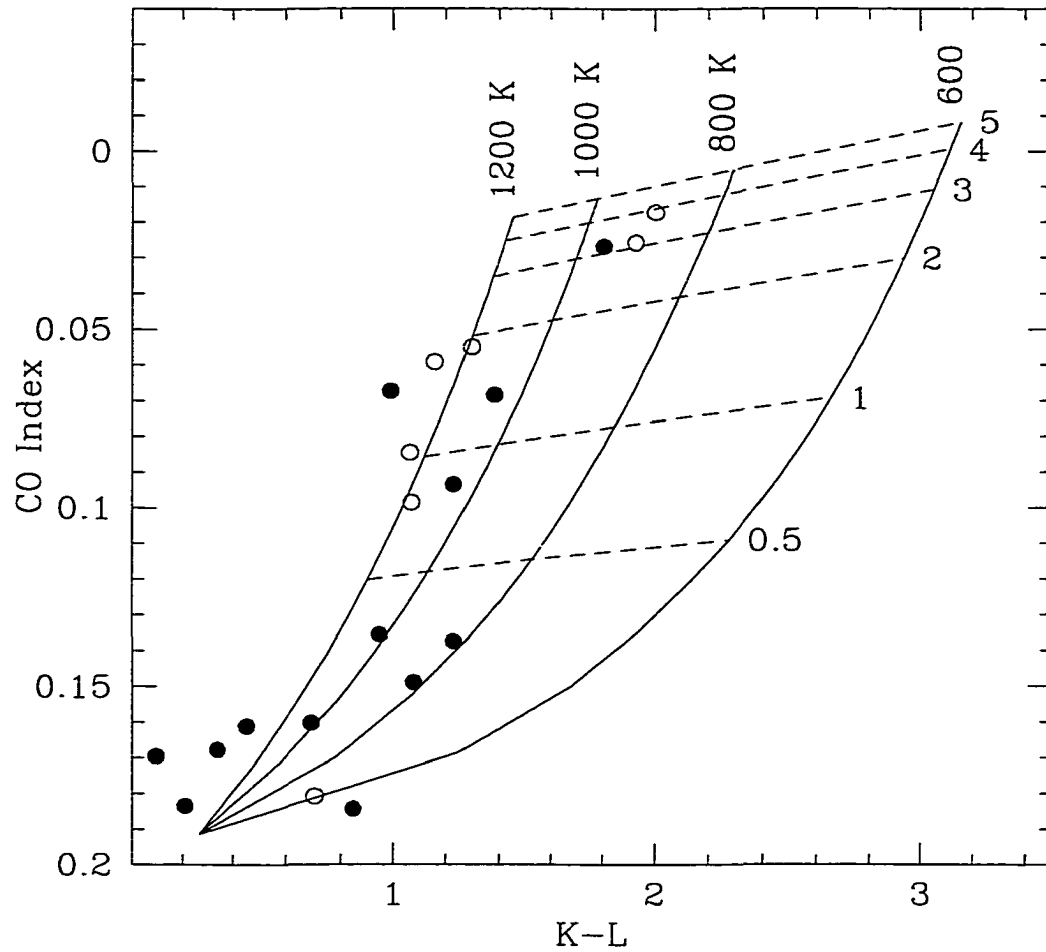


Figure 2.4 CO index versus $K-L$ diagram. The solid dots represent Seyfert galaxies of Type 1.8 and later, and the open circles represent the earlier Type Seyfert galaxies. The grid represents the CO index and infrared colors of a combination of an elliptical galaxy spectrum and a diluting black body (solid lines, the temperature is labeled on the top) spectrum, in various ratios (dashed lines, the black body-to-elliptical spectrum ratio is labeled on the right).

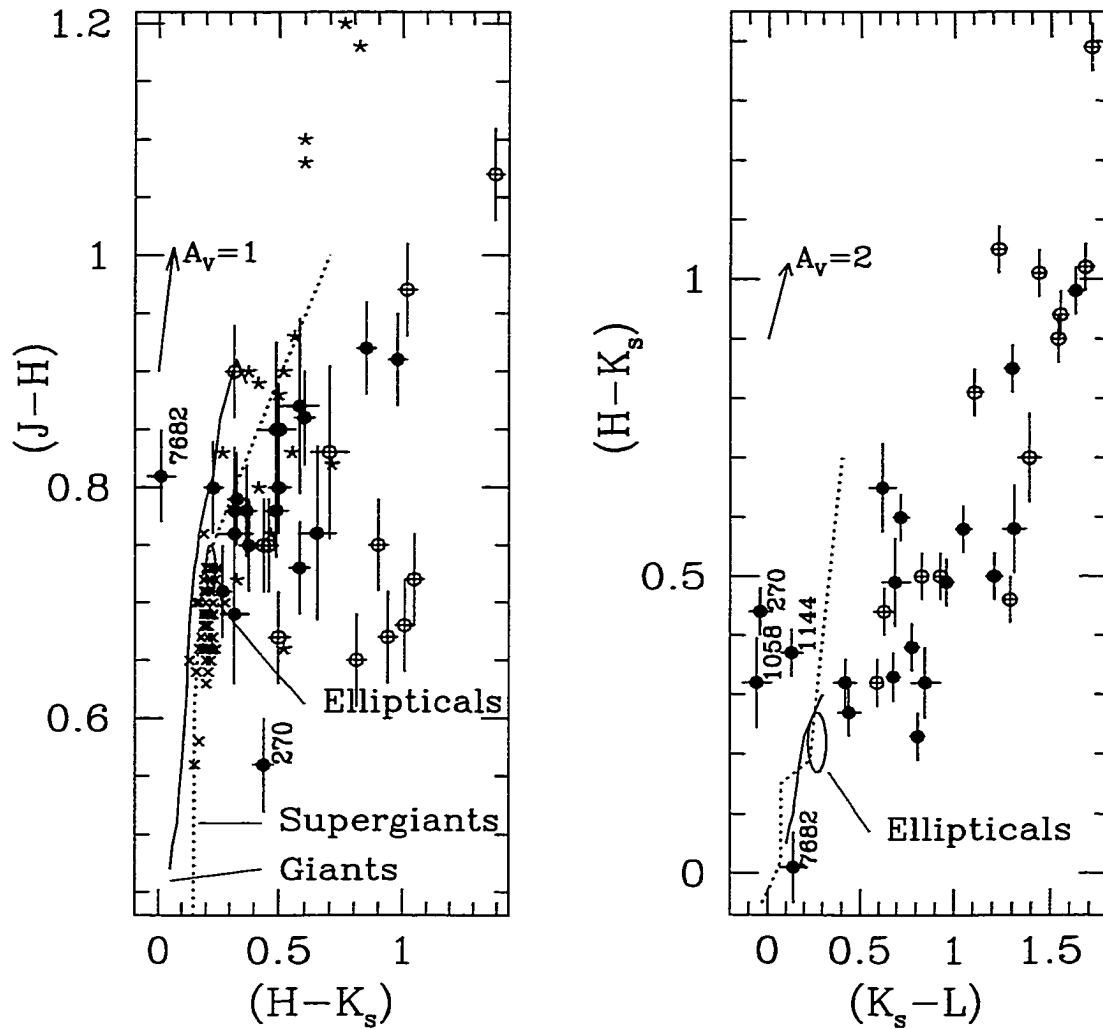


Figure 2.5 Infrared color-color diagrams for our Seyfert galaxies, with 1σ errors. Solid dots represent Seyferts 1.8 and later, and open circles represent earlier Seyferts. Crosses and stars are ellipticals (Frogel et al. 1978) and starbursts (Engelbracht 1997), respectively. The oval loci represent the adopted colors of ellipticals and their uncertainties. Giant (G5-M8) and supergiant (B0-M5) sequences are indicated (Johnson 1966, Frogel et al. 1978). See section 3.2 for details.

3. NEAR INFRARED EMISSION PROPERTIES OF THE CFA SEYFERTS

3.1. Introduction

Emission line properties of active galaxies have been a subject of intense studies in the optical (e.g. Veilleux & Osterbrock 1987; Corbin, Baldwin, & Wilson 1988; Whittle et al. 1988). They took advantage of the diagnostic power of the collisionally excited forbidden lines like [OIII], [NII], [SII] and [OI], produced mostly in the partially ionized regions of AGNs. These regions are larger in active galaxies than in starbursts because the AGNs produce more higher energy photons than stars. Subsequently, polarimetric diagnostics led to such great advances as the development of the unified model (Antonucci 1983; Antonucci & Miller 1985) that combines the two classes of Seyferts by means of an obscuring torus, observed under different viewing angles.

Optical studies are subject to severe limitations due to the extinction. In the dusty central environment in Seyfert galaxies the optical extinction A_V toward the circumnuclear stellar populations can easily exceed 3-5 mag, and prevent the observers from sampling the innermost regions, ensuring that the spectral lines originate in different spatial regions depending on their wavelength. The obvious way to circumvent this difficulty is to shift the observational effort towards the

infrared where the extinction decreases tenfold in magnitudes (a factor of 10,000 in terms of flux), compared to the optical ($A_K = 0.112 \times A_V$; Rieke & Lebofsky 1985).

The rapid development of the infrared instrumentation in the recent years has led to the collection of a considerable amount of data on emission line properties of active galaxies in the near-infrared. The JHK atmospheric windows offer hydrogen recombination lines ($\text{Pa}\beta$ at $1.2818 \mu\text{m}$, $\text{Br}\gamma$ at $2.1655 \mu\text{m}$), some low and high ionization metal emission lines ($[\text{FeII}]$ at $1.2567 \mu\text{m}$, $1.321 \mu\text{m}$, $1.328 \mu\text{m}$, $1.533 \mu\text{m}$, $1.599 \mu\text{m}$, $1.644 \mu\text{m}$, $1.677 \mu\text{m}$; $[\text{SiX}]$ at $1.2524 \mu\text{m}$; $[\text{SiVI}]$ at $1.962 \mu\text{m}$), and a number of molecular hydrogen lines ($1.493 \mu\text{m}$, $1.510 \mu\text{m}$, $1.601 \mu\text{m}$, $1.613 \mu\text{m}$, $1.732 \mu\text{m}$, $2.033 \mu\text{m}$, $2.073 \mu\text{m}$, $2.121 \mu\text{m}$, $2.154 \mu\text{m}$, $2.223 \mu\text{m}$, $2.247 \mu\text{m}$).

Here we analyze the infrared emission lines for 46 members of the Seyfert CfA sample, and compare them with previous observations. The major goals of this study are: (i) to take advantage of the completeness of the Seyfert sample to explore the AGN versus starburst discrimination power of various line ratios, and (ii) to address the question of the nature of the energy source in Ultraluminous Infrared Galaxies (ULIRG), comparing our sample and the complete sample of ULIRGs from Murphy et al. (2000).

3.2. Previous Work

The pioneering works by Blanco, Ward, & Wright (1990), Hines (1991), and Nakajima, Carleton, & Nishinda (1991) used low resolution ($R=200\text{-}300$) near-infrared spectroscopy to look for broad hydrogen emission lines hidden by dust at optical wavelengths. Goodrich et al. (1994) and Veilleux et al. (1997) provided the first high quality, high-resolution ($R=1200\text{-}1400$) comprehensive sample of 33 J and K-band spectra of Seyfert galaxies. They found broad emission lines in about a

fifth of the sample. This detection rate was consistent with both the unified and the dusty wind model (Königl & Kartje 1994) of Seyferts.

Simpson et al. (1996) showed that the $([\text{FeII}] \ 1.257 \ \mu\text{m})/\text{Pa}\beta$ ratio, similar to the $([\text{OI}] \ 6300\text{\AA})/\text{H}\alpha$ ratio, provides a good - although not perfect - separation of Seyfert and starburst galaxies. Alonso-Herrero et al. (1997) extended that conclusion to the $([\text{FeII}] \ 1.644 \ \mu\text{m})/\text{Br}\gamma$ ratio. The discriminating power of these ratios comes from the difference in the ionizing UV flux produced in AGNs and starbursts. The harder spectra of the Seyferts, with more hydrogen ionizing photons, penetrate deeper in the host galaxy interstellar matter, producing more extended photodissociation regions in comparison to the starburst. The later resemble ordinary HII regions where the transition from fully ionized to neutral hydrogen is abrupt.

The major advantage of the pure infrared ratios over the optical ones is that they suffer less extinction, and include lines which are relatively close in wavelength, and henceforth are subject to the same extinction. One potential problem with this diagnostic is seen in the imaging spectroscopy of the composite Seyfert-starburst galaxy NGC 7469 (Genzel et al. 1995). Although both $[\text{FeII}] \ 1.644 \ \mu\text{m}$ and $\text{Br}\gamma$ are centrally concentrated, the latter shows an extended component, most likely related to the circumnuclear star formation region. The extended hydrogen emission profile may cause aperture dependent effects in the interpretation of line ratios.

Even earlier, Moorwood & Oliva (1988) proposed to use a pure infrared line ratio-based diagram: $([\text{FeII}] \ 1.644 \ \mu\text{m})/\text{Br}\gamma$ versus $(\text{H}_2 \ 2.12 \ \mu\text{m})/\text{Br}\gamma$, to separate the starbursts and AGNs. Unfortunately no obvious separation was found in their sample of 35 galaxies. Hill et al. (1999) confirmed this conclusion with a sample of better spectra, and tried sulfur-based ratios with the same negative

result. Knop (1997) demonstrated a correlation between $(\text{H}_2\ 2.12\ \mu\text{m})/\text{Br}\gamma$ and $([\text{FeII}]\ 1.257\ \mu\text{m})/\text{Pa}\beta$ but pointed out that it was weaker in the nuclear than in the off-nuclear spectra, and in Type 1 Seyferts compared to Type 2 Seyferts. These differences suggest that it may be more indicative of the underlying stellar populations rather than of the nature of the central engine.

Recently, high quality data, including three-dimensional infrared spectroscopy, became available for some nearby bright Seyferts. Blietz et al. (1994) reported narrow band imaging of NGC 1068 - the prototypical Type 2 Seyfert galaxy - in $[\text{FeII}]$ at $1.6435\ \mu\text{m}$ and $\text{H}_2\ v = 1 - 0\ S(1)\ 2.1212\ \mu\text{m}$ lines. They found that the $[\text{FeII}]$ emission is more extended than the H_2 emission, and is probably produced in outflows and related to the shocks. The same group (Genzel et al. 1995) also observed NGC 7469, and extended their spatial distribution study to $\text{Br}\gamma$, HeI , $[\text{SiVI}]$ and CO. They separated the emission into three distinct sources: nucleus, circumnuclear starburst, and a stream of blue-shifted off-nucleus gas. The authors find traces of recent massive star formation in both galaxies, as well as in Mkn 231 (Krabbe et al. 1997), and NGC 3227 (Schinnerer, Eckart, & Tacconi 2000), and these results have fueled speculation about the possible AGN-starburst connection. However, NGC 1068 possesses a bar, and NGC 7469 and NGC 3227 interact with close companions (IC 5283 and NGC 3226, respectively), which are both well known mechanisms to trigger star formation in starburst galaxies. Notably, Krabbe et al. (2000) reported H and K-band imaging spectroscopy of the cD/AGN galaxy NGC 1275, and found no traces of excessive recent star formation. Finally, Mkn 231 is not a typical Seyfert galaxy. It is often cited as the prototypical ULIRG - a class of extremely gas and dust rich galaxies, with elevated star formation.

Maiolino et al. (2000) detected nuclear star forming activity in Circinus.

This is a barred galaxy, and H_2 S(1) ($1 - 0$) emission line spectroscopy suggested streaming motions along the bar which could account for feeding the AGN and contribute to triggering the nuclear starburst.

Rhee & Larkin (2000) undertook a somewhat less ambitious study estimating the dust extinction in the infrared using the $\text{Pa}\beta/\text{Br}\gamma$ ratio. After subtracting the underlying stellar continuum and deconvolving the broad and narrow line components, they concluded that the observed line ratios are consistent with case B recombination, both for narrow and broad components. The measured extinction in Type 1 Seyferts was negligible, and only the broad line components in Type 1.9 Seyferts suffered any detectable extinction. In agreement with the unified model, Type 2 Seyferts suggested much higher obscuration, to the point that in most of them both emission lines were not detected.

A new comprehensive Z, J, and K-band spectroscopy survey has been reported by Storchi-Bergmann et al. (1999) and Winge et al. (2000). They examine the spatial distribution of the emission lines, and show that while the jet driven shocks play important role in the forbidden iron lines excitation, the molecular hydrogen is primarily excited by X-rays emitted from the central engine. This result calls for a caution in interpreting line ratios.

Active nuclei and violent star formation have been considered as the possible energy sources in the ULIRG. Near-infrared spectroscopy of a large sample of ULIRGs was presented by Goldader et al. (1995, 1997a, 1997b). The data suggested that the star formation - rather than the AGN - was responsible for producing the bulk of the energy. More recently, Murphy et al. (1999, 2000) confirmed that conclusion, and pointed out that extremely high extinction, $A_V \geq 25$, mag was necessary to hide an active nuclei emitting half of the bolometric luminosity.

LINERS (Low Ionization Nuclear Emission-line Region galaxies) posed a similar problem. While Alonso-Herrero et al. (1999) demonstrated that the emission line properties of many LINERs could be explained in terms of post-starburst evolution. Larkin et al. (1998) divided them into two categories, and considered "weak" [FeII] LINERs prime candidates for low-luminosity Seyfert nuclei. The AGN hypothesis finds further support in K-band spectral modeling and X-ray variability, at least for some objects (e.g. Schinnerer, Eckart, & Boller 2000). The question of the nature of LINERs remains open, and future near infrared spectroscopic studies might help to achieve a definitive answer.

Despite of the significant scope of observations collected through the years, the sample selection has remained a major problem. Usually the observed objects include just the brightest Seyferts, which introduces a strong bias towards galaxies with strong star formation. Even if a small fraction of the galaxy mass is turned into young stars, it easily can account for a sizable fraction of the bolometric luminosity. For example, the dynamical mass of the starburst ring in NGC 7469 is only $(4.5 \pm 1) \times 10^9 M_{\odot}$, but it contributes two-thirds of the bolometric luminosity of the entire galaxy, including the AGN (Genzel et al. 1995).

The answer to that problem is to use the an unbiased sample of Seyfert galaxies - the CfA Seyfert sample (Huchra & Burg 1992). This is a complete sample of 48 Seyferts. Although its degree of completeness has been questioned by the recent discovery that so called "dwarf" Seyfert nuclei are present in as much as 20% of the galaxies (Maiolino & Rieke 1995, Ho, Filippenko & Sargent 1997), the CfA Seyfert sample remains the most unbiased Seyfert sample to date. For correctness, we will limit our conclusions to "classical" Seyfert galaxies, represented by NGC 1068, NGC 4105, etc. Here we report the first study of the infrared

emission line properties of 46 out of the 48 CfA Seyfert galaxies, and carry out a detailed comparison with properties of other classes of emission line galaxies from the literature.

3.3. Data Reduction and Line Measurements

3.3.1. Observations and Data Reduction

The infrared spectra were taken at the original MMT and Steward Observatory 2.3m and 1.55m telescopes, with FSpec (Williams et al. 1993), with slit widths 1.2, 2.4 and 3.6 arcsec, and plate scales 0.4, 1.2, and 1.8 arcsec/pixels, respectively. The extraction aperture was 2 pixels wide. We used three different settings with spectral resolution $R \sim 700$, 1200, and 3000. The emission line measurements reported in this paper are based solely on our $R \sim 700$ data because the rest lack the necessary spectral coverage. The atmospheric correction was carried out by observing a solar analog, following (Maiolino, Rieke & Rieke 1996). The observing log, the signal-to-noise ratios, and more details of the data reduction, including the error analysis, are given in Chapter 2.

3.3.2. Continuum Subtraction

In the near-infrared spectral region of Seyfert galaxies, the continuum consists of two components: (i) stellar continuum with absorption featureless, which is a luminosity and absorption weighted combination of the spectra of stars in the galaxy, and (ii) a featureless continuum produced in the circumnuclear region, most probably by warm dust.

The continuum subtraction is essential to measure accurately the emission lines in the spectra of galaxies because it removes the underlying absorption

features. We carried it out by subtracting a stellar template, corrected for the non-stellar component.

We demonstrated in our analysis of the dilution-corrected strength of the CO index at $2.3 \mu\text{m}$ Chapter 2 that once the featureless continuum is subtracted, the remaining spectrum for most of the Seyfert galaxies is consistent with old stellar populations, rather than with populations dominated by young stars. This result implies that the dilution can be determined to first order by a simple comparison of the observed Seyfert CO band strength (see Table 2.3) with the typical CO band strength of elliptical galaxies ($\text{COindex}^{\text{elliptical}} = 0.20 \text{ mag}$, Chapter 2). We assigned zero non-stellar component in the galaxies with CO indices stronger than 0.20 mag . The estimated non-stellar fraction F_K of the total K-band flux is given in Table 3.1. Note that our narrow spectroscopic CO index (Chapter 2) is very close to the photometric CO index.

First, we had imposed on the spectra a continuum slope determined from the aperture photometry, because the intrinsic continuum shape is difficult to recover after the telluric absorption correction (see Chapter 2 for details). For the few remaining spectra without photometry, we carried out the dilution correction procedure on the spectra with the observed continuum slopes. Then the dilution was removed by subtracting a flat continuum (in F_λ units, same as the spectra), normalized to F_K , from the Seyfert spectra.

The next step was to subtract the stellar continuum. To explore the possibility of different underlying stellar populations, we tried two stellar continua: (i) a combination of the elliptical galaxies spectra from Chapter 2, and (ii) a template of stellar spectra from our library (Chapter 4) combined to match the CO absorption in NGC 253 (Engelbracht, 2000). Even better templates can be constructed in the

future, using the library in conjunction with the modified evolutionary synthesis model Starburst99 (Chapter 5).

The starburst template has typically $\sim 10 - 15\%$ stronger features. We smoothed the templates to match the velocity dispersions of the Seyfert. We used the velocity dispersions from de Vaucouleurs et al. (1991), and if those were not available, we assumed $\sigma_V = 250 \text{ km s}^{-1}$. Whenever necessary, we adjusted the velocity dispersion of the template to minimize the residuals from the subtraction near the CO band head. Next, we divided the template spectra by low-order polynomial continuum fits, and imposed the same continuum slopes as for the individual Seyfert galaxies. The result was a set of emission line spectra, with zero continuum level. The spectra of Seyferts with K-band imaging from McLeod & Rieke (1995) were flux calibrated by measuring the fluxes within rectangular slit-apertures (Chapter 2 for details). For each Seyfert galaxy we obtained a set of six spectra - with and without the dilution correction; with no continuum subtraction, or with subtracted elliptical or starburst stellar continua.

3.3.3. Infrared Line Measurements

We measured the line fluxes, and full widths at half maximum (FWHM) on the continuum subtracted spectra, and the equivalent widths on the spectra with continua, using the *splot* task from *IRAF*. The dominant source of error was the continuum placement. To estimate it, we carried out multiple measurements and determined their dispersion. The data for narrow $\text{Br}\gamma(2.16 \mu\text{m})$ and $\text{H}_2(2.12 \mu\text{m})$, and their uncertainties are shown in Table 3.2. Broad $\text{Br}\gamma$ seemed to appear in some spectra, but the detections were uncertain, and we refrained from line decomposition. For broad line detections in the CfA Seyferts see Knop (1997).

The choice of the stellar continuum (elliptical versus starburst template) did not make a significant difference for $\text{Br}\gamma(2.16\ \mu\text{m})$ and $\text{H}_2(2.12\ \mu\text{m})$ because they are stronger compared to the underlying stellar absorption features. Hence, we include in Table 3.2 only the fluxes for the elliptical stellar template. The FWHM is measured only on the original spectra since carrying out the dilution correction and the continuum subtraction led to identical measurements, within the observational errors. To correct the observed FWHMs for the instrumental profile, we assumed that the latter is a Gaussian with $\text{FWHM} = 430\ \text{km s}^{-1}$, and subtracted it from the observed FWHM in quadrature. Any effects from residuals from the sky emission lines were neglected.

Our emission line ratio $\text{Br}\gamma/\text{H}_2$ and FWHM measurements are compared to the available data from the literature on Figure 3.1. The uncertainties are typically of order of 10-20 %. The majority of the observations are consistent, with the exception of Mkn 573 from Winge et al. (2000) (the triangle symbols), and Mkn 533, for which Veilleux, Goodrich, & Hill (1997) report an extremely strong $\text{Br}\gamma$ (filled square on the left panel). The spatially resolved infrared spectroscopy of Knop (1997) (circles) is the most consistent with our observations. Finally, we will point out that some spread is to be expected because of the different slit sizes and orientations used in various studies. Some measurements of additional emission lines are reported in Table 3.3.

3.4. Results

3.4.1. $\text{Br}\gamma$ and $\text{H}_2\ v = 1 - 0\ S(1)\ 2.12\ \mu\text{m}$

The $\text{Br}\gamma$ and $\text{H}_2\ 2.12\ \mu\text{m}$ are present in most of the galaxies from our sample. Figure 3.2 compares the strengths of $\text{H}_2\ 2.12\ \mu\text{m}$ and $\text{Br}\gamma$ for our sample, and a

set of AGNs, LINERS, and starburst galaxies from the literature.

The H_2 2.12 $\mu\text{m}/\text{Br}\gamma$ ratio can provide a test of whether the UV excitation from the central engine in Seyferts is the main source of H_2 excitation. Pure UV excitation models predict H_2 2.12 $\mu\text{m}/\text{Br}\gamma$ ratio of 0.05-0.1 and smaller (Fischer et al. 1987; Moorwood & Oliva 1990; Kawara, Nishida, & Gregory 1990; Doyon, Joseph, & Wright 1994a; Moorwood & Oliva 1994).

The H_2 excitation mechanism in starburst galaxies is poorly understood. At one extreme, Luhman et al. (1994) demonstrated that the UV radiation from OB stars accounts for about 98-99% of the H_2 emission in Orion A molecular cloud, a prototypical site of active star formation. Usuda et al. (1996) studied the Orion Nebula and concluded that shock excitation caused by wind from young stellar objects contributes a significant part of the observed H_2 emission, at least in some regions of the Orion nebula. The H_2 2.12 $\mu\text{m}/\text{Br}\gamma$ ratio they quote for the photodissociation regions is 0.17, close to the values observed in the blue dwarf galaxies of Vanzi et al. (1996), and Vanzi & Rieke (1997), but smaller than that in the more massive star forming galaxies from the sample of Engelbracht (1997).

The Seyferts in our sample tend to show slightly stronger H_2 2.12 μm than the starbursts, at a given $\text{Br}\gamma$ (Figure 3.2, top panels), in agreement with Kawara, Nishida, & Gregory (1990). This result suggests that the shock excitation of the molecular hydrogen tends to be relatively more important in active galaxies than in the starbursts, perhaps due to the stronger shocks driven by the nuclear jets, encountering the ambient interstellar matter.

The few LINERs from Larkin et al. (1998) concentrate in a tight group well away from the rest of the galaxies, but we would refrain from further conclusions because their infrared line ratios were derived from the optical ones after corrections

for the relative optical-to-infrared extinction and the different aperture sizes.

We also tested whether the absolute line fluxes (at 10 kpc) of H_2 2.12 μm and $\text{Br}\gamma$ correlate with their ratio, and found no apparent relation (Figure 3.2, bottom panels). The Seyferts tend to be a relatively more homogeneous class of objects, spanning a narrower range of absolute fluxes compared to the starburst galaxies which extend to fainter fluxes. We contribute this to the larger spread of parameters of the starbursts, related to their ages.

The H_2 2.12 $\mu\text{m}/\text{Br}\gamma$ ratio has to be considered with caution because the two lines probably originate in different regions. The atomic hydrogen is closer to the central engine, where the UV field is stronger and the conditions are too harsh for molecular hydrogen. This also implies that the radiation in the two lines suffers different extinction, complicating the interpretation even further. The lower extinction in the infrared partially alleviates this problem, making the infrared line ratios a better tool to probe the circumnuclear regions in Seyferts than the optical emission lines. Multiple emission line ratios are necessary to investigate the excitation mechanism and extinction. However, the specific combination of redshifts and wavelength coverage, together with the insufficient signal-to-noise ratio permit to measure additional molecular hydrogen lines only in a few of the galaxies in our sample. They will be discussed in a separate paper (Groppi, Ivanov & Rieke 2001).

3.4.2. Separating Seyfert and Starburst Activity

The problem of separating the Seyfert and starburst activity in galaxies is hampered by the similarity of their line ratios (for a recent review see Hill et al. 1999). We combined our data with some optical and infrared line measurements

from the literature to compare the emission line behavior in these two classes of galaxies. Figure 3.3 shows Oxygen-to-hydrogen and iron-to-hydrogen line ratios versus $\text{H}_2\ 2.12\ \mu\text{m}/\text{Br}\gamma$. We find only weak trends among the Seyfert galaxies, and some separation between them and the starbursts. The stronger [OI] and [OIII] emission in Seyferts is expected, because the central engines produce harder ionizing spectra compared to the starbursts, with more UV photons, capable of producing a more extended partially ionized regions, where these lines originate. An underlying assumption here is that the central regions of both Seyferts and starburst galaxies are gas rich, so the ionizing regions are limited by the number of ionizing photons, rather than by the amount of gas to be excited. Indeed, all the galaxies under consideration here are gas rich spirals or irregulars, and safely satisfy this assumption. Similarly to Hill et al. (1999), who find correlation on the $[\text{FeII}]^{1.64}\ \mu\text{m}/\text{Br}\gamma^{2.16}\ \mu\text{m}$ versus $\text{H}_2^{2.121}\ \mu\text{m}/\text{Br}\gamma^{2.16}\ \mu\text{m}$ plot, we see a correlation on the $[\text{FeII}]^{1.26}\ \mu\text{m}/\text{Pa}\beta^{1.28}\ \mu\text{m}$ versus $\text{H}_2^{2.121}\ \mu\text{m}/\text{Br}\gamma^{2.16}\ \mu\text{m}$ plot, although in our case the Seyfert versus starburst separation is somewhat more obvious. This analysis is somewhat hampered by the different aperture sizes of the literature data and our observations.

3.4.3. Power Sources in the Ultraluminous Infrared Galaxies

The ULIRGs represent a different direction of the same separation problem. Generally they feature heavily disturbed morphologies, which are typical for the late stages of mergers (Surace, Sanders & Evans 2000; Scoville et al. 2001), and merging is known to trigger active star formation. Recent radio, optical and X-ray observations have revealed the presence of obscured active nuclei in several of these galaxies (e.g. Smith et al. 1998; Veilleux, Sanders & Kim 1999; Risaliti et al. 2000). Soifer et al. (2000) reported the presence of compact mid-infrared structures

in the centers of six out of seven observed ULIRGs, which also indicated hidden AGNs. However, the ISO observations (Genzel et al. 1998, Lutz et al. 1998) led to a conclusion, that most of ULIRGs are powered by massive young starbursts.

To address the question of the nature of the nuclear energy source, we compared the emission line strengths in the complete Seyfert sample to the complete sample of ULIRGs from Murphy et al. (2000). Figure 3.4 shows the histograms of the equivalent widths EW and full widths at half maximum FWHM for $\text{Br}\gamma$ and H_2 2.12 μm for the CfA Seyfert sample, the complete sample of ULIRGs (Murphy et al. 2000), and a sample of bright nearby starburst galaxies (Engelbracht 1997). Seyfert galaxies tend to have stronger emission lines than the ULIRGs, but weaker than the typical starbursts. The FWHM comparison is less reliable because of the different instrumental resolutions of each survey. We carried Kolmogorov-Smirnov test on the equivalent width distributions, to quantify the similarity of the three sets. The probabilities that distributions are drawn from the same parent distribution are shown in Table 3.4 (low values indicate that they are intrinsically different). The probabilities are low, suggesting that all three sets are indeed different, particularly in terms of the $\text{Br}\gamma$ strength. Our result renders unlikely the hypothesis that all ULIRGs are powered by hidden AGNs, in agreement with the lack of $[\text{SiVI}]$ emission and broad component of hydrogen recombination lines found by Murphy et al. (2000).

An extreme cautions should be exercised while comparing data from different surveys, spanning different areas of the parametric space, obtained with different instruments, and reduced with different techniques. However, in this case, the main bias of the two surveys - the redshift span - only strengthen our result. The majority of Seyfert galaxies in the CfA sample have redshifts less than $z < 0.04$.

Murphy et al. (2000) imposed on their data a constraint $0.055 < z < 0.108$. The expected observational bias would lead to intrinsically stronger (with larger equivalent widths) emission lines in the more distant sample than in the local one, simply because the intrinsically weaker objects would fall below the sensitivity limit of the more distant survey first. However, our Kolmogorov-Smirnov test demonstrates that their sample shows lower equivalent widths than ours on a statistically significant level (see also Figure 3.4).

Murphy et al. (2000) used the $\text{Pa}\alpha/\text{Br}\gamma$ line ratio to estimate the extinction of their sample of ULIRGs, and obtained extremely high values, with the distribution peaking at about $A_V \sim 8 \pm 5$ mag. This corresponds to $A_K \sim 0.9 \pm 0.6$ mag which is equivalent to K-band optical depth $\tau_K \sim 0.8 \pm 0.5$. Naturally, the extinction of regions with $\tau_K > 1$ can not be probed by means of these two emission lines, because the emission that originates in the center would be completely reprocessed by the intervening material. Instead, the lines would probe the outer parts of the galaxy. This easily could be the case with about $\sim 1/3$ of the ULIRGs in the Murphy et al. (2000) sample, because according to their A_V distribution (their Figure 4), about a third of the galaxies satisfy the K-band optical thickness condition. Therefore, $\sim 1/3$ of the ULIRGs sample may contain AGNs, completely obscured by the dust in the K-band. We refrain from further conclusions based on the Seyfert-starburst comparison, because the starburst sample was selected somewhat arbitrarily (see Engelbracht 1997 for details).

3.5. Summary

For the first time we assembled a set of K-band emission line data for a complete set of 46 Seyferts selected from the CfA Seyfert sample. We found the behavior

of $\text{Br}\gamma$ 2.16 μm and H_2 2.12 μm similar to that of previously studied Seyfert galaxies. We explored the starburst versus Seyfert diagnostic power of a number of optical-infrared and infrared-infrared line ratio diagrams and found a good correlation on the $[\text{FeII}]^{1.26} \mu\text{m} / \text{Pa}\beta^{1.28} \mu\text{m}$ versus $\text{H}_2^{2.121} \mu\text{m} / \text{Br}\gamma^{2.16} \mu\text{m}$ diagram, which also offers a better Seyfert versus starburst separation than previously thought (Hill et al. 1999). Finally, we addressed specifically the question if the ULIRGs have hidden AGNs by comparing our complete Seyfert sample with the complete ULIRGs sample of Murphy et al. (2000). The probability that the distributions of the $\text{Br}\gamma$ equivalent widths are drawn from the same parent distribution is only $\sim 1\%$. We concluded that the emission line properties of the two samples are significantly different, which implies that at least $\sim 2/3$ of the ULIRGs are not powered by AGNs. The other $\sim 1/3$ can still harbor AGNs, completely obscured in the K-band.

Table 3.1 Estimated non-stellar fraction F_K of the total K-band flux.

Gal.	F_K
Mkn334	0.63
0048+29	0.08
Mkn993	0.00
Mkn573	0.23
0152+06	0.18
Mkn590	0.68
NGC1144	0.23
Mkn3	0.00
NGC2273	0.33
NGC3081	0.00
Mkn1243	0.79
NGC3227	0.48
1058+45	0.00
NGC3516	0.68
Mkn744	0.53
NGC3982	0.13
NGC4051	0.68
NGC4151	0.94
NGC4235	0.53
Mkn766	0.89
NGC4258	0.08

Gal.	F_K
NGC4388	0.53
Mkn231	0.94
NGC5033	0.28
Mkn789	0.33
1335+39	0.79
NGC5252	0.48
Mkn266	0.13
Mkn270	0.43
NGC5273	0.00
Mkn461	0.03
Mkn279	0.84
NGC5427	0.73
NGC5548	0.84
NGC5674	0.28
Mkn686	0.18
Mkn841	0.89
NGC5929	0.13
NGC5940	0.84
1614+35	0.73
IIZw136	0.94
2237+07	0.68
NGC7469	0.00
Mkn530	0.68

Table 3.2 Effective widths and line fluxes of narrow Br γ (2.16 μm) and H $_2$ (2.12 μm) for the CfA Seyfert sample.

Gal.	λ_c	$c\ z$	Br γ (2.16 μm)									
	μm	km/s	EW ₀	F ₀	fwhm ₀	F ₀ ^{cs}	EW _d	F _d	F _d ^{cs}			
(1)	(2)	(3)	(4)	(5)	(6)	(7)	(8)	(9)	(10)			
			H ₂ (2.12 μm)									
			EW ₀	F ₀	fwhm ₀	F ₀ ^{cs}	EW _d	F _d	F _d ^{cs}			
			(11)	(12)	(13)	(14)	(15)	(16)	(17)			
M334	2.25	6582	-6.5	0.88.4	1.0	349 14	8.0 0.6	-18.4 2.4	8.9 1.1	8.2 0.8		
			-2.0	0.22.5	0.2	107 28	3.1 0.3	-5.4 0.6	2.5 0.3	3.1 0.3		
0048+29	2.25	10770	-3.1	1.21.5	0.6	489 69	1.0 0.2	-3.2 0.6	1.4 0.3	1.0 0.2		
			-1.2	0.20.6	0.1	≤ 430	0.9 0.1	-1.4 0.3	0.6 0.1	1.0 0.2		
M573	2.25	5174	-4.8	0.74.2	0.6	349 42	4.2 0.6	-6.4 1.1	4.3 0.7	4.4 0.6		
			-3.2	0.62.9	0.5	≤ 430	3.1 0.3	-4.4 0.7	3.0 0.4	3.2 0.3		
0152+06	2.25	5208	-5.9	0.72.0	0.2	≤ 430	1.8 0.3	-7.1 0.9	1.9 0.2	1.9 0.2		
			-4.3	0.81.5	0.3	279 28	1.7 0.3	-5.8 1.0	1.6 0.3	1.8 0.2		
M590	2.25	7910	-1.8	0.24.4	0.8	155 55	3.6 0.4	-7.7 1.1	5.0 0.6	3.8 0.4		
			-1.0	0.41.6	0.7	0 0	0.8 0.1	-1.8 0.5	0.9 0.3	0.8 0.2		
M1243	2.25	10608	-2.5	0.70.3	0.1	0 0	0.3 0.1	-16.7 2.6	0.4 0.1	0.3 0.1		
			-2.7	0.40.4	0.1	≤ 430	0.5 0.2	-14.1 3.1	0.4 0.1	0.5 0.1		
N3227	2.20	1157	-6.2	0.76.2	0.7	1199 42	5.2 0.4	-10.3 1.2	5.4 0.6	5.5 0.6		
			-4.6	0.24.7	0.2	412 14	4.5 0.2	-9.2 0.5	4.8 0.2	4.6 0.2		
1058+45	2.20	8778	-5.1	0.60.7	0.1	≤ 430	0.8 0.1	-6.1 0.7	0.9 0.1	0.7 0.1		
			-4.0	0.70.6	0.1	≤ 430	0.8 0.1	-4.8 0.6	0.7 0.1	0.7 0.1		

Gal.	λ_c	$c z$	----- Br γ (2.16 μm) -----									
	μm	km/s	EW ₀	F ₀	fwhm ₀	F ₀ ^{cs}	EW _d	F _d	F _d ^{cs}			
(1)	(2)	(3)	(4)	(5)	(6)	(7)	(8)	(9)	(10)			
			----- H ₂ (2.12 μm) -----									
			EW ₀	F ₀	fwhm ₀	F ₀ ^{cs}	EW _d	F _d	F _d ^{cs}			
			(11)	(12)	(13)	(14)	(15)	(16)	(17)			
M744	2.25	2678	-0.8 0.1	0.4 0.1	≤ 430	0.5 0.1	-2.2 0.3	0.5 0.1	0.5 0.1			
			-1.9 0.2	1.0 0.1	≤ 430	1.1 0.1	-4.1 0.6	1.0 0.1	1.0 0.1			
N3982	2.20	1109	-2.1 0.4	-2.1 0.4	412 42	-2.0 0.3	-2.4 0.5	-2.1 0.4	-2.2 0.5			
			-6.4 0.4	-6.4 0.3	252 14	-6.0 0.3	-7.3 0.5	-6.3 0.4	6.1 0.3			
N4051	2.20	725	-4.9 0.5	5.3 0.5	759 42	5.4 0.4	-14.7 1.2	5.2 0.4	5.3 0.5			
			-1.4 0.3	1.6 0.3	252 14	1.8 0.2	-4.5 0.9	1.5 0.3	1.8 0.2			
N4151	2.20	995	-2.8 0.3	5.4 0.8	646 42	5.4 0.8	-40.7 6.8	5.3 0.7	5.0 0.6			
			-1.6 0.3	3.3 0.5	525 55	3.9 0.7	-31.1 5.1	3.5 0.5	4.1 0.8			
N4235	2.20	2410	0.0 0.0	0.0 0.0	0 0	0.0 0.0	0.0 0.0	0.0 0.0	0.0 0.0			
			-0.8 0.4	0.5 0.3	0 0	0.3 0.2	-1.6 0.4	0.3 0.1	0.3 0.1			
M766	2.20	3876	-5.9 0.6	4.1 0.4	775 55	-4.1 0.3	-50.3 5.8	4.1 0.3	3.9 0.2			
			-1.6 0.2	1.0 0.1	451 28	0.7 0.1	-13.9 1.2	0.9 0.1	0.8 0.1			
N4388	2.25	2524	-7.8 0.8	-7.8 0.8	371 28	-7.5 0.6	-16.2 1.5	-7.7 0.6	-7.5 0.5			
			-10.3 0.6	-10.4 0.6	392 28	-10.8 0.6	-20.0 1.3	-10.1 0.5	-10.6 0.5			
M231	2.21	12651	-0.7 0.1	3.2 0.7	≤ 430	2.7 0.4	-9.0 1.3	2.6 0.3	2.9 0.5			
			-1.3 0.3	5.2 1.1	≤ 430	4.7 0.6	-21.8 5.2	4.3 0.8	6.4 0.7			
N5033	2.25	875	-0.3 0.1	0.2 0.1	0 0	0.2 0.1	-0.5 0.2	0.2 0.1	0.2 0.1			
			-1.8 0.3	0.9 0.1	432 55	1.1 0.1	-2.8 0.4	1.1 0.1	1.1 0.1			

Gal.	λ_c	$c z$	----- Br γ (2.16 μm) -----									
	μm	km/s	EW ₀	F ₀	fwhm ₀	F ₀ ^{cs}	EW _d	F _d	F _d ^{cs}			
(1)	(2)	(3)	(4)	(5)	(6)	(7)	(8)	(9)	(10)			
			----- H ₂ (2.12 μm) -----									
			EW ₀	F ₀	fwhm ₀	F ₀ ^{cs}	EW _d	F _d	F _d ^{cs}			
			(11)	(12)	(13)	(14)	(15)	(16)	(17)			
M789	2.20	9476	-24.2 1.9-24.1 1.6 595 14	-23.4 0.8-36.9 2.5-24.4 1.3-23.6 1.1	-15.1 1.0-15.1 0.9 507 14	-13.7 0.5-20.4 1.1-13.8 0.6-14.3 0.5						
1335	2.20	6023	-2.0 0.5 2.4 0.6 ≤ 430	0.3 0.1-12.0 2.7 0.3 0.1 0.3 0.1	0.0 0.0 0.0 0.0 0 0	0.0 0.0 0.0 0.0 0.0 0.0						
+39			0.0 0.0 0.0 0.0 0 0	0.0 0.0 0.0 0.0 0.0 0.0								
N5252	2.20	6926	-2.1 0.6 0.5 0.2 0 0	0.4 0.2 -1.9 0.7 0.4 0.1 0.4 0.2	-1.8 0.5 0.4 0.1 0 0	0.4 0.1 -1.7 0.4 0.3 0.1 0.4 0.1						
M266a	2.20	8360	-12.8 1.9 2.1 0.3 727 28	1.9 0.2-15.2 2.4 2.2 0.3 2.0 0.2	-7.8 1.5 1.3 0.2 560 42	1.2 0.1 -8.6 1.6 1.3 0.2 1.3 0.1						
M266b	2.20	8360	-9.0 0.9 1.9 0.2 349 28	1.9 0.1-10.0 1.1 1.8 0.2 1.9 0.2	-5.8 0.6 1.2 0.1 432 14	1.2 0.1 -6.6 0.7 1.2 0.1 1.2 0.1						
M270	2.20	2700	-0.5 0.4 0.2 0.1 371 28	0.1 0.1 -0.6 0.4 0.1 0.1 0.2 0.1	-0.9 0.5 0.4 0.2 543 42	0.3 0.2 -1.5 0.8 0.3 0.2 0.3 0.2						
N5273	2.20	1089	-0.3 0.2 -0.3 0.2 0 0	-0.4 0.2 -0.4 0.2 -0.4 0.2 -0.4 0.2	-4.6 0.4 -4.5 0.4 279 14	-5.5 0.4 -4.6 0.5 -4.6 0.4 -5.4 0.2						
M461	2.20	4856	-5.8 0.9 1.0 0.1 711 28	1.0 0.1 -5.9 0.9 0.9 0.1 1.0 0.1	-5.3 0.8 0.9 0.1 349 28	0.7 0.1 -4.4 0.6 0.7 0.1 0.7 0.1						
M279	2.20	4856	-1.0 0.6 0.5 0.3 0 0	0.4 0.3 -2.7 1.7 0.2 0.1 0.5 0.2	-0.6 0.3 0.3 0.2 759 111	0.5 0.2-11.0 4.1 0.8 0.3 0.8 0.3						

Gal.	λ_c	$c\ z$	----- Br γ (2.16 μm) -----											
	μm	km/s	EW ₀	F ₀	fwhm ₀	F ₀ ^{cs}	EW _d	F _d	F _d ^{cs}					
(1)	(2)	(3)	(4)	(5)	(6)	(7)	(8)	(9)	(10)					
			----- H ₂ (2.12 μm) -----											
			EW ₀	F ₀	fwhm ₀	F ₀ ^{cs}	EW _d	F _d	F _d ^{cs}					
			(11)	(12)	(13)	(14)	(15)	(16)	(17)					
N5548	2.20	5149	0.0 0.0 0.0 0.0	0 0	0.0 0.0	0.0 0.0	0.0 0.0	0.0 0.0	0.0 0.0	0.0 0.0	0.0 0.0	0.0 0.0	0.0 0.0	0.0 0.0
			0.0 0.0 0.0 0.0	0 0	0.0 0.0	0.0 0.0	0.0 0.0	0.0 0.0	0.0 0.0	0.0 0.0	0.0 0.0	0.0 0.0	0.0 0.0	0.0 0.0
N5674	2.20	7442	-2.6 0.4 1.0 0.1	543 42	0.7 0.2	-4.0 0.6	1.0 0.1	0.7 0.2	-3.4 0.3 1.3 0.1	155 28	1.4 0.1	-4.4 0.5	1.2 0.1	1.4 0.1
			-3.4 0.3 1.3 0.1	155 28	1.4 0.1	-4.4 0.5	1.2 0.1	1.4 0.1	-0.6 0.4 0.1 0.1	≤430	0.2 0.1	-0.8 0.5	0.1 0.1	0.3 0.1
M686	2.20	4225	-0.6 0.4 0.1 0.1	≤430	0.1 0.1	-0.5 0.4	0.1 0.1	0.1 0.1	-0.7 0.5 0.1 0.1	≤430	0.1 0.1	-0.5 0.4	0.1 0.1	0.1 0.1
			-0.7 0.5 0.1 0.1	≤430	0.1 0.1	-0.5 0.4	0.1 0.1	0.1 0.1	-2.4 0.3 -2.4 0.3	0 0	-2.3 0.2	-22.2 2.3	-2.4 0.2	-2.2 0.2
M841	2.20	10860	-2.4 0.3 -2.4 0.3	0 0	-2.3 0.2	-22.2 2.3	-2.4 0.2	-2.2 0.2	-0.1 0.1 -0.1 0.1	451 28	-0.1 0.1	-0.9 0.5	-0.1 0.1	-0.1 0.1
			-0.1 0.1 -0.1 0.1	451 28	-0.1 0.1	-0.9 0.5	-0.1 0.1	-0.1 0.1	-2.4 0.5 0.6 0.1	629 55	0.5 0.1	-2.6 0.7	0.6 0.1	0.6 0.1
N5929	2.20	2492	-2.4 0.5 0.6 0.1	629 55	0.5 0.1	-2.6 0.7	0.6 0.1	0.6 0.1	-4.8 0.6 1.3 0.1	412 14	1.2 0.1	-5.4 0.4	1.2 0.1	1.3 0.1
			-4.8 0.6 1.3 0.1	412 14	1.2 0.1	-5.4 0.4	1.2 0.1	1.3 0.1	0.0 0.0 0.0 0.0	0 0	0.0 0.0	0.0 0.0	0.0 0.0	0.0 0.0
N5940	2.20	10122	0.0 0.0 0.0 0.0	0 0	0.0 0.0	0.0 0.0	0.0 0.0	0.0 0.0	0.0 0.0 0.0 0.0	0 0	0.0 0.0	0.0 0.0	0.0 0.0	0.0 0.0
			0.0 0.0 0.0 0.0	0 0	0.0 0.0	0.0 0.0	0.0 0.0	0.0 0.0	0.0 0.0 0.0 0.0	0 0	0.0 0.0	0.0 0.0	0.0 0.0	0.0 0.0
1614+35	2.25	8382	0.0 0.0 0.0 0.0	0 0	0.0 0.0	0.0 0.0	0.0 0.0	0.0 0.0	0.0 0.0 0.0 0.0	0 0	0.0 0.0	0.0 0.0	0.0 0.0	0.0 0.0
			0.0 0.0 0.0 0.0	0 0	0.0 0.0	0.0 0.0	0.0 0.0	0.0 0.0	0.0 0.0 0.0 0.0	0 0	0.0 0.0	0.0 0.0	0.0 0.0	0.0 0.0
IIZw136	2.25	18630	0.0 0.0 0.0 0.0	0 0	0.0 0.0	0.0 0.0	0.0 0.0	0.0 0.0	0.0 0.0 0.0 0.0	0 0	0.0 0.0	0.0 0.0	0.0 0.0	0.0 0.0
			0.0 0.0 0.0 0.0	0 0	0.0 0.0	0.0 0.0	0.0 0.0	0.0 0.0	0.0 0.0 0.0 0.0	0 0	0.0 0.0	0.0 0.0	0.0 0.0	0.0 0.0
2237+07	2.20	7375	-4.6 0.3 3.5 0.3	470 28	3.8 0.3	-16.2 1.9	4.0 0.4	4.4 0.4	-3.1 0.3 2.4 0.2	252 28	1.9 0.2	-10.0 1.0	2.4 0.2	2.0 0.2
			-3.1 0.3 2.4 0.2	252 28	1.9 0.2	-10.0 1.0	2.4 0.2	2.0 0.2						

Gal.	λ_c	$c\ z$	----- Br γ (2.16 μm) -----													
	μm	km/s	EW ₀	F ₀	fwhm ₀	F ₀ ^{cs}	EW _d	F _d	F _d ^{cs}							
(1)	(2)	(3)	(4)	(5)	(6)	(7)	(8)	(9)	(10)							
			----- H ₂ (2.12 μm) -----													
			EW ₀	F ₀	fwhm ₀	F ₀ ^{cs}	EW _d	F _d	F _d ^{cs}							
			(11)	(12)	(13)	(14)	(15)	(16)	(17)							
2237+07	2.25	7375	-2.6	0.71	9.05	≤ 430	2.9	0.7	-6.1	1.8	1.4	0.4	2.3	0.6		
			-3.5	0.62	7.05	107	28	2.1	0.2	-10.6	1.0	2.5	0.2	2.0	0.1	
M530	2.20	8851	-2.6	0.62	6.06	107	55	2.3	0.5	-7.2	2.2	2.3	0.6	2.4	0.6	
			0.0	0.00	0.0	0	0	0.0	0.0	0.0	0.0	0.0	0.0	0.0	0.0	
M530	2.25	8851	-1.1	0.51	1.1	0.4	578	42	1.2	0.3	-4.9	2.0	1.5	0.6	1.3	0.6
			-1.8	0.31	7.03	107	14	1.9	0.3	-4.9	2.0	1.5	0.6	1.5	0.3	
M533	2.25	8713	-3.2	0.53	1.1	0.5	224	28	3.3	0.6	-29.0	7.9	4.4	1.1	3.5	0.4
			-4.0	0.43	5.03	252	14	4.0	0.4	-23.4	2.4	3.4	0.3	3.8	0.2	
N7682	2.25	5107	-2.8	0.51	1.1	0.2	224	28	1.2	0.1	-3.5	0.5	1.2	0.2	1.2	0.1
			-13.8	0.45	5.02	303	14	5.7	0.2	-15.2	0.6	5.5	0.2	5.7	0.2	

NOTE: The equivalent widths are measured in \AA , the fluxes are given in units of $10^{-15} \text{ ergs s}^{-1} \text{ cm}^{-2}$, and FWHM is in units of km s^{-1} . Negative fluxes are in arbitrary units for lack of flux calibration. They were used only for line ratio analysis. Zero fluxes indicate no detection or uncertain measurement. Columns: (1) Object name. For alternative identification see Chapter 2; N=NGC, M=Mkn; (2) Central wavelength of the spectrum; (3) Radial velocity of the galaxy, from NED; (4-6) and (11-13) Equivalent width, flux, and corrected FWHM of Br γ and H₂ measured from the

Gal.	λ_c	$c z$	Br γ (2.16 μm)						
	μm	km/s	EW ₀	F ₀	fwhm ₀	F ₀ ^{cs}	EW _d	F _d	F _d ^{cs}
(1)	(2)	(3)	(4)	(5)	(6)	(7)	(8)	(9)	(10)
			H ₂ (2.12 μm)						
			EW ₀	F ₀	fwhm ₀	F ₀ ^{cs}	EW _d	F _d	F _d ^{cs}
			(11)	(12)	(13)	(14)	(15)	(16)	(17)

spectra, not corrected for dilution, and without subtracting the stellar original continuum; (7) and (14) Br γ and H₂ flux measured after the stellar continuum was subtracted, but without dilution correction; Equivalent width and Br γ and H₂ flux measured from the dilution (8-9) and (15-16) corrected spectra, without subtracting the stellar continuum; (10) and (17) Br γ and H₂ flux measured from the dilution corrected and stellar continuum subtracted spectra.

Table 3.3 Measurements of some additional emission lines.

Gal.	λ_c	$F_0, 10^{-15}$	EW	FWHM	Possible Line
Name	\AA	$\text{ergs s}^{-1} \text{ cm}^{-2}$	\AA	km s^{-1}	Identification
IIZw136	19576(2)		-82(2)	2164(46)	H ₂ 19570, [SiVI]19630, [FeII]19670
1058+45	19572(2)	3.4(0.1)	-20(1)	1166(15)	H ₂ 19570, [SiVI]19630, [FeII]19670
<p>NOTE: Central wavelengths λ_c, line fluxes F_0, effective widths EW, full widths at half maximum FWHM (corrected for the instrumental line profile), and possible identification of some additional emission lines, detected in our Seyfert sample. Measurement uncertainties are given in brackets. Missing fluxes indicate lack of flux calibration.</p>					

Table 3.4 Results from the Kolmogorov-Smirnov test.

	Seyfert	ULIRG	Starburst
	40/40	35/40	17/17
Seyfert	-	0.73(1.1)	0.0048(0.0024)
ULIRG	23.1	-	8.7×10^{-6}
Starburst	0.87	0.0026	-

NOTE: Probabilities (in %) that the distributions of Br γ (above the diagonal) and H $_2$ 2.12 μ m (below the diagonal) effective widths EW of our Seyfert sample, the Ultraluminous infrared galaxy sample (Murphy et al. 2000), and the starburst sample (Engelbracht 1997) are derived from the same parent distribution, from the Kolmogorov-Smirnov test. The numbers of galaxies used for the Br γ /H $_2$ histograms are given in the table heading. Numbers in brackets indicate the probabilities if the Seyfert galaxy with the strongest Br γ is omitted - for a consistency test.

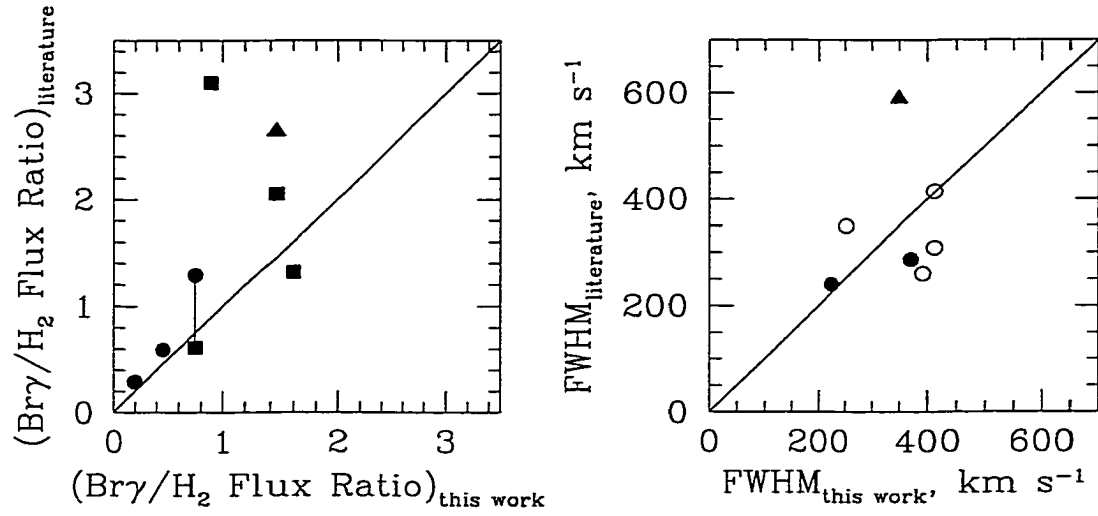


Figure 3.1 Comparison of our measurements with data from the literature: triangles - Winge et al. (2000), squares - Veilleux, Goodrich, & Hill (1997), and circles - Knop (1997). The left panel shows the $\text{Br}\gamma/\text{H}_2$ flux ratio, and the right panel shows the FWHM of $\text{Br}\gamma$ (solid symbols) and H_2 $2.12\ \mu\text{m}$ (open symbols). The two connected symbols on the left panel represent two independent measurements of NGC 4388. The relative errors are 15% for the ratios, and 10% for the FWHMs.

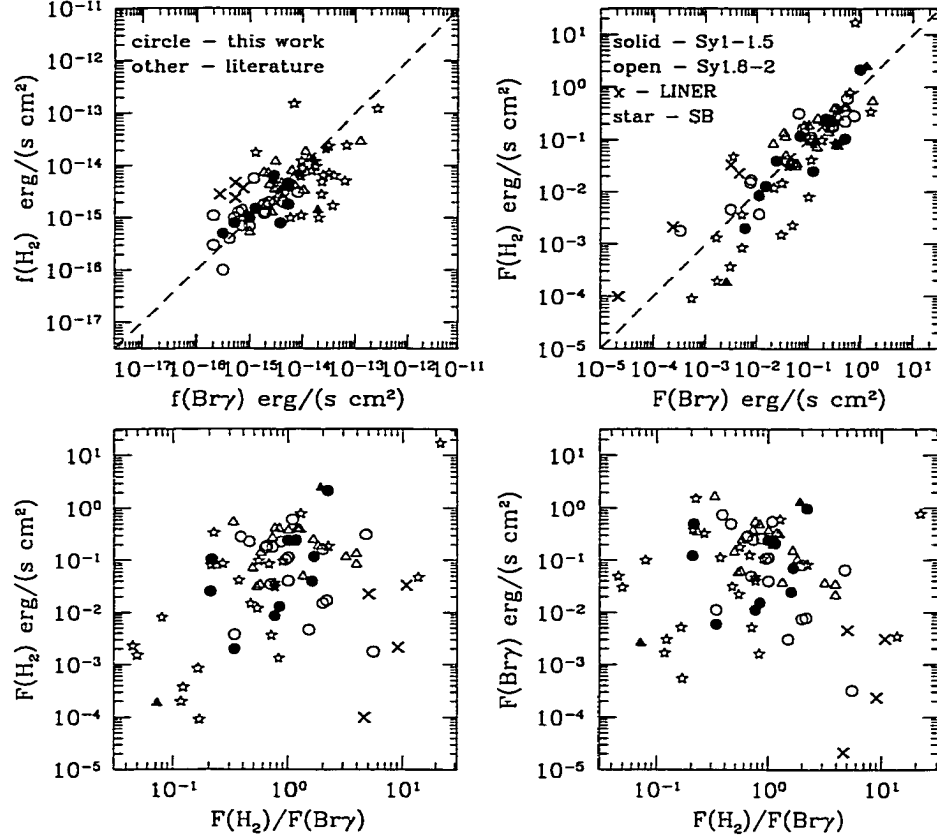


Figure 3.2 Comparison of the strengths of H₂ 2.12 μm and Brγ. Solid and open circles are respectively Type 1 and 2 Seyfert galaxies from this work. Solid and open triangles are respectively Type 1 and 2 Seyfert galaxies from Veilleux et al. (1997). Stars are actively star forming galaxies from Engelbracht (1997), Vanzi et al. (1996), and Vanzi & Rieke (1997). Crosses are LINERS from Larkin et al. (1998). The top panels show the observed fluxes on the left, the absolute fluxes (at distance 10 kpc) on the right. The bottom panels show the H₂ 2.12 μm (on the left) and Brγ (on the right) versus H₂ 2.12 μm/Brγ ratio. The UV excitation models predict $F(\text{H}_2)/F(\text{Br}\gamma) = 0.05 - 0.1$ (see Section 3.4 for details).

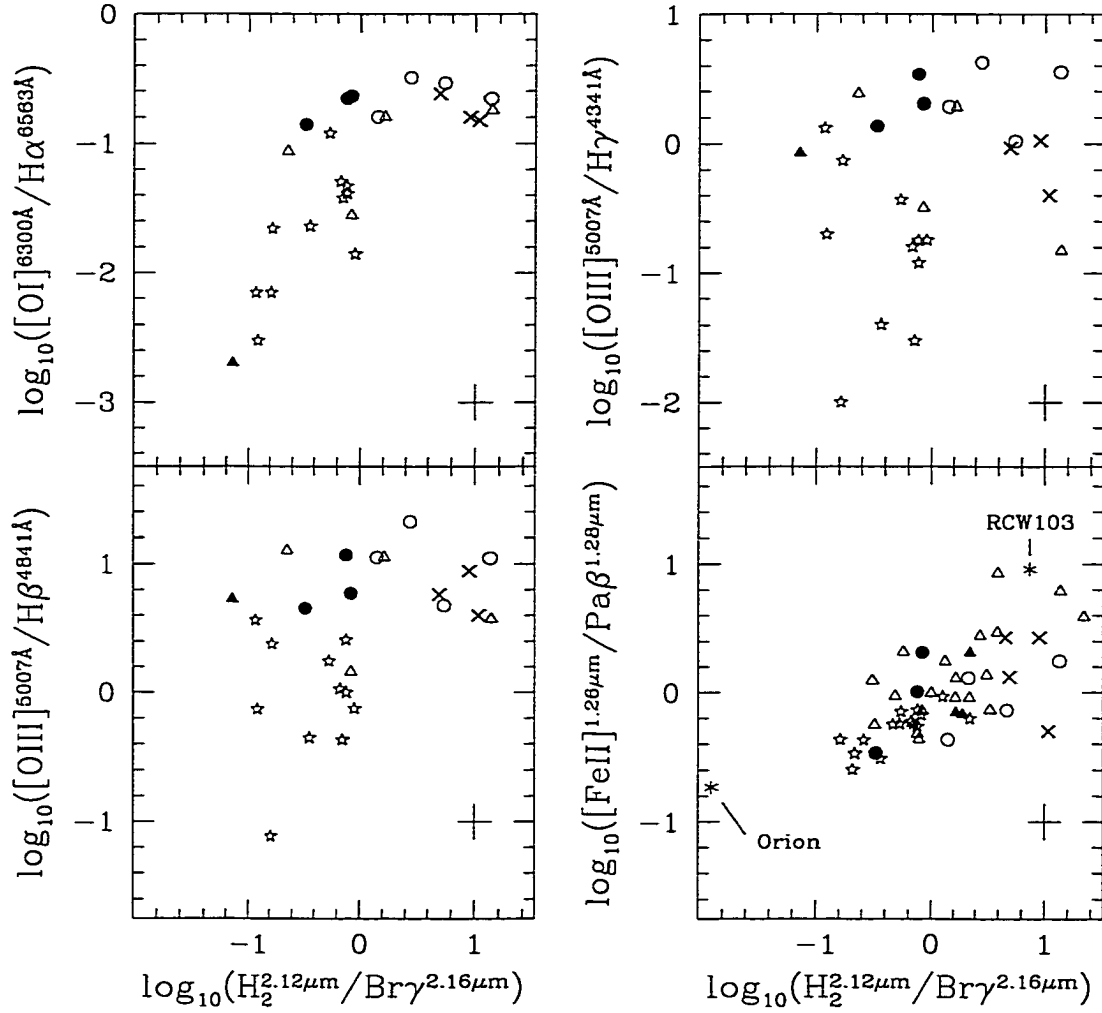


Figure 3.3 Optical and infrared emission line ratios. The symbols are the same as in Figure 3.2. Seyfert galaxies from Knop (1997) are also included. Crosses in the right lower corner indicate the typical observational errors. The infrared line ratios for Orion region and the Galactic supernova remnant RCW 103 are shown (see Alonso-Herrero et al. 1994 for details).

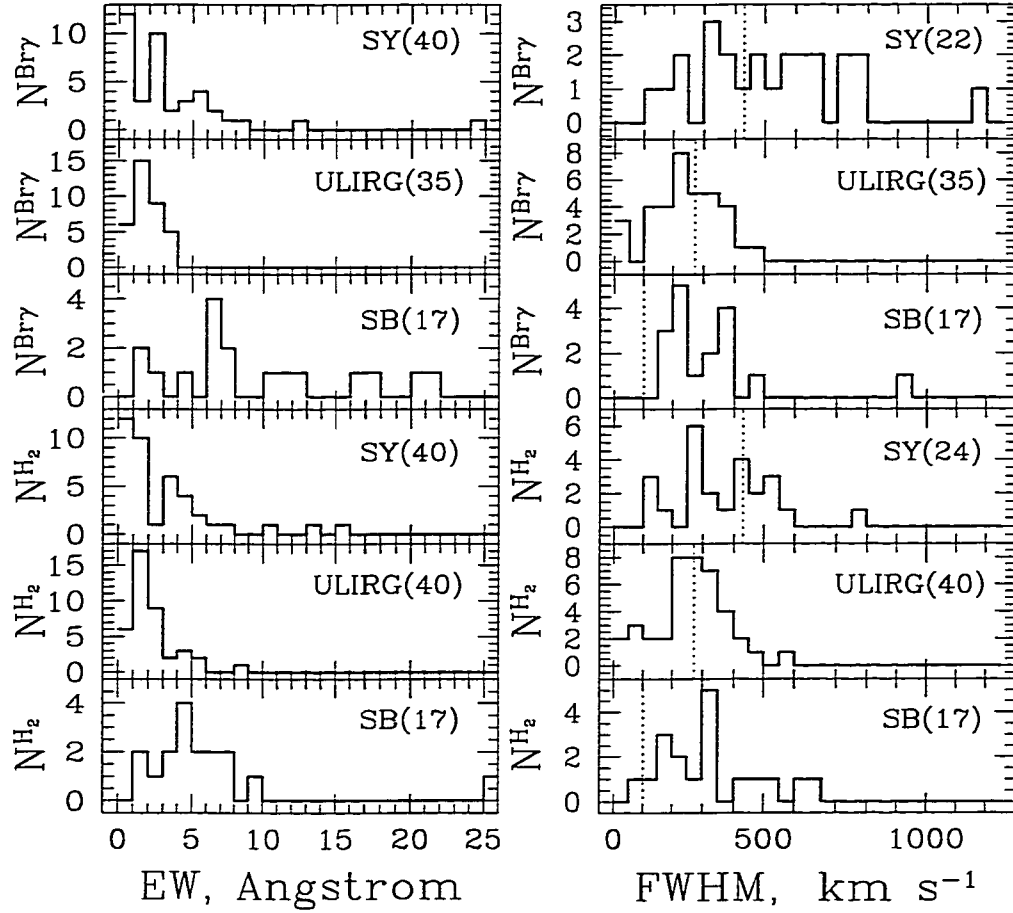


Figure 3.4 Histograms of the equivalent widths EW (left panels), and full widths at half maximum FWHM (right panels) for Br γ (top three rows) and H $_2$ 2.12 μ m (bottom three rows), for the CfA Seyfert sample (this work), the complete sample of ULIRGs (Murphy et al. 2000), and a sample of bright nearby starburst galaxies (Engelbracht 1997). The total number of objects included in each histogram is shown in the brackets. Seyfert galaxies tend to have stronger emission lines than the ULIRGs, but weaker than the starbursts. The typical instrumental spectral resolutions for each sample are indicated by vertical dotted lines on the right panels.

4. AN INFRARED STELLAR LIBRARY FOR SPECTRAL SYNTHESIS OF STARBURST GALAXIES

4.1. Introduction

Starbursts are events with profound effect on the evolution of galaxies. Even though the period of active star formation lasts for a short interval compared to the galaxy life span, the consequences can be observed over extended period of time. They affect the extent of the gaseous reservoir, the thermal and pressure balance of the interstellar medium in the bursting galaxy, and the metallicity of the next generation of stars. The red supergiants and giants continue to dominate the infrared galaxy emission even after the star formation has ceased. The dust, heated by hot young stars, dominates the mid- and far-IR emission of the hosts. To estimate qualitatively the extent of this feedback, better constraints on the stellar population are needed. They can be provided by realistic evolutionary population synthesis modeling which requires an extensive spectral atlas of stars spanning a range of ages, luminosities, spectral classes, - and last but not least - metallicities.

Typically starbursts are heavily obscured ($A_V \geq 5$ mag; Engelbracht 1997), making the optical wavebands an inadequate tool to study the stellar populations in their innermost regions. Instead, the infrared bands have the advantage of approximately tenfold lower extinction than the optical ($A_K/A_V = 0.112$, Rieke &

Lebofsky 1985).

Over the last 20 years, the evolutionary spectral stellar population synthesis have become a standard tool to study unresolved galaxies in the optical and UV passbands (e.g. Bruzual & Charlot 1993; Worthey 1994a; Vazdekis 1999; Leitherer 1999). This work has been aimed at answering a number of specific questions, including the age and metallicity estimates of the stellar systems. However, no colors or spectral indices sensitive to either the age or the abundance alone were found. Another problem is the often adopted simplification to describe the metallicity with a single parameter. The abundance ratios of elements do change, as a function of the star formation history of the stellar systems, and the nearby and best studied galaxies exhibit a large variety of star formation histories (e.g. Hodge 1989; Grebel 1996).

Traditionally, the optical extragalactic studies rely on iron and magnesium metallicity indices which represent two classes of chemical elements, produced as a result of different nuclear reactions. The dominant magnesium isotope ^{24}Mg , is an α -element formed by capture of α particles. It can be formed regardless of the initial abundance of the stars. Iron belongs to a group of elements that requires prior production of light elements. Core-collapse (Type II) supernovae, produced by massive progenitors form both α and iron-peak elements. Type Ia supernovae, produced by collapse of white dwarfs contribute more to the iron-peak elements.

Therefore, it is not surprising that the metallicities, measured by means of Fe and Mg often give different values. Henry & Worthey (1999) reviewed the subject and pointed out that $[\text{Mg}/\text{Fe}]$ increases from 0 in dwarf ellipticals to 0.3-0.5 in giant ones, and the lighter elements (C, N, O, etc.) track Mg, while the heavier elements (Ca, Ni, etc.) track Fe.

This work reports the first results from assembling a comprehensive stellar library in the infrared, and applying it to the stellar populations in actively star forming galaxies. We looked at the behavior of metal lines and some molecular bands in the infrared, aiming to compare their relative sensitivity toward the stellar parameters, particularly the metal abundance. We selected lines, that are strong enough to be detected reliably in the spectra of real starburst and "normal" galaxies with the currently available instrumentation. Therefore, detecting and successfully measuring these features in real galaxy spectra was the most important selection criterion. Our primary goal was to find indices that would constrain the metallicity in traditional sense ($[\text{Fe}/\text{H}]$ or Z). We also searched for potential tools to constrain the elemental abundance ratios, or at least the relative abundance of iron-peak to α -elements, and the importance of Type II supernovae for the starburst self enrichment. However, the limited number of sufficiently strong features in the infrared puts strong limits on this attempt.

The line behavior was studied by means of polynomial fits of their strength versus the stellar parameters. We concentrated on the red giant stars because (i) giants dominate the infrared flux in "normal" galaxies, and contribute significantly to the total flux in the starbursts, and (ii) this part of the library covers a sufficient metallicity range. Unfortunately, observing in the northern hemisphere, with a small telescope, precluded us from including metal poor supergiants (closest examples of which are in the Magellanic Clouds) in the library. As will be discussed later, this deficiency was circumvented by drawing conclusions using gravity independent indices.

Finally, different spectral classification schemes and stellar population applications in the presence of diluting featureless continuum were also explored.

Section 4.2 offers a review of the previous work. Section 4.3 describes the observations and the data reduction, Section 4.4 gives details on the sample stars. Spectral indices are defined in Section 4.5, and the fitting functions are described in Section 4.6. The results of the fitting are summarized in Section 4.7, and Sections 4.8 and 4.9 discuss some diagnostic applications.

4.2. Infrared Libraries and Population Synthesis

The lack of comprehensive infrared libraries have prevented the development of infrared spectral synthesis models, comparable to the optical ones. So far only a few attempts to address this issue have been undertaken (e.g. Lançon & Rocca-Volmerange 1996; Schreiber 1998; Origlia et al. 1999; Gilbert & Graham 2000). Unfortunately, all these models suffer from the inadequacy of the available spectral libraries, which have either low resolution, or poor quality spectra, or insufficient coverage of the stellar types. Most importantly, all existing libraries cover predominantly stars with solar metallicities.

There are a number of infrared spectral libraries available in the literature. The properties of the most prominent of them are summarized in Table 4.1. We did not include the signal-to-noise ratio as it varies within wide margins for the stars from each library. The field was pioneered by Johnson & Mèndez (1970). Kleinmann & Hall (1986) produced undoubtedly the most widely used atlas despite the relatively limited number of stars. The library of Lançon & Rocca-Volmerange (1992) suffers from insufficient signal-to-noise ratio and low spectral resolution for measuring the weaker metal lines. Origlia, Moorwood & Oliva (1993) covered only the H-band, omitting a number of important spectral features in the K-band. In addition, the atlases of Ali et al. (1995), Ramírez et al. (1997), were restricted to

the K-band NaI, CaI and CO features. Förster – Schreiber (2000) also obtained only K-band spectra of 31 stars. Dallier, Boisson & Joly (1996) covered a very narrow spectral region, and many of the important lines were left unobserved. Hanson, Conti & Rieke (1996) took spectra exclusively of hot stars. Only recently Wallace & Hinkle (1997), Meyer et al. (1998), and Wallace et al. (2000) provided a large ($\gtrsim 100$) and consistent set of JHK infrared spectra. However, they selected stars with solar and near solar metallicity. The library of Lançon & Wood (2000) is an exception, for it includes some Galactic Bulge and Magellanic Cloud stars, providing at least some metallicity spread. However, the resolving power is only ~ 1100 , making it difficult to measure MgI and FeI lines. Joyce (1998) assembled a ZJHKL low resolution ($R=500-1500$) library of 29 carbon stars revealing strong CN and C₂ bands. Hicks et al. (2000) presented $R=650$ J-band spectra of 105 stars, and discussed some spectral classification tools.

Wallace & Hinkle (1996) obtained extremely high resolution ($R \sim 42,000$) spectra of a small number of stars and identified many previously unknown lines. Although this is important for detailed stellar abundance studies (e.g. Carr, Sellgren & Balachandran 2000; Ramírez et al. 2000a), a resolution of 3000 is satisfactory for stellar population modeling, because the velocity dispersion within the galaxies smooths the integrated spectra.

For a review of the work in the field before 1980 (usually done at $R \sim 200$) we refer the reader to Merrill & Ridgway (1979).

In conclusion, despite the sizable quantity of available data, there is still no uniform set of data with high signal-to-noise and resolution, spanning the entire range of spectral and luminosity classes, and providing all the metallicities, necessary for a comprehensive evolutionary population synthesis in the infrared.

4.3. Observations and Data reduction

The infrared spectra were taken over a period of four years mainly at Steward Observatory 2.3m Bok telescope on Kitt Peak. Some stars were observed at the original 4.5m MMT, and a few at the Steward Observatory 1.55m Kuiper telescope. We used FSpec (Williams et al. 1993), a cryogenic long slit near infrared spectrometer utilizing a NICMOS3 256x256 array. The vast majority of the stars were observed with a 600 lines mm^{-1} grating, corresponding to $R \approx 2000 - 3000$. A few stars were observed with 300 lines mm^{-1} grating and $R \approx 1000 - 1500$. The slit width was 2.4 arcsec at 2.3m, 1.2 arcsec at the MMT, and 3.6 arcsec at the 1.55m. The plate scales were 1.2, 0.4, and 1.8 arcsec pixel^{-1} respectively. The limited physical size of the infrared array required the acquisition of spectra using 10-12 different grating positions, corresponding to different central wavelengths, to cover the entire H and K atmospheric windows with sufficient overlap. Usually, one of the following two combination of settings was used: 1.54, 1.62, 1.70, 2.06, 2.13, 2.19, 2.245, 2.31, 2.37, 2.42 μm , or 1.50, 1.57, 1.64, 1.71, 2.05, 2.10, 2.15, 2.20, 2.25, 2.30, 2.35, 2.40 μm .

The observing strategy for a single setting included nodding the telescope to obtain spectra at 4 (at the MMT) or 6 (at the 2.3m and 1.55m) different positions along the slit, and integrating at each position for 3-20 sec, depending on the apparent brightness of the object and the sky background. This was necessary (i) in order to carry out the sky subtraction and account for the sky background variations by having a sky taken at the same slit position as the object, just before and after the science exposures; (ii) to improve the pixel sampling, flat fielding and bad pixel correction by having the object placed at various positions on the array. Next, we repeated the same procedure at a standard star for the atmospheric

correction. Then we changed the setting, took a sequence of 4-6 spectra of the standard, moved the telescope back to the object and repeated the same procedure at the new grating setting. Occasionally, if two or three target stars were available nearby on the sky, we increased the observing efficiency by using the same standard for all of them.

The spectra were reduced using *IRAF* tasks written specifically for FSpec (Engelbracht 1999). An average of the sky backgrounds taken immediately before and after each object image at the same location on the array were subtracted to remove the sky emission lines, and simultaneously, the dark current and bias level. Dark-subtracted illuminated dome flats taken at the same central wavelengths as used for the science exposures were applied to correct for pixel-to-pixel variations. The known bad pixels were masked out. The object images were shifted (using centroid fits across the continuum), and median combined to produce a single two-dimensional spectrum. The large number of object images allowed us to exclude any remaining bad pixels and cosmic rays. The one-dimensional spectrum was extracted by fitting a polynomial of 3-5 order to the continuum in the two-dimensional image with the *IRAF* task *apall*. The spatial width of the extraction apertures was usually 3-5 pixels.

In most cases the object spectra were divided by spectra of solar analog stars observed at the same airmass, and then multiplied by a solar spectrum (Livingston & Wallace 1991) to remove the effects of the atmospheric absorption (Maiolino, Rieke & Rieke 1996). The standard stars were not always exactly G2 dwarfs (usually ranging from F5 V to G5 V), and the true shape of the continuum had to be restored by multiplying the spectra by the ratio of black bodies with standard star and solar effective temperatures. In some cases we chose for standards nearby

A stars, and in the K-band we removed the hydrogen feature ($\text{Br}\gamma$) in their spectra by hand, fitting it with Gaussians with *splot*, or by multiplying by another A star spectrum for the H-band, already corrected for the atmospheric absorption with a G2 V star. We carried out the wavelength calibration using the OH airglow lines (Oliva & Origlia 1992), complemented whenever necessary by Ne-Kr lamp spectra.

Each different setting was divided by a 3-5 order polynomial continuum fit, and combined to form a single HK stellar spectrum. Finally, we multiplied the spectrum by a black body with the stellar effective temperature corresponding to the spectral type. This normalization procedure effectively removes the broad vapor absorption features in the coolest stars but it is preferable because the spectral coverage of a single setting is only 0.075-0.095 μm and does not present a sufficient coverage for a good estimate of the continuum shape. Furthermore, the true continuum shape was distorted by imperfect spectral type match of the standards for the atmospheric absorption correction, as discussed above.

The imposed continuum shape deviates most from the real one for the late M stars, where the molecular absorption is most important. A possibility to alleviate this problem completely is to impose on our spectra empirical continuum shapes taken from lower resolution spectra, for instance from the libraries of Lançon & Rocca-Volmerange (1992) or Lançon & Wood (2000). We intent to explore this avenue in the future.

The error analysis of spectra that consist of "pieces" taken at different times, and often on different nights, is particularly complicated. The uncertainties in most of our data are dominated by systematic errors due to the changes in the observing conditions rather than the statistical uncertainties. An example is given in Figure 4.1, where the difference between the "final" spectra of two different

K3 III stars with near solar metallicity is shown. The difference is divided by the average of the two spectra. The inset shows the distribution of these differences. Their average is statistically indistinguishable from zero, and the sigma suggests that each spectrum has $S/N \sim 100$. At the same time, the photon statistics suggests $S/N > 150$. The inconsistency is largely due to the variation of the sky background. Therefore, simple signal-to-noise ratios would not represent the quality of the data well. Furthermore, the measurements of individual features of interest include additional systematic uncertainties, like the continuum placement during the continuum normalization, and differences between the stars used for the telluric correction and the Sun.

Because we were interested in the uncertainties of the measurements rather than just of the spectra, and because of the large variations of the signal-to-noise ratio across the spectra, we adopted an alternative error treatment. First, we adopted a model for the errors as function of the indices: $error = f(index\ value)$. The second step was to scale the errors so that the χ^2 per degree of freedom for the fits to the indices (see Section 4.6 for details on the fitting) would approach one. After some experiments we choose a simple linear model, with an lower limit for the errors, and applied it to all indices: $\sigma(Index) = 0.2 \times Index$, with $\sigma(Index) = 0.02$ mag as a lower limit. These errors are easily transferable to the corresponding equivalent widths, given the index definitions (see Section 4.5). This technique gives an uniform upper limit of the uncertainties in the entire library, which is acceptable in applications like population synthesis. Our tests showed that the adopted model error suggests 30-50% lower signal-to-noise ratio than the photon statistics.

One more possibility is to estimate the signal-to-noise ratio locally, over a

"clean" continuum region near the spectral feature of interest. We recommend this method for applications concerning parameters of individual stars.

4.4. Sample Selection and Stellar Parameters

We have selected most of our giant and dwarf stars from the sample of the Lick group (Worthey et al. 1994b) assuring that they have high quality optical spectra and known spectral type, surface gravity and metallicity. We supplemented this set with super-metal rich stars from Baade's Window region from McWilliam & Rich (1994). The supergiant stars are mostly from White & Wing (1978) and Luck & Bond (1989). In addition, we observed stars with known metal abundance from the catalog of Cayrel de Strobel et al. (1997). The observational log, with standard spectral types, grating settings, and the telluric correction star is given in Table 4.2.

The atmospheric data for the program stars are summarized in Table 4.3. About half of them (111 out of 218 stellar metallicities) were already available from Faber et al. (1985), Gorgas et al. (1993), and Worthey et al. (1994b). The last work even offers re-calculated stellar parameters based on their own spectral line measurements and calibrations. To assure that our system is as close as possible to theirs (and as homogeneous as possible, given the usage of a variety of literature sources), we used these new estimates whenever they were available. In addition, we carried out an extensive literature search for atmospheric data for the rest of our program stars. Our main source was the catalog of $[\text{Fe}/\text{H}]$ determination of Cayrel de Strobel et al. (1997) which contains all metallicity estimates in the literature up to 1995. Naturally, this is an inhomogeneous compilation. However, we made an effort to "homogenize" the sample, at least in terms of abundance estimate methods. We preferred spectroscopic estimates, and if there were none available,

we used narrow band photometry. Broad band photometry based metallicities were adopted only in a few limited cases, for which no other measurements existed. Finally, we made a number of assumptions in some easily justifiable cases, which are described at the end of Table 4.3. The distribution of our stars on the $\log g$ versus T_{eff} diagram is shown in Figure 4.2. We included in Table 4.3 some color information (B-V, V-K) because the colors are often used as proxies for the spectral class. Although they might be affected by reddening, the colors (particularly V-K) are thought to be reliable temperature indicators (e.g. Worthey et al. 1994b), and are more readily available than T_{eff} estimates based on sophisticated spectral fitting techniques. The reddening is not a problem for most of our sample members, because they are field stars, within 50-100 pc from the Sun.

The metallicity distributions for stars of different luminosity classes in the library are shown in Figure 4.3. One of our most important assumptions involves the supergiants with unknown metallicities. We set their $[\text{Fe}/\text{H}]$ to 0.0, because most of the young disk stars have nearly solar abundances.

The $[\text{Fe}/\text{H}]$ histogram for giants shows the largest spread by far, although the supergiants also span a relatively broad range. Unfortunately, pure astrophysical constraints prevent us from observing stars over the entire $[\text{Fe}/\text{H}]$ range of interest. Particularly, the massive metal poor stars from Population II (and possibly III) in our Galaxy have exploded as supernovae a long time ago. The Magellanic clouds provide a possibility to complement the library with some supergiants with 1/5 to 1/20 of the solar metallicity (e.g. Luck et al. 1998; Hill 1999). However, obtaining such spectra is out of the scope of this work.

4.5. Index Definitions

Some of the spectral features in the infrared have been observed and measured, and suitable spectral indices have already been defined by Kleinmann & Hall (1986), Origlia, Moorwood & Oliva (1993), Doyon, Joseph & Wright (1994a), and Ramírez et al. (1997). We adopted their definitions for compatibility, with two deviations. First, for the NaI and CaI indices of Ramírez et al. (1997) we used only the two nearest continuum bands. Second, for the CO index of Doyon, Joseph & Wright (1994a) we carried a polynomial, rather than a power-law fit to the continuum. Both changes produced no significant effects.

Because our spectra do not always span the wavelength range of the original photometric index of Frogel et al. (1978) we restricted our measurements to the spectral indices only. We also measured the CO index defined by Ivanov et al. (2000). It is somewhat intermediate between the narrow and broad CO indices. Our index is less affected by the variations of the atmospheric transmission because it is placed further from the edge of the K window, compared to the photometric CO indices. At the same time, our index delivers better signal-to-noise than the narrower spectroscopic indices.

Finally, we defined some new indices for atomic lines (index names containing "V") that had not been measured before, or in the cases where the previous definitions could be affected by the loss of the true continuum shape (for example the indices defined by Kleinmann & Hall 1986, where the continuum bands are very far apart). The definitions of all measured spectral indices are summarized in Table 4.4, and their bandpasses are shown in Figure 4.4. The measured indices are given in Table 4.5.

4.6. Fitting Functions

We carried out a fitting of the infrared spectral indices of giants (the most numerous class of stars in the library, and a major contributor to the integral infrared emission in a galaxy) versus the stellar atmospheric parameters, to determine which features are most sensitive to the metal content, and to facilitate future practical applications of our data. In general terms, the strength of the infrared lines and bands depends on the stellar effective temperature, surface gravity, and metallicity:

$$\text{IR Index} = f(Z, T, G), \quad (4.1)$$

where Z is the metallicity variable. We explored a number of possibilities: $[\text{Fe}/\text{H}]$ as shown in Table 4.3, and - for the stars we have in common with the Lick group, - some of their optical metal indices: Fe4383 , Fe4668 , Fe5015 , and Mg_2 . These particular indices were chosen because Worthey et al. (1994b) considered them the most promising metallicity indicators. T is the temperature variable - either the effective stellar temperature in the form of $\Theta = \log(5040/T_{\text{eff}})$ or the V-K color (see Table 4.3). The V-K might be preferable in some cases, because it is available for more stars than T_{eff} , and is somewhat more robust - it does not require sophisticated spectral atmosphere modeling. Finally, G is the surface gravity $\log g$.

Following the examples of previous work (e.g. Gorgas et al. 1993; Worthey et al. 1994b), we adopted polynomial functions and experimented widely with the polynomial orders and terms. Polynomials are continuous functions, and their derivatives exist at any point of the parametric space, which is important for comparing the sensitivity of the indices to the different independent variables. Furthermore, the effects of temperature and metallicity can be easily separated by omitting the cross terms, as suggested by Gorgas et al. (1993). Although there are

other functions that fulfill these requirements, the polynomials present the simplest and the most straightforward option.

We tried to fit the data with cubic polynomials in all three dimensions, with a full set of cross-terms, bringing the number of fitting coefficients up to 20, but 60-80 stars are insufficient to constrain well so many unknowns. The incomplete coverage of the parametric space constitutes an additional difficulty. Most of our metal poor stars are concentrated in a relatively narrow temperature region between K0 and K5 (Figure 4.5). Although these stars are amongst the primary contributors to the integral infrared light in many galaxies, having spectra of metal deficient stars over a larger temperature interval is highly desirable, particularly for stellar applications of the library. Therefore, the current status of the library requires some extrapolation. Skipping the cross-terms facilitates this procedure, because it represents the assumption that the derivatives with respect to one of the independent variables do not include the other independent variables. For instance, we assume that the metallicity dependence of the indices is the same (or changes insignificantly) over the entire range of temperatures and gravities. A further simplification takes advantage of the weak surface gravity dependence of some indices, allowing one to restrict the independent variables only to T and Z .

We experimented with various polynomials for each index, and in most of the cases selected quadratic form, with no cross terms. The fit coefficients for all combinations of the independent variables, are given in Table 4.6 where the fits to each index are separated in a different block. The Z , T , and G lines in the heading span all possible combinations of variables, and the columns underneath give the coefficients for different orders (orders are specified in the leftmost column). The Z -line specifies which metallicity variables are used. The T -line specifies the

temperature variables, and the G-line is given just for completeness, because the only surface gravity variable is $\log g$. The number of measurements used in each fit, the normalized χ^2_{PDF} per degree of freedom, and the r.m.s. of every fit are also indicated beneath the coefficients.

4.7. Behavior of the Infrared Features

Representative subsets of our spectra are shown in Figures 4.6, 4.7, and 4.8, for supergiants, giants, and dwarfs, respectively. Figure 4.9 demonstrates the effect of changing $[\text{Fe}/\text{H}]$. Detailed line identifications were carried out in Origlia, Moorwood & Oliva (1993; H band), and Wallace & Hinkle (1996; K-band). Both the temperature and metallicity effects on the line strengths are clearly visible.

The fits for some of the infrared spectral indices are shown in the Appendix. We plotted only the case of $Z=[\text{Fe}/\text{H}]$ and $T = \Theta$ because the differences between the various combinations of variables (note: Z can be either $[\text{Fe}/\text{H}]$ or one of a few optical iron indices, and T can be either Θ or V-K) proved to be statistically insignificant (Table 4.6). This is expected because we used the $[\text{Fe}/\text{H}]$ re-calculated by Worthey et al. (1994b) based on the same metal line indices. In the case of V-K and T_{eff} any differences were negligible because of the tight relation between the two (see for example Ramírez et al. 1997).

4.7.1. MgI

The well-known metallicity sensitivity of the optical Mg absorption features (e.g. Worthey et al. 1994b) is a strong motivation to explore whether their infrared counterparts can be used as abundance indicators.

There are five MgI lines in the infrared, strong enough to be measurable in

good quality spectra of galaxies (Engelbracht 1997). Johnson & Mèndez (1970) identified two H-band MgI lines but Mould (1978) was the first to measure the strength of MgI ($4s^1S - 4p^1P^0$) at $1.71 \mu\text{m}$ in some M dwarfs. He pointed out that dwarfs with higher metallicity tend to have stronger MgI. However, Origlia, Moorwood & Oliva (1993; see their Figure 4a) demonstrate that in M2 supergiants and cooler stars this MgI line is somewhat contaminated by OH, and is blended with one of the $\Delta v = 3$ CO bands. Ali et al. (1995) found only a weak variation of the $2.28 \mu\text{m}$ MgI with the temperature in dwarf stars. Meyer et al. (1998) measured the strength of the MgI 1.557 and $1.7109 \mu\text{m}$ lines in 85 stars and found that in presence of high surface gravity (in dwarf and sub-dwarf stars), the line strength peaks at ~ 4500 K, while in stars with extended atmospheres (giants and supergiants) the line strength increases monotonically towards the cooler stars, in accordance with the Saha and Boltzman equations. A hint for a similar behavior is demonstrated for the much weaker MgI ($4d^3D_{3,2,1} - 6f^3F_{2,3,4}^0$) line at $2.28 \mu\text{m}$ by Förster – Schreiber (2000). Although MgI lines can be clearly seen in some other literature data (e.g. Kleinmann & Hall 1986; Lançon & Rocca-Volmerange 1992; Wallace & Hinkle 1997), no further quantitative analyses were carried out.

We measured four MgI features: at $1.50 \mu\text{m}$, a line at $1.71 \mu\text{m}$, a doublet ($4f^3F_{2,3,4}^0 - 7g^3G_{3,4,5}^0$, $4f^1F_3^0 - 7g^1G_4$) at $2.1065 - 2.1067 \mu\text{m}$, and a line at $2.28 \mu\text{m}$. The first feature is actually a multiplet ($4s^3S_1 - 4p^3P_{0,1,2}^0$; at 1.5029 , 1.5044 , and $1.5052 \mu\text{m}$; Lançon & Rocca-Volmerange 1992) but we will call it a line for convenience. We omitted the $1.557 \mu\text{m}$ line because it is affected by the presence of a strong CO band nearby (Origlia, Moorwood & Oliva 1993). However, all the features are somewhat "contaminated" by weaker lines of other species, as can be easily seen from the high resolution spectra of Wallace & Hinkle (1996). For the purpose of this analysis we will neglect these contributions because they are small

compared to the main feature.

Our fits to the MgI indices for the giant stars are shown in Figures A.1, A.2, A.3, A.4, and A.5. The H-band features appear to be governed strongly by the abundance. The temperature (V-K color) trend is negligible, except for the $1.71\ \mu\text{m}$ feature, due to the additional OH opacity. This is a very important result because it enables us to use the H-band indices for metallicity estimates, at least for systems dominated by light from red giant stars. Both lines are of comparable strength to the NaI, SiI and CaI lines, used for similar purposes before. An additional advantage is that the MgI $1.50\ \mu\text{m}$ line will still fall in the H atmospheric window, even for galaxies with $z \simeq 0.13$.

The lines in the K-band are weaker, and for them we applied even simpler fitting functions. Nevertheless, we found that they follow the same behavior. Utilizing them will require data of better signal-to-noise and resolution. The $2.28\ \mu\text{m}$ line is difficult, because it is close to the $2.3\ \mu\text{m}$ CO band head which makes it difficult to place the long-wavelength continuum reliably, particularly in galaxies with high velocity dispersion. We found that neither of two definitions of the $2.28\ \mu\text{m}$ (Ramírez et al. 1997, and this work) offers a significant advantage over the other.

In the context of the stellar populations in external galaxies, our result implies that a pure infrared diagram of MgI index and a temperature sensitive index (e.g. Br γ ; see also Section 4.8) would potentially disentangle the age-metallicity degeneracy, just as the H β versus Mg $_2$ plot of Worthey (1994) does it in the optical.

4.7.2. NaI and CaI

These two multiplets have often been studied together, because they both appear to have similar behavior, and similar wavelengths. The first measurements, as in the case of MgI, are presented by Mould (1978), and lead to the conclusion that the strength of these lines does depend on the metal content. This result is backed up by a comparison with stellar atmosphere models. Kleinmann & Hall (1986) found that the two lines are good temperature indicators. However, they lacked the necessary metallicity coverage to test for any abundance effects. Kleinmann & Hall went on further, to base their two-dimensional spectral classification on the strength of NaI, CaI, Br γ and $^{12}\text{CO}(2,0)$ features (see their Figure 7). Terndrup, Frogel & Whitford (1991) show that the NaI and CaI absorptions correlate to within the measurement errors, as expected if they both trace the same physical quantity. They also employ a simple line strength scaling relation to prove that the Baade Window giant have $[M/H]=+0.3$. More recently Wallace & Hinkle (1996) also saw a strong temperature dependence. Ali et al. (1995) confirmed this strong temperature sensitivity in main sequence stars.

Perhaps the most detailed study of these two lines to date was undertaken by Ramírez et al. (1997). They took advantage of the similar temperature dependence of the $2.3\ \mu\text{m}$ CO band and the NaI and CaI lines, to define a luminosity sensitive parameter $\log[\text{EW}(\text{CO})/(\text{EW}(\text{Na})+\text{EW}(\text{Ca}))]$, independent of the temperature. A similar point was made by Förster – Schreiber (2000). Ramírez et al. preferred to use the CO band as a temperature indicator, because the CO feature is stronger than NaI and CaI, and the CO measurements are more robust. Frogel et al. (1999) developed for the first time a red giant abundance scale based on the same spectral features in globular cluster stars. Although their calibration was used on Galactic

bulge red giants (Ramírez et al. 2000b), the details are still not available. Recently, Lançon & Wood (2000) report a qualitative conclusion that more metal poor stars tend to have weaker NaI and CaI lines.

We confirm the intertwined dependence of the NaI and CaI features on the stellar temperature and metallicity (Figure A.6, A.7, A.8, A.9). Both indices become stronger as the metallicity grows higher, and the stellar temperature lowers. The amplitudes of these effects are comparable. Therefore, the indices can be used as direct indicators of neither T_{eff} , nor $[\text{Fe}/\text{H}]$, contrary to previous conclusions. This result indicates the necessity of some additional assumptions constraining the stellar temperature, to justify the abundance estimate technique of Frogel et al. (1999). The broadband J-K color used in one of their calibrations is a poor temperature indicator in the high reddening direction towards the Galactic bulge.

4.7.3. SiI

The $1.59 \mu\text{m}$ SiI is a strong and relatively easy to measure H-band feature. Many authors detected (Johnson & Mèndez 1970; Mould 1978; Lançon & Rocca-Volmerange 1992), and even measured (Meyer et al. 1998) the line but did not comment on its behavior.

Origlia, Moorwood & Oliva (1993) modeled the stellar H-band spectrum and pointed that the SiI feature suffers some contamination from the OH, particularly in stars cooler than 3500K. The silicon increase towards later spectra type is slow, at least compared with most of the other features in the H-band. They explain this as result from silicon becoming neutral in mid-G stars. It is only a fortunate coincidence that the line behavior does not change in stars with spectral class later than M2, where the OH dominates the absorption. Later, Origlia et al. (1997)

defined a metallicity scale based on synthetic H-band spectra. Although their method is based on the $1.62\ \mu\text{m}$ CO band, they show that the SiI line is also a promising abundance indicator (see their Figure 1). Dallier, Boisson & Joly (1996) combined the SiI feature with CO band measurements to create temperature and luminosity indicators.

Our fit to the SiI index of Origlia, Moorwood & Oliva (1993) is shown in Figure A.10. We incorporated in the fit all second order terms except for the cross terms, as discussed in Section 4.6. Within the uncertainties, the index strength is independent from V-K (top center panel) and $\log g$ (top right panel). However, the metallicity dependence is strong and well pronounced (top left panel). Our data support the result of Origlia et al. (1997) stellar atmosphere models.

4.7.4. FeI and Other Weak Atomic Lines

The strongest unblended iron absorption line in the infrared is at $1.58\ \mu\text{m}$. Unfortunately, it is close to a number of other prominent features which makes it difficult to place the continuum nearby. Although Johnson & Mèndez (1970) detected the line, Mould (1978) was the first to measure it in a few of his spectra. Lançon & Rocca-Volmerange (1992) and Origlia, Moorwood & Oliva (1993) just identified the line. Dallier, Boisson & Joly (1996) and Förster – Schreiber (2000) measured a few iron lines, including some blends, and inferred only a general tendency that the Fe grows stronger towards cooler stars. The limited statistics prevented them for analyzing the abundance effects. Ramírez et al. (2000a) used resolution $R \sim 40,000$ spectra and stellar atmosphere models to infer $[\text{Fe}/\text{H}]$ for red giants and supergiants in the Galactic center, proving the great potential of these lines for metallicity estimates in the infrared. A great advantage of the Fe lines is the direct compatibility with the established optical metallicity scale for

extragalactic objects.

Our calibration (Figure A.11) confirms the expected strong line increase with metallicity and much shallower change with the effective temperature. However, the fit coefficients given in Table 4.6 should be treated with caution because the line strength is comparable to the observational uncertainties.

A number of other weak atomic lines of various species have been identified in moderate resolution H and K spectra, including TiI, AlI, SiI, MgII (Mould 1978; Kleinmann & Hall 1986; Lançon & Rocca-Volmerange 1992; Dallier, Boisson & Joly 1996; Meyer et al. 1998; Förster – Schreiber 2000) but they are too faint to be measured reliably in galactic spectra. These identifications were provided by high resolution infrared spectroscopy of sunspots (Livingston & Wallace 1991) or a limited number of stars (Wallace & Hinkle 1996). Mould (1978) carried out curve of growth abundance estimates of TiI lines in main sequence stars. High quality data would permit a similar analysis of the multiple (but weaker) AlI lines in the K-band. Although we detect many of the features mentioned above in our spectra, they are unsuitable for stellar population studies, and therefore their analysis remains out of the scope of this project.

4.7.5. CO Bands

The CO bands, as the most prominent and easy to measure features in the near infrared spectra or cool stars, have long attracted attention (e.g. Hall 1970; Johnson & Mèndez 1970). Mould (1978) predicts a rather weak metallicity sensitivity of the CO, consistent with saturated CO band. Kleinmann & Hall (1986), and Ali et al. (1995) demonstrated a strong temperature dependence of the CO which makes it suitable for spectral classification of stars. They also confirmed that the CO is

stronger in supergiants than in giants because of the more extended atmospheres of the former. The microturbulent velocity, higher in supergiants than in giants, also contributes to this effect, because it broadens these saturated features, effectively transferring opacity from the central wavelength to the wings (McWilliam & Lambert 1984).

Terndrup, Frogel & Whitford (1991 and the references therein) explore the metallicity effects on the CO band strength and demonstrate that the Baade Window giants are super metal rich ($[\text{Fe}/\text{H}] = +0.2$). Lançon & Rocca-Volmerange (1992) discuss in detail the behavior of both H and K band CO absorption features, and their contamination by OH and H_2O , particularly strong in stars cooler than 3800 K. They find that the CO equivalent width is a linear function of the infrared color temperature.

Origlia, Moorwood & Oliva (1993) provide the best study of the H-band CO feature to date, complete with modeling. The OH contamination to the $1.62 \mu\text{m}$ CO band, that has caused so much concern, actually does not exceed 30% for stars with $T_e \leq 3000$ K and reasonably small microturbulent velocities. Independent of the contamination, the CO appears to be a good temperature, and therefore spectral class indicator, particularly if considered as $W_\lambda(\text{CO}1.62)/W_\lambda(\text{Si}1.59)$ or $W_\lambda(\text{CO}1.62)/W_\lambda(\text{CO}2.29)$ ratio. The ratios have the advantage of eliminating the surface gravity effects. These conclusions were confirmed independently by Dallier, Boisson & Joly (1996), and Meyer et al. (1998).

The CO bands strengths were measured for various samples of stars, and from spectra with different spectral resolution (see Table 4.1 for references), and they all exhibit a dual stellar temperature and surface gravity dependence. Our fits are shown in Figures A.12, A.13, A.14, A.15, A.16, A.17, and A.18. The metallicity

and temperature dependences are obvious in all cases, although more globular clusters stars, spanning broader range of colors are desirable. We attribute the lack of surface gravity trend in the fits to a selection effect. Our sample of stars includes mostly the red giants, with very few stars with intermediate temperature. As Figure 4.2 demonstrates, this leads to a correlation between the temperature and the surface gravity, which were supposed to be independent variables. Therefore, the change of the strength of a spectral feature that depends strongly on both T_{eff} and $\log g$ can be attributed in the fit to only one of these variables. We left out the surface gravity in the case of $1.62 \mu\text{m}$ CO index only, and included it for all $2.29 \mu\text{m}$ CO indices but the derived gravity gradient in those cases are generally smaller in comparison to the abundance and temperature effects. This surface gravity - temperature interplay effects to some degree all our fits, but is stronger for the CO bands, because the molecular abundance depends strongly on the extent of the stellar atmosphere compared to the atomic metal lines. Our fitting functions retain their usefulness for population synthesis, because they still represent well the behavior of the CO indices in the stars that contribute a significant fraction of the infrared flux. Indeed, the spectral energy distributions of hotter stars peak at shorter wavelengths, and the features we discuss here are absent from their spectra. The flattening of the fits at the $V-K=7-8$ mag is due to the very steep color-temperature relation.

4.8. Two-Dimensional Spectral Classification

The previous section clearly demonstrated that many infrared spectral features are good tracers of the stellar temperature by themselves (e.g. the CO bands, NaI, CaI). However, some line ratios are even better, because the division cancels any additional luminosity, metallicity, and reddening effects, e.g.

EW(CO1.62)/EW(Si1.59) (Origlia, Moorwood & Oliva 1993; Dallier, Boisson & Joly 1996; Förster – Schreiber 2000). Based on our sample, we derived (Figure 4.10) for giants and supergiants with $2500 \leq T_{\text{eff}} \leq 6500$:

$$\log[\text{EW}(\text{CO1.62})/\text{EW}(\text{Si1.59})] = (1.61 \pm 0.10) - (3.77 \pm 0.23) \times 10^{-4} * T_{\text{eff}} \quad (4.2)$$

The r.m.s. of the relation is 0.14, which corresponds to ~ 300 deg for the inverse equation, and accounts for the observational errors, the intrinsic scatter, and the fit quality. Here, and throughout this and the next section we use the CO indices defined by Origlia, Moorwood & Oliva (1993), MgI indices from this work, and Na and Ca indices of Ramírez et al. (1997).

A similar relation exists for the $1.50 \mu\text{m}$ MgI line:

$$\log[\text{EW}(\text{CO1.62})/\text{EW}(\text{Mg1.50})] = (1.32 \pm 0.09) - (3.40 \pm 0.22) \times 10^{-4} * T_{\text{eff}} \quad (4.3)$$

Here the r.m.s. is 0.13 or ~ 320 deg. Treating the giants or supergiants separately leads to the same relationships, within the observational uncertainties. In the K-band, $\log[\text{EW}(\text{CO})/\text{EW}(\text{Mg})]$ provides the same diagnostics, although with larger dispersion because of the weaker MgI lines.

Including the CO index in a temperature dependent ratio has a disadvantage - the CO is sensitive to the surface gravity as well. Therefore, the relations derived above can be applied only if the luminosity class is known. This problem motivated us to search for an universal temperature indicator for supergiants, giants, and dwarfs. Figure 4.11 represents two candidates: $\log[\text{EW}(\text{Mg1.50})/\text{EW}(\text{Ca2.26})]$ and $\log[\text{EW}(\text{Mg1.50})/\text{EW}(\text{Na2.21})]$:

$$\log[\text{EW}(\text{Mg1.50})/\text{EW}(\text{Ca2.26})] = -(0.78 \pm 0.13) + (2.42 \pm 0.30) \times 10^{-4} * T_{\text{eff}} \quad (4.4)$$

The r.m.s. is 0.18 or ~ 450 deg for the inverse equation, and

$$\log[\text{EW}(\text{Mg1.50})/\text{EW}(\text{Na2.21})] = -(0.95 \pm 0.13) + (2.83 \pm 0.30) \times 10^{-4} * T_{\text{eff}} \quad (4.5)$$

with 0.19 and ~ 430 deg, respectively. Similar relations exist for the MgI features in K-band but we choose to use the strongest feature. MgI at $1.71 \mu\text{m}$ is also suitable, but we preferred the $1.50 \mu\text{m}$ line to avoid the OH contamination (Origlia, Moorwood & Oliva 1993).

We tested the classification power of a number of diagnostic diagrams suggested in previous works. Kleinmann & Hall (1986) took advantage of the temperature dependence of the NaI, CaI and Br γ K-band features, to discriminate between stars of different spectral, and to some extent, luminosity classes (see their Figure 7). Because we used spectral reference stars with prominent Br γ in the telluric correction, (see Section 4.3), our Br γ measurements are not reliable. Therefore, we limited ourselves to NaI and CaI features only. The result is shown in Figure 4.12. The supergiant-giant separation demonstrated by Kleinmann & Hall (1986) is absent. It can not be achieved even if we omit the low metallicity stars (bottom panel), minimizing the relative errors. Alvarez et al. (2000) find no separation as well, suggesting that the correlation between the CO and Na+Ca strength extends to supergiant luminosities. However, the dwarf stars in our sample do separate from the giants and supergiants.

Ramírez et al. (1997) proposed to use $\log\{\text{EW}(\text{CO}2.29)/[\text{EW}(\text{Na}2.21)+\text{EW}(\text{Ca}2.26)]\}$, plotted against stellar effective temperature, to separate giants from dwarfs. Although our data confirm their result (Figure 4.13, bottom panel), the separation quickly disappears at $T_{\text{eff}} \geq 4000$. We obtained a much better separation with $\log\{\text{EW}(\text{CO}1.62)/[\text{EW}(\text{Mg}1.50)+\text{EW}(\text{Mg}1.71)]\}$ (Figure 4.13, top panel). The well defined lower envelope of the giant and supergiant locus suggests that the H-band technique would work with even hotter stars, up to $T_{\text{eff}} \sim 4800$. We expect that the better signal-to-noise ratio achievable in the H atmospheric

window and the stronger lines accounts for this improvement. Only stars with $[\text{Fe}/\text{H}] \geq -0.35$ were considered here, again to minimize the effects of larger relative errors in severely metal poor stars. Meyer et al. (1998) explored a diagram using CO and OH for two dimensional spectral classification. However, our diagnostics are better because we improve on the signal-to-noise ratio by including two Mg lines, stronger than the $1.576 \mu\text{m}$ feature alone.

The signal-to-noise ratio, needed to use the diagnostics, discussed before, varies greatly from one diagram to another, and generally depends on the temperature of the stars. It is safe to assume that S/N of about 30 is necessary for the K5-M stars, and it increases up to 50 for early K stars. The lines become too weak to implement the techniques for stars with effective temperatures hotter than 4800 K.

4.9. Disentangling Flat Continuum Contamination

The problem of removing flat continuum contamination (e.g. originating in the central engine in Seyferts) from the total galaxy spectra is addressed by Origlia, Moorwood & Oliva (1993), Oliva et al. (1995) and Ivanov et al. (2000) in the context of Seyfert galaxies where a featureless continuum spectrum emitted from the nuclear source dilutes the stellar absorption features. The dilution spectrum peaks to the red from the K-band, making the CO at $2.29 \mu\text{m}$ the most affected feature. Solving the dilution problem is crucial for studying circumnuclear stellar populations in AGNs, because the infrared band passes are less affected by the significant dust extinction in the centers of these galaxies.

One approach to alleviate the dilution is to build diagnostics based on spectral features that are nearby in wavelength space. Oliva et al. (1995) suggested the $\text{EW}(\text{CO}1.62)/\text{EW}(\text{Si}1.59)$ ratio as temperature indicator (see Section 4.8), and

Förster — Schreiber (2000) demonstrated that the $\text{EW}(\text{CO}2.29)/\text{EW}(\text{Mg}2.28)$ has similar properties. We showed in the previous Section the same for $\text{EW}(\text{CO}1.62)/\text{EW}(\text{Mg}1.50)$. Here the similar behavior of giants and supergiants works to our advantage, alleviating the necessity to know the nature of the underlying stellar populations in detail. The H-band ratios are preferable also because they minimize the dilution further, just by the natural decrease of the diluting flux to the blue. The next step is to plot a feature strongly affected by the dilution, preferably from the K-band (e.g. CO 2.29 μm or Ca 2.26 μm), against one of these ratios. The displacement of the Seyferts from the stellar sequence is a dilution measure (Figure 4.14).

An alternative approach is to use a set of lines, whose line ratio is constant but whose wavelengths are as far apart as possible. Having four lines of the same species (MgI, Figure 4.15), nearly evenly spaced across the HK windows opens new possibilities to constrain the nature of the nonstellar flux in Seyfert galaxies. Each of the MgI lines would be diluted to a different degree, providing a new tool to constrain the slope of the diluting spectrum. However, this technique is rather demanding on the data quality because the most diluted K-band MgI lines are the weakest.

Further possibility is to use the $\log\{\text{EW}(\text{CO}1.62)/[\text{EW}(\text{Na}2.21)+\text{EW}(\text{Ca}2.26)]\}$ or $\log\{\text{EW}(\text{CO}2.29)/[\text{EW}(\text{Mg}1.50)+\text{EW}(\text{Mg}1.71)]\}$ (Figure 4.16). Similar expressions were discussed in Section 4.8 (Figure 4.13), and showed almost constant behavior for giants and supergiants with $T_{\text{eff}} \leq 4000$ deg.

4.10. Elemental Abundance Ratios

Perhaps, the most disappointing result in this study is the lack of a spectral feature in the infrared to measure directly the abundance of the iron-peak elements (except for the unreliable FeI line at $1.58\ \mu\text{m}$; see Section 4.7.4). Estimating separately the α element content, and the iron-peak abundances is a particularly important problem in starburst galaxies, where the active recent star formation with a top-heavy initial mass function (suggested by Rieke et al. 1980), would enrich greatly the host galaxy light element content. Therefore, the $[\text{Fe}/\text{H}]$ ratio ceases to represent adequately the overall metallicity of these systems. An additional parameter, representing the α -element enrichment is necessary.

The CaI line at $2.26\ \mu\text{m}$ offers the only viable alternative to estimate the $[\text{Mg}/\text{Fe}]$ ratio. Worthey (1998) compared the behavior of optical indices in elliptical galaxies and spheroids, and concluded that the Ca follows the Fe. Therefore the Mg-to-Ca ratio could be used to constrain the light-to-heavy element enrichment, and potentially, the star formation history of stellar systems. Sodium is a product of CNO burning. Worthey (1998) confirmed based on Milky Way data, that it behaves like Mg. Any analysis of external galaxies, based on a combination of Na $2.21\ \mu\text{m}$ and Ca $2.26\ \mu\text{m}$ indices has to be treated with caution because of variation of the star formation and enrichment history.

4.11. Summary

We have obtained moderately high resolution ($R \approx 2000\text{-}3000$) H and K spectra of over 218 red stars, mostly supergiants and giants. These stars dominate the infrared emission in starbursts. Our library spans a range of effective temperatures, and covers abundances from $[\text{Fe}/\text{H}] = -2.2$ to $+0.3$. This library provides an

unique opportunity to study directly the most obscured stellar populations in starburst galaxies.

(i) We found that MgI indices are particularly promising metallicity indicators because they are less sensitive to the effective stellar temperature than other lines, particularly for cool K-M giants. Because these are the stars that contribute a significant fraction of the near infrared radiation in many galaxies, we conclude that the H and K band MgI indices are expected to be just as good indicators for the abundance in composite systems, as their optical counterparts. Our result suggests a new method to break the age-metallicity degeneracy in stellar populations of galaxies, in the infrared.

(ii) NaI and CaI lines, used before as metallicity indicators in globular clusters, proved to be affected strongly by the stellar temperature dependence. Such a technique does require an independent temperature estimate - perhaps based on the strength of the CO bands.

(iii) The CO bands demonstrate a significant metallicity dependence. However, the restrictions of our sample prevent us from separating the stellar temperature and surface gravity effects.

(iv) To facilitate further applications of the data, polynomial fits were derived, connecting the spectral indices to the metallicity, effective temperature, and surface gravity for the giants in the library.

(v) We fitted a number of line ratios ($EW(CO1.62)/EW(Si1.59)$, $EW(CO1.62)/EW(Mg1.50)$, $EW(Mg1.50)/EW(Ca2.26)$, and $EW(Mg1.50)/EW(Na2.21)$) as temperature indicators. The later two have the advantage of being relatively luminosity independent.

(vi) We demonstrated that $\log\{\text{EW}(\text{CO1.62})/[\text{EW}(\text{Mg1.50})+\text{EW}(\text{Mg1.71})]\}$ is a good giant/supergiant versus dwarf separator. It is better than $\log\{\text{EW}(\text{CO2.29})/[\text{EW}(\text{Na2.21})+\text{EW}(\text{Ca2.26})]\}$, suggested by Ramírez et al. (1997), because sodium and calcium lines do bear some surface gravity dependence, stronger than the magnesium lines.

(vii) We proposed a new MgI based method to constrain the slope of the featureless continuum, originating in the non-stellar source in galaxies with active galactic nuclei. The contamination increases with wavelength, so the 1.50 μm line would suffer least contamination and can be used to predict the true strength of 1.71, 2.11, and 2.28 μm lines, which would be more contaminated.

(viii) Our data demonstrate that $\text{EW}(\text{CO1.62})/[\text{EW}(\text{Na2.21})+\text{EW}(\text{Ca2.26})]$ and $\text{EW}(\text{CO2.29})/[\text{EW}(\text{Mg1.50})+\text{EW}(\text{Mg1.71})]$ parameters change weakly with temperature, therefore providing additional tools to constrain the non-stellar continuum shape in AGNs.

(ix) Despite the lack of suitable iron lines, the light-to-heavy element abundance ratio can be estimated in the infrared by using the CaI 2.26 μm line.

Table 4.1 Properties of previous infrared spectral libraries.

Spectral Library	λ	Cove-	No.	Spectr.
Reference	μm	rage	Stars	Resolution
Johnson & Mèndez (1970)	1.2-2.5	A-M I-V	32	550
Kleinmann & Hall (1986)	2.0-2.5	F-M I-V	26	2500-3100
Lançon & Rocca-Volmerange (1992)	1.4-2.5	O-M I-V	56	550
Origlia, Moorwood & Oliva (1993)	1.5-1.7	G-M I-V	40	1500
Ali et al. (1995)	2.0-2.4	F-M V	33	1380
Wallace & Hinkle (1996)	2.02-2.41	G-M I-V	12	45000
Dallier, Boisson & Joly (1996)	1.57-1.64	O-M I-V	37	1500-2000
Hanson, Conti & Rieke (1996)	2.0-2.4	O-B O-V	180	800-3000
Ramírez et al. (1997)	2.19-2.34	K-M III	43	1380,4830
Wallace & Hinkle (1997)	2.0-2.4	O-M I-V	115	3000
Meyer et al. (1998)	1.5-1.7	O-M I-V	85	3000
Joyce (1998)	1.0-2.5	K-M III	29	500-1500
Förster – Schreiber (2000)	1.90-2.45	G-M I-III	31	830,3000
Wallace et al. (2000)	1.05-1.34	O-M I-V	88	3000
Lançon & Wood (2000)	0.5-2.5	K-M I-III	77	1100
Hicks et al. (2000)	1.08-1.35	O-M I-V	105	650

Table 4.2 Log of spectroscopic observations.

Date	Site	Obs.	Star	Std.	Sp.T.	Gr.	Range
(1)	(2)	(3)	(4)	(5)	(6)	(7)	(8)
951209	61	CE,KL S074439	S074506	A3 V	600		HK
951209	61	CE,KL S060890	HR3348	A0 V	600		HK
951209	61	CE,KL S027179	HR3592	A2 V	600		HK
951209	61	CE,KL VYLeo	HR4244	A3 V	600		H
951210	61	CE,KL S074175	HR0277	A2 V	600		HK
951210	61	CE,KL S109474	HR0081	A0 V	600		HK
951210	61	CE,KL S109471	HR0081	A0 V	600		HK
951210	61	CE,KL S074883	HR0669	A1 V	600		2.30-2.40
951210	61	CE,KL S080333	HR3481	A1 V	600		HK
951210	61	CE,KL S098021	HR3481	A1 V	600		HK
951210	61	CE,KL S098087	HR3481	A1 V	600		HK
951210	61	CE,KL GL406	HR4244	A3 V	600		H,2.05-2.15
951211	61	CE,KL GL905	HR0001	A1 V	600		2.20-2.40
951211	61	CE,KLGL15NE	HR0001	A1 V	600		2.20-2.40
951211	61	CE,KLGL15SW	HR0001	A1 V	600		2.20-2.40
951211	61	CE,KL S074883	HR0669	A1 V	600		1.50-2.25
951213	61	CE,KL GL905	HR0001	A1 V	600		1.50-2.15
951213	61	CE,KLGL15NE	HR0001	A1 V	600		1.50-2.15
951213	61	CE,KLGL15SW	HR0001	A1 V	600		1.50-2.15
951213	61	CE,KL GL83-1	HR2578	A6 V	600		HK
951213	61	CE,KLGL65AB	HR0451	A3 V	600		HK

Date	Site	Obs.	Star	Std.	Sp.T.	Gr.	Range
(1)	(2)	(3)	(4)	(5)	(6)	(7)	(8)
951213	61	CE,KL	HR1324	HR1272	A3 V	600	HK
951213	61	CE,KL	GL166C	HR1272	A3 V	600	HK
951213	61	CE,KLS	116988	HR3406	A3 V	600	HK
951213	61	CE,KLS	116569	HR3406	A3 V	600	HK
951213	61	CE,KL	VYLeo	HR4244	A3 V	600	2.20-2.40
951213	61	CE,KL	GL402	HR4244	A3 V	600	2.20-2.40
951213	61	CE,KL	GL412A	HR4380	A2 V	600	2.05-2.30
951213	61	CE,KL	GL411	HR4380	A2 V	600	2.05-2.30
951214	61	CE,KL	GL866	HR8816	A0 V	600	HK
951214	61	CE,KL	HR8841	HR8816	A0 V	600	HK
951214	61	CE,KL	HR0617	HR0669	A1 V	600	2.25-2.40
951214	61	CE,KL	GL213	HR1819	A4 V	600	HK
951214	61	CE,KL	HR1907	HR1819	A4 V	600	HK
951214	61	CE,KL	GL206	HR1819	A4 V	600	HK
951214	61	CE,KL	HR3905	HR4041	A0 V	600	HK
951214	61	CE,KL	GL388	HR4041	A0 V	600	HK
951215	61	CE,KL	HR0617	HR0669	A1 V	600	1.50-2.20
951215	61	CE,KL	HR0867	HR0972	A1 V	600	HK
951215	61	CE,KL	HR1015	HR0972	A1 V	600	HK
951218	61	CE,KL	HR8795	HR8826	A5 V	600	HK
951218	61	CE,KL	HR8860	HR8837	A0 V	600	1.50-2.20
951218	61	CE,KL	HR8832	HR8837	A0 V	600	1.50-2.20

Date	Site	Obs.	Star	Std.	Sp.T.	Gr.	Range
(1)	(2)	(3)	(4)	(5)	(6)	(7)	(8)
960301	61	CE,KL	HR3538	HR3314	A0 V	600	HK
960301	61	CE,KL	HR4299	HR4356	A0 V	600	HK
960301	61	CE,KL	HR4883	HR4738	A4 V	600	HK
960301	61	CE,KL	HR4954	HR4738	A4 V	600	HK
960301	61	CE,KL	S44383	HR5169	A1 V	600	HK
960302	61	CE,KL	HR3359	HR3314	A0 V	600	HK
960302	61	CE,KL	HR4069	HR4113	A4 V	600	HK
960302	61	CE,KL	HR4184	HR4113	A4 V	600	HK
960302	61	CE,KL	GL411	HR4380	A2 V	600	1.50-2.25
960302	61	CE,KL	GL412A	HR4380	A2 V	600	1.50-2.25
960302	61	CE,KL	HR4932	HR4805	A1 V	600	2.35-2.40
960302	61	CE,KL	S119433	HR4805	A1 V	600	2.35-2.40
960505	61	CE,KL	HR4362	HR4357	A4 V	600	HK
960505	61	CE,KL	S082106	HR4357	A4 V	600	HK
960505	61	CE,KL	HR5072	HR5144	A1 V	600	H
960505	61	CE,KL	GL526	HR5144	A1 V	600	H
960505	61	CE,KL	HR5072	HR5010	F0 V	600	K
960505	61	CE,KL	GL526	HR5010	F0 V	600	K
960505	61	CE,KL	HR6242	HR6123	A5 V	600	HK
960505	61	CE,KL	S045933	HR6123	A5 V	600	HK
960505	61	CE,KL	HR7475	HR7546	A3 V	600	K
960505	61	CE,KL	H339034	HR7546	A3 V	600	K

Date	Site	Obs.	Star	Std.	Sp.T.	Gr.	Range
(1)	(2)	(3)	(4)	(5)	(6)	(7)	(8)
960506	61	CE,KL	HR4496	HR4380	A2 V	600	HK
960506	61	CE,KL	HR4716	HR5142	A3 V	600	HK
960506	61	CE,KL	HR5019	HR4776	F2 V	600	HK
960506	61	CE,KL	HR5853	HR6093	F2 V	600	HK
960506	61	CE,KL	HR6014	HR6093	F2 V	600	HK
960506	61	CE,KL	HR6623	HR6324	A0 V	600	HK
960506	61	CE,KL	HR6418	HR6324	A0 V	600	HK
960506	61	CE,KL	HR6212	HR6324	A0 V	600	HK
960505	61	CE,KL	HR7475	HR7546	A3 V	600	H
960506	61	CE,KL	H339034	HR7546	A3 V	600	H
960506	61	CE,KL	HR8465	HR8585	A1 V	600	H
960506	61	CE,KL	S034529	HR8585	A1 V	600	H
960507	61	CE,KL	GL380	HR3799	A2 V	600	HK
960507	61	CE,KL	HR5270	HR5392	A5 V	600	HK
960507	61	CE,KL	HR5409	HR5392	A5 V	600	HK
960507	61	CE,KL	HR5594	HR5392	A5 V	600	HK
960507	61	CE,KL	GL570A	HR5570	F0 V	600	HK
960507	61	CE,KL	GL570B	HR5570	F0 V	600	HK
960507	61	CE,KL	NR6713	HR6629	A0 V	600	HK
960507	61	CE,KL	NR8465	HR8585	A1 V	600	K
960507	61	CE,KL	S034529	HR8585	A1 V	600	K
960508	61	CE,KL	GL328	HR3651	A0 V	300	HK

Date	Site	Obs.	Star	Std.	Sp.T.	Gr.	Range
(1)	(2)	(3)	(4)	(5)	(6)	(7)	(8)
960508	61	CE,KL	GL338	HR3592	A2 V	300	HK
960508	61	CE,KL	GL352	HR3909	A1 V	300	HK
960508	61	CE,KL	GL381	HR3909	A1 V	300	HK
960508	61	CE,KL	GL382	HR3909	A1 V	300	HK
960508	61	CE,KL	GL402	HR4227	A2 V	300	HK
960508	61	CE,KL	GL406	HR4227	A2 V	300	HK
960508	61	CE,KL	GL411	HR4422	A2 V	300	HK
960508	61	CE,KL	HR4375	HR4422	A2 V	300	HK
960508	61	CE,KL	GL436	HR4738	A4 V	300	HK
960508	61	CE,KLS	028414	HR5142	A3 V	300	HK
960508	61	CE,KL	HR5553	HR5386	A0 V	600	HK
960508	61	CE,KL	HR5235	HR5386	A0 V	600	HK
960508	61	CE,KL	HR6498	HR6629	A0 V	600	HK
960508	61	CE,KLS	122610	HR6629	A0 V	600	HK
960508	61	CE,KL	HR6752	HR6629	A0 V	600	HK
960508	61	CE,KL	HR8085	HR8028	A1 V	600	K
960508	61	CE,KL	HR8086	HR8028	A1 V	600	K
960509	61	CE,KL	HR4400	HR4356	A0 V	600	HK
960509	61	CE,KL	HR4418	HR4356	A0 V	600	HK
960509	61	CE,KL	HR5901	HR5774	A5 V	600	HK
960509	61	CE,KL	HR5800	HR5774	A5 V	600	HK
960509	61	CE,KL	HR5770	HR5870	A3 V	600	1.70

Date	Site	Obs.	Star	Std.	Sp.T.	Gr.	Range
(1)	(2)	(3)	(4)	(5)	(6)	(7)	(8)
960509	61	CE,KL	HR6092	HR5874	A5 V	600	1.70
960509	61	CE,KL	HR6588	HR6509	A4 V	600	1.70
960509	61	CE,KL	HR6353	HR6534	A5 V	600	1.70
960509	61	CE,KL	HR5932	HR6123	A5 V	600	HK
960509	61	CE,KL	HR6146	HR6123	A5 V	600	HK
960509	61	CE,KL	HR7009	HR7051	A4 V	600	HK
960509	61	CE,KL	HR7139	HR7051	A4 V	600	HK
960509	61	CE,KL	HR8085	HR8028	A1 V	600	H
960509	61	CE,KL	HR8086	HR8028	A1 V	600	H
960510	61	CE,KL	HR4666	HR4738	A4 V	600	HK
960510	61	CE,KL	HR4668	HR4738	A4 V	600	HK
960510	61	CE,KL	HR5600	HR5676	A2 V	600	HK
960510	61	CE,KL	HR5616	HR5676	A2 V	600	HK
960510	61	CE,KL	HR6364	HR6457	A2 V	600	HK
960510	61	CE,KL	HR7063	HR6930	A3 V	600	HK
960510	61	CE,KL	HR7957	HR7619	A4 V	600	HK
960510	61	CE,KL	S033232	HR7619	A4 V	600	HK
960625	90	CE,R2	BMB239	HR6836	G0 V	600	2.20-2.40
960625	90	CE,R2	BMB181	HR6836	G0 V	600	2.20-2.40
960625	90	CE,R2	TLE205	HR6836	G0 V	600	2.20-2.40
960625	90	CE,R2	BMB289	HR6836	G0 V	600	2.20-2.40
960625	90	CE,R2	BMB194	HR6836	G0 V	600	2.20-2.40

Date	Site	Obs.	Star	Std.	Sp.T.	Gr.	Range
(1)	(2)	(3)	(4)	(5)	(6)	(7)	(8)
960625	90	CE,R2	BMB39	HR6836	G0 V	600	2.20-2.40
960625	90	CE,R2	C669	HR0005	G5 V	600	2.10-2.20
960625	90	CE,R2	C501	HR0005	G5 V	600	2.10-2.20
960625	90	CE,R2	C468	HR0005	G5 V	600	2.10-2.20
960625	90	CE,R2	C971	HR0005	G5 V	600	2.10-2.20
960626	90	CE	BMB239	HR6836	G0 V	600	2.10-2.15
960626	90	CE	BMB181	HR6836	G0 V	600	2.10-2.15
960626	90	CE	TLE205	HR6836	G0 V	600	2.10-2.15
960626	90	CE	BMB289	HR6836	G0 V	600	2.10-2.15
960626	90	CE	BMB194	HR6836	G0 V	600	2.10-2.15
960626	90	CE	BMB39	HR6836	G0 V	600	2.10-2.15
960626	90	CE	HR8085	HR8028	A1 V	600	2.10-2.15
960626	90	CE	HR8086	HR8028	A1 V	600	2.10-2.15
960626	90	CE	C669	HR0005	G5 V	600	2.25-2.40
960626	90	CE	C501	HR0005	G5 V	600	2.25-2.40
960626	90	CE	C468	HR0005	G5 V	600	2.25-2.40
960626	90	CE	C971	HR0005	G5 V	600	2.25-2.40
960627	90	CE,KL	GL626	HR5853	G5 V	300	K
960627	90	CE,KL	HR6156	HR5853	G5 V	300	K
960627	90	CE,KL	S045933	HR5853	G5 V	300	K
960627	90	CE,KL	HR6014	HR5853	G5 V	300	K
960627	90	CE,KL	HR5859	HR5853	G5 V	300	K

Date	Site	Obs.	Star	Std.	Sp.T.	Gr.	Range
(1)	(2)	(3)	(4)	(5)	(6)	(7)	(8)
960627	90	CE,KL	GL644	HR5853	G5 V	300	K
960627	90	CE,KL	HR6033	HR5853	G5 V	300	K
960627	90	CE,KLBMB	285	HR6836	G0 V	300	HK
960627	90	CE,KL	B133	HR6836	G0 V	300	HK
960627	90	CE,KLBMB	179	HR6836	G0 V	300	HK
960627	90	CE,KL	BMB87	HR6836	G0 V	300	HK
960627	90	CE,KLBMB	142	HR6836	G0 V	300	HK
960627	90	CE,KL	HR7162	HR6836	G4.5 V	300	K
960627	90	CE,KL	HR7102	HR6836	G4.5 V	300	K
960627	90	CE,KL	HR7368	HR6836	G4.5 V	300	K
960627	90	CE,KL	GL725B	HR6836	G4.5 V	300	K
960627	90	CE,Kk	GL725A	HR6836	G4.5 V	300	K
960627	90	CE,KL	HR7251	HR6836	G4.5 V	300	K
960627	90	CE,KL	S031745	HR6836	G4.5 V	300	K
960627	90	CE,KL	HR7957	HR6836	G4.5 V	300	K
960627	90	CE,KL	GL752B	HR6836	G4.5 V	300	K
960627	90	CE,KL	GL752A	HR6836	G4.5 V	300	K
960627	90	CE,KL	HR7332	HR6836	G4.5 V	300	K
960627	90	CE,KL	S126068	HR6836	G4.5 V	300	K
960627	90	CE,KL	HR8086	HR6836	G4.5 V	300	K
960627	90	CE,KL	HR8085	HR6836	G4.5 V	300	K
960627	90	CE,KL	HR8028	HR6836	G4.5 V	300	K

Date	Site	Obs.	Star	Std.	Sp.T.	Gr.	Range
(1)	(2)	(3)	(4)	(5)	(6)	(7)	(8)
960627	90	CE,KL	C415	HR0005	G5 V	300	K
960627	90	CE,KL	C575	HR0005	G5 V	300	K
960627	90	CE,KL	C676	HR0005	G5 V	300	K
960627	90	CE,KL	C857	HR0005	G5 V	300	K
960627	90	CE,KL	C875	HR0005	G5 V	300	K
960627	90	CE,KL	C897	HR0005	G5 V	300	K
960628	90	CE,KL	S045933	HR6156	A1 V	300	K
960628	90	CE,KL	GL625	HR6156	A1 V	300	K
960628	90	CE,KL	S122610	HR6629	A0 V	300	HK
960628	90	CE,KL	S031745	HR7251	A0 V	300	H
960628	90	CE,KL	GL673	HR6629	A0 V	300	HK
960628	90	CE,KL	HR6752	HR6629	A0 V	300	HK
960628	90	CE,KL	GL725A	HR7251	A0 V	300	H
960701	90	CE,KL	GL380	HR3799	A2 V	300	K
960701	90	CE,KL	GL411	HR4380	A2 V	300	K
960701	90	CE,KL	GL412A	HR4380	A2 V	300	K
960701	90	CE,KL	HR4785	HR5142	A3 V	300	K
960701	90	CE,KL	S028414	HR5142	A3 V	300	K
960701	90	CE,KL	HR5072	HR5144	A1 V	300	K
960701	90	CE,KL	GL526	HR5144	A1 V	300	K
960701	90	CE,KL	BMB239	HR6836	G0 V	600	1.65-1.70
960701	90	CE,KL	BMB181	HR6836	G0 V	600	1.65-1.70

Date	Site	Obs.	Star	Std.	Sp.T.	Gr.	Range
(1)	(2)	(3)	(4)	(5)	(6)	(7)	(8)
960701	90	CE,KL TLE205	HR6836	G0 V	600	1.65-1.70	
960701	90	CE,KL BMB289	HR6836	G0 V	600	1.65-1.70	
960701	90	CE,KL BMB194	HR6836	G0 V	600	1.65-1.70	
960701	90	CE,KL BMB39	HR6836	G0 V	600	1.65-1.70	
961030	90	KL,CEN188II72	HR0240	A4 V	600	HK	
961030	90	KL,CEN188I105	HR0240	A4 V	600	HK	
961031	90	CE,KL S105082	HR7390	A0 V	600	HK(-2.40)	
961031	90	CE,KL HR8841	HR8840	A3 V	600	HK(-2.40)	
961031	90	CE,KL HR8924	HR8840	A3 V	600	HK(-2.40)	
961031	90	CE,KLN188-359	HR0240	A4 V	600	HK(-2.40)	
961031	90	CE,KLN188-473	HR0240	A4 V	600	HK(-2.40)	
961031	90	CE,KL HR1726	HR1752	A1 V	600	HK(-2.40)	
961031	90	CE,KL HR1805	HR1752	A1 V	600	HK(-2.40)	
970327	90	CE,KL HR3905	HR3792	A3 V	600	HK	
970327	90	CE,KL HR4365	HR4437	G0 V	600	HK	
970613	MM	CE,KLM92III13	HR6469	F9 V	600	K	
980405	90	VI,R2 HR3428	HR3510	G1 V	600	K(-2.42)	
980405	90	VI,R2 HR4521	HR4439	G1 V	600	HK	
980406	90	VI,MR HR3428	HR3510	G1 V	600	1.62-1.70	
980406	90	VI,MR HR3905	HR3951	G3 V	600	1.50-2.19	
980406	90	VI,MR M3III28	HR4983	G0 V	600	1.50-2.19	
980407	90	VI,MR HR2503	HR2779	G0 V	600	2.24-2.42	

Date	Site	Obs.	Star	Std.	Sp.T.	Gr.	Range
(1)	(2)	(3)	(4)	(5)	(6)	(7)	(8)
980407	90	VI,MR	HR3905	HR3951	G3 V	600	2.24-2.42
980407	90	VI,MR	HR4287	HR4005	F6 V	600	2.24-2.37
980407	90	VI,MR	M3III28	HR4983	G0 V	600	2.24-2.37
980408	90	VI,MR	HR2289	HR2483	G0 V	600	2.02-2.32
980408	90	VI,MR	H77729	HR3563	F6 V	600	2.32
980408	90	VI,MR	HR4986	HR5011	G0 V	600	2.32
980408	90	VI,MR	M3III28	HR4983	G0 V	600	2.24
980408	90	VI,MR	S185981	HR6595	F6 V	600	2.20-2.32
980408	90	VI,MR	BMB289	HR6836	G0 V	600	2.19-2.24
980408	90	VI,MRB+	243902	HR7386	F7 V	600	2.32
980409	90	VI,MR	HR2289	HR2483	G0 V	600	H,2.37-2.42
980409	90	VI,R2	HR3428	HR3510	G1 V	600	2.42
980409	90	VI,MR	M3III28	HR4983	G0 V	600	2.06,2.24
980409	90	VI,MR	BMB289	HR6836	G0 V	600	H,2.19-2.24
980410	90	VI,R2	HR2854	HR2918	G0 V	600	HK
980410	90	VI,R2	H77729	HR3563	F6 V	600	1.54-62,K(-2.32)
980410	90	VI,R2	HR3994	HR4158	F7 V	600	HK
980410	90	VI,R2	HR4287	HR4005	F6 V	600	1.54-1.62
980410	90	VI,R2	M2III28	HR4983	G0 V	600	H
980410	90	VI,R2	HR5370	HR5346	G0 V	600	HK
980410	90	VI,R2	HR5829	HR5583	F8 V	600	HK
980410	90	VI,R2	S008274	HR5596	F9 V	600	HK

Date	Site	Obs.	Star	Std.	Sp.T.	Gr.	Range
(1)	(2)	(3)	(4)	(5)	(6)	(7)	(8)
980410	90	VI,R2	BMB289	HR6836	G0 V	600	2.31-2.42
980603	90	R2	HR4986	HR5011	G0 V	600	HK
980603	90	R2	M5III3	HR5721	F0 V	600	1.54-1.62
980605	90	VI,MR	M5III3	HR5721	F0 V	600	2.06-2.24
980606	90	VI,MR	S119734	HR5011	G0 V	600	HK
980607	90	VI,MRM13B786	HR6064	G1 V	600		K
980607	90	VI,MR	M71A6	HR7580	B9.5 V	600	2.13-2.42
980608	90	VI	HR5366	HR5384	G2 V	600	HK
980608	90	VI	HR5681	HR5968	G2 V	600	1.54-2.24
980608	90	VI	BMB239	HR6836	G2 V	600	1.54
980608	90	VI	BMB181	HR6836	G2 V	600	1.54
980608	90	VI	TLE205	HR6836	G2 V	600	1.54
980608	90	VI	BMB194	HR6836	G2 V	600	1.54
980608	90	VI	BMB039	HR6836	G2 V	600	1.54
980608	90	VI	BMB289	HR6836	G2 V	600	2.06-2.13
980608	90	VI	M71A6	HR7580	B9.5 V	600	H
980608	90	VI	M71A4	HR7580	B9.5 V	600	H
980609	90	VI,R2	HR5366	HR5384	G2 V	600	HK
980609	90	VI,R2	M5III3	HR5721	F0 V	600	1.62-70,2.31-37
980609	90	VI,R2	S185981	HR6595	F6 V	600	1.54-2.13,2.37-42
980609	90	VI,R2	H339034	HR7386	F7 V	600	HK(-1.71)
980609	90	VI,R2	BCCyg	HR7887	F0 V	600	2.24-2.42

Date	Site	Obs.	Star	Std.	Sp.T.	Gr.	Range
(1)	(2)	(3)	(4)	(5)	(6)	(7)	(8)
980609	90	VI,R2	BICyg	HR7887	F0 V	600	2.24-2.42
980609	90	VI,R2	KYCyg	HR7887	F0 V	600	2.24-2.42
980610	90	VI	HR5196	HR5019	G6 V	600	HK
980610	90	VI	HR5582	HR5455	F5 V	600	HK(-1.70)
980610	90	VI	HR5681	HR5968	G2 V	600	2.31-2.42
980610	90	VI	M5III3	HR5721	F0 V	600	2.42
980611	90	VI,MR	M5III3	HR5721	F0 V	600	2.42
980611	90	VI,MRM13B786	HR6064	G1 V	600		H
980611	90	VI,MR	HR2697	HR5581	F7 V	600	HK
980611	90	VI,MR	HR5947	HR5968	G2 V	600	HK
980611	90	VI,MRM92XII8	HR6469	F9 V	600		H
980611	90	VI,MR	M71A6	HR7580	B9.5 V	600	2.06
980611	90	VI,MR	HR6018	HR6064	G1 V	600	HK
980611	90	VI,MR	HR2701	HR6064	G1 V	600	HK
980611	90	VI,MR	BCCyg	HR7887	F0 V	600	1.54-2.19
980611	90	VI,MR	BICyg	HR7887	F0 V	600	1.54-2.19
980611	90	VI,MR	KYCyg	HR7887	F0 V	600	1.54-2.19
981002	90	VI,MR	HR6817	HR6847	F7 V	600	HK
981002	90	VI,MR	S089499	HR8250	F7 V	600	HK
981002	90	VI,MR	HR0843	HR0761	F8 V	600	HK
981002	90	VI,MR	HR1939	HR2141	G0 V	600	H,2.06-2.19
981003	90	VI	S050265	HR8170	F7 V	600	2.245-2.42

Date	Site	Obs.	Star	Std.	Sp.T.	Gr.	Range
(1)	(2)	(3)	(4)	(5)	(6)	(7)	(8)
981003	90	VI	S050296	HR8170	F7 V	600	2.245-2.42
981003	90	VI	S050381	HR8170	F7 V	600	2.245-2.42
981003	90	VI	HR8062	HR8170	F7 V	600	2.24-2.42
981003	90	VI	HR8860	HR8853	F0 V	600	2.25-2.35
981003	90	VI	HR8832	HR8853	F0 V	600	2.25-2.35
981003	90	VI	HR0265	HR0297	F6 V	600	2.19-2.42
981003	90	VI	S011591	HR0297	F6 V	600	2.19-2.42
981003	90	VI	S011620	HR0297	F6 V	600	2.19-2.42
981003	90	VI	S022188	HR0297	F6 V	600	2.19-2.42
981003	90	VI	HR1015	HR0869	F6 V	600	2.24-2.42
981004	90	VI	H339034	HR7386	F7 V	600	1.71
981004	90	VI	M71A9	HR7580	B9.5 V	600	2.06-2.19
981004	90	VI	N188II181	HR0357	F5 V	600	2.06-2.245
981004	90	VI	N188II181	HR9034	F5 V	600	2.31-2.42
981004	90	VI	HR1939	HR2141	G0 V	600	2.24-2.42
981004	90	VI	HR1779	HR2141	G0 V	600	2.37-2.42
981004	90	VI	HR1726	HR2141	G0 V	600	2.37-2.42
981004	90	VI	HR1805	HR2141	G0 V	600	2.37-2.42
981004	90	VI	S77179	HR2141	G0 V	600	2.37-2.42
981005	90	VI	M71A9	HR7580	B9.5 V	600	1.62-71,2.24-42
981005	90	VI	C468	HR0005	G5 V	600	H
981005	90	VI	C501	HR0005	G5 V	600	H

Date	Site	Obs.	Star	Std.	Sp.T.	Gr.	Range
(1)	(2)	(3)	(4)	(5)	(6)	(7)	(8)
981005	90	VI	C669	HR0005	G5 V	600	H
981005	90	VI	C971	HR0005	G5 V	600	H
981005	90	VI	HR0265	HR0297	F6 V	600	1.54-1.62
981005	90	VI	S011591	HR0297	F6 V	600	1.54-1.62
981005	90	VI	S011620	HR0297	F6 V	600	1.54-1.62
981005	90	VI	S022188	HR0297	F6 V	600	1.54-1.62
981005	90	VI	HR1015	HR0869	F6 V	600	HK
981005	90	VI	HR1779	HR2141	G0 V	600	2.24-2.31
981005	90	VI	HR1726	HR2141	G0 V	600	2.24-2.31
981005	90	VI	HR1805	HR2141	G0 V	600	2.24-2.31
981005	90	VI	S077179	HR2141	G0 V	600	2.24-2.31
981006	90	VI	M71A9	HR7580	B9.5 V	600	1.54
981006	90	VI	M71A4	HR7580	B9.5 V	600	2.06-2.24
981006	90	VI	S105082	HR7580	B9.5 V	600	1.54-2.24
981006	90	VI	S050265	HR8170	F7 V	600	1.54-2.19
981006	90	VI	S050296	HR8170	F7 V	600	1.54-2.19
981006	90	VI	S050381	HR8170	F7 V	600	1.54-2.19
981006	90	VI	HR8062	HR8170	F7 V	600	1.54-2.19
981006	90	VI	HR0265	HR0297	F6 V	600	2.06-2.13
981006	90	VI	S011591	HR0297	F6 V	600	2.06-2.13
981006	90	VI	S011620	HR0297	F6 V	600	2.06-2.13
981006	90	VI	N188II181	HR9034	F6 V	600	H

Date	Site	Obs.	Star	Std.	Sp.T.	Gr.	Range
(1)	(2)	(3)	(4)	(5)	(6)	(7)	(8)
981006	90	VI	N188I69	HR9034	F6 V	600	1.54-2.13
981006	90	VI	HR1779	HR2141	G0 V	600	1.70-2.19
981006	90	VI	HR1726	HR2141	G0 V	600	1.70-2.19
981006	90	VI	HR1805	HR2141	G0 V	600	1.70-2.19
981006	90	VI	S077179	HR2141	G0 V	600	1.70-2.19
981007	90	VI	HR7317	HR7454	F5 V	600	H
981007	90	VI	HR7430	HR7454	F5 V	600	H
981007	90	VI	HR7429	HR7560	F8 V	600	H
981007	90	VI	HR7576	HR7451	F7 V	600	H
981007	90	VI	M71A4	HR7580	B9.5 V	600	2.31-2.42
981007	90	VI	N188I69	HR0357	F5 V	600	2.13-2.42
981007	90	VI	HR1779	HR2141	G0 V	600	1.54-1.62
981007	90	VI	HR1726	HR2141	G0 V	600	1.54-1.62
981007	90	VI	HR1805	HR2141	G0 V	600	1.54-1.62
981007	90	VI	S077179	HR2141	G0 V	600	1.54-1.62
990403	90	VI	HR4932	HR5011	G0 V	600	HK
990403	90	VI	HR5366	HR5011	G0 V	600	1.54-2.13
990403	90	VI	HR5480	HR5384	G0 V	600	1.54-2.13
990404	90	VI	HR4932	HR5011	G0 V	600	1.71,2.42
990404	90	VI	HR5366	HR5384	G1 V	600	2.13-2.42
990404	90	VI	HR5480	HR5384	G1 V	600	2.13-2.42
990405	90	VI	HR1907	HR2208	G2 V	600	H

Date	Site	Obs.	Star	Std.	Sp.T.	Gr.	Range
(1)	(2)	(3)	(4)	(5)	(6)	(7)	(8)
990405	90	VI	HR2600	HR2483	G0 V	600	HK
990405	90	VI	HR2459	HR2483	G0 V	600	HK
990405	90	VI	HR2153	HR2483	G0 V	600	H,2.06
990405	90	VI	HR4267	HR4079	F6 V	600	K
990405	90	VI	M3IV25	HR4983	G0 V	600	HK
990406	90	VI	HR2574	HR2866	F8 V	600	K
990406	90	VI	HR2970	HR2866	F8 V	600	HK
990406	90	VI	HR3845	HR3901	F8 V	600	HK
990406	90	VI	HR4365	HR4437	G0 V	600	H
990406	90	VI	M5IV19	HR5721	F0 V	600	H,2.06,2.13
990406	90	VI	M5IV59	HR5721	F0 V	600	H
990406	90	VI	HR5582	HR5455	F5 V	600	1.70
990406	90	VI	HR5690	HR5583	F8 V	600	HK
990406	90	VI	HR5694	HR5583	F8 V	600	HK
990406	90	VI	HR6815	HR6831	F8 V	600	H
990406	90	VI	HR6872	HR6831	F8 V	600	H
990521	90	VI,R2	M5IV19	HR5721	F0 V	600	2.06-2.31
990521	90	VI,R2	M5IV59	HR5721	F0 V	600	2.06-2.31
990521	90	VI,R2	B133	HR6836	G0 V	600	2.06,2.13
990521	90	VI,R2	BMB285	HR6836	G0 V	600	2.06,2.13
990521	90	VI,R2	BMB179	HR6836	G0 V	600	2.06,2.13
990521	90	VI,R2	BMB142	HR6836	G0 V	600	2.06,2.13

Date	Site	Obs.	Star	Std.	Sp.T.	Gr.	Range
(1)	(2)	(3)	(4)	(5)	(6)	(7)	(8)
990521	90	VI,R2	BMB087	HR6836	G0 V	600	2.13
990521	90	VI,R2	M92XII8	HR6469	G9 V	600	2.06-2.24
990522	90	VI	HR6815	HR6831	F8 V	600	K
990522	90	VI	HR6872	HR6831	F8 V	600	K
990522	90	VI	M92XII8	HR6469	G9 V	600	2.31-2.42
990522	90	VI	S089499	HR8250	F7 V	600	2.37-2.42
990522	90	VI	HR8165	HR8250	F7 V	600	2.37-2.42
990523	90	VI	M5IV19	HR5721	F0 V	600	2.37-2.42
990523	90	VI	M5IV59	HR5721	F0 V	600	2.37-2.42
990523	90	VI	BMB239	HR6836	G0 V	600	1.60
990523	90	VI	BMB181	HR6836	G0 V	600	1.60
990523	90	VI	BMB289	HR6836	G0 V	600	1.60
990523	90	VI	TLE205	HR6836	G0 V	600	1.60
990523	90	VI	HR7317	HR7454	F7 V	600	K
990523	90	VI	HR7430	HR7454	F7 V	600	K
990523	90	VI	S089499	HR8250	F7 V	600	2.06-2.31
990523	90	VI	HR8165	HR8250	F7 V	600	2.06-2.31
990524	90	VI	HR5854	HR5859	F7 V	600	2.06
990524	90	VI	HR5854	HR5779	F7 V	600	2.13
990524	90	VI	S121191	HR5859	A0 V	600	2.06,2.245-42
990524	90	VI	S121191	HR5779	F7 V	600	2.13,2.19
990524	90	VI	HR5888	HR5859	A0 V	600	2.06,2.245-42

Date	Site	Obs.	Star	Std.	Sp.T.	Gr.	Range
(1)	(2)	(3)	(4)	(5)	(6)	(7)	(8)
990524	90	VI	HR5888	HR5779	F7 V	600	2.13,2.19
990524	90	VI	HR6136	HR5859	A0 V	600	2.06,2.245-42
990524	90	VI	HR6136	HR5779	F7 V	600	2.13,2.19
990524	90	VI	BMB194	HR6836	G0 V	600	1.60
990524	90	VI	BMB039	HR6836	G0 V	600	1.60
990524	90	VI	HR7148	HR7079	F8 V	600	H
990524	90	VI	HR7171	HR7079	F8 V	600	H
990524	90	VI	S089499	HR8250	F7 V	600	H
990524	90	VI	HR8165	HR8250	F7 V	600	H
990525	90	VI	HR5739	HR5933	F6IV	600	HK
990525	90	VI	HR5744	S029078	F9 V	600	K
990525	90	VI	S121191	HR5859	A0 V	600	H
990525	90	VI	HR5888	HR5859	A0 V	600	1.54-1.62
990525	90	VI	HR6136	HR5859	A0 V	600	H
990525	90	VI	HR6770	HR6976	A1 V	600	1.54-2.13
990525	90	VI	S123779	HR6976	A1 V	600	1.54-2.13
990525	90	VI	HR7176	HR6976	A1 V	600	1.54-2.13
990525	90	VI	HR7429	HR7560	F8 V	600	K
990525	90	VI	HR7576	HR7522	G0 V	600	K
990525	90	VI	S021465	HR0244	F8 V	600	H,2.06
990525	90	VI	HR0265	HR0244	F8 V	600	H,2.06
990526	90	VI	S082685	HR4983	F9.5 V	600	2.06

Date	Site	Obs.	Star	Std.	Sp.T.	Gr.	Range
(1)	(2)	(3)	(4)	(5)	(6)	(7)	(8)
990526	90	VI	HR6770	HR6976	A1 V	600	2.19-2.42
990526	90	VI	S123779	HR6976	A1 V	600	2.19-2.42
990526	90	VI	HR7176	HR6976	A1 V	600	2.19-2.42
990526	90	VI	HR7759	HR7638	A3 V	600	HK
990526	90	VI	HR7762	HR7638	A3 V	600	HK
990526	90	VI	HR7314	HR7638	A3 V	600	HK
990526	90	VI	HR7735	HR7638	A3 V	600	1.70
990526	90	VI	S069578	HR7638	A3 V	600	HK
990526	90	VI	S069825	HR7638	A3 V	600	HK
990526	90	VI	HR8924	HR8931	F8 V	600	HK
990527	90	VI	HR7576	HR7522	G0 V	600	H
990527	90	VI	S105082	HR7560	F8 V	600	HK
990527	90	VI	HR7609	HR7560	F8 V	600	HK
990527	90	VI	HR7847	HR8170	F7 V	600	H
990527	90	VI	HR8665	HR8548	F7 V	600	H
990527	90	VI	HR0163	HR9107	G2 V	600	H
990202	90	VI	N188I105	HR0357	F5 V	600	H,2.17
990202	90	VI	N188II72	HR0357	F5 V	600	H,2.17
990202	90	VI	HR2503	HR2779	G0 V	600	2.25
990202	90	VI	HR3428	HR3510	G1 V	600	1.54
990202	90	VI	H77729	HR3563	F6 V	600	HK
990203	90	VI	HR0617	HR0869	F6 V	600	K

Date	Site	Obs.	Star	Std.	Sp.T.	Gr.	Range
(1)	(2)	(3)	(4)	(5)	(6)	(7)	(8)
990203	90	VI	HR0843	HR0869	F6 V	600	HK
990203	90	VI	HR0867	HR0869	F6 V	600	K
990203	90	VI	HR1015	HR0869	F6 V	600	HK
990203	90	VI	HR3369	HR3299	F6 V	600	2.24-2.42
990203	90	VI	HR3427	HR3299	F6 V	600	2.24-2.42
990203	90	VI	HR3428	HR3299	F6 V	600	2.24-2.42
990203	90	VI	HR3461	HR3299	F6 V	600	2.31-2.42

Columns: (1) In yymmdd format, e.g. 990203 is the night of Feb 3-4, 1999; (2) Sites: 61,90,MM - Steward Observatory 1.55-m, 2.3-m, and the original MMT telescopes, respectively; (3) Observers: I - V.D. Ivanov, E - C.W. Engelbracht, L - K. Luhman, R - M.J. Rieke, RR - M.J. Rieke and G.H. Rieke; (4) Object, S=SAO,H=HD,N=NGC,B=BD; (5) Standard for the atmospheric correction; (6) Spectral Type for the standard star; (7) Grating: 600 lines mm⁻¹ corresponds to spectral resolution $R \approx 3000$, 300 lines mm⁻¹ corresponds to spectral resolution $R \approx 1500$; (8) Spectral range covered, in terms of atmospheric windows, or in terms of central wavelength (in μm), of the grating settings. A number in brackets with a minus indicates a missing setting. See Section 4.3 for details.

Table 4.3 Adopted atmospheric parameters of the stars.

Stellar ID ^a					Sp.	Std ^b	Atmosph. Parameters ^c				
HR	HD	SAO	BD	Other	Class		T _{eff}	log <i>g</i>	[Fe/H]	(B-V)	(V-K)
0 104452	82106	22 2430	1Com	G0 II	A	5702 1	2.29 1	0.00 1	0.64 73	1.44 76	
7063 173764	142618	-4 4582	<i>β</i> Sct	G4 II	A	4700 2	0.94 2	-0.15 2	1.09 8	1.89 76	
4418 99648	118875	3 2504	<i>τ</i> Leo	G8 Iab	A	4850 2	1.90 2	0.36 2	1.01 38	1.99 76	
3461 74442	98087	18 2027	<i>δ</i> Cnc	K0 II-III	G	4651 3	2.10 3	0.16 3	1.09 8	2.43 3	
7314 180809	68065	37 3398	<i>θ</i> Lyr	K0 II	A	4550 2	1.77 2	0.14 2	1.26 8	2.16 76	
6713 164349	103285	16 3335	93Her	K0.5 II	A	4383 2	1.80 2	-0.32 2	1.42 8	2.23 76	
0 193515	69825	37 3882	PPM84702	K1 II	A	4295 1	1.66 1	0.00 1	0.00 0	2.29 76	
8465 210745	34137	57 2475	<i>ζ</i> Cep	K1.5 Ib	A	4159 2	0.88 2	0.23 2	1.57 8	2.37 76	
7735 192557	32042	52 2547	<i>ο</i> 01Cyg	K2 II	A	4155 2	1.33 2	-0.14 2	1.24 8	2.44 76	
0 192041	69578	38 3939	PPM84402	K2 II	A	4155 1	1.33 1	0.00 1	1.45 31	2.44 76	
6418 156283	65890	36 2844	<i>π</i> Her	K3 Iab	A	4100 2	1.68 2	-0.18 2	1.45 38	2.72 76	
6498 157999	122387	4 3422	<i>σ</i> Oph	K3 Iab	A	4100 2	1.68 1	0.01 2	1.50 8	2.72 76	
7762 193217	49425	39 4114	GC28197	K4 II-III	A	4000 1	0.40 1	0.06 50	1.65 49	3.12 76	

Stellar ID ^a					Sp.	Std ^b	Atmosph. Parameters ^c					
HR	HD	SAO	BD	Other	Class		T _{eff}	log <i>g</i>	[Fe/H]	(B-V)	(V-K)	
0	232078	105082	16 3924	V339Sge	K4.5 II-III	A	4000 12	0.40 12	-1.60 12	1.85 8	3.35 76	
2289	44537	41076	49 1488	<i>ψ</i> 01Aur	M0 Iab	G	4000 2	0.30 1	0.08 2	1.96 8	3.79 76	
7475	185622	105104	16 3936	GC27195	M0 Iab-Ib	A	4000 33	0.70 33	-0.12 33	1.99 31	3.79 76	
5594	132933	120798	0 3297	GC20212	M0.5 II	A	3648 1	0.93 1	0.00 1	1.50 8	3.86 76	
0	339034	0 24	3902	NRVul	M1 Ia	G	4000 1	0.70 1	0.00 1	1.71 5	3.92 76	
4666	106609	44097	41 2284	2CVn	M1 Iab	A	3597 1	0.19 1	0.00 1	1.59 8	3.92 76	
0	163428	185981	0 0	GC24397	M1 Ib	G	3800 33	0.60 33	-0.14 33	2.03 33	3.92 76	
0	236697	22188	57 258	V466Cas	M1.5 Ib	G	3500 30	0.60 1	0.00 1	1.71 30	3.97 76	
0	35601	77179	29 897	V362Aur	M1.5 Ia	G	4000 2	0.70 2	-0.24 2	1.71 30	3.97 76	
0	202380	33232	59 2342	V419Cep	M2 Ib	A	3600 33	0.60 33	-0.24 33	2.39 54	4.11 76	
0	239978	34529	56 2793	STCep	M2 Ia-Iab	A	3499 1	-0.02 1	0.00 1	2.28 30	4.11 76	
4362	97778	81736	23 2322	72Leo	M3 II	A	3300 76	0.38 1	0.00 1	1.65 8	4.58 76	
0	0	11591	62 207	HSCas	M3 Iab	G	3296 1	-0.16 1	0.00 1	2.54 27	4.58 76	
0	0	50296	45 3349	AZCyg	M3 Ia	G	3200 30	-0.34 1	0.00 1	1.73 30	4.58 76	

Stellar ID ^a					Sp.	Std ^b	Atmosph. Parameters ^c					
HR	HD	SAO	BD	Other	Class		T _{eff}	log <i>g</i>	[Fe/H]	(B-V)	(V-K)	
0	0	0	0 0	KYCyg	M3.9 Iab	G	3100 25	-0.16 1	0.00 1	1.70 5	5.24 76	
0	0	0	37 3903	BCCyg	M4 Ia	G	3673 4	-0.34 1	0.00 1	1.72 5	5.24 76	
0	0	0	36 4025	BICyg	M4 Ia	G	3673 4	-0.34 1	0.00 1	1.72 5	5.24 76	
7139	175588	67559	36 3319	δ02Lyr	M4 II	A	3637 4	0.38 1	0.00 1	1.65 8	5.24 76	
7009	172380	67193	39 3476	XYLyr	M4.5 II	A	3351 4	0.38 1	0.00 1	0.76 8	5.65 76	
7171	176301	104272	17 3779	GC25999	B7 III-IV	G	13100 12	3.50 12	0.00 12	1.12 8	-0.35 76	
5694	136202	120946	2 2944	5Ser	F8 III-IV	G	6030 12	3.89 12	-0.07 12	0.54 8	1.27 76	
4883	111812	82537	28 2156	31Com	G0 III	A	5794 1	3.80 1	0.00 0	0.67 8	1.35 76	
0	0	0	0 0	N7789K676	G6 III	G	4988 3	2.51 3	-0.10 3	0.00 0	2.12 3	
4716	107950	28366	52 1626	5CVn	G6 III	A	5030 2	2.61 2	-0.16 2	0.87 38	2.12 76	
5019	115617	157844	-17 3813	61Vir	G6 III	G	5600 2	4.24 2	0.22 3	1.51 21	1.57 3	
0	0	0	0 0	N7789K875	G8 III	G	4965 3	2.39 3	-0.10 3	0.00 0	2.16 3	
0	0	0	0 0	N7789K897	G8 III	G	4965 3	2.45 3	-0.10 3	0.00 0	2.16 3	
0	0	0	36 4025	M67F84	G8 III	G	4763 3	2.30 3	-0.10 3	0.00 0	2.32 3	

Stellar ID ^a					Sp.	Std ^b	Atmosph. Parameters ^c				
HR	HD	SAO	BD	Other	Class		T _{eff}	log <i>g</i>	[Fe/H]	(B-V)	(V-K)
163	3546	74164	28 103	εAnd	G8 III	G	4957 3	2.60 3	-0.81 3	1.58 8	2.17 3
4400	99055	118831	2 2418	79Leo	G8 III	A	4866 77	2.01 1	0.29 10	0.94 38	2.16 76
4932	113226	100384	11 2529	εVir	G8 III	G	4994 3	2.10 3	0.12 3	0.94 8	2.11 3
5480	129312	120601	8 2903	31Boo	G8 III	G	4834 3	1.55 3	-0.08 3	1.01 20	2.27 3
5681	135722	64589	33 2564	δBoo	G8 III	G	4834 3	2.45 3	-0.39 3	0.95 8	2.27 3
5888	141680	121215	2 3007	ωSer	G8 III	A	4707 3	1.95 3	-0.29 3	1.02 8	2.37 3
6770	165760	123140	8 3582	71Oph	G8 III	A	4957 3	2.00 3	-0.01 3	0.95 8	2.17 3
265	5395	21855	58 138	νCas	G8.5 III	G	4819 3	2.40 3	-0.62 3	0.95 8	2.28 3
2153	41636	40881	41 1365	GC7780	G9 III	G	4690 12	2.50 12	-0.16 12	1.04 8	2.26 76
3369	72324	80245	24 1946	ν02Cnc	G9 III	G	4864 3	1.60 3	-0.02 3	1.04 8	2.25 3
5366	125454	139866	-1 2938	νVir	G9 III	G	4755 12	2.50 12	-0.10 12	1.04 8	2.26 76
7430	184492	162792	-10 5122	37Aql	G9 III	G	4536 3	1.50 3	-0.12 3	1.13 24	2.57 3
0	0	0	0 0	N7789K859	K0 III	G	4626 3	2.18 3	-0.10 3	0.00 0	2.46 3
0	0	0	0 0	N7789K575	K0 III	G	4512 3	2.00 3	-0.10 3	0.00 0	2.60 3

Stellar ID ^a					Sp.	Std ^b	Atmosph. Parameters ^c				
HR	HD	SAO	BD	Other	Class		T _{eff}	log <i>g</i>	[Fe/H]	(B-V)	(V-K)
1907	37160	112958	9 898	ϕ 02Ori	K0 III	A	4751 3	2.90 3	-0.70 3	0.95 8	2.90 3
2701	54810	134282	-4 1840	20Mon	K0 III	G	4697 3	2.35 3	-0.25 3	1.02 8	2.38 3
2970	61935	134986	-9 2172	α Mon	K0 III	G	4776 3	2.20 3	-0.03 3	1.04 8	2.31 3
3427	73665	80333	20 2158	39Cnc	K0 III	G	4965 3	2.35 3	0.24 3	0.98 8	2.16 3
3428	73710	98021	20 2166	GC11899	K0 III	G	4864 3	2.10 3	0.16 3	1.02 8	2.25 3
3994	88284	155785	-11 2820	λ Hya	K0 III	G	4971 3	2.70 3	0.39 3	1.00 20	2.15 3
4287	95272	156375	-17 3273	α Crt	K0 III	G	4635 3	2.15 3	0.05 3	1.10 8	2.45 3
6018	145328	65108	36 2699	τ CrB	K0 III-IV	G	4678 3	2.50 3	-0.14 3	1.01 20	2.39 3
8841	219449	146598	-9 6156	ψ 01Aqr	K0 III	A	4635 3	2.55 3	-0.04 3	1.10 8	2.45 3
0	141144	121191	1 3131	GC21220	K0 III	A	4565 77	2.55 1	0.00 0	1.14 58	2.65 14
0	172401	123779	8 3791	PPM166313	K0 III	A	4565 77	2.55 1	0.00 0	1.07 59	2.35 76
0	114401	82685	29 2374	UBV11896	K0 III	G	4565 77	2.55 1	0.00 0	1.21 31	2.35 76
0	0	0	0 0	N188I105	K0 III	G	4585 3	2.29 3	0.00 3	0.00 0	2.51 3
0	0	0	0 0	M92XII8	K0.5 III	G	4488 3	1.93 3	-2.20 3	0.00 0	2.63 3

Stellar ID ^a					Sp.	Std ^b	Atmosph. Parameters ^c					
HR	HD	SAO	BD	Other	Class		T _{eff}	log <i>g</i>	[Fe/H]	(B-V)	(V-K)	
4668	106760	62928	33 2213	GC16754	K0.5 III	A	4510 2	2.70 2	-0.29 2	1.14 8	0.00 0	
5196	120452	158186	-17 3937	89Vir	K0.5 III	G	4760 12	2.60 12	0.03 12	1.06 12	2.42 76	
0	0	0	0 0	N188I69	K1 III	G	4401 3	2.36 3	0.00 3	0.00 0	2.75 3	
0	0	0	0 0	N188II72	K1 III	G	4387 3	1.93 3	0.00 3	0.00 0	2.77 3	
1779	35295	57999	34 1031	GC6650	K1 III-IV	G	4426 77	2.80 11	0.29 10	1.12 8	2.48 76	
6817	167042	30784	54 1950	GC24820	K1 III	G	4949 3	3.05 3	-0.11 3	0.93 20	2.18 3	
7148	175743	104272	17 3779	GC25999	K1 III	G	4635 3	2.45 3	0.02 3	1.12 8	2.45 3	
7176	176411	104318	14 3736	εAql	K1 III	A	4687 3	2.10 3	0.08 3	1.08 38	2.39 3	
8165	203344	89640	23 4294	34Vul	K1 III	G	4669 3	2.60 3	-0.24 3	1.05 8	2.41 3	
0	0	0	0 0	M03IV25	K1.5 III	G	4355 3	1.04 3	-1.70 3	0.00 0	2.82 3	
0	0	0	0 0	N188II181	K2 III	G	4276 3	1.35 3	0.00 3	0.00 0	2.95 3	
0	0	0	0 0	M05IV59	K2 III	G	4300 3	1.46 3	-1.30 3	0.00 0	2.91 3	
617	12929	75151	22 306	αAri	K2 III	A	4480 3	2.10 3	-0.22 3	1.16 8	2.64 3	
2600	51440	59658	38 1656	62Aur	K2 III	G	4381 3	2.20 3	-0.52 3	1.20 13	2.78 3	

Stellar ID ^a					Sp.	Std ^b	Atmosph. Parameters ^c				
HR	HD	SAO	BD	Other	Class		T _{eff}	log <i>g</i>	[Fe/H]	(B-V)	(V-K)
2697	54719	59858	30 1439	τ Gem	K2 III	G	4381 3	1.35 3	0.18 3	1.23 13	2.78 3
3905	85503	81064	26 2019	μ Leo	K2 III	G	4480 3	2.15 3	0.41 3	1.23 8	2.64 3
5616	133582	83645	27 2447	43Boo	K2 III	A	4280 2	2.30 2	-0.35 2	1.23 38	2.59 76
5744	137759	29520	59 1654	ι Dra	K2 III	G	4504 3	2.05 3	0.08 3	1.17 8	2.61 3
5854	140573	121157	6 3088	α Ser	K2 III	G	4528 3	2.10 3	0.23 3	1.16 8	2.58 3
5947	143107	84098	27 2558	ϵ CrB	K2 III	G	4318 3	1.70 3	-0.34 3	1.16 8	2.88 3
6872	168775	66869	36 3094	κ Lyr	K2 III	G	4520 3	1.70 3	0.04 3	1.14 8	2.59 3
3360	72184	60890	38 1920	GC11684	K2 III	A	4669 3	2.65 3	0.33 3	1.10 8	2.41 3
3418	73471	116569	3 2026	σ Hya	K2 III	A	4480 3	1.70 3	0.24 3	1.21 8	2.64 3
0	201626	89499	26 4091	UBV18320	K2 III	G	4941 2	2.20 1	-1.45 14	1.10 32	2.36 14
0	0	0	0 0	N7789K468	K2.5 III	G	4228 3	1.72 3	-0.10 3	0.00 0	3.03 3
0	0	0	0 0	N7789K669	K2.5 III	G	4216 3	1.71 3	-0.10 3	0.00 0	3.05 3
3845	83618	137035	0 2231	ι Hya	K2.5 III	G	4240 3	1.15 3	-0.03 3	1.32 8	3.01 3
0	0	0	0 0	M03III28	K3 III	G	4122 3	0.86 3	-1.70 3	0.00 0	3.21 3

Stellar ID ^a					Sp.	Std ^b	Atmosph. Parameters ^c				
HR	HD	SAO	BD	Other	Class		T _{eff}	log <i>g</i>	[Fe/H]	(B-V)	(V-K)
0	0	0	0 0	M05IV19	K3 III	G	4139 3	1.13 3	-1.30 3	0.00 0	3.18 3
0	0	0	0 0	M71A9	K3 III	G	4156 3	1.66 3	-0.56 3	0.00 0	3.15 3
1015	20893	75899	20 551	τ Ari	K3 III	G	4355 3	1.95 3	0.07 3	1.22 8	2.82 3
1726	34334	57853	33 1000	16Ari	K3 III	G	4234 3	2.15 3	-0.30 3	1.26 8	3.02 3
1805	35620	58051	34 1048	ϕ Aur	K3 III	G	4156 3	1.20 3	0.22 3	1.40 8	3.15 3
2854	58972	115478	9 1660	γ CMi	K3 III	G	4023 14	2.00 14	-0.30 14	1.42 15	3.41 14
4365	97907	99525	14 2367	nLeo	K3 III	G	4351 14	2.07 14	-0.04 14	1.18 20	2.87 14
4521	102328	28142	56 1544	GC16153	K3 III	G	4457 3	2.35 3	0.46 3	1.28 41	2.67 3
5370	125560	100908	16 2637	20Boo	K3 III	G	4381 3	1.65 3	0.22 3	1.23 8	2.78 3
5582	132345	120601	8 2903	GC20157	K3 III	G	4374 3	1.60 3	0.48 3	1.26 8	2.79 3
6364	154733	84835	22 3073	GC23089	K3 III	A	4220 2	2.20 2	-0.14 2	1.30 38	2.92 76
7317	180928	162462	-15 5310	GC26626	K3 III	G	3969 3	1.30 3	-0.49 3	1.42 8	3.55 3
7429	184406	124799	7 4132	μ Aql	K3 III	G	4428 3	2.45 3	0.08 3	1.18 20	2.71 3
7576	188056	32042	52 2547	20Cyg	K3 III	G	4355 3	2.15 3	0.43 3	1.28 8	2.82 3

Stellar ID ^a					Sp.	Std ^b	Atmosph. Parameters ^c					
HR	HD	SAO	BD	Other	Class		T _{eff}	log <i>g</i>	[Fe/H]	(B-V)	(V-K)	
7759	193092	49410	39 4114	GC28197	K3 III	A	4065 48	1.74 1	0.12 10	1.66 47	3.15 76	
8924	221148	146736	-5 5999	34Vul	K3 III	G	4643 3	3.05 3	0.50 3	1.10 8	2.44 3	
0	0	0	0 0	M05III3	K3.5 III	G	4095 3	1.50 3	-1.30 3	0.00 0	3.26 3	
0	0	0	0 0	M71A4	K4 III	G	4028 3	1.90 3	-0.56 3	0.00 0	3.40 3	
0	0	0	0 0	M71A6	K4 III	G	4028 1	1.90 1	-0.56 3	0.00 0	3.60 14	
0	0	0	0 0	N7789K501	K4 III	G	4085 3	1.58 3	-0.10 3	0.00 0	3.28 3	
0	77729	80616	26 1895	HIP44592	K4 III	G	4271 2	2.00 2	-0.40 2	1.38 8	3.24 76	
2503	49161	114410	8 1496	17Mon	K4 III	G	4276 3	1.85 3	0.13 3	1.39 8	2.95 3	
2574	50778	152071	-11 1681	θ CMa	K4 III	G	4019 3	1.35 3	-0.20 3	1.39 8	3.42 3	
5600	133124	83624	25 2861	41Boo	K4 III	A	3960 2	1.68 2	-0.04 2	1.50 8	3.24 76	
6136	148513	121623	0 3529	GC22148	K4 III	A	4046 3	1.00 3	0.25 3	1.45 8	3.36 3	
3249	69267	116569	9 1917	β Cnc	K4 III	A	4032 3	1.60 3	-0.12 3	1.48 8	3.39 3	
0	0	0	0 0	M13B786	K4.5 III	G	3963 3	0.62 3	-1.50 3	0.00 0	3.57 3	
5826	139669	8274	77 592	θ UMi	K5 III	G	3915 3	1.00 3	-0.02 3	1.58 8	3.72 3	

Stellar ID ^a					Sp.	Std ^b	Atmosph. Parameters ^c					
HR	HD	SAO	BD	Other	Class		T _{eff}	log <i>g</i>	[Fe/H]	(B-V)	(V-K)	
2459	47914	41288	44 1518	ψ 04Aur	K5 III	G	3999 3	1.40 3	0.09 3	1.50 8	3.47 3	
4954	113996	82659	28 2185	41Com	K5 III	G	3970 2	1.69 2	-0.26 2	1.50 8	3.67 76	
5690	136028	140444	0 3337	GC20750	K5 III	G	4040 14	1.90 14	0.14 14	1.51 8	3.70 14	
224	4656	109474	6 107	δ Psc	K5 III	A	3953 3	1.10 3	-0.08 3	1.50 8	3.60 3	
843	17709	55946	34 527	17Per	K7 III	G	3905 14	1.10 14	-0.18 14	1.53 8	3.75 14	
0	0	0	0 0	N7789K971	M0 III	G	3831 3	0.89 3	-0.10 3	0.00 0	3.96 3	
0	0	0	0 0	N7789K415	M0 III	G	3859 3	0.78 3	-0.10 3	0.00 0	3.88 3	
4069	89758	43310	42 2115	μ UMa	M0 III	A	3880 75	1.06 75	0.00 36	1.57 8	3.79 76	
4299	95578	137947	-1 2471	61Leo	M0 III	A	3700 2	1.40 2	-0.23 2	1.60 8	3.79 76	
4986	114780	100460	12 2565	GC17884	M0 III	G	3845 77	1.23 1	0.00 0	1.51 21	3.79 76	
5739	137471	101545	15 2585	τ 01Ser	M1 III	G	3810 12	1.10 12	0.00 12	1.65 8	3.92 76	
5800	139153	64790	39 2889	μ CrB	M1.5 III	A	3752 77	0.93 1	0.00 0	1.62 8	4.02 76	
1939	37536	58322	31 1049	ϕ Aur	M2 III	G	3789 2	0.70 2	-0.15 2	2.06 8	4.11 76	
4184	92620	62206	32 2066	RXLMi	M2 III	A	3740 75	0.81 75	0.00 36	1.61 8	4.11 76	

Stellar ID ^a					Sp.	Std ^b	Atmosph. Parameters ^c					
HR	HD	SAO	BD	Other	Class		T _{eff}	log <i>g</i>	[Fe/H]	(B-V)	(V-K)	
8795	218329	127976	8 4997	55Peg	M2 III	A	3810 12	1.10 12	0.00 0	1.56 8	4.11 76	
8860	219734	52871	48 3991	8And	M2 III	A	3730 12	0.90 12	0.00 0	1.66 8	4.11 76	
5932	142780	45788	43 2542	2Her	M3 III	A	3756 46	0.70 1	0.00 0	1.64 8	4.58 76	
6815	167006	66737	31 1536	104Her	M3 III	G	3640 12	0.70 12	0.00 12	1.64 8	4.58 76	
0	0	0	0 0	B133	M4 III	G	3595 75	0.54 75	0.30 1	1.61 75	5.24 76	
8062	200527	50381	44 3679	V1981Cyg	M4 III	G	3452 2	0.70 2	0.16 2	1.67 30	5.24 76	
6242	151732	46288	42 2749	GC22611	M4.5 III	A	3394 1	0.53 1	0.00 0	1.60 8	5.65 76	
0	112264	44383	47 2003	TUCVn	M5 III	A	3350 4	0.37 1	0.00 0	1.61 8	6.06 76	
4267	94705	118576	6 2369	VYLeo	M5.5 III	G	3335 12	0.20 12	0.00 0	1.45 8	6.54 76	
867	18191	93189	17 457	ρ 02Ari	M6 III	A	3250 12	0.30 12	0.00 0	1.51 8	7.01 76	
6146	148783	46108	42 2714	GHer	M6 III	A	3250 12	0.20 12	-0.06 12	1.56 8	7.01 76	
0	0	0	0 0	BMB194	M6.5 III	G	3295 75	0.04 75	0.30 1	1.45 75	6.54 74	
0	0	0	0 0	BMB239	M6.5 III	G	3295 75	0.04 75	0.30 1	1.45 75	6.54 74	
0	0	0	0 0	BMB179	M7 III	G	3210 75	-0.10 75	0.30 1	1.37 75	6.90 74	

Stellar ID ^a					Sp.	Std ^b	Atmosph. Parameters ^c					
HR	HD	SAO	BD	Other	Class		T _{eff}	log <i>g</i>	[Fe/H]	(B-V)	(V-K)	
0	0	0	0 0	BMB181	M7 III	G	3210 75	-0.10 75	0.30 1	1.37 75	6.90 74	
0	0	0	0 0	BMB285	M7 III	G	3210 75	-0.10 75	0.30 1	1.37 75	6.90 74	
0	0	0	0 0	BMB087	M8 III	G	3040 75	-0.37 75	0.30 1	1.20 75	7.65 74	
0	0	0	0 0	BMB142	M8 III	G	3040 75	-0.37 75	0.30 1	1.20 75	7.56 74	
0	0	0	0 0	BMB039	M9 III	G	2870 75	-0.37 75	0.30 1	1.20 75	7.73 74	
0	0	0	0 0	BMB289	M9 III	G	2870 75	-0.37 75	0.30 1	1.20 75	7.73 74	
0	0	0	0 0	N188s359	0 III	G	0 0	0.00 0	0.00 3	0.00 0	0.00 0	
0	0	0	0 0	N188s473	0 III	G	0 0	0.00 0	0.00 3	0.00 0	0.00 0	
0	0	0	0 0	TLE205	0 III	G	0 0	0.00 0	0.30 1	0.00 0	0.00 0	
3314	71155	135896	-3 2339	30Mon	A0 V	G	9806 17	4.00 1	0.00 1	-0.02 8	-0.07 17	
3481	74873	98117	12 1904	δCnc	A0 V	G	9806 1	4.00 1	0.00 1	0.11 19	-0.03 76	
5144	119055	82942	20 2858	lBoo	A1 V	G	9485 76	4.00 1	0.00 1	0.03 21	0.05 76	
4380	98353	62491	38 2225	55UMa	A2 V	G	9120 76	4.00 1	0.00 1	0.09 8	0.13 76	
7451	184960	31782	50 1326	GC27068	F7 V	G	6272 2	4.37 2	-0.16 2	0.45 8	1.20 76	

Stellar ID ^a					Sp.	Std ^b	Atmosph. Parameters ^c				
HR	HD	SAO	BD	Other	Class		T _{eff}	log <i>g</i>	[Fe/H]	(B-V)	(V-K)
5270	122563	120251	10 2617	GC18965	F8 IV	A	4626 3	1.50 3	-2.67 3	0.60 8	2.51 3
4785	109358	44230	42 2321	β CVn	G0 V	G	5870 2	4.46 2	-0.19 2	0.58 8	1.35 76
5235	121370	100766	19 2725	η Boo	G0 IV	A	6036 12	3.72 12	0.38 12	0.60 8	1.35 76
5829	139777	2556	80 480	GC20929	G0 V	G	5870 1	4.46 1	0.00 0	0.66 8	1.35 76
6212	150680	65485	31 2884	ζ HerA	G0 IV	A	5740 2	3.70 2	-0.07 2	0.65 8	1.35 76
3538	76151	136389	-4 2490	GC12307	G2 V	A	5697 2	4.42 2	0.02 2	0.66 19	1.44 76
5409	126868	139951	-1 2957	ϕ Vir	G2 IV	A	5640 43	3.80 43	-0.07 10	0.74 38	1.72 76
5072	117176	100582	14 2621	70Vir	G2.5 V	A	5370 19	4.42 1	-0.17 19	0.32 8	1.74 3
5853	140538	121152	2 2989	ψ Ser	G2.5 V	A	5697 1	4.42 1	0.01 45	0.68 8	1.47 76
6623	161797	85397	27 2888	μ Her	G5 IV	A	5390 12	3.83 12	0.23 12	0.76 3	1.49 76
4496	101501	62655	35 2270	61UMA	G8 V	A	5360 3	4.35 3	-0.39 3	0.70 8	1.74 3
0	6009	74439	24 163	GC1231	G8 IV	A	5120 1	3.63 1	0.00 0	0.78 56	1.63 76
3259	69830	154093	-12 2449	GC11325	K0 V	A	5485 34	4.50 34	-0.03 34	0.75 8	1.83 76
6014	145148	121392	6 3169	G16-32	K0 IV	A	4849 3	3.45 3	0.10 3	0.99 8	2.26 3

Stellar ID ^a					Sp.	Std ^b	Atmosph. Parameters ^c				
HR	HD	SAO	BD	Other	Class		T _{eff}	log <i>g</i>	[Fe/H]	(B-V)	(V-K)
6752	165341	123107	2 3482	70Oph	K0 V	A	5343 2	4.47 2	-0.06 2	0.86 38	1.83 76
7957	198149	19019 61	2050	η Cep	K0 IV	A	4971 3	3.20 3	-0.26 3	0.92 8	2.16 3
0	7010	11620	59 199	UBV1226	K0 IV	G	4971 1	3.20 1	-0.28 14	1.05 29	2.16 1
0	145675	45933 44	2594	14Her	K0 V	A	5353 3	4.55 3	0.27 3	0.87 8	1.73 3
166	3651	74175	20 85	54Psc	K0 V	A	5487 3	4.50 3	0.17 3	0.85 8	1.89 3
1325	26965	131063	-7 780	α 02Eri	K1 V	A	5050 3	4.66 3	-0.17 3	0.81 8	2.02 3
5901	142091	64948 36	2652	κ CrB	K1 IV	A	4751 3	2.85 3	0.00 3	0.99 8	2.33 3
493	10476	74883	19 279	107Psc	K1 V	A	5065 3	4.55 3	-0.10 3	0.78 56	2.03 3
0	199580	50265 42	3915	GC29247	K1 IV	G	5039 3	3.50 3	-0.05 3	0.98 8	2.06 3
5553	131511	101276 19	2881	DE Boo	K2 V	A	4960 1	4.35 1	-0.13 45	0.84 8	2.15 76
0	109011	28414 55	1536	GJ1160	K2 V	A	4960 1	4.35 1	-0.28 53	0.94 52	2.15 76
0	184467	28414 58	1929	GJ762.1	K2 V	A	4960 1	4.35 1	-0.20 45	0.87 8	2.15 76
222	4628	109471	4 123	V339Sge	K2 V	A	4960 3	4.35 3	-0.32 3	0.89 8	2.15 3
8832	219134	35236 56	2966	GC32329	K3 V	A	4824 3	4.41 3	-0.04 3	1.00 8	2.34 3

Stellar ID ^a					Sp.	Std ^b	Atmosph. Parameters ^c						
HR	HD	SAO	BD	Other	Class		T _{eff}	log <i>g</i>	[Fe/H]	(B-V)	(V-K)		
0	160346	122610	3 3465	GJ688	K3 V	A	4824 1	4.41 1	-0.15 45	0.96 49	2.34 1		
5568	131977	183040	-20 4125	GJ570A	K4 V	G	4624 2	4.70 3	0.10 3	1.10 8	2.65 3		
8085	201091	70919	38 4343	61CygA	K5 V	A	4364 2	4.55 2	-0.05 2	1.19 8	2.75 76		
0	88230	43223	50 1725	LHS280	K7 V	A	3917 3	4.68 3	0.28 3	1.38 8	3.34 3		
0	157881	122374	2 3312	LHS447	K7 V	A	4000 2	4.50 2	0.40 2	1.36 8	3.21 76		
8086	201092	0	38 4343	61CygB	K7 V	A	3893 2	4.65 2	-0.05 2	1.37 8	3.21 76		
0	79211	22188	53 1321	GJ338B	M0 V	A	3769 12	4.71 12	0.06 51	1.42 8	3.60 76		
0	131976	183039	-20 4123	GJ570B	M1 V	G	3506 3	4.73 3	0.00 3	1.51 8	4.10 3		
0	1326	36248	43 44	GJ15A	M1 V	A	3721 42	5.00 42	-1.50 42	1.56 8	3.95 76		
0	0	0	0 0	HIP80459	M1.5 V	A	3550 1	4.85 1	0.00 0	1.60 65	4.16 76		
0	95735	62377	36 2147	LHS37	M2 V	A	3429 2	4.80 2	-0.20 2	1.51 8	4.27 76		
0	0	43609	44 2051	LHS38	M2 V	A	3544 3	4.85 3	-0.19 51	1.52 8	4.04 3		
0	119850	100695	15 2620	LHS47	M3 V	A	3300 76	5.00 1	0.05 51	1.44 8	4.57 76		
0	0	0	0 0	HIP25953	M4 V	A	3400 68	4.85 68	0.10 68	1.62 70	4.87 76		

Stellar ID ^a					Sp.	Std ^b	Atmosph. Parameters ^c					
HR	HD	SAO	BD	Other	Class		T _{eff}	log <i>g</i>	[Fe/H]	(B-V)	(V-K)	
0	0	0	0 0	LHS31	M4 V	A	3250 68	5.00 68	0.00 68	1.26 69	4.87 76	
0	0	0	0 0	LHS294	M4 V	A	3367 1	4.93 1	0.00 0	1.66 51	4.87 76	
0 173739	31128	59 1915		LHS58	M4 V	A	3450 64	4.93 1	0.08 51	1.54 8	4.87 76	
0	0	81292 20 2465		ADLeo	M4.5 V	A	3400 68	4.85 68	0.00 68	1.55 8	5.02 76	
0	0	0	0 0	LHS511	M4.5 V	A	3400 1	4.85 1	0.00 0	1.67 61	5.02 76	
0	0	0	0 0	LHS9	M5.5 V	A	3025 76	5.15 68	0.00 68	1.89 61	5.38 76	
0	1326	0	43 44	GJ15B	M6 V	A	3107 3	5.08 3	-0.50 71	1.78 72	5.58 76	
0	0	0	0 0	GJ905	M6 V	A	2799 3	5.12 3	0.00 71	1.92 8	6.37 3	
0	0	0	0 0	Luyton789.6	M7 V	A	2747 3	5.09 3	0.00 0	1.96 60	6.64 3	

^a Zeros indicate that the star is not in the catalog. N=NGC. For details - Worthey et al. (1994b)

^b Spectral type of the telluric correction standard: G - solar analog, A - A star.

^c The first number is the parameter, and the second is the reference source.

A zero reference number indicates that the parameter value is unknown.

Stellar ID ^a					Sp.	Std ^b	Atmosph. Parameters ^c				
HR	HD	SAO	BD	Other	Class	T_{eff}	$\log g$	[Fe/H]	(B-V)	(V-K)	
COMMENTS: (1) Unknown metallicities of supergiants assumed Solar; (2) HR3481: parameters same as HR3314; (3) HR6498: T_{eff} , $\log g$ same as HR6418; (4) SAO089499: $\log g$ same as HR2600; (5) SAO022188: $\log g$ same as SAO185981; (6) GJ015NE: $\log g$ same as GJ412A; (7) GJ725A: $\log g$ set to the average of GJ206 & GJ213; (8) HR7762: T_{eff} , $\log g$ same as SAO105082; (9) SAO069578: T_{eff} , $\log g$ same as HR7735; (10) HR2289,HR4362,SAO050296,KYCyg,BCCyg,HR7139,HR7009: $\log g$ from Straižys (1992); (11) SAO082106,SAO069825,HR5594,HR4666,SAO034529,SAO011591: T_{eff} , $\log g$ from Straižys (1992); (12) T_{eff} , $\log g$ for Baade Window giants - from 75 (for [Fe/H]=0) based on the Spectral Types from 74; extrapolations for M8 & M9; (13) M71A6: T_{eff} , $\log g$ same as M71A4 - close V-K; (14) SAO011620: T_{eff} , $\log g$ same as HR7957; (15) HR5853: T_{eff} , $\log g$ same as HR3538; (16) GJ526: $\log g$ same as GJ213; (17) SAO028414: T_{eff} , $\log g$ same as SAO109471; (18) V-K adopted from 76, only for stars with $-0.1 \leq [\text{Fe}/\text{H}] \leq +0.1$, and from 75 for stars with $+0.15 \leq [\text{Fe}/\text{H}] \leq +0.35$, if not available from observations;(19) HR5829: T_{eff} , $\log g$ set as HR4785; (20) SAO074439: T_{eff} , $\log g$ interpolated from IV stars; (21) HR5553, SAO28414, SAO31745: T_{eff} , $\log g$ set as SAO109471;(22) SAO122610: T_{eff} , $\log g$ set as HR8832; (23) GJ625: T_{eff} , $\log g$ interpolated from MIV & M2V stars; (24) GJ402: T_{eff} , $\log g$ average of M4V stars; (25) GJ831: T_{eff} , $\log g$ set as GJ388; (26) HR4400: $\log g$ average of G8III stars;											

Stellar ID ^a					Sp.	Std ^b	Atmosph. Parameters ^c				
HR	HD	SAO	BD	Other	Class	T_{eff}	$\log g$	[Fe/H]	(B-V)	(V-K)	
<p>(27) SAO121191,SAO123779,SAO082685: $\log g$ same as HR8841; (28) HR4986: $\log g$ average of HR4069 & HR4069; (29) HR5800: $\log g$ average of MIV & M2V stars; (30) HR5932: $\log g$ same as HR5932; (31) HR6242,SAO044383: $\log g$ interpolated between SAO050381 & HR4267; (32) HR4883: T_{eff}, $\log g$ interpolated from HR5694 & HR4716; (33) HR2289: T_{eff} same as HR7475; (34) HR5072: $\log g$ same as HR3538</p> <p>REFERENCES: (1) tentatively assumed; (2) Cayrel de Strobel et al. (1997) and references therein; (3) Gorgas et al. (1993) and references therein; (4) Dyck et al. (1998); (5) Elias et al. (1985); (6) Keenan & McNail (1989); (7) Houk & Smith-Moore (1988); (8) Mermilliod (1986); (9) Schmitt (1971); (10) Taylor (1999) and references therein; (11) Zhou Xu (1991); (12) Worthey et al. (1994b) and references therein; (13) Argue (1966); (14) Faber et al. (1985) and references therein; (15) Neckel (1974); (16) Johnson & Morgan (1953); (17) Di Benedetto (1998); (18) Cowley et al. (1969); (19) Osawa (1959); (20) Jennens & Helfer (1975); (21) Haggkvist & Oja (1969); (22) Appenzeler (1967); (23) Eggen (1964); (24) McClure (1970); (25) Garmany & Stencel (1992); (26) Weaver & Torres-Dogen (1997); (27) Neckel (1974); (28) Nassau & van Albada (1947); (29) Siogren (1964); (30) Lee (1970); (31) Fernie (1983);</p>											

Stellar ID ^a					Sp.	Std ^b	Atmosph. Parameters ^c				
HR	HD	SAO	BD	Other	Class		T _{eff}	log g	[Fe/H]	(B-V)	(V-K)
(32) Mendoza & Johnson (1965); (33) Luck & Bond (1989); (34) Feltzing & Gustafsson (1998); (35) Morgan & Keenan (1973); (36) Taylor et al. (1972); (37) Kerschbaum & Hron (1994); (38) Johnson et al. (1966); (39) Harlan (1974b); (40) Schild (1973); (41) Ardeberg et al. (1973); (42) Alonso et al. (1994); (43) Bell & Gustafsson (1989); (44) Cowley et al. (1967); (45) Eggen (1998); (46) Dumm & Schild (1998) Ljunggren & Oja (1964); (48) van Belle et al. (1999); (49) Argue (1963); (50) Taylor (1991); (51) Eggen (1996); (52) Mendoza (1967); (53) Zakhozaj & Shaparenko (1996); (54) Humphreys (1970); (55) Barbier (1963); (56) Oja (1987); (57) Harlan (1974a); (58) Gunn & Stryker (1983); (59) Fernie (1959); (60) Eggen & Greenstein (1965) (61) Bessel (1990); (62) Henry et al. (1994); (63) Joy & Abt (1974); (64) Kirkpatrick et al. (1993); (65) Leggett (1992); (66) Cowley et al. (1967); (67) Veeder (1974) (68) Leggett et al. (1996); (69) Erro (1971); (70) Weistrop (1977) (71) Leggett et al. (2000); (72) Sandage (1997); (73) Parsons & Montemayor (1982); (74) Frogel & Whitford (1987); (75) Houdashelt et al. (2000); (76) Johnson (1966); (77) from the Spectral Class versus T _{eff} relation of Ramírez et al. (1997)											

Table 4.4 Definitions of spectral bands.

Species	ID ^a	Line	Cont.		Ref.
			No. 1	No. 2	
MgI (1.50 μ m)	Mg150V	15040 40	15005 30	15075 30	1
FeI (1.58 μ m)	Fe158V	15830 40	15800 20	15857.5 15	1
SiI (1.59 μ m)	Si159O	15890 40	15850 40	15930 40	3
CO (1.62 μ m)	CO162O	16197.5 45	16160 30	16270 30	3
MgI (1.71 μ m)	Mg171V	17115 30	17092.5 15	17145 30	1
MgI (2.11 μ m)	Mg211V	21075 70	21020 40	21130 40	1
Br γ (2.16 μ m)	Br216K	21662.5 47	20929 44	22899 52	2
NaI (2.21 μ m)	Na221R	22075 70	22170 60	22350 40	4
NaI (2.21 μ m)	Na221K	22077 48	20929 44	22899 52	2
CaI (2.26 μ m)	Ca226R	22635 110	22510 40	22720 40	4
CaI (2.26 μ m)	Ca226K	22636.5 51	20929 44	22899 52	2
MgI (2.28 μ m)	Mg228V	22806 52	22750 60	22857 50	1
MgI (2.28 μ m)	Mg228R	22820 60	22720 40	22886 30	4
CO (2.29 μ m)	CO229O	22950.5 53	22899 52	- -	3
¹² CO(2, 0)(2.29 μ m)	2CO22K	22957 52	22899 52	- -	2
CO (2.29 μ m)	CO229V	22980 100	22850 100	- -	1
¹² CO(3, 1)(2.32 μ m)	C2O23K	23245 54	22899 52	- -	2
¹³ CO(2, 0)(2.35 μ m)	C3O23K	23463.5 55	22899 52	- -	2

Species	ID ^a	Line	Cont.	Cont.	Ref.
			No. 1	No. 2	
CO (2.35 μ m)	CO236D	23550 900	- -	- -	5

^a Line designations, used through this work.

COMMENTS: The first number gives the central wavelength and the second gives the width in Å. See Section 4.5 for details.

REFERENCES: (1) This work; (2) Kleinmann & Hall (1986); (3) Origlia, Moorwood & Oliva (1993); (4) Ramírez et al. (1997); (5) Doyon, Joseph & Wright (1994a).

Star	Mg _v	Fe _v	Si _o	CO _o	Mg _v	Mg _v	Brγ _k	Na _r	Na _k
ID	1.50	1.58	1.59	1.62	1.71	2.11	2.16	2.21	2.21
Ca _r	Ca _k	Mg _v	Mg _r	CO _o	CO _k	CO _v	CO _k	CO _k	CO _d
2.26	2.26	2.28	2.28	2.29	2.30	2.30	2.32	2.36	2.36
SAO069578	0.11	0.03	0.04	0.07	0.04	0.01	0.03	0.04	0.06
	0.03	0.05	0.01	0.01	0.06	0.10	0.12	0.06	0.08
HR6418	0.09	0.03	0.10	0.06	0.04	0.01	0.02	0.05	0.06
	0.01	0.02	0.01	0.01	0.25	0.24	0.15	0.22	0.04
HR6498	0.10	0.02	0.08	0.11	0.03	-0.01	0.00	0.03	0.03
	0.00	0.02	0.00	-0.01	0.34	0.34	0.26	0.20	0.02
HR7762	0.10	0.04	0.05	0.09	0.04	0.01	0.02	0.05	0.06
	0.03	0.05	0.01	0.01	0.09	0.14	0.17	0.26	0.06
SAO105082	0.02	-0.01	0.07	0.04	-0.06	0.01	-0.04	0.00	-0.07
	0.00	-0.11	0.00	-0.01	0.03	0.01	0.09	-0.02	-0.09
HR2289	0.15	0.07	0.11	0.15	0.07	-0.00	0.03	0.08	0.09
	0.00	0.02	0.02	0.01	0.20	0.22	0.13	0.45	0.12
HR7475	0.11	0.05	0.07	0.11	0.05	0.02	0.02	0.05	0.08
	0.05	0.10	0.02	0.00	0.40	0.38	0.22	0.40	0.07
HR5594	0.06	0.03	0.08	0.08	0.04	0.01	0.02	0.05	0.05
	0.03	0.05	0.00	0.00	0.30	0.32	0.21	0.28	0.16
HD339034	0.14	0.09	0.11	0.10	0.06	0.01	0.01	0.08	0.10
	0.02	0.06	0.03	0.02	0.42	0.45	0.32	0.46	0.08
HR4666	0.09	0.04	0.04	0.07	0.06	0.02	0.01	0.03	0.06
	0.03	0.07	0.01	0.01	0.29	0.32	0.20	0.27	0.08

Star	Mg _v	Fe _v	Si _o	CO _o	Mg _v	Mg _v	Brγ _k	Na _r	Na _k
ID	1.50	1.58	1.59	1.62	1.71	2.11	2.16	2.21	2.21
Ca _r	Ca _k	Mg _v	Mg _r	CO _o	CO _k	CO _v	CO _k	CO _k	CO _d
2.26	2.26	2.28	2.28	2.29	2.30	2.30	2.32	2.36	2.36
SAO185981	0.15	0.06	0.11	0.15	0.08	0.02	0.01	0.08	0.10
	0.05	0.11	0.04	0.04	0.44	0.48	0.29	0.45	0.12
SAO022188	0.17	0.06	0.09	0.17	-	0.02	-0.01	0.07	0.09
	0.04	0.08	0.03	0.02	0.47	0.50	0.32	0.43	0.10
SAO077179	0.14	0.07	0.11	0.15	0.06	0.01	-0.00	0.07	0.09
	0.04	0.08	0.03	0.01	0.42	0.45	0.27	0.39	0.13
SAO033232	0.10	0.06	0.06	0.15	0.06	0.02	0.03	0.06	0.10
	0.04	0.07	0.01	0.01	0.45	0.48	0.30	0.38	0.11
SAO034529	0.10	0.03	0.10	0.19	0.02	0.01	0.00	0.07	0.09
	0.05	0.08	0.03	0.00	0.53	0.52	0.38	0.42	0.06
HR4362	0.09	0.04	0.05	0.11	0.08	0.01	0.00	0.04	0.06
	0.03	0.05	0.01	0.01	0.32	0.35	0.22	0.28	0.13
SAO011591	0.17	0.08	0.09	0.17	-	0.02	0.00	0.08	0.08
	0.03	0.07	0.03	0.02	0.47	0.48	0.33	0.38	0.11
SAO050296	0.16	0.04	0.09	0.19	0.06	-0.01	0.01	0.05	0.11
	0.03	0.08	0.03	0.02	0.47	0.49	0.32	0.38	0.10
KYCyg	0.19	0.08	0.08	0.21	0.09	0.03	-0.00	0.09	0.14
	0.04	0.10	0.03	0.02	0.51	0.57	0.37	0.46	0.14
BCCyg	0.18	0.07	0.08	0.18	0.07	0.05	-0.02	0.10	0.11
	0.06	0.12	0.02	-0.00	0.43	0.47	0.29	0.39	0.10

Star	Mg _v	Fe _v	Si _o	CO _o	Mg _v	Mg _v	Brγ _k	Na _r	Na _k
ID	1.50	1.58	1.59	1.62	1.71	2.11	2.16	2.21	2.21
Ca _r	Ca _k	Mg _v	Mg _r	CO _o	CO _k	CO _v	CO _k	CO _k	CO _d
2.26	2.26	2.28	2.28	2.29	2.30	2.30	2.32	2.36	2.36
BICyg	0.19	0.08	0.10	0.18	0.08	0.02	-0.02	0.07	0.10
	0.02	0.06	0.02	0.02	0.46	0.51	0.34	0.44	0.11
HR7139	0.08	0.04	0.07	0.15	0.04	0.01	0.01	0.06	0.08
	0.05	0.10	0.02	0.01	0.40	0.40	0.25	0.36	0.15
HR7009	0.06	0.04	0.07	0.16	0.05	0.01	0.01	0.07	0.09
	0.04	0.08	0.01	0.01	0.33	0.35	0.22	0.37	0.16
TLE205	0.16	0.05	0.09	0.08	0.07	0.03	-0.01	0.08	0.05
	0.03	0.05	0.04	0.04	0.31	0.27	0.17	0.26	0.09
M03III28	0.03	-0.00	0.08	0.01	0.02	0.02	0.02	0.02	0.03
	0.00	0.01	0.00	-0.00	0.10	0.08	0.05	0.08	0.02
M03IV25	0.02	0.03	0.04	-0.01	0.01	0.01	-0.04	0.01	-0.08
	0.00	-0.10	-0.05	-0.08	-0.05	-0.07	-0.07	-0.04	-0.14
M05III3	0.11	0.04	0.07	0.04	0.07	0.01	-0.01	0.02	0.02
	0.03	0.05	0.02	0.01	0.15	0.16	0.10	0.17	0.07
M05IV19	-	-	-	-	-	0.01	-0.01	0.03	0.02
	0.02	0.02	0.03	0.01	0.01	0.04	0.05	0.14	0.02
M05IV59	-	-	-	-	-	0.00	-0.01	0.01	0.02
	0.02	0.03	0.01	-0.00	-0.00	0.03	0.05	0.13	0.03
M13B786	0.03	0.01	0.04	0.01	-0.01	0.00	0.03	0.01	-0.01
	-0.00	-0.02	0.01	0.02	0.04	0.03	0.02	-0.01	0.01

Star	Mg _v	Fe _v	Si _o	CO _o	Mg _v	Mg _v	Brγ _k	Na _r	Na _k
ID	1.50	1.58	1.59	1.62	1.71	2.11	2.16	2.21	2.21
Ca _r	Ca _k	Mg _v	Mg _r	CO _o	CO _k	CO _v	CO _k	CO _k	CO _d
2.26	2.26	2.28	2.28	2.29	2.30	2.30	2.32	2.36	2.36
M71A4	0.11	0.04	0.10	0.07	0.07	0.01	0.00	0.03	0.06
	0.01	0.05	0.00	0.02	0.20	0.21	0.13	0.21	0.06
M71A6	0.11	0.04	0.09	0.09	0.07	0.01	-0.01	0.03	0.05
	0.02	0.04	0.01	0.01	0.25	0.27	0.17	0.26	0.15
M71A9	0.10	0.03	0.09	0.04	0.07	0.00	0.00	0.01	0.02
	0.01	0.03	0.00	0.00	0.21	0.23	0.15	0.20	0.08
M92XII8	0.03	0.00	0.03	0.01	0.03	0.00	0.03	0.00	-0.01
	0.01	-0.00	0.00	0.01	0.01	0.00	0.01	-0.01	-0.00
ngc188I69	0.16	0.04	0.10	0.07	0.08	0.02	0.00	0.03	0.05
	0.02	0.05	0.03	0.03	0.23	0.23	0.15	0.22	0.03
ngc188II181	0.17	0.05	0.10	0.08	0.07	0.02	-0.00	0.04	0.04
	0.02	0.04	0.02	0.01	0.23	0.24	0.16	0.19	0.03
ngc188I105	0.14	0.05	0.08	0.05	0.08	0.01	0.01	0.04	0.05
	0.01	0.02	0.01	0.01	0.19	0.20	0.13	0.14	0.05
ngc188II72	0.17	0.03	0.09	0.04	0.06	0.01	0.00	0.03	0.03
	0.01	0.03	0.02	0.01	0.22	0.23	0.17	0.16	0.04
ngc188s359	0.07	0.02	0.06	0.06	0.03	0.01	0.01	0.02	0.02
	0.01	0.02	0.01	-0.00	0.23	0.23	0.15	0.20	0.06
ngc188s473	0.08	0.02	0.07	0.10	0.07	0.01	0.00	0.04	0.05
	0.02	0.03	0.02	-0.00	0.26	0.26	0.16	0.22	0.07

Star	Mg _v	Fe _v	Si _o	CO _o	Mg _v	Mg _v	Brγ _k	Na _r	Na _k
ID	1.50	1.58	1.59	1.62	1.71	2.11	2.16	2.21	2.21
Ca _r	Ca _k	Mg _v	Mg _r	CO _o	CO _k	CO _v	CO _k	CO _k	CO _d
2.26	2.26	2.28	2.28	2.29	2.30	2.30	2.32	2.36	2.36
HR7171	0.04	0.00	0.07	-0.00	0.04	-	-	-	-
-	-	-	-	-	-	-	-	-	-
HR5694	0.09	0.03	0.05	0.01	0.04	0.02	0.08	0.01	0.03
0.01	0.02	0.02	0.02	-0.00	0.00	-0.01	0.02	0.00	0.01
HR4883	-	0.02	0.02	0.02	0.01	0.01	0.06	0.01	0.00
-0.01	-0.00	-0.02	-0.01	0.02	0.02	0.02	0.01	0.01	0.01
HR4716	0.06	0.02	0.07	0.02	0.03	0.02	0.05	0.01	0.02
0.01	0.03	0.02	0.02	0.07	0.08	0.04	0.06	-0.00	0.02
HR5019	0.18	0.05	0.08	0.04	0.08	0.02	0.00	0.03	0.03
0.02	0.03	0.02	0.03	0.05	0.04	0.01	0.05	0.01	0.02
HR0163	0.11	0.02	0.08	0.05	0.03	-	-	-	-
-	-	-	-	-	-	-	-	-	-
HR4400	0.06	0.02	0.04	0.03	0.02	0.01	0.03	0.01	0.02
0.01	0.02	0.02	0.02	0.09	0.10	0.06	0.10	-0.00	0.04
HR4932	0.09	0.03	0.07	0.03	0.04	0.02	0.03	0.02	0.03
0.01	0.02	0.03	0.03	0.07	0.07	0.03	0.07	0.01	0.03
HR5480	0.08	0.03	0.10	0.04	-	0.02	0.04	0.02	0.04
0.02	0.05	0.03	0.03	0.11	0.11	0.05	0.13	0.01	0.04
HR5681	0.09	0.03	0.10	0.04	0.04	0.02	0.03	0.02	0.04
0.02	0.03	0.03	0.03	0.11	0.12	0.07	0.13	0.02	0.03

Star	Mg _v	Fe _v	Si _o	CO _o	Mg _v	Mg _v	Brγ _k	Na _r	Na _k
ID	1.50	1.58	1.59	1.62	1.71	2.11	2.16	2.21	2.21
Ca _r	Ca _k	Mg _v	Mg _r	CO _o	CO _k	CO _v	CO _k	CO _k	CO _d
2.26	2.26	2.28	2.28	2.29	2.30	2.30	2.32	2.36	2.36
HR5888	-	0.04	0.06	0.04	0.03	0.02	0.03	0.03	0.03
	0.02	0.02	0.01	0.01	0.11	0.12	0.12	0.01	0.03
HR6770	0.06	0.03	0.04	0.02	0.02	0.01	0.05	0.01	0.02
	0.01	0.02	0.01	0.02	0.02	0.03	0.02	0.09	0.04
HR0265	0.12	0.04	0.07	0.03	-	0.02	0.01	0.03	0.03
	0.01	0.03	0.03	0.03	0.15	0.15	0.10	0.16	0.00
HR2153	0.11	0.02	0.08	0.04	0.04	0.00	-	-	-
	-	-	-	-	-	-	-	-	-
HR3369	-	-	-	-	-	-	-	-	-
	0.01	0.03	0.02	0.02	0.13	0.14	0.08	0.10	0.02
HR5366	0.09	0.03	0.09	0.03	0.04	0.02	0.05	0.02	0.03
	0.02	0.03	0.01	0.02	0.14	0.14	0.09	0.13	0.01
HR7430	0.13	0.03	0.11	0.04	0.06	0.01	0.02	0.04	0.04
	-0.00	0.02	0.02	0.01	0.04	0.05	0.04	0.14	-0.00
HR1907	-	-	-	-	-	-	-	-	-
	0.02	0.02	0.03	0.03	0.16	0.17	0.11	0.11	-0.00
HR2701	0.10	0.02	0.08	0.03	0.03	0.02	0.06	0.02	0.02
	0.01	0.03	0.02	0.03	0.11	0.12	0.06	0.10	0.02
HR2970	0.10	0.03	0.08	0.03	0.07	0.02	-0.00	0.02	0.02
	0.02	0.03	0.03	0.03	0.13	0.15	0.09	0.15	0.05

Star	Mg _v	Fe _v	Si _o	CO _o	Mg _v	Mg _v	Brγ _k	Na _r	Na _k
ID	1.50	1.58	1.59	1.62	1.71	2.11	2.16	2.21	2.21
Ca _r	Ca _k	Mg _v	Mg _r	CO _o	CO _k	CO _v	CO _k	CO _k	CO _d
2.26	2.26	2.28	2.28	2.29	2.30	2.30	2.32	2.36	2.36
HR3427	0.11	0.05	0.08	0.04	0.04	-0.01	0.07	0.03	0.05
	0.02	0.04	0.02	0.03	0.12	0.14	0.08	0.12	0.05
HR3428	0.10	0.04	0.08	0.07	0.04	0.01	0.03	0.04	0.04
	0.02	0.03	0.03	0.01	0.13	0.14	0.09	0.10	-0.00
HR3994	0.14	0.03	0.12	0.06	0.06	0.03	0.03	0.02	0.03
	0.01	0.02	0.03	0.01	0.11	0.12	0.08	0.12	-0.01
HR4287	0.11	0.03	0.08	0.04	-	-	-	-	-
	0.02	0.05	0.01	0.02	0.17	0.18	0.12	0.18	0.02
HR6018	0.11	0.02	0.08	0.04	0.04	0.00	0.07	0.02	0.03
	0.02	0.04	0.02	0.02	0.10	0.11	0.05	0.11	0.02
HR8841	0.08	0.02	0.06	0.04	0.03	0.02	0.03	0.01	0.03
	0.01	0.03	0.02	0.02	0.17	0.18	0.13	0.15	0.03
SAO121191	0.09	0.03	0.06	0.05	0.04	0.01	0.01	0.05	0.05
	0.02	0.03	0.01	0.02	0.13	0.14	0.08	0.16	0.02
SAO123779	0.07	0.03	0.06	0.04	0.04	0.01	-0.01	-0.00	0.02
	-0.00	0.02	0.01	0.00	0.03	0.04	0.05	0.13	-0.00
SAO082685	-	-	-	-	-	0.03	-	-	-
	-	-	-	-	-	-	-	-	-
HR4668	0.08	0.02	0.05	0.05	0.04	0.01	0.01	0.02	0.03
	0.01	0.02	0.01	0.01	0.17	0.18	0.12	0.15	0.03

Star	Mg _v	Fe _v	Si _o	CO _o	Mg _v	Mg _v	Brγ _k	Na _r	Na _k
ID	1.50	1.58	1.59	1.62	1.71	2.11	2.16	2.21	2.21
Ca _r	Ca _k	Mg _v	Mg _r	CO _o	CO _k	CO _v	CO _k	CO _k	CO _d
2.26	2.26	2.28	2.28	2.29	2.30	2.30	2.32	2.36	2.36
HR5196	0.06	0.01	0.10	0.04	0.06	0.02	0.04	0.02	0.03
	0.01	0.02	0.03	0.03	0.07	0.06	0.08	0.01	0.04
HR1779	0.13	0.06	0.10	0.04	0.07	0.01	0.01	0.04	0.05
	0.02	0.04	0.02	0.02	0.15	0.15	0.09	0.14	0.05
HR6817	0.10	0.04	0.08	0.03	0.04	0.02	0.02	0.01	0.02
	0.01	0.02	0.01	0.01	0.03	0.03	0.07	0.01	0.02
HR7148	0.14	0.06	0.09	0.05	0.06	-	-	-	-
	-	-	-	-	-	-	-	-	-
HR7176	0.12	0.03	0.08	0.04	0.04	0.02	0.08	0.02	0.01
	0.02	0.02	0.01	0.01	0.03	0.05	0.05	0.13	0.04
HR8165	0.10	0.03	0.08	0.05	0.05	0.01	0.01	0.03	0.03
	0.02	0.04	0.02	0.02	0.07	0.08	0.06	0.16	0.05
HR0617	0.08	0.02	0.05	0.08	0.03	0.02	0.03	0.01	0.02
	0.00	0.02	0.00	0.01	0.14	0.15	0.08	0.15	0.04
HR2600	0.09	0.02	0.06	0.05	0.06	0.03	0.01	0.02	0.03
	0.02	0.03	0.00	0.01	0.15	0.17	0.08	0.18	0.05
HR2697	0.13	0.04	0.09	0.06	0.06	0.01	0.01	0.02	0.04
	0.03	0.03	0.05	0.04	0.17	0.18	0.10	-0.00	0.04
HR3905	0.10	0.03	0.06	0.05	0.05	0.01	0.03	0.05	0.07
	0.01	0.02	0.03	0.03	0.19	0.19	0.11	0.03	0.05

Star	Mg _v	Fe _v	Si _o	CO _o	Mg _v	Mg _v	Brγ _k	Na _r	Na _k
ID	1.50	1.58	1.59	1.62	1.71	2.11	2.16	2.21	2.21
Ca _r	Ca _k	Mg _v	Mg _r	CO _o	CO _k	CO _v	CO _k	CO _k	CO _d
2.26	2.26	2.28	2.28	2.29	2.30	2.30	2.32	2.36	2.36
HR5616	0.08	0.03	0.07	0.06	0.04	0.01	0.01	0.01	0.03
	0.02	0.02	0.01	0.01	0.22	0.23	0.16	0.17	0.06
HR5744	-	-	-	-	-	0.01	0.02	0.04	0.05
	0.03	0.07	0.02	0.02	0.05	0.07	0.07	0.17	0.03
HR5854	-	-	-	-	-	0.01	0.02	-	-
	-	-	-	-	-	-	-	-	-
HR5947	0.10	0.06	0.08	0.05	0.04	0.02	0.02	0.04	0.03
	0.02	0.02	0.00	-0.01	0.11	0.12	0.04	0.16	0.02
HR6872	0.15	0.05	0.09	0.05	0.06	0.00	0.02	0.04	0.05
	0.03	0.04	0.02	0.02	0.18	0.18	0.10	0.19	0.02
SAO060890	0.10	0.04	0.04	0.06	0.02	0.01	0.02	0.03	0.06
	0.01	0.04	0.01	0.01	0.19	0.21	0.14	0.16	0.04
SAO116988	0.08	0.03	0.04	0.01	0.06	0.01	-0.00	0.02	0.03
	0.00	0.02	0.01	0.01	0.15	0.17	0.08	0.21	0.00
SAO089499	0.08	0.02	0.04	0.01	0.04	-0.00	0.02	0.01	-0.00
	0.00	-0.01	0.02	0.02	0.12	0.12	0.11	0.12	-0.01
HR3845	0.12	0.03	0.09	0.06	0.06	0.02	0.00	0.03	0.05
	0.03	0.04	0.01	0.02	0.22	0.25	0.18	0.21	0.04
HR1015	-	0.05	0.09	0.06	0.07	0.02	-0.01	0.02	0.04
	0.03	0.04	0.02	0.02	0.17	0.19	0.14	0.17	0.04

Star	Mg _v	Fe _v	Si _o	CO _o	Mg _v	Mg _v	Brγ _k	Na _r	Na _k
ID	1.50	1.58	1.59	1.62	1.71	2.11	2.16	2.21	2.21
Ca _r	Ca _k	Mg _v	Mg _r	CO _o	CO _k	CO _v	CO _k	CO _k	CO _d
2.26	2.26	2.28	2.28	2.29	2.30	2.30	2.32	2.36	2.36
HR1726	0.11	0.03	0.10	0.06	0.06	0.03	0.01	0.03	0.03
	0.03	0.04	0.02	0.01	0.20	0.21	0.12	0.19	0.07
HR1805	0.13	0.02	0.12	0.10	0.07	0.00	0.00	0.04	0.06
	0.03	0.05	0.02	0.02	0.25	0.27	0.17	0.24	0.09
HR2854	0.12	0.02	0.08	0.08	0.07	0.01	0.02	0.01	0.05
	0.02	0.04	0.02	0.02	0.18	0.21	0.13	0.22	0.06
HR4365	0.11	0.05	0.08	0.06	0.05	-	-	-	-
	-	-	-	-	-	-	-	-	-
HR4521	0.17	0.04	0.11	0.08	0.07	0.02	0.01	0.05	0.06
	0.03	0.05	0.02	0.02	0.21	0.19	0.09	0.20	0.06
HR5370	0.15	0.05	0.10	0.06	0.07	0.03	-0.01	0.05	0.05
	0.03	0.05	0.02	0.03	0.21	0.18	0.12	0.20	0.07
HR5582	0.18	0.04	0.12	0.08	-	0.03	0.00	0.05	0.07
	0.03	0.06	0.03	0.03	0.19	0.20	0.10	0.20	0.04
HR6364	0.08	0.02	0.07	0.07	0.04	0.02	0.02	0.03	0.03
	0.02	0.04	0.02	0.02	0.21	0.18	0.11	0.18	0.06
HR7317	0.12	0.02	0.10	0.09	0.09	0.02	0.00	0.03	0.04
	0.02	0.04	0.02	0.02	0.08	0.11	0.11	0.21	0.07
HR7429	0.15	0.06	0.07	0.08	0.06	0.02	0.01	0.03	0.04
	0.02	0.05	0.02	0.03	0.20	0.21	0.13	0.19	0.06

Star	Mg _v	Fe _v	Si _o	CO _o	Mg _v	Mg _v	Brγ _k	Na _r	Na _k
ID	1.50	1.58	1.59	1.62	1.71	2.11	2.16	2.21	2.21
Ca _r	Ca _k	Mg _v	Mg _r	CO _o	CO _k	CO _v	CO _k	CO _k	CO _d
2.26	2.26	2.28	2.28	2.29	2.30	2.30	2.32	2.36	2.36
HR7576	0.17	0.04	0.10	0.07	0.07	0.01	0.01	0.03	0.04
	0.03	0.05	0.03	0.02	0.22	0.23	0.14	0.23	0.06
HR7759	0.10	0.04	0.06	0.11	0.04	0.01	0.03	0.06	0.08
	0.03	0.06	0.01	0.01	0.09	0.14	0.15	0.30	0.09
HR8924	0.17	0.05	0.12	0.06	0.08	0.03	0.01	0.05	0.07
	0.03	0.05	0.03	0.03	0.08	0.09	0.05	0.14	0.03
HD077729	0.14	0.02	0.09	0.08	0.10	0.03	-0.00	0.04	0.05
	0.03	0.04	0.03	0.04	0.20	0.24	0.14	0.23	0.11
HR2503	0.12	0.04	0.07	0.06	0.06	0.02	0.03	0.03	0.05
	0.02	0.05	0.02	0.03	0.20	0.22	0.13	0.23	0.06
HR2574	-	-	-	-	-	0.02	0.01	0.00	0.02
	0.04	0.06	0.01	0.01	0.20	0.24	0.16	0.19	0.09
HR5600	0.10	0.04	0.06	0.08	0.06	0.03	0.02	0.03	0.05
	0.02	0.05	0.02	0.02	0.27	0.29	0.20	0.22	0.03
HR6136	0.11	0.03	0.08	0.10	0.05	-	-	-	-
	-	-	-	-	-	-	-	-	-
SAO116569	0.03	0.03	0.03	0.05	0.08	0.01	-0.01	0.02	0.02
	0.03	-0.02	0.00	-0.01	0.20	0.23	0.13	0.24	-0.00
HD139669	0.14	0.05	0.12	0.13	0.06	0.01	0.01	0.06	0.07
	0.02	0.04	-0.00	0.02	0.22	0.19	0.14	0.21	0.03

Star	Mg _v	Fe _v	Si _o	CO _o	Mg _v	Mg _v	Brγ _k	Na _r	Na _k
ID	1.50	1.58	1.59	1.62	1.71	2.11	2.16	2.21	2.21
Ca _r	Ca _k	Mg _v	Mg _r	CO _o	CO _k	CO _v	CO _k	CO _k	CO _d
2.26	2.26	2.28	2.28	2.29	2.30	2.30	2.32	2.36	2.36
HR2459	0.15	0.04	0.09	0.12	0.06	0.01	-0.00	0.06	0.07
	0.03	0.05	0.03	0.02	0.26	0.27	0.16	0.22	0.09
HR4954	0.09	0.09	0.09	0.10	0.05	0.01	0.05	0.01	0.02
	0.01	0.03	0.02	0.02	0.29	0.30	0.18	0.22	0.06
HR5690	0.13	0.05	0.10	0.09	0.07	0.02	-0.00	0.03	0.05
	0.03	0.05	0.02	0.01	0.29	0.31	0.22	0.24	0.07
SAO109474	0.08	0.01	0.06	0.06	0.07	0.00	0.05	0.07	0.06
	0.02	-0.00	0.01	0.02	0.25	0.26	0.18	0.24	0.06
HR0843	0.13	0.05	0.09	0.07	0.08	0.02	-0.00	0.04	0.06
	0.03	0.05	0.02	0.02	0.21	0.24	0.16	0.20	0.08
HR4069	0.07	0.04	0.05	0.14	0.01	0.01	0.00	0.03	0.01
	0.03	0.03	0.04	0.01	0.34	0.39	0.30	0.21	0.06
HR4299	0.10	0.04	0.05	0.12	0.03	0.03	0.01	0.03	0.07
	0.02	0.05	0.02	0.01	0.30	0.31	0.19	0.28	0.11
HR4986	0.10	0.01	0.08	0.10	0.09	0.01	-0.03	0.04	-0.01
	0.02	-0.07	-0.01	-0.08	0.07	0.08	0.09	0.14	-0.01
HR5739	0.13	0.02	0.11	0.13	0.09	0.02	0.00	0.07	0.08
	0.05	0.06	0.03	0.03	0.21	0.24	0.18	0.27	0.10
HR5800	0.05	-0.00	0.02	0.02	0.05	0.05	0.01	0.01	0.02
	0.03	0.03	0.01	-0.01	0.27	0.30	0.20	0.23	0.10

Star	Mg _v	Fe _v	Si _o	CO _o	Mg _v	Mg _v	Brγ _k	Na _r	Na _k
ID	1.50	1.58	1.59	1.62	1.71	2.11	2.16	2.21	2.21
Ca _r	Ca _k	Mg _v	Mg _r	CO _o	CO _k	CO _v	CO _k	CO _k	CO _d
2.26	2.26	2.28	2.28	2.29	2.30	2.30	2.32	2.36	2.36
HR1939	0.13	0.04	0.11	0.16	0.06	0.02	-0.00	0.10	0.11
	0.04	0.07	0.03	0.01	0.46	0.50	0.34	0.50	0.13
HR4184	0.08	0.08	0.08	0.14	0.11	0.01	0.01	0.03	0.05
	0.02	0.01	0.02	0.00	0.38	0.45	0.31	0.29	0.09
HR8795	0.12	0.02	0.06	0.10	0.05	-0.00	0.01	0.05	0.06
	0.02	0.04	0.01	-0.00	0.26	0.29	0.18	0.25	0.07
HR8860	0.10	0.02	0.06	0.13	0.09	0.01	0.00	0.03	0.07
	0.02	0.05	0.01	0.01	0.35	0.38	0.24	0.28	0.06
HR5932	0.07	0.03	0.06	0.10	0.08	0.01	0.03	0.06	0.07
	0.02	0.05	0.00	0.00	0.35	0.38	0.28	0.26	0.11
HR5932	0.07	0.03	0.06	0.10	0.08	0.01	0.03	0.06	0.07
	0.02	0.05	0.00	0.00	0.35	0.38	0.28	0.26	0.11
B133	0.12	0.03	0.07	0.09	0.05	0.02	0.01	0.06	0.05
	0.02	0.08	0.04	0.04	0.32	0.36	0.23	0.26	0.07
SAO050381	0.13	0.04	0.11	0.16	0.07	-0.01	0.01	0.06	0.09
	0.03	0.06	0.02	0.00	0.36	0.39	0.22	0.30	0.11
HR6242	0.08	0.05	0.06	0.15	0.07	0.01	0.01	0.06	0.07
	0.05	0.09	0.02	-0.00	0.32	0.35	0.22	0.29	0.10
SAO044383	0.09	0.03	0.05	0.15	0.11	0.01	-0.01	0.05	0.04
	0.04	0.03	0.03	-0.00	0.38	0.39	0.30	0.27	0.17

Star	Mg _v	Fe _v	Si _o	CO _o	Mg _v	Mg _v	Brγ _k	Na _r	Na _k
ID	1.50	1.58	1.59	1.62	1.71	2.11	2.16	2.21	2.21
Ca _r	Ca _k	Mg _v	Mg _r	CO _o	CO _k	CO _v	CO _k	CO _k	CO _d
	2.26	2.26	2.28	2.28	2.29	2.30	2.30	2.32	2.36
HR4267	-	-	-	-	-	0.02	0.01	0.07	0.10
	0.04	0.08	0.01	0.02	0.35	0.37	0.25	0.30	0.11
HR0867	0.07	0.03	0.02	0.16	0.09	0.00	0.01	0.06	0.09
	0.04	0.06	0.01	0.01	0.31	0.35	0.25	0.25	0.08
HR6146	0.08	0.03	0.05	0.16	0.08	0.01	0.00	0.07	0.09
	0.04	0.07	0.01	-0.00	0.44	0.50	0.34	0.37	0.10
BMB194	0.13	0.04	0.08	0.17	0.10	0.04	-0.05	0.05	-0.02
	-0.03	-0.09	0.05	0.03	0.24	0.20	0.19	0.15	0.10
BMB239	0.12	0.04	0.07	0.14	0.05	0.02	-0.01	0.09	0.09
	0.05	0.06	0.02	-0.01	0.38	0.34	0.20	0.29	0.12
BMB179	0.10	0.05	0.06	0.13	0.07	0.02	0.01	0.10	0.10
	0.05	0.13	0.04	0.04	0.44	0.45	0.28	0.33	0.06
BMB181	0.14	0.06	0.08	0.15	0.12	0.03	0.00	0.07	0.10
	0.03	0.08	0.03	0.00	0.43	0.42	0.26	0.35	0.14
BMB285	0.13	0.00	0.02	0.05	0.02	0.02	0.02	0.02	0.04
	0.02	0.10	0.07	0.11	0.41	0.44	0.26	0.26	0.05
BMB087	-	-	-	-0.03	-0.01	0.02	0.03	-0.02	0.03
	0.03	0.05	0.02	-0.01	0.17	0.16	0.10	0.12	0.03
BMB142	0.09	-0.02	0.06	0.12	0.07	0.02	0.02	0.09	0.11
	0.05	0.15	0.04	0.04	0.43	0.47	0.29	0.40	0.10

Star	Mg _v	Fe _v	Si _o	CO _o	Mg _v	Mg _v	Brγ _k	Na _r	Na _k
ID	1.50	1.58	1.59	1.62	1.71	2.11	2.16	2.21	2.21
Ca _r	Ca _k	Mg _v	Mg _r	CO _o	CO _k	CO _v	CO _k	CO _k	CO _d
2.26	2.26	2.28	2.28	2.29	2.30	2.30	2.32	2.36	2.36
BMB039	0.13	0.03	0.07	0.09	0.06	0.05	0.05	0.03	0.08
	-0.00	0.06	0.05	0.06	0.35	0.35	0.21	0.12	0.11
BMB289	0.11	0.03	0.11	0.16	0.07	0.02	-0.02	0.06	0.06
	0.03	0.07	0.03	0.01	0.42	0.38	0.24	0.11	0.11
HR3314	0.00	-0.02	0.03	-0.04	0.00	0.00	0.17	0.00	0.01
	0.00	0.00	0.00	0.01	0.01	0.01	-0.00	0.02	0.01
HR3481	0.01	-0.03	0.05	-0.00	-0.01	-0.00	0.15	-0.02	0.03
	0.03	0.04	0.00	0.00	-	-	-	-	-
HR5144	0.02	-0.00	0.05	0.01	0.01	-	-	-	-
	-	-	-	-	-	-	-	-	-
HR4380	0.00	-0.02	0.04	-0.02	-0.00	0.00	0.22	0.00	-0.01
	0.00	-0.00	0.01	0.01	-0.00	-0.01	-0.01	-0.00	0.01
HR7451	0.04	0.01	-0.00	-0.00	0.01	-	-	-	-
	-	-	-	-	-	-	-	-	-
HR5270	0.00	-0.01	0.03	-0.00	-0.00	-0.00	0.02	0.01	0.00
	-0.00	-0.01	-0.00	-0.01	0.00	0.01	-0.00	0.00	0.00
HR4785	-	-	-	-	-	-	-0.01	-0.02	-0.01
	0.03	0.04	0.02	0.01	0.01	0.01	0.03	0.02	0.02
HR5235	-	0.01	0.06	0.02	0.03	0.00	0.08	0.02	0.02
	0.02	0.02	0.02	0.01	0.01	0.00	0.01	-0.01	0.01

Star	Mg _v	Fe _v	Si _o	CO _o	Mg _v	Mg _v	Brγ _k	Na _r	Na _k
ID	1.50	1.58	1.59	1.62	1.71	2.11	2.16	2.21	2.21
Ca _r	Ca _k	Mg _v	Mg _r	CO _o	CO _k	CO _v	CO _k	CO _k	CO _d
2.26	2.26	2.28	2.28	2.29	2.30	2.30	2.32	2.36	2.36
HR5829	0.13	0.03	0.09	0.09	0.07	0.03	-0.00	0.03	0.05
	0.01	0.04	0.02	0.03	0.28	0.24	0.15	0.23	0.09
HR6212	0.06	0.01	0.07	0.01	0.03	0.01	0.05	0.02	0.02
	0.02	0.03	0.02	0.01	0.02	0.01	0.01	0.02	-0.01
HR3538	0.10	0.03	0.08	-	-	0.02	-0.02	0.04	0.02
	-0.01	-0.03	0.01	0.02	-0.02	-0.02	0.01	-0.04	0.02
HR5409	0.06	0.01	0.05	0.01	0.02	0.03	0.05	0.02	0.02
	0.01	0.01	0.01	0.02	0.02	0.00	0.02	0.00	0.02
HR5072	0.08	0.01	0.05	-0.01	0.03	0.02	0.10	0.00	0.01
	0.00	0.00	0.02	0.02	0.02	0.01	0.03	-0.00	0.01
HR5853	0.09	0.02	0.06	-0.00	0.04	0.01	0.07	0.02	0.02
	0.01	0.02	0.01	0.01	0.00	-0.01	0.01	0.01	0.01
HR6623	0.09	0.02	0.09	0.05	0.04	0.02	0.04	0.02	0.01
	0.01	0.00	0.03	0.02	0.04	0.04	0.02	0.03	-0.02
HR4496	0.11	0.02	0.06	0.02	0.05	0.02	0.03	0.02	0.02
	0.02	0.03	0.02	0.01	0.02	0.03	0.01	0.02	0.00
SAO074439	0.07	0.01	0.07	0.06	0.03	0.01	0.06	0.01	-0.02
	-0.00	-0.05	0.01	-0.02	0.02	0.03	-0.03	-0.06	0.02
HR3259	0.13	0.04	0.06	0.00	0.09	0.00	0.03	0.01	0.03
	0.01	0.01	0.00	0.02	0.01	0.02	0.04	0.01	0.07

Star	Mg _v	Fe _v	Si _o	CO _o	Mg _v	Mg _v	Brγ _k	Na _r	Na _k
ID	1.50	1.58	1.59	1.62	1.71	2.11	2.16	2.21	2.21
Ca _r	Ca _k	Mg _v	Mg _r	CO _o	CO _k	CO _v	CO _k	CO _k	CO _d
2.26	2.26	2.28	2.28	2.29	2.30	2.30	2.32	2.36	2.36
HR6014	0.10	0.02	0.07	0.03	0.05	0.01	0.06	0.03	0.03
0.01	0.03	0.02	0.02	0.11	0.11	0.06	0.15	0.00	0.04
HR6752	0.16	0.02	0.07	0.02	0.07	0.02	0.23	0.00	0.01
0.01	0.03	0.02	0.03	0.11	0.12	0.08	0.09	-0.00	0.09
HR7957	0.05	0.01	0.06	0.01	0.02	0.02	0.05	0.01	0.01
0.01	0.01	0.01	0.01	0.08	0.07	0.03	0.10	-0.03	0.04
SAO011620	0.14	0.05	0.06	0.04	-	0.02	0.00	0.03	0.04
0.02	0.03	0.03	0.03	0.13	0.14	0.09	0.14	0.02	0.05
SAO045933	0.15	0.05	0.07	0.02	0.08	0.03	0.02	0.03	0.04
0.01	0.02	0.04	0.03	0.06	0.06	0.02	0.07	-0.00	0.04
SAO074175	0.17	0.04	0.06	0.01	0.07	0.02	0.06	0.00	0.05
0.01	0.02	0.03	0.03	0.06	0.06	0.04	0.13	0.01	0.06
HR1325	0.08	0.03	0.01	0.00	0.06	0.00	0.01	0.03	0.04
0.02	0.04	0.03	0.02	0.07	0.08	0.04	0.09	0.07	0.04
HR5901	0.10	0.02	0.05	0.01	0.03	0.05	0.01	0.02	0.02
0.02	0.00	0.02	-0.00	0.07	0.09	0.05	0.06	-0.03	0.04
SAO074883	0.13	0.03	0.04	0.01	0.07	0.02	0.02	0.01	0.03
0.00	0.02	0.02	0.04	0.00	0.00	-0.01	0.03	-0.01	0.03
SAO050265	0.13	0.02	0.12	0.03	0.04	0.01	0.02	0.02	0.02
0.01	0.03	0.02	0.02	0.10	0.10	0.06	0.09	-0.01	0.04

Star	Mg _v	Fe _v	Si _o	CO _o	Mg _v	Mg _v	Brγ _k	Na _r	Na _k
ID	1.50	1.58	1.59	1.62	1.71	2.11	2.16	2.21	2.21
Ca _r	Ca _k	Mg _v	Mg _r	CO _o	CO _k	CO _v	CO _k	CO _k	CO _d
2.26	2.26	2.28	2.28	2.29	2.30	2.30	2.32	2.36	2.36
HR5553	0.14	0.03	0.07	0.03	0.07	0.03	0.05	0.04	0.05
	0.02	0.05	0.03	0.03	0.07	0.07	0.03	0.05	0.00
SAO028414	-	-	-	-	-	-	0.01	0.03	0.02
	0.02	0.03	0.02	0.02	0.04	0.03	0.04	0.06	0.03
SAO031745	0.12	0.02	0.06	0.01	0.07	-	-	-	-
	-	-	-	-	-	-	-	-	-
SAO109471	0.14	0.02	0.06	0.00	0.07	0.02	-0.00	0.04	0.04
	0.01	0.03	0.02	0.03	0.07	0.08	0.05	0.05	0.01
HR8832	0.23	0.03	0.08	0.07	0.12	0.01	-0.01	0.05	0.06
	0.03	0.04	0.03	0.03	0.11	0.11	0.07	0.11	0.00
SAO122610	0.13	0.02	0.05	0.02	0.09	0.03	-0.02	0.04	0.05
	0.02	0.04	0.03	0.02	0.05	0.04	0.04	0.09	-0.01
GJ570A	0.30	0.08	0.09	0.06	0.14	0.06	-0.03	0.07	0.09
	0.03	0.06	0.03	0.04	0.11	0.12	0.06	0.08	-0.03
HR8085	0.15	0.03	0.05	0.00	0.10	0.02	0.03	0.03	0.04
	0.04	0.05	0.03	0.03	0.10	0.09	0.04	0.08	-0.00
GJ380	0.20	0.04	0.07	0.04	0.15	0.03	0.01	0.07	0.11
	0.05	0.09	0.04	0.04	0.07	0.08	0.02	0.12	-0.02
GJ673	0.17	0.04	0.07	0.03	0.13	-	-0.02	0.06	0.07
	0.08	0.09	0.04	0.04	0.07	0.06	0.04	0.06	-0.02

Star	Mg _v	Fe _v	Si _o	CO _o	Mg _v	Mg _v	Brγ _k	Na _r	Na _k
ID	1.50	1.58	1.59	1.62	1.71	2.11	2.16	2.21	2.21
Ca _r	Ca _k	Mg _v	Mg _r	CO _o	CO _k	CO _v	CO _k	CO _k	CO _d
2.26	2.26	2.28	2.28	2.29	2.30	2.30	2.32	2.36	2.36
HR8086	0.13	0.03	0.04	0.03	0.11	0.03	0.04	0.07	0.08
	0.04	0.05	0.03	0.01	0.12	0.11	0.07	-0.00	0.04
SAO027179	0.17	0.03	0.05	0.02	0.12	0.02	0.02	0.09	0.12
	0.04	0.07	0.01	0.01	0.10	0.10	0.08	0.01	0.02
GJ570B	0.20	0.05	0.04	0.02	0.13	0.03	-0.01	0.11	0.14
	0.07	0.08	0.02	0.02	0.13	0.14	0.09	-0.03	0.05
GJ015SW	0.09	0.01	-0.01	-0.01	0.07	0.01	0.08	0.09	0.09
	0.05	0.07	0.01	0.02	0.13	0.14	0.12	-0.00	0.02
GJ625	-	-	-	-	-	-	-	0.07	0.05
	0.03	0.02	0.01	0.02	0.03	0.03	0.02	-0.02	0.01
GJ411	0.05	0.01	0.02	0.01	0.11	0.02	0.01	0.02	0.04
	0.01	0.02	-0.01	-0.02	0.08	0.07	0.04	-	0.01
GJ412A	-	-	-	-	-	0.02	-0.00	0.05	0.07
	0.02	0.07	0.01	0.01	0.06	0.07	0.04	-	0.03
GJ015NE	0.02	-0.03	-0.02	-0.01	0.01	-0.00	0.00	0.08	0.06
	-0.00	0.02	-0.00	0.01	0.12	0.12	0.09	0.01	0.02
GJ526	0.10	0.01	0.02	0.01	0.10	0.01	0.01	0.05	0.08
	0.02	0.06	0.01	-0.00	0.09	0.10	0.06	0.01	0.02
GJ206	0.03	0.01	-0.02	0.01	0.05	-0.01	0.01	0.06	0.08
	0.06	0.08	0.01	0.00	0.12	0.12	0.07	0.02	0.03

Star	Mg _v	Fe _v	Si _o	CO _o	Mg _v	Mg _v	Brγ _k	Na _r	Na _k
ID	1.50	1.58	1.59	1.62	1.71	2.11	2.16	2.21	2.21
Ca _r	Ca _k	Mg _v	Mg _r	CO _o	CO _k	CO _v	CO _k	CO _k	CO _d
2.26	2.26	2.28	2.28	2.29	2.30	2.30	2.32	2.36	2.36
GJ213	0.00	-0.01	-0.03	-0.01	0.02	-0.00	0.03	0.08	0.08
	0.04	0.07	0.00	0.00	0.10	0.11	0.06	0.00	0.03
GJ402	0.02	0.01	-0.02	0.01	0.04	-0.00	-0.02	0.13	0.13
	0.03	0.04	0.00	-0.01	0.09	0.09	0.07	-0.02	0.04
GJ725A	0.06	0.00	0.00	0.00	0.08	-	0.15	0.05	0.04
	0.05	0.02	0.02	0.00	0.03	0.02	-0.00	-0.02	0.02
GJ388	0.09	0.00	0.02	0.04	0.07	0.01	0.01	0.09	0.12
	0.07	0.11	0.00	-0.00	0.11	0.11	0.08	0.00	0.04
GJ831	-0.01	-0.02	-0.03	-0.01	0.03	-0.00	-0.01	0.06	0.08
	0.02	0.06	0.00	0.02	0.07	0.09	0.06	-0.01	0.05
GJ065	-0.01	-0.00	-0.01	-0.04	-0.01	0.01	0.04	0.07	0.09
	0.01	0.03	0.01	0.02	0.12	0.13	0.08	0.10	0.02
GJ905	0.01	-	-	-	-	-0.00	0.02	0.15	0.14
	0.00	0.03	-0.00	0.00	0.14	0.14	0.12	0.13	0.00
GJ866	0.00	-0.03	-0.01	-0.04	-0.01	-0.00	-0.01	0.10	0.12
	-0.01	0.00	-0.00	-0.02	0.15	0.16	0.11	0.08	-0.03
ngc7789k415	-	-	-	-	-	-	0.01	0.04	0.04
	0.02	0.03	0.01	0.01	0.27	0.25	0.17	0.24	0.04
ngc7789k468	0.09	0.02	0.09	0.11	0.06	0.01	0.02	0.03	0.02
	0.01	-0.00	0.01	0.00	0.21	0.17	0.13	0.19	0.03

Star	Mg _v	Fe _v	Si _o	CO _o	Mg _v	Mg _v	Brγ _k	Na _r	Na _k
ID	1.50	1.58	1.59	1.62	1.71	2.11	2.16	2.21	2.21
Ca _r	Ca _k	Mg _v	Mg _r	CO _o	CO _k	CO _v	CO _k	CO _k	CO _d
2.26	2.26	2.28	2.28	2.29	2.30	2.30	2.32	2.36	2.36
ngc7789k501	0.10	0.03	0.10	0.09	0.05	0.02	0.02	0.04	0.04
	0.02	0.01	0.02	0.02	0.20	0.16	0.12	0.04	0.07
ngc7789k575	-	-	-	-	-	-	0.03	0.03	0.02
	0.01	0.02	0.00	0.02	0.14	0.13	0.09	0.01	0.04
ngc7789k669	0.09	0.02	0.09	0.06	0.04	0.02	0.02	0.03	0.03
	0.01	0.01	0.01	0.01	0.20	0.16	0.12	0.05	0.08
ngc7789k676	-	-	-	-	-	-	0.06	0.04	0.02
	-0.01	0.03	0.00	0.02	0.11	0.10	0.06	0.11	0.00
ngc7789k859	-	-	-	-	-	-	0.03	0.03	0.01
	0.02	0.01	0.01	0.03	0.10	0.08	0.06	0.09	-0.01
ngc7789k875	-	-	-	-	-	-	0.04	0.04	0.03
	0.04	0.03	0.01	0.02	0.07	0.06	0.04	0.06	0.02
ngc7789k897	-	-	-	-	-	-	0.01	0.02	-0.02
	0.02	-0.03	0.02	0.03	0.06	0.05	0.06	-0.05	0.04
ngc7789k971	0.10	0.02	0.09	0.11	0.05	0.02	0.01	0.04	0.02
	0.01	0.00	0.01	-0.00	0.29	0.24	0.20	0.07	0.10

Table 4.6 Calibrations for the spectral indices.

Var. ^a		Coefficients for Polynomial Fits								
Z	[Fe/H]	Fe4383		Fe4668		Fe5015		Mg ₂		
T	Θ ^b	V-K	Θ	V-K	Θ	V-K	Θ	V-K	Θ	V-K
G	log <i>g</i>									

Term	Coefficients for Mg15V									
1	-0.1332	0.0974	-0.2746	-0.0085	-0.2034	0.0045	-0.2908	-0.0055	-0.2586	0.0021
Z	0.0287	0.0288	0.0008	0.0009	0.0036	0.0039	0.0032	0.0032	0.2207	0.2551
Z ²	-0.0035	-0.0038	0.0000	0.0000	-0.0001	-0.0002	-0.0001	-0.0001	-0.3402	-0.3931
T	0.3677	0.0053	0.6152	0.0688	0.4868	0.0566	0.6325	0.0626	0.5693	0.0486
T ²	-0.1381	-0.0005	-0.2542	-0.0111	-0.2015	-0.0094	-0.2627	-0.0102	-0.2420	-0.0085
No.	81	74	66	61	66	61	66	61	66	61
χ ² _{PDF}	1.28	1.20	1.99	2.10	1.88	1.98	1.96	2.08	1.83	1.91
rms	0.0275	0.0268	0.0340	0.0349	0.0331	0.0340	0.0337	0.0347	0.0329	0.0338

Var. ^a		Coefficients for Polynomial Fits								
Z	[Fe/H]		Fe4383		Fe4668		Fe5015		Mg ₂	
T	Θ ^b	V-K	Θ	V-K	Θ	V-K	Θ	V-K	Θ	V-K
G	log <i>g</i>									
<hr/>										
Term		Coefficients for Fe158V								
1	0.0323	0.0354	0.0378	0.0442	0.0352	0.0431	0.0155	0.0426	0.0576	0.0432
Z	0.0106	0.0113	-0.0001	0.0002	0.0014	0.0016	0.0011	0.0010	0.0888	0.0978
Z ²	-0.0021	-0.0018	0.0001	0.0000	-0.0000	-0.0001	-0.0000	-0.0000	-0.1403	-0.1584
T	-0.0081	-0.0003	-0.0012	-0.0069	-0.0004	-0.0078	0.0327	-0.0070	-0.0426	-0.0109
T ²	0.0088	0.0001	-0.0049	0.0006	-0.0062	0.0007	-0.0195	0.0006	0.0095	0.0010
No.	82	75	69	64	69	64	69	64	69	64
χ ² _{PDF}	0.42	0.33	0.43	0.45	0.41	0.43	0.43	0.45	0.40	0.42
rms	0.0125	0.0109	0.0125	0.0128	0.0121	0.0124	0.0125	0.0127	0.0121	0.0123

Var. ^a		Coefficients for Polynomial Fits								
Z	[Fe/H]	Fe4383		Fe4668		Fe5015		Mg ₂		
T	Θ ^b	V-K	Θ	V-K	Θ	V-K	Θ	V-K	Θ	V-K
G	log <i>g</i>									
Term		Coefficients for Si159O								
1	-0.2779	0.0539	-0.4008	-0.0301	-0.4482	-0.0504	-0.4692	-0.0506	-0.3997	-0.0208
Z	0.0092	0.0123	-0.0008	-0.0015	0.0008	-0.0002	0.0015	0.0007	0.0952	0.0930
Z ²	-0.0072	-0.0049	0.0002	0.0002	-0.0000	0.0001	-0.0000	0.0000	-0.1238	-0.1315
T	0.6034	0.0091	0.6988	0.0358	0.7794	0.0419	0.8062	0.0411	0.7139	0.0291
T ²	-0.2448	-0.0009	-0.2718	-0.0036	-0.3074	-0.0042	-0.3177	-0.0041	-0.2877	-0.0032
G	-0.0113	0.0073	0.0297	0.0323	0.0317	0.0367	0.0319	0.0361	0.0246	0.0281
G ²	0.0034	-0.0010	-0.0055	-0.0059	-0.0062	-0.0066	-0.0062	-0.0064	-0.0050	-0.0055
No.	81	74	66	61	66	61	66	61	66	61
χ ² _{PDF}	0.84	0.87	1.01	1.04	1.02	1.01	1.01	1.01	0.98	1.02
rms	0.0182	0.0185	0.0200	0.0202	0.0200	0.0199	0.0199	0.0199	0.0196	0.0199

Var. ^a		Coefficients for Polynomial Fits									
Z	[Fe/H]		Fe4383		Fe4668		Fe5015		Mg ₂		
T	Θ ^b	V-K	Θ	V-K	Θ	V-K	Θ	V-K	Θ	V-K	
G	log <i>g</i>										
<hr/>											
Term		Coefficients for CO162O									
1	-0.9017	-0.1428	0.0241	-0.0671	0.0598	-0.0646	0.0181	-0.0707	0.0877	-0.0597	
Z	0.0188	0.0238	0.0011	0.0013	0.0016	0.0019	0.0019	0.0022	0.0828	0.1053	
Z ²	-0.0020	0.0006	-0.0000	-0.0001	-0.0001	-0.0001	-0.0001	-0.0001	-0.1525	-0.1944	
T	1.4323	0.1011	-0.1521	0.0514	-0.2122	0.0493	-0.1467	0.0511	-0.2588	0.0446	
T ²	-0.5110	-0.0096	0.1556	-0.0028	0.1798	-0.0026	0.1528	-0.0028	0.1971	-0.0020	
No.	81	73	66	61	66	61	66	61	66	61	
χ ² _{PDF}	1.25	1.08	0.78	0.83	0.76	0.80	0.77	0.81	0.77	0.81	
rms	0.0256	0.0236	0.0176	0.0182	0.0175	0.0179	0.0175	0.0179	0.0176	0.0180	

Var. ^a		Coefficients for Polynomial Fits									
Z	[Fe/H]	Fe4383		Fe4668		Fe5015		Mg ₂			
T	Θ ^b	V-K	Θ	V-K	Θ	V-K	Θ	V-K	Θ	V-K	
G	log <i>g</i>										
<hr/>											
Term		Coefficients for Mg171V									
1	-0.2009	-0.0005	-0.1568	-0.0157	-0.1865	-0.0172	-0.1901	-0.0183	-0.1844	-0.0173	
Z	0.0106	0.0103	-0.0004	-0.0001	0.0004	-0.0000	0.0006	0.0002	0.0316	0.0514	
Z ²	0.0004	-0.0002	0.0001	0.0000	-0.0000	0.0000	-0.0000	0.0000	-0.0215	-0.0635	
T	0.3531	0.0260	0.2684	0.0324	0.3184	0.0327	0.3220	0.0330	0.3081	0.0299	
T ²	-0.1133	-0.0022	-0.0735	-0.0026	-0.0953	-0.0027	-0.0964	-0.0027	-0.0912	-0.0024	
No.	72	64	62	57	62	57	62	57	62	57	
χ ² _{PDF}	0.60	0.54	0.54	0.56	0.54	0.55	0.54	0.55	0.52	0.54	
rms	0.0148	0.0139	0.0140	0.0141	0.0139	0.0140	0.0140	0.0140	0.0137	0.0138	

Var. ^a		Coefficients for Polynomial Fits									
Z	[Fe/H]		Fe4383		Fe4668		Fe5015		Mg ₂		
T	Θ ^b	V-K	Θ	V-K	Θ	V-K	Θ	V-K	Θ	V-K	
G	log <i>g</i>										
<hr/>											
Term		Coefficients for Mg211V									
1	0.1327	0.0217	0.0270	0.0657	0.0356	0.0667	0.0345	0.0666	-0.2094	0.0792	
Z	0.0038	0.0038	-0.0005	-0.0006	0.0003	0.0001	-0.0000	-0.0003	0.0258	0.0339	
Z ²	-0.0012	-0.0013	0.0001	0.0001	-0.0000	-0.0000	-0.0000	0.0000	-0.0351	-0.0537	
T	-0.2774	-0.0035	-0.0035	-0.0388	-0.0099	-0.0407	-0.0084	-0.0395	0.5584	-0.0541	
T ²	0.2140	0.0006	-0.0105	0.0094	-0.0191	0.0099	-0.0173	0.0096	-0.4576	0.0133	
T ³	-0.0533	-0.0000	0.0036	-0.0007	0.0098	-0.0007	0.0084	-0.0007	0.1207	-0.0010	
No.	82	74	69	64	69	64	69	64	69	64	
χ ² _{PDF}	0.13	0.13	0.16	0.15	0.16	0.15	0.17	0.15	0.16	0.15	
rms	0.0070	0.0069	0.0077	0.0074	0.0077	0.0074	0.0077	0.0074	0.0076	0.0073	

Var. ^a		Coefficients for Polynomial Fits									
Z	[Fe/H]	Fe4383		Fe4668		Fe5015		Mg ₂			
T	Θ ^b V-K	Θ	V-K	Θ	V-K	Θ	V-K	Θ	V-K	Θ	V-K
G	log <i>g</i>										
Term		Coefficients for Na221R									
1		0.0331	-0.0053	0.1607	0.0059	0.1558	-0.0012	0.1394	-0.0015	0.1638	-0.0004
Z		0.0195	0.0209	-0.0006	-0.0013	0.0018	0.0014	0.0016	0.0012	0.0962	0.0832
Z ²		0.0035	0.0043	0.0002	0.0002	-0.0001	-0.0000	-0.0000	-0.0000	-0.1463	-0.1239
T		-0.0754	0.0150	-0.2889	0.0067	-0.2853	0.0082	-0.2588	0.0084	-0.3035	0.0052
T ²		0.0644	-0.0006	0.1486	0.0004	0.1467	0.0002	0.1358	0.0002	0.1523	0.0006
No.		88	81	74	70	74	70	74	70	74	70
χ _{PDF} ²		0.42	0.34	0.46	0.46	0.45	0.45	0.47	0.47	0.45	0.45
rms		0.0125	0.0113	0.0129	0.0129	0.0128	0.0128	0.0131	0.0131	0.0128	0.0128

Var. ^a		Coefficients for Polynomial Fits								
Z	[Fe/H]		Fe4383		Fe4668		Fe5015		Mg ₂	
T	Θ ^b	V-K	Θ	V-K	Θ	V-K	Θ	V-K	Θ	V-K
G	log <i>g</i>									
<hr/>										
Term		Coefficients for Na221K								
1	-0.1222	-0.0153	0.1861	0.0104	0.1489	0.0029	0.1517	0.0031	0.2013	0.0021
Z	0.0257	0.0273	-0.0010	-0.0012	0.0006	0.0006	0.0005	0.0006	0.0933	0.1112
Z ²	0.0045	0.0054	0.0001	0.0002	-0.0000	0.0000	-0.0000	-0.0000	-0.1535	-0.1796
T	0.1901	0.0251	-0.3372	0.0072	-0.2787	0.0095	-0.2828	0.0095	-0.3760	0.0049
T ²	-0.0424	-0.0019	0.1795	0.0008	0.1551	0.0005	0.1570	0.0005	0.1939	0.0010
No.	85	79	72	68	72	68	72	68	72	68
χ ² _{PDF}	0.89	0.85	0.76	0.79	0.76	0.78	0.77	0.80	0.74	0.76
rms	0.0183	0.0177	0.0167	0.0169	0.0167	0.0169	0.0168	0.0170	0.0164	0.0166

Var. ^a		Coefficients for Polynomial Fits									
Z	[Fe/H]		Fe4383		Fe4668		Fe5015		Mg ₂		
T	Θ ^b	V-K	Θ	V-K	Θ	V-K	Θ	V-K	Θ	V-K	
G	log <i>g</i>										
<hr/>											
Term		Coefficients for Ca226R									
1	0.2235	-0.0088	0.0160	0.0091	0.0082	0.0024	0.0103	0.0046	0.2074	0.0099	
Z	0.0081	0.0089	-0.0001	-0.0003	0.0001	-0.0002	-0.0003	-0.0006	0.0131	0.0016	
Z ²	0.0007	0.0010	-0.0000	-0.0000	0.0000	0.0000	0.0000	0.0000	-0.0278	-0.0109	
T	-0.5666	0.0135	-0.0063	0.0019	-0.0021	0.0057	-0.0021	0.0056	-0.4659	0.0001	
T ²	0.4864	-0.0013	-0.0084	0.0009	-0.0022	0.0001	-0.0028	0.0001	0.3520	0.0014	
T ³	-0.1287	0.0000	0.0137	-0.0001	0.0094	-0.0000	0.0097	-0.0000	-0.0793	-0.0001	
No.	92	85	77	73	77	73	77	73	77	73	
χ ² _{PDF}	0.20	0.20	0.23	0.23	0.23	0.23	0.23	0.22	0.23	0.23	
rms	0.0086	0.0085	0.0091	0.0091	0.0091	0.0091	0.0091	0.0091	0.0091	0.0091	

Var. ^a		Coefficients for Polynomial Fits								
Z	[Fe/H]		Fe4383		Fe4668		Fe5015		Mg ₂	
T	Θ ^b	V-K	Θ	V-K	Θ	V-K	Θ	V-K	Θ	V-K
G	log <i>g</i>									
<hr/>										
Term		Coefficients for Ca226K								
1	-0.0350	-0.0845	0.9069	0.0688	1.2592	0.0680	1.0227	0.0640	1.1281	0.0656
Z	0.0253	0.0275	0.0007	0.0006	0.0008	0.0010	0.0004	0.0006	0.0334	0.0344
Z ²	-0.0176	-0.0422	0.4535	0.0344	0.6297	0.0340	0.5114	0.0320	0.5642	0.0328
T	-0.0843	0.1127	-3.2104	-0.0779	-4.5541	-0.0809	-3.6692	-0.0738	-4.0564	-0.0785
T ²	0.2778	-0.0236	2.4976	0.0231	3.6248	0.0244	2.9000	0.0224	3.2015	0.0234
T ³	-0.1190	0.0015	-0.6218	-0.0018	-0.9340	-0.0019	-0.7382	-0.0018	-0.8153	-0.0018
No.	78	72	67	63	67	63	67	63	67	63
χ ² _{PDF}	1.41	1.44	1.04	1.10	1.01	1.05	1.03	1.08	0.99	1.05
rms	0.0228	0.0229	0.0194	0.0199	0.0191	0.0195	0.0194	0.0197	0.0190	0.0194

Var. ^a		Coefficients for Polynomial Fits									
Z	[Fe/H]	Fe4383		Fe4668		Fe5015		Mg ₂			
T	Θ ^b	V-K	Θ	V-K	Θ	V-K	Θ	V-K	Θ	V-K	
G	log <i>g</i>										
<hr/>											
Term		Coefficients for Mg228V									
1	0.0122	0.0150	0.0420	0.0242	0.0431	0.0244	0.0430	0.0244	0.0420	0.0238	
Z	0.0088	0.0090	0.0001	0.0001	0.0001	0.0001	0.0001	0.0001	0.0063	0.0048	
T	0.0059	0.0014	-0.0229	-0.0028	-0.0238	-0.0028	-0.0237	-0.0028	-0.0235	-0.0029	
No.	90	84	75	71	75	71	75	71	75	71	
χ ² _{PDF}	0.24	0.26	0.22	0.23	0.22	0.23	0.22	0.23	0.22	0.23	
rms	0.0094	0.0099	0.0090	0.0092	0.0090	0.0092	0.0090	0.0092	0.0090	0.0092	

Var. ^a		Coefficients for Polynomial Fits									
Z	[Fe/H]	Fe4383		Fe4668		Fe5015		Mg ₂			
T	Θ ^b	V-K	Θ	V-K	Θ	V-K	Θ	V-K	Θ	V-K	
G	log <i>g</i>										
<hr/>											
Term		Coefficients for Mg228R									
1	0.0275	0.0218	0.0507	0.0279	0.0495	0.0261	0.0495	0.0255	0.0492	0.0269	
Z	0.0065	0.0067	-0.0001	-0.0003	0.0001	-0.0000	0.0001	0.0001	0.0021	-0.0025	
T	-0.0068	-0.0007	-0.0281	-0.0027	-0.0280	-0.0026	-0.0280	-0.0026	-0.0276	-0.0027	
No.	85	78	72	68	72	68	72	68	72	68	
χ ² _{PDF}	0.25	0.26	0.23	0.23	0.23	0.23	0.23	0.23	0.23	0.23	
rms	0.0097	0.0097	0.0092	0.0092	0.0092	0.0092	0.0092	0.0092	0.0092	0.0092	

Var. ^a		Coefficients for Polynomial Fits									
Z	[Fe/H]		Fe4383		Fe4668		Fe5015		Mg ₂		
T	Θ ^b	V-K	Θ	V-K	Θ	V-K	Θ	V-K	Θ	V-K	
G	log <i>g</i>										
<hr/>											
Term		Coefficients for CO229O									
1	1.3251	-0.3958	0.2617	-0.4284	1.2132	-0.4569	0.2250	-0.5345	-0.4245	-0.4636	
Z	0.0955	0.1056	0.0070	0.0062	0.0027	0.0024	0.0021	0.0020	0.1148	0.1024	
T	-4.3545	0.2774	-1.2007	0.2610	-3.8180	0.3032	-1.4443	0.3635	0.4924	0.3337	
T ²	4.2020	-0.0337	1.0797	-0.0412	3.5220	-0.0520	1.6304	-0.0675	-0.1608	-0.0644	
T ³	-1.1515	0.0014	-0.1791	0.0029	-0.9317	0.0037	-0.4327	0.0050	0.0948	0.0049	
G	0.0189	0.0059	0.0297	0.0304	0.0290	0.0304	0.0313	0.0331	0.0172	0.0204	
No.	80	73	67	63	67	63	67	63	67	63	
χ ² _{PDF}	2.33	2.21	3.85	3.73	4.14	3.96	4.21	4.00	4.03	3.87	
rms	0.0479	0.0410	0.0592	0.0565	0.0602	0.0571	0.0610	0.0580	0.0596	0.0564	

Var. ^a		Coefficients for Polynomial Fits									
Z	[Fe/H]		Fe4383		Fe4668		Fe5015		Mg ₂		
T	Θ ^b	V-K	Θ	V-K	Θ	V-K	Θ	V-K	Θ	V-K	
G	log <i>g</i>										
Term		Coefficients for 2CO22K									
1	1.0158	-0.4229	-2.5625	-0.5792	-1.7069	-0.6090	-2.4198	-0.6709	-2.9961	-0.6007	
Z	0.0980	0.1082	0.0062	0.0055	0.0023	0.0021	0.0019	0.0018	0.1107	0.1007	
T	-3.6053	0.2927	5.9047	0.3933	3.5408	0.4335	5.2380	0.4795	6.9805	0.4502	
T ²	3.5925	-0.0361	-4.8443	-0.0781	-2.6352	-0.0880	-3.9796	-0.0995	-5.6030	-0.0969	
T ³	-0.9843	0.0015	1.4582	0.0061	0.7780	0.0069	1.1313	0.0078	1.6106	0.0078	
G	0.0213	0.0093	0.0338	0.0352	0.0331	0.0351	0.0353	0.0377	0.0220	0.0253	
No.	80	73	67	63	67	63	67	63	67	63	
χ ² _{PDF}	2.31	2.18	3.81	3.68	4.03	3.86	4.08	3.88	3.90	3.75	
rms	0.0558	0.0481	0.0645	0.0611	0.0648	0.0611	0.0652	0.0617	0.0643	0.0603	

Var. ^a		Coefficients for Polynomial Fits									
Z	[Fe/H]		Fe4383		Fe4668		Fe5015		Mg ₂		
T	Θ ^b	V-K	Θ	V-K	Θ	V-K	Θ	V-K	Θ	V-K	
G	log <i>g</i>										
Term		Coefficients for CO229V									
1	0.2848	-0.3340	-0.3261	-0.2493	0.7426	-0.2467	0.1737	-0.2708	0.0257	-0.2397	
Z	0.0409	0.0430	0.0029	0.0028	0.0018	0.0018	0.0012	0.0013	0.0722	0.0741	
T	-1.6312	0.2088	0.3925	0.1152	-2.4063	0.1134	-1.0003	0.1338	-0.4772	0.1204	
T ²	1.8557	-0.0271	-0.3175	-0.0083	2.1176	-0.0069	0.9708	-0.0123	0.4336	-0.0113	
T ³	-0.5347	0.0012	0.1992	0.0003	-0.5015	0.0002	-0.1922	0.0006	-0.0223	0.0006	
G	0.0311	0.0232	0.0370	0.0336	0.0380	0.0344	0.0384	0.0353	0.0321	0.0288	
No.	84	78	72	68	72	68	72	68	72	68	
χ ² _{PDF}	1.32	1.25	2.15	2.14	2.16	2.14	2.22	2.20	2.09	2.07	
rms	0.0334	0.0285	0.0363	0.0351	0.0363	0.0349	0.0368	0.0355	0.0362	0.0347	

Var. ^a		Coefficients for Polynomial Fits									
Z	[Fe/H]		Fe4383		Fe4668		Fe5015		Mg ₂		
T	Θ ^b	V-K	Θ	V-K	Θ	V-K	Θ	V-K	Θ	V-K	
G	log <i>g</i>										
Term		Coefficients for C2O23K									
1	0.2862	-0.4529	3.7239	-0.1544	5.1356	-0.1404	4.6823	-0.1643	3.8122	-0.1809	
Z	0.0552	0.0585	0.0032	0.0035	0.0021	0.0023	0.0016	0.0017	0.0953	0.1114	
T	-2.0589	0.3723	-10.2142	0.0936	-13.8964	0.0851	-12.8019	0.1032	-10.4274	0.1414	
T ²	2.7334	-0.0627	9.0112	0.0066	12.2076	0.0098	11.3289	0.0055	9.2498	-0.0097	
T ³	-0.9063	0.0035	-2.4922	-0.0016	-3.4106	-0.0019	-3.1762	-0.0016	-2.5878	-0.0002	
G	0.0098	-0.0012	0.0172	0.0051	0.0170	0.0047	0.0183	0.0061	0.0083	-0.0041	
No.	85	77	72	68	72	68	72	68	72	68	
χ ² _{PDF}	0.81	0.80	1.53	1.70	1.52	1.69	1.57	1.75	1.43	1.54	
rms	0.0374	0.0272	0.0342	0.0365	0.0338	0.0356	0.0340	0.0359	0.0334	0.0351	

Var. ^a		Coefficients for Polynomial Fits									
Z	[Fe/H]	Fe4383				Fe4668		Fe5015		Mg ₂	
T	Θ ^b	V-K	Θ	V-K	Θ	V-K	Θ	V-K	Θ	V-K	
G	log <i>g</i>										
<hr/>											
Term		Coefficients for C3O23K									
1	1.3282	-0.2232	-0.2773	0.0064	-0.2648	-0.0166	-0.2603	-0.0046	3.1312	0.0171	
Z	0.0063	0.0087	-0.0025	-0.0043	0.0001	-0.0005	-0.0012	-0.0018	0.0810	0.0623	
Z ²	-0.0053	-0.0048	0.0003	0.0004	-0.0000	0.0000	0.0000	0.0001	-0.1416	-0.1173	
T	-3.8134	0.1252	0.0882	-0.0737	0.0821	-0.0605	0.0828	-0.0650	-8.1980	-0.0897	
T ²	3.3890	-0.0165	0.2305	0.0352	0.2175	0.0322	0.2161	0.0332	6.8443	0.0390	
T ³	-0.9294	0.0007	-0.0825	-0.0032	-0.0749	-0.0030	-0.0741	-0.0031	-1.8210	-0.0035	
G	0.0130	0.0125	0.0180	0.0171	0.0166	0.0166	0.0170	0.0167	0.0192	0.0154	
No.	86	80	72	68	72	68	72	68	72	68	
χ ² _{PDF}	1.16	1.01	1.12	1.10	1.13	1.14	1.12	1.12	1.07	1.13	
rms	0.0216	0.0197	0.0211	0.0203	0.0211	0.0205	0.0210	0.0203	0.0205	0.0205	

Var ^a		Coefficients for Polynomial Fits									
Z	[Fe/H]		Fe4383		Fe4668		Fe5015		Mg ₂		
T	Θ ^b	V-K	Θ	V-K	Θ	V-K	Θ	V-K	Θ	V-K	
G	log <i>g</i>										
<hr/>											
Term		Coefficients for CO236D									
1	0.4256	-0.1259	2.0281	-0.0204	2.2588	-0.0157	2.0776	-0.0159	2.1146	-0.0161	
Z	0.0133	0.0145	0.0010	0.0010	0.0003	0.0005	0.0001	0.0002	0.0252	0.0261	
T	-1.3702	0.1014	-5.3089	-0.0013	-5.8848	-0.0034	-5.4272	-0.0021	-5.5243	-0.0008	
T ²	1.3765	-0.0157	4.5094	0.0109	4.9956	0.0116	4.6171	0.0112	4.7002	0.0104	
T ³	-0.4065	0.0008	-1.2225	-0.0012	-1.3588	-0.0013	-1.2554	-0.0013	-1.2804	-0.0012	
G	0.0040	0.0038	0.0113	0.0077	0.0111	0.0077	0.0111	0.0079	0.0095	0.0060	
No.	93	87	77	73	77	73	77	73	77	73	
χ ² _{PDF}	0.61	0.53	0.59	0.63	0.60	0.64	0.61	0.65	0.58	0.62	
rms	0.0172	0.0142	0.0147	0.0152	0.0149	0.0153	0.0150	0.0154	0.0146	0.0150	

Var ^a		Coefficients for Polynomial Fits									
Z	[Fe/H]	Fe4383		Fe4668		Fe5015		Mg ₂			
T	Θ ^b	V-K	Θ	V-K	Θ	V-K	Θ	V-K	Θ	V-K	
G		$\log g$									

COMMENTS: The table head indicates which independent variables were used in each fit, and the table body shows the fit coefficients at every term. The number of measurements used in the fit, the normalized χ^2_{PDF} per degree of freedom, and the r.m.s. of every fit are also shown. See Section 4.6 for details.

^a Independent variables.

^b $\Theta = \log(5040/T_{\text{eff}})$

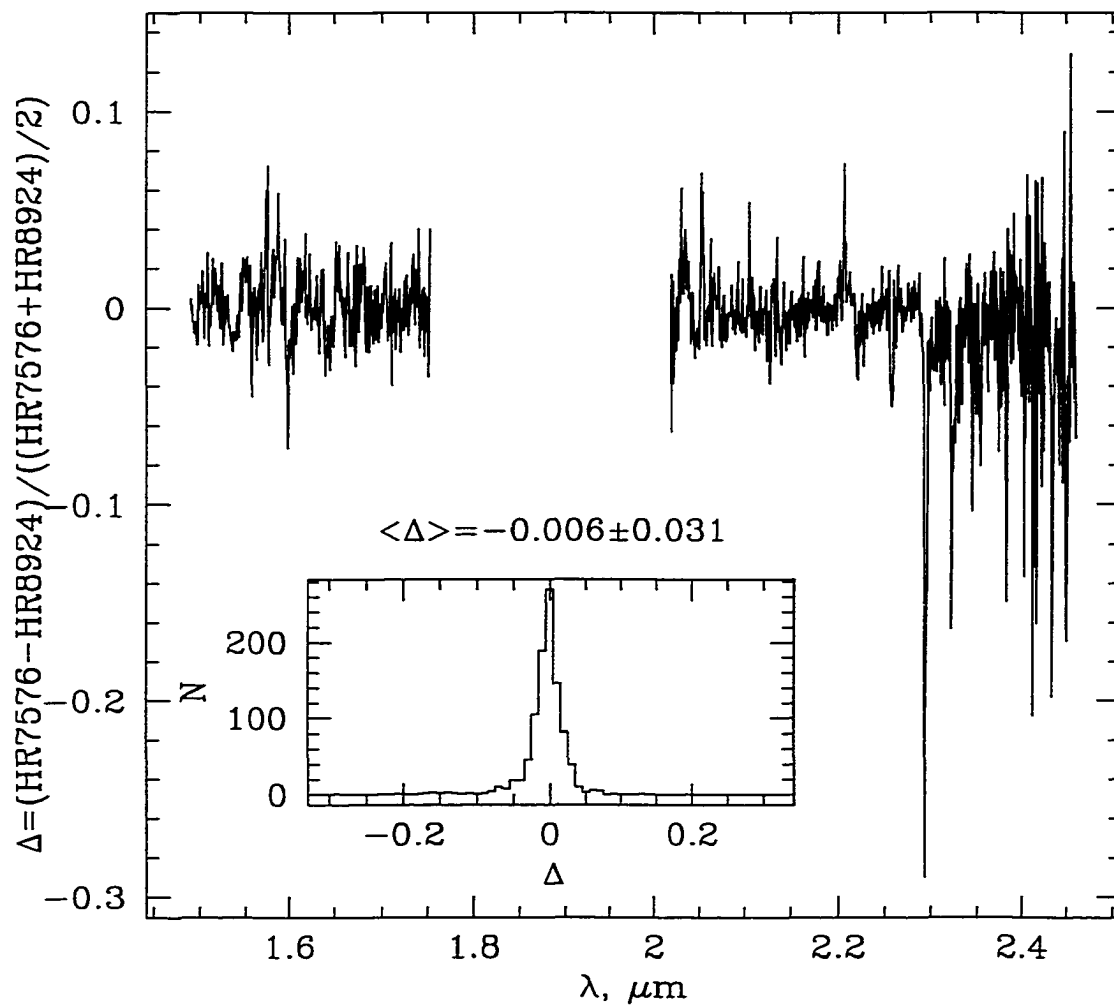


Figure 4.1 Difference between the spectra of two K3 III stars, normalized by the average of the two spectra. The inset shows the histogram of the differences. The means and the standard deviation of the distribution are also shown.

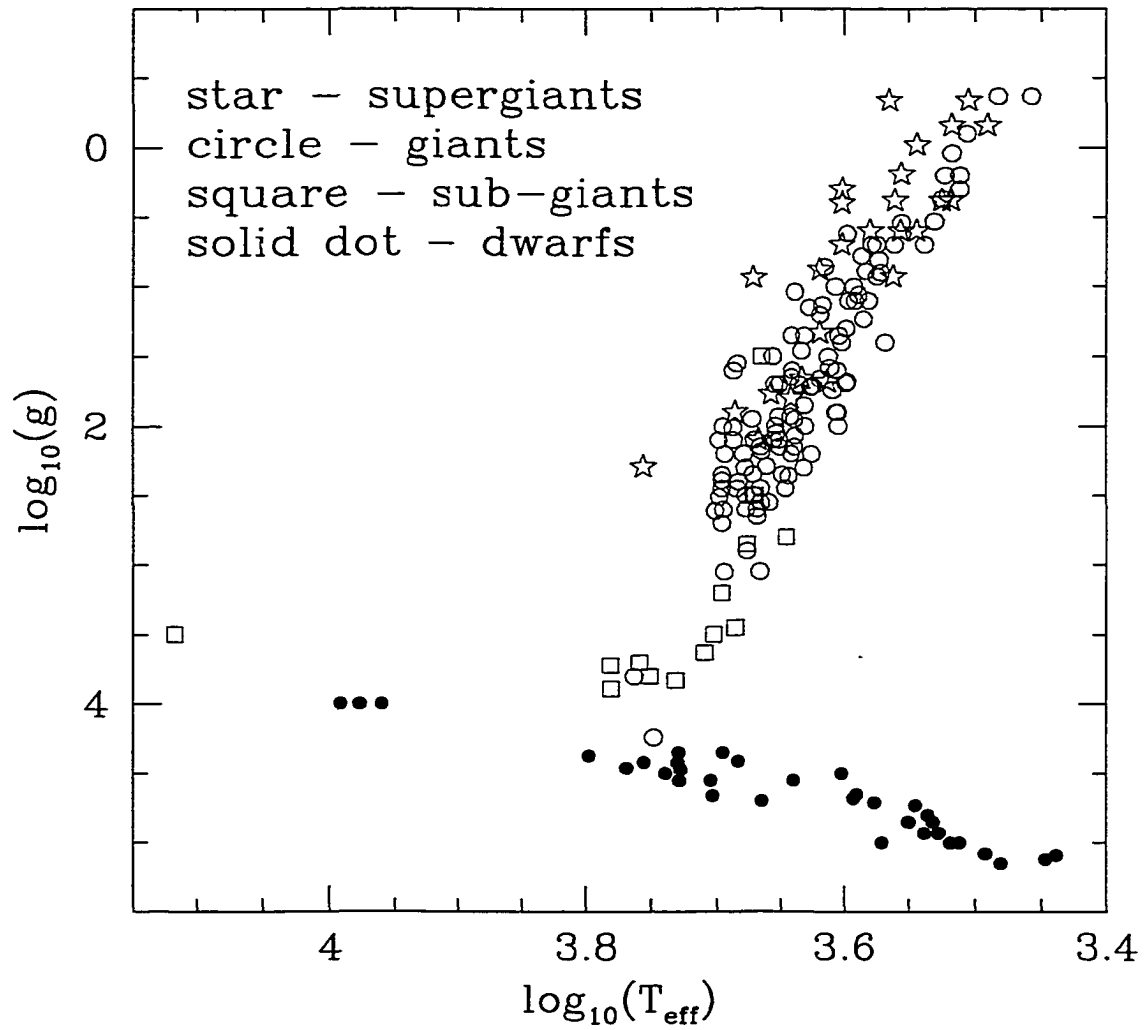


Figure 4.2 Distribution of the library stars on the $\log g$ versus T_{eff} plane.

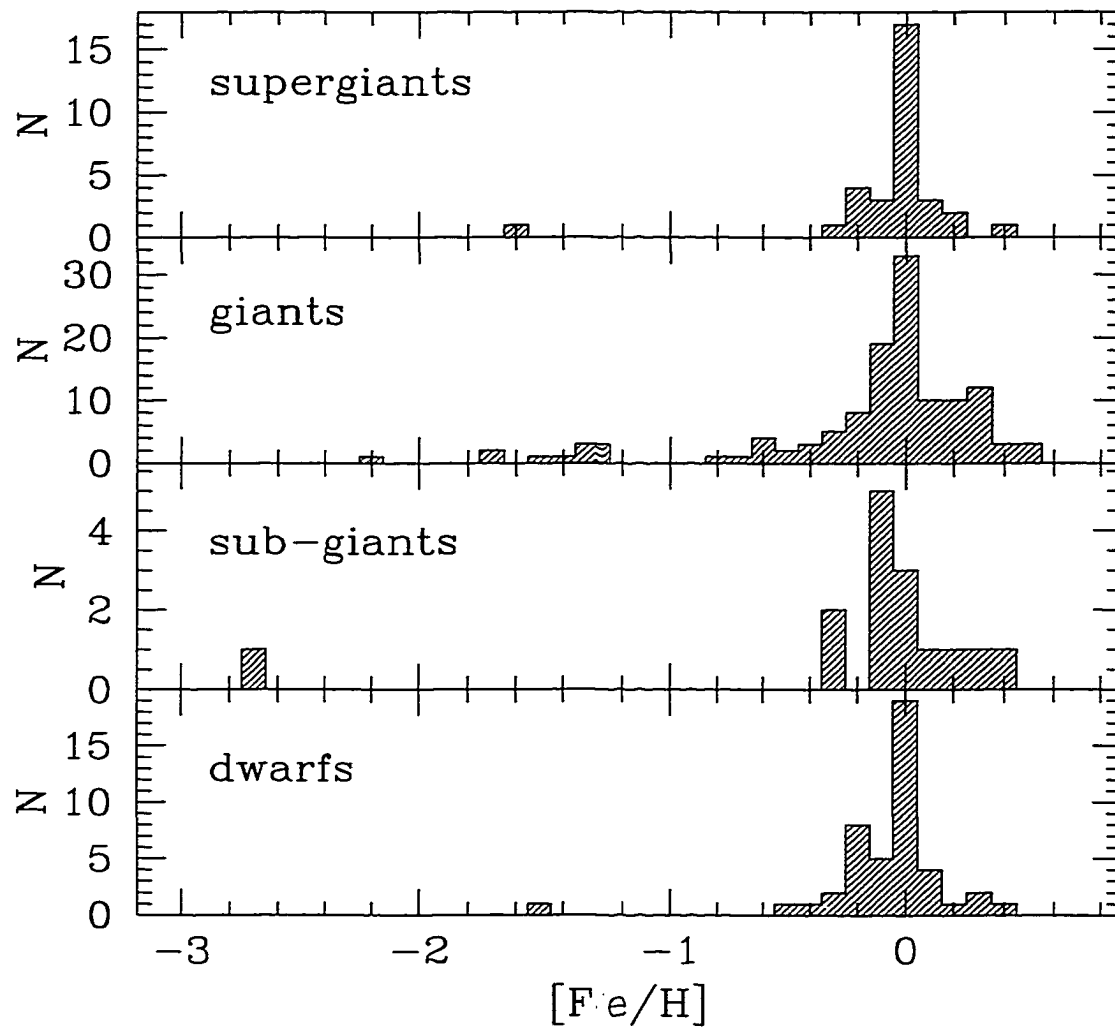


Figure 4.3 Metallicity distribution of stars in the library. The luminosity classes are indicated.

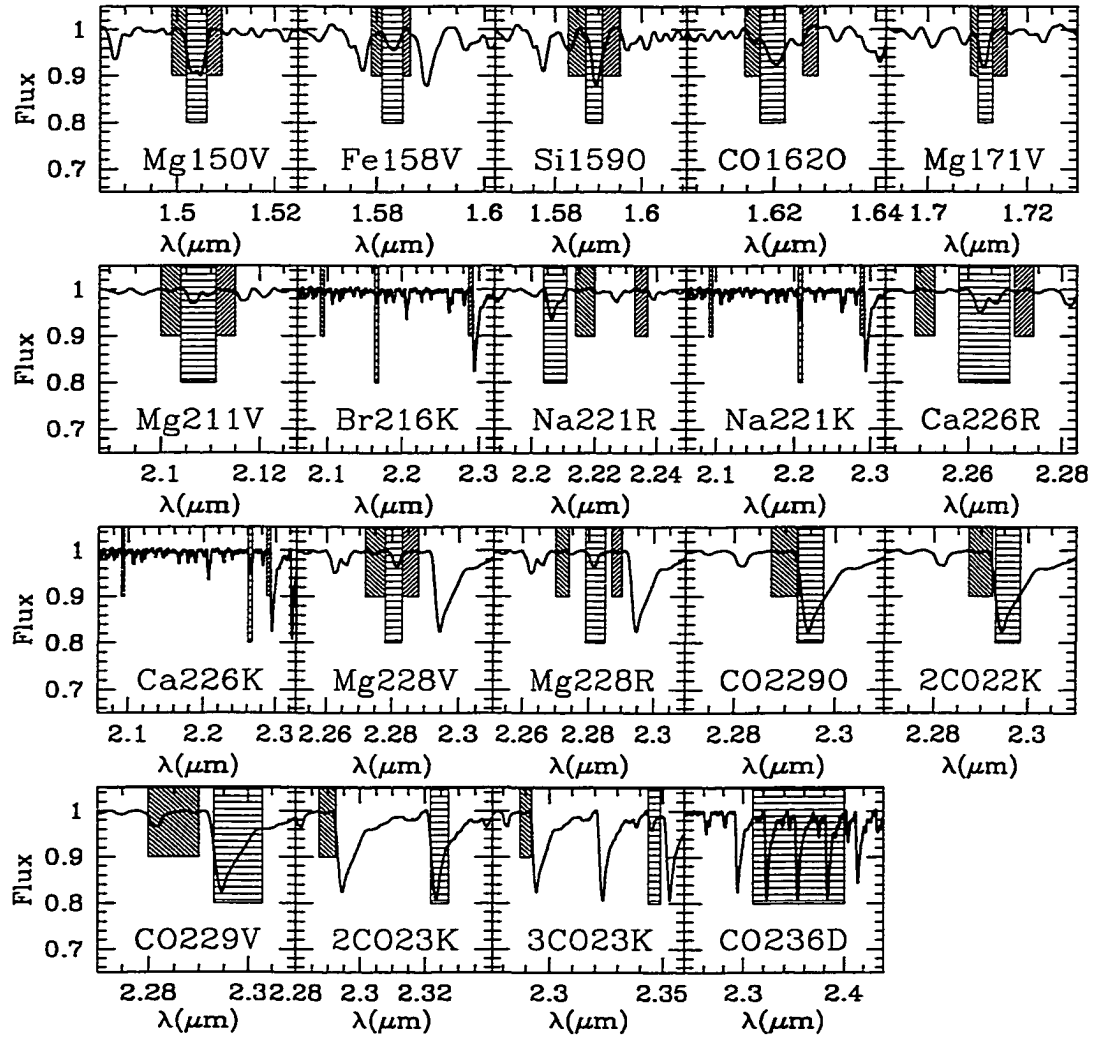


Figure 4.4 Definitions of the spectral indices. The horizontally shaded area represents the line band, and the diagonally shaded areas are the continuum bands. The spectrum is an average of all stars in the library. The last index is measured after continuum fit over the entire K window, and has no specific continuum band (see Doyon, Joseph & Wright 1994 for details).

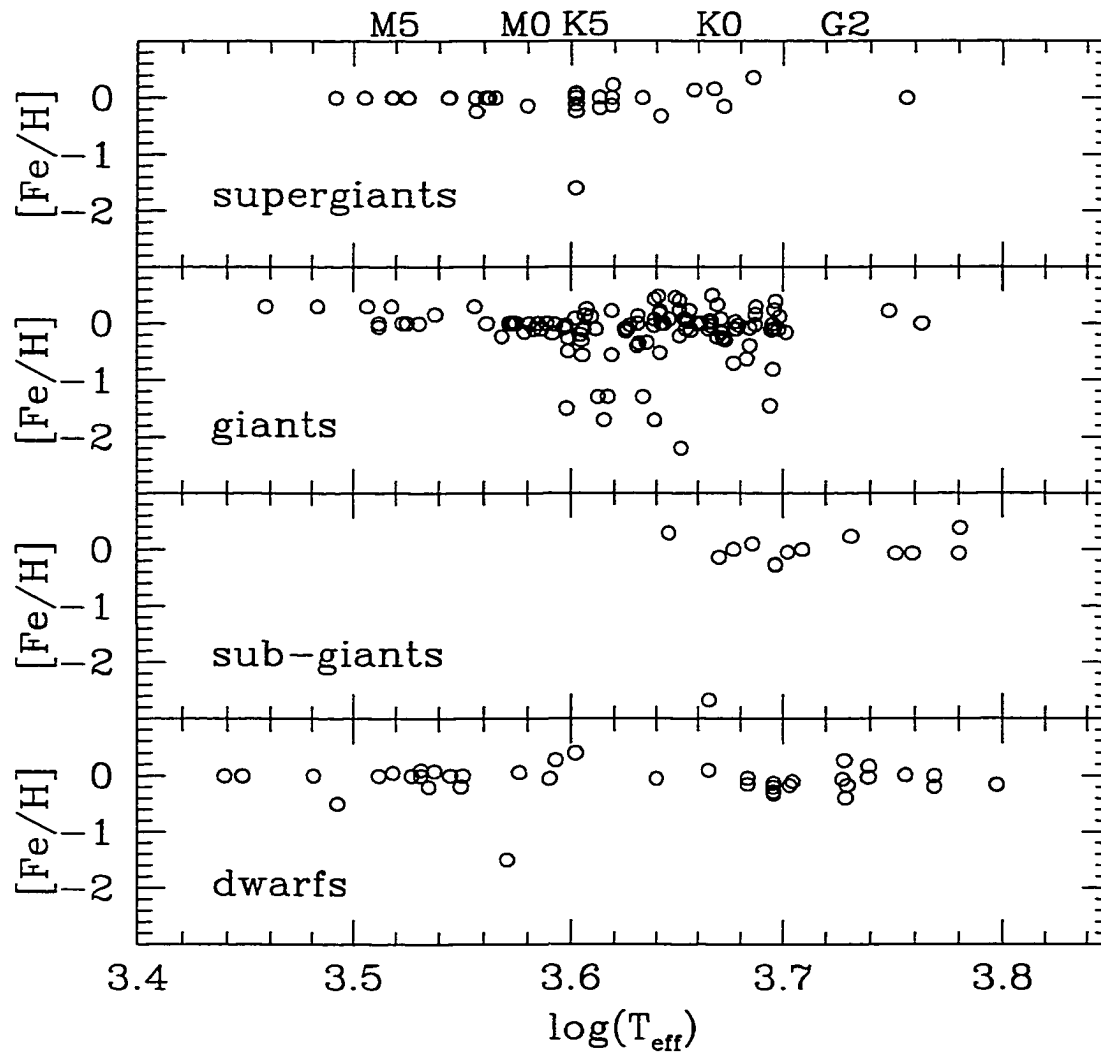


Figure 4.5 Metallicity of library stars versus the effective stellar temperature for different luminosity classes (indicated on each panel). The approximate positions of some spectral classes are shown on the top.

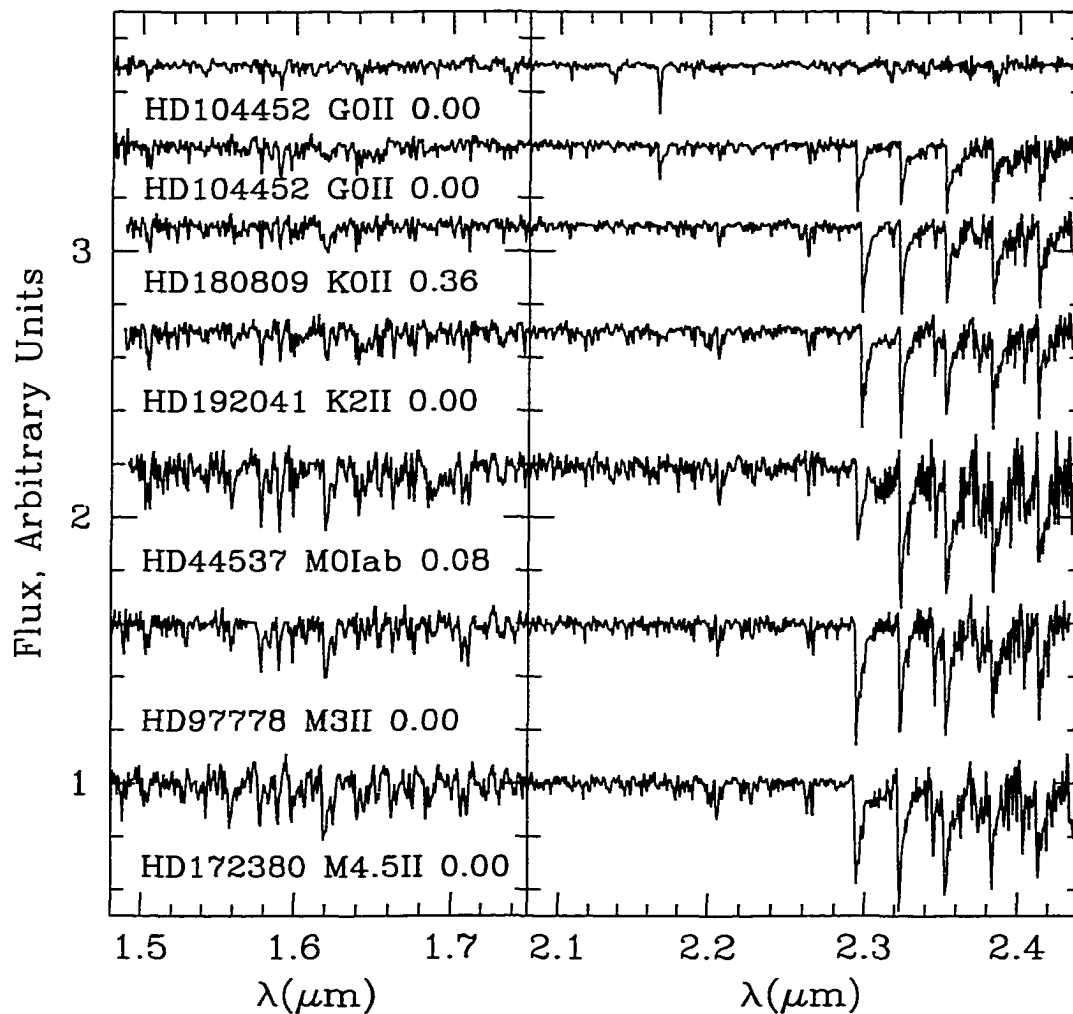


Figure 4.6 A subset of H and K spectra of supergiants. The names of the stars, spectral types, and $[\text{Fe}/\text{H}]$ are indicated. The spectra are continuum divided and shifted vertically for display purposes by adding (from bottom to top): 0.0, 0.6, 1.2, 1.7, 2.1, 2.4, and 2.7, i.e. for each spectrum, the flux interval from zero to the continuum level spans one arbitrary flux unit.

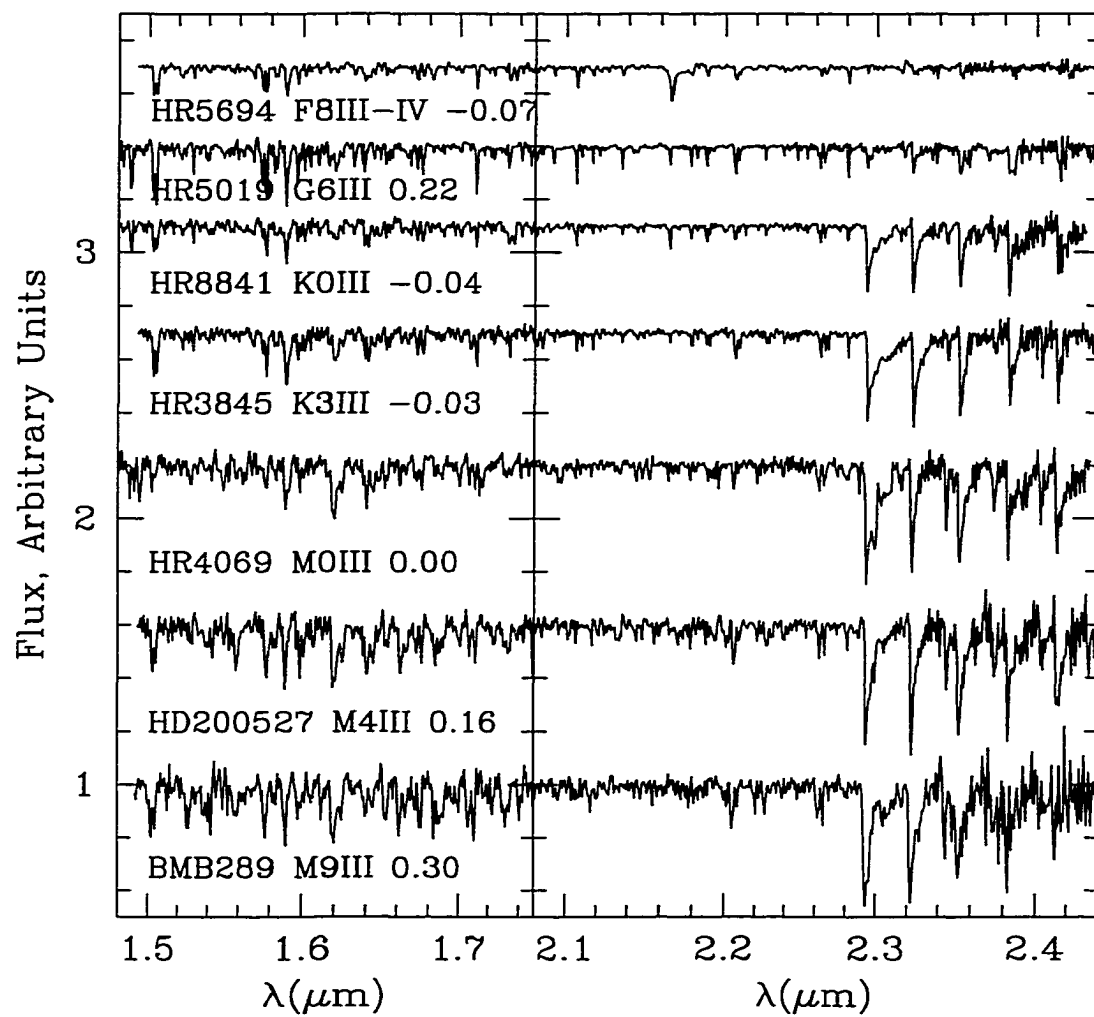


Figure 4.7 A subset of H and K spectra of giants. For the basic description see Figure 4.6.

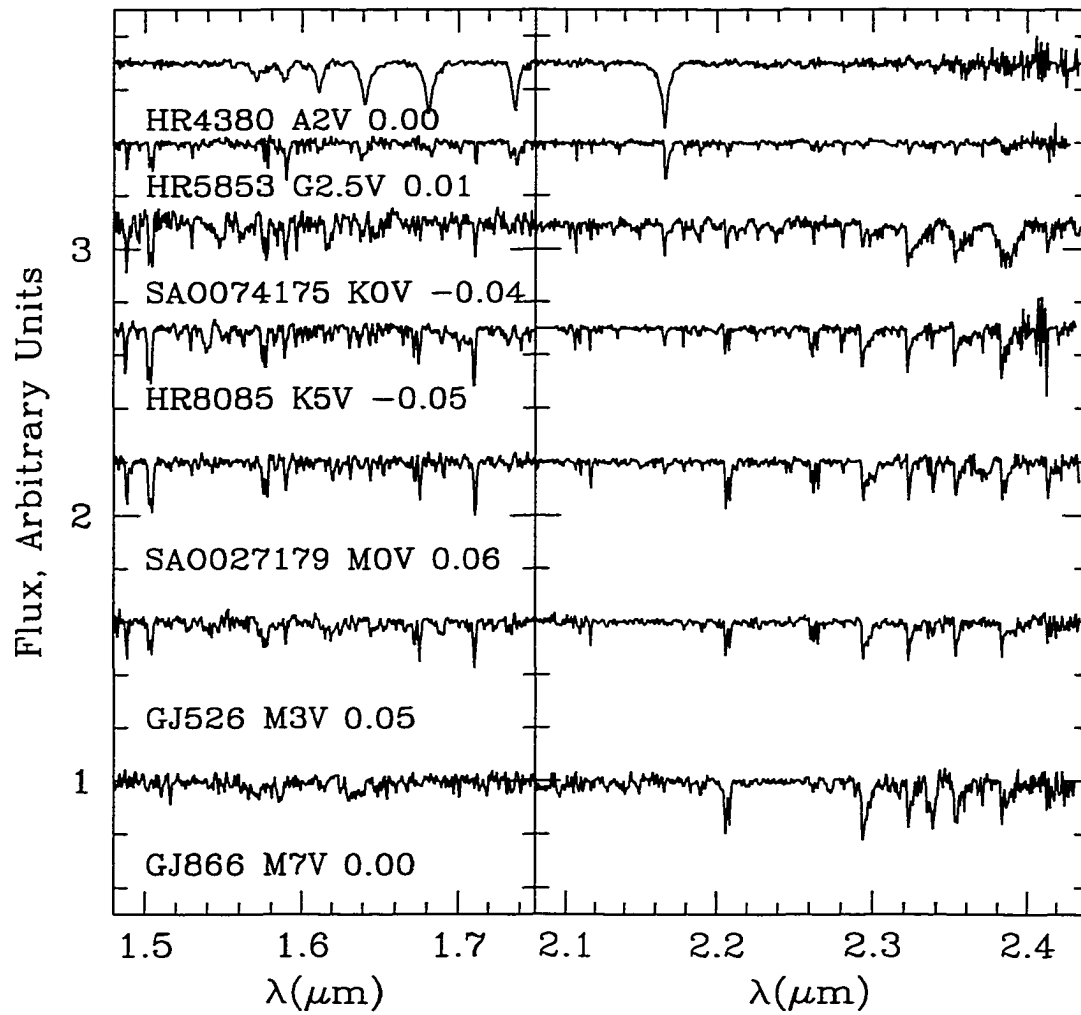


Figure 4.8 A subset of H and K spectra of dwarf. For the basic description see Figure 4.6.

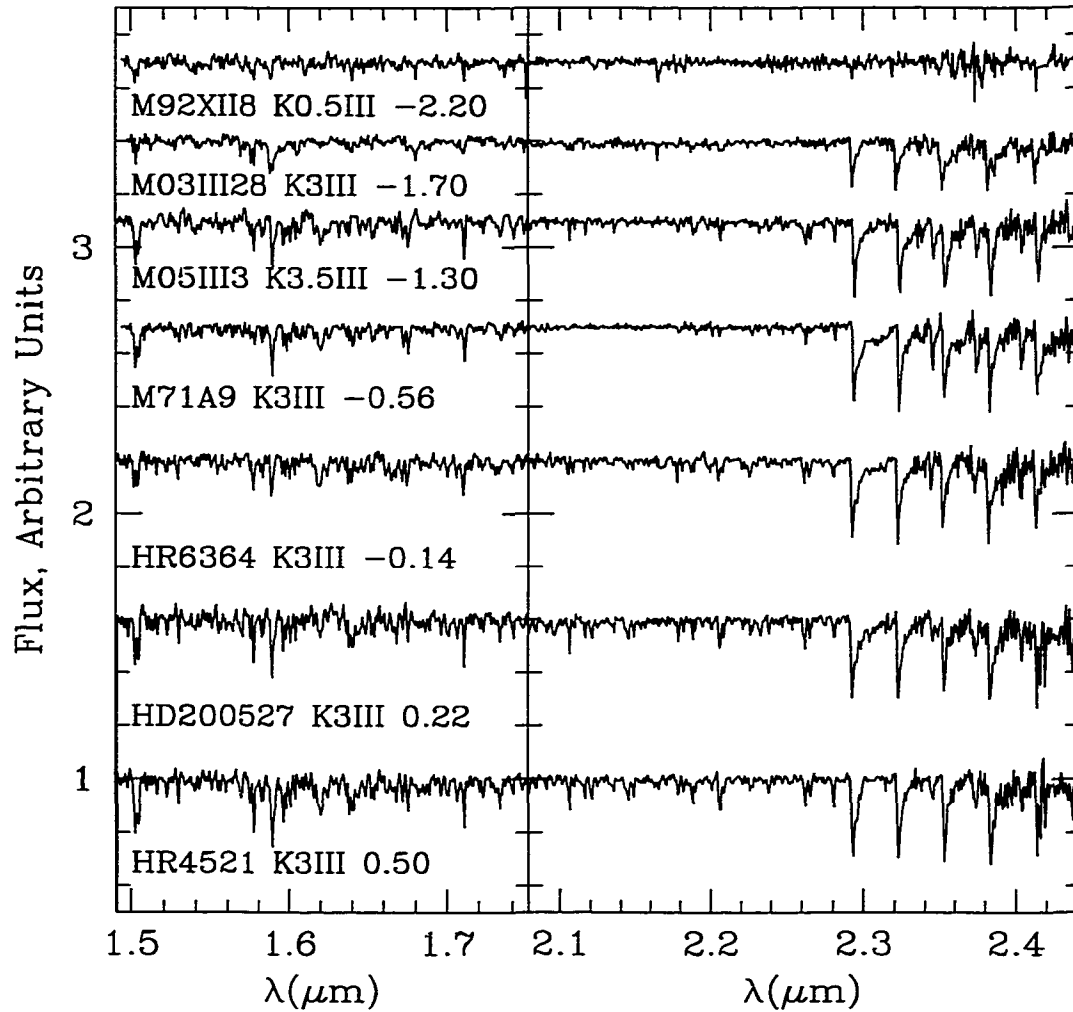


Figure 4.9 A selection of H and K spectra of K giants spanning a range of metallicities. For the basic description see Figure 4.6.

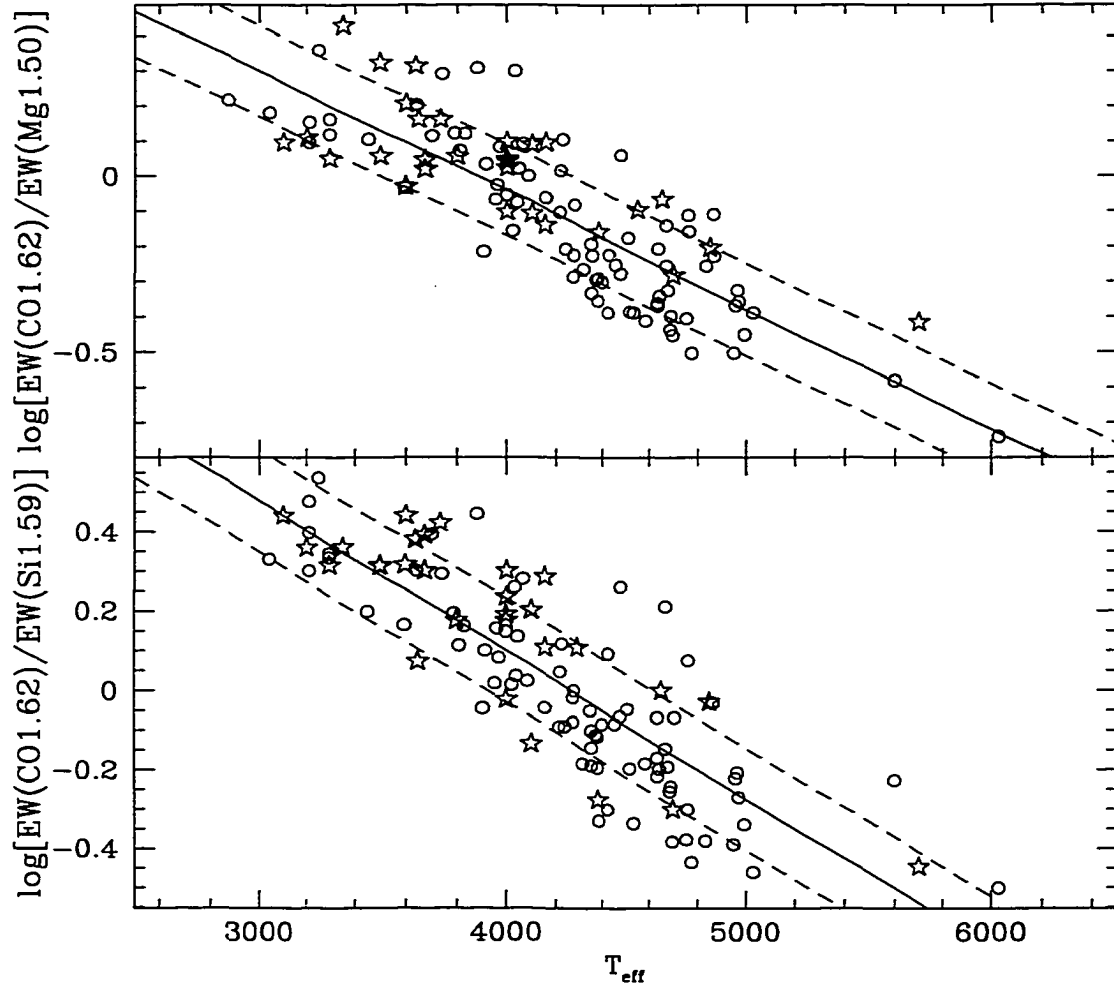


Figure 4.10 Line ratios as temperature indicators: $\log[\text{EW}(\text{CO1.62})/\text{EW}(\text{Mg1.50})]$ versus T_{eff} (top panel), and $\log[\text{EW}(\text{CO1.62})/\text{EW}(\text{Si1.59})]$ versus T_{eff} (bottom panel). Stars indicate supergiants and open circles are giants. The best linear fits are shown with solid lines and the zones of 1σ are indicated with dashed lines.

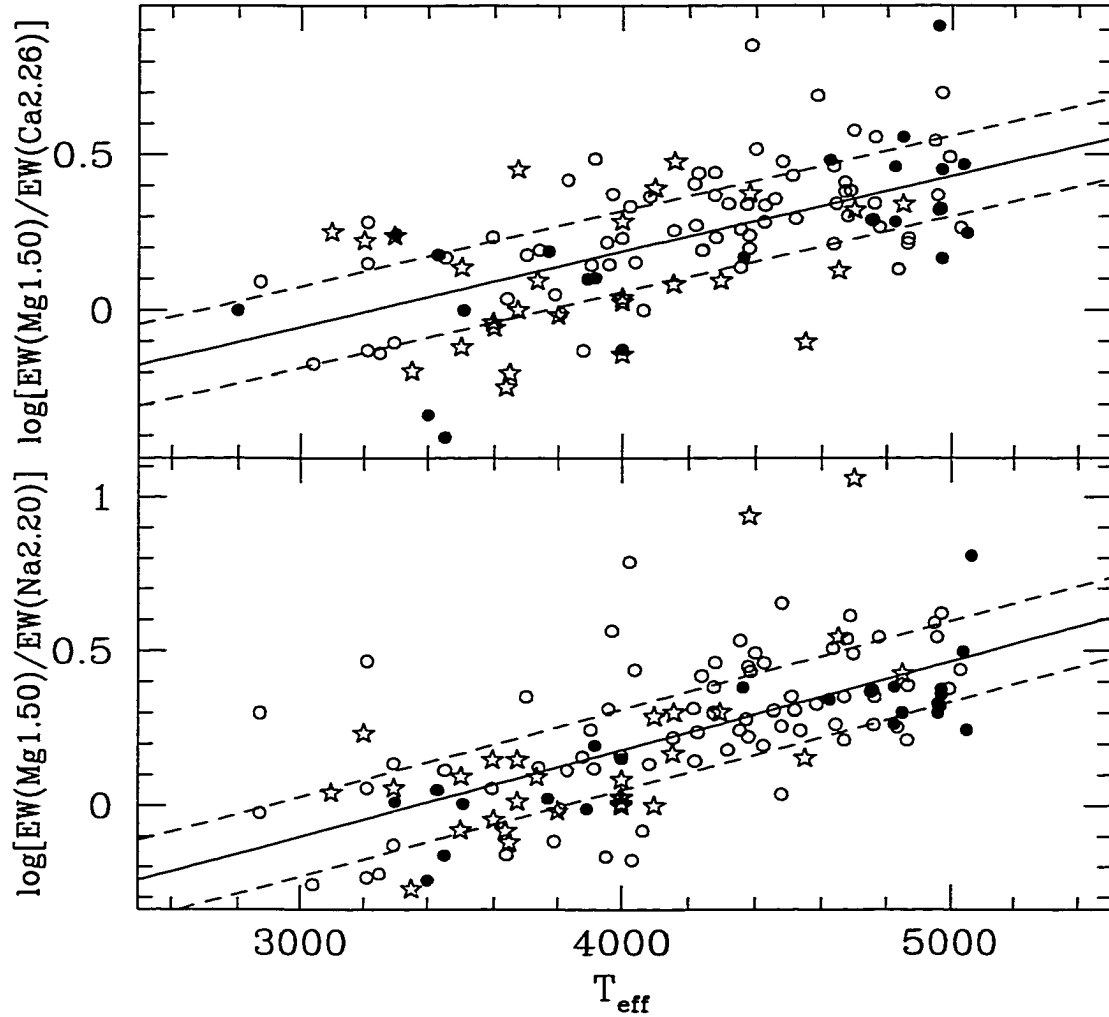


Figure 4.11 Line ratios as temperature indicators: $\log[\text{EW}(\text{CO}1.62)/\text{EW}(\text{Mg}1.50)]$ versus T_{eff} (top panel), and $\log[\text{EW}(\text{CO}1.62)/\text{EW}(\text{Si}1.59)]$ versus T_{eff} (bottom panel). Stars indicate supergiants and open circles are giants. The best linear fits are shown with solid lines and the zones of 1σ are indicated with dashed lines.

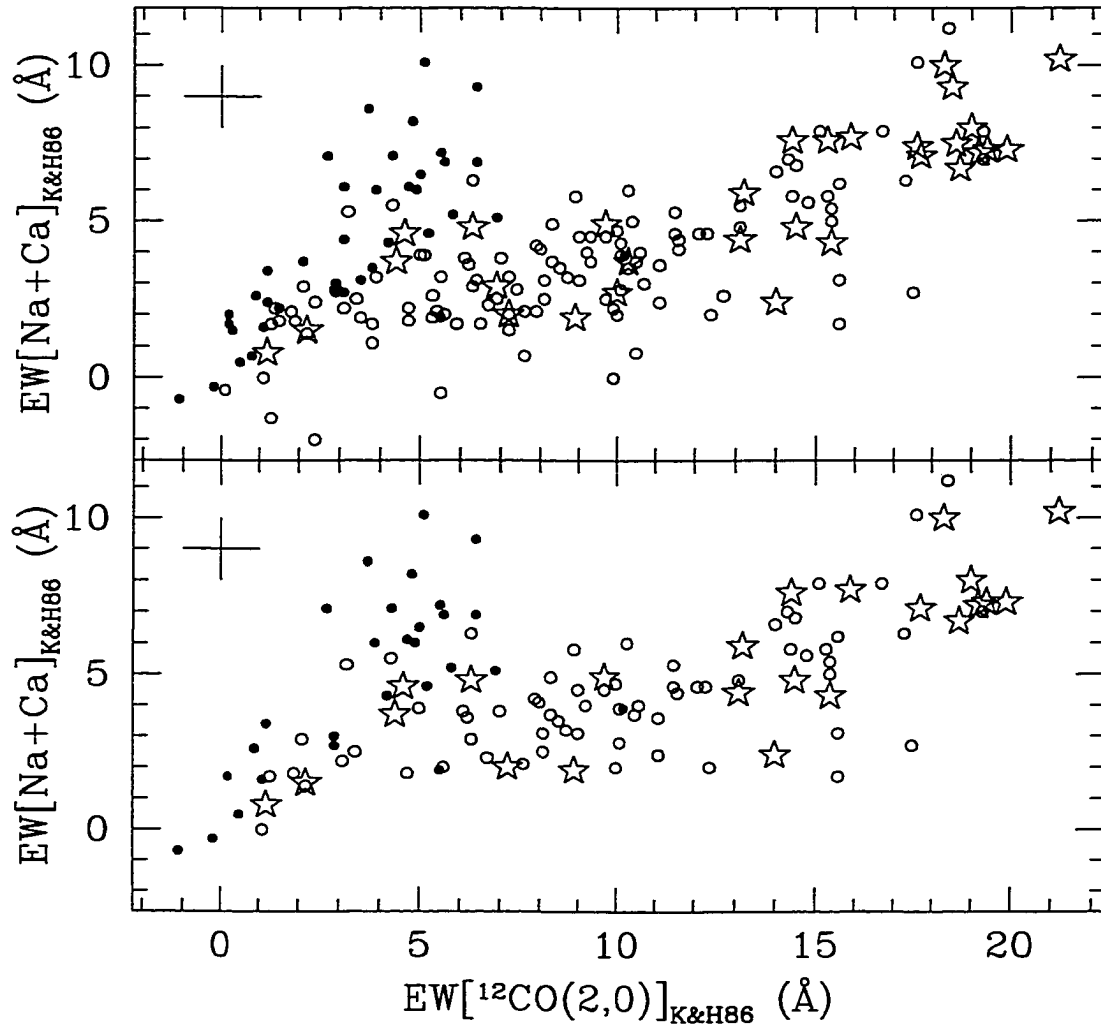


Figure 4.12 Spectral and luminosity class diagnostics, following Kleinmann & Hall (1986) - comparison of the strengths of NaI and CaI atomic features and the $2.29\mu\text{m}$ CO bandhead absorption. Stars indicate supergiants, circles are giants, and dots are dwarf stars. The typical observational uncertainties are shown. The top panel includes all stars, the bottom panel shows only stars with $[\text{Fe}/\text{H}] \geq -0.1$.

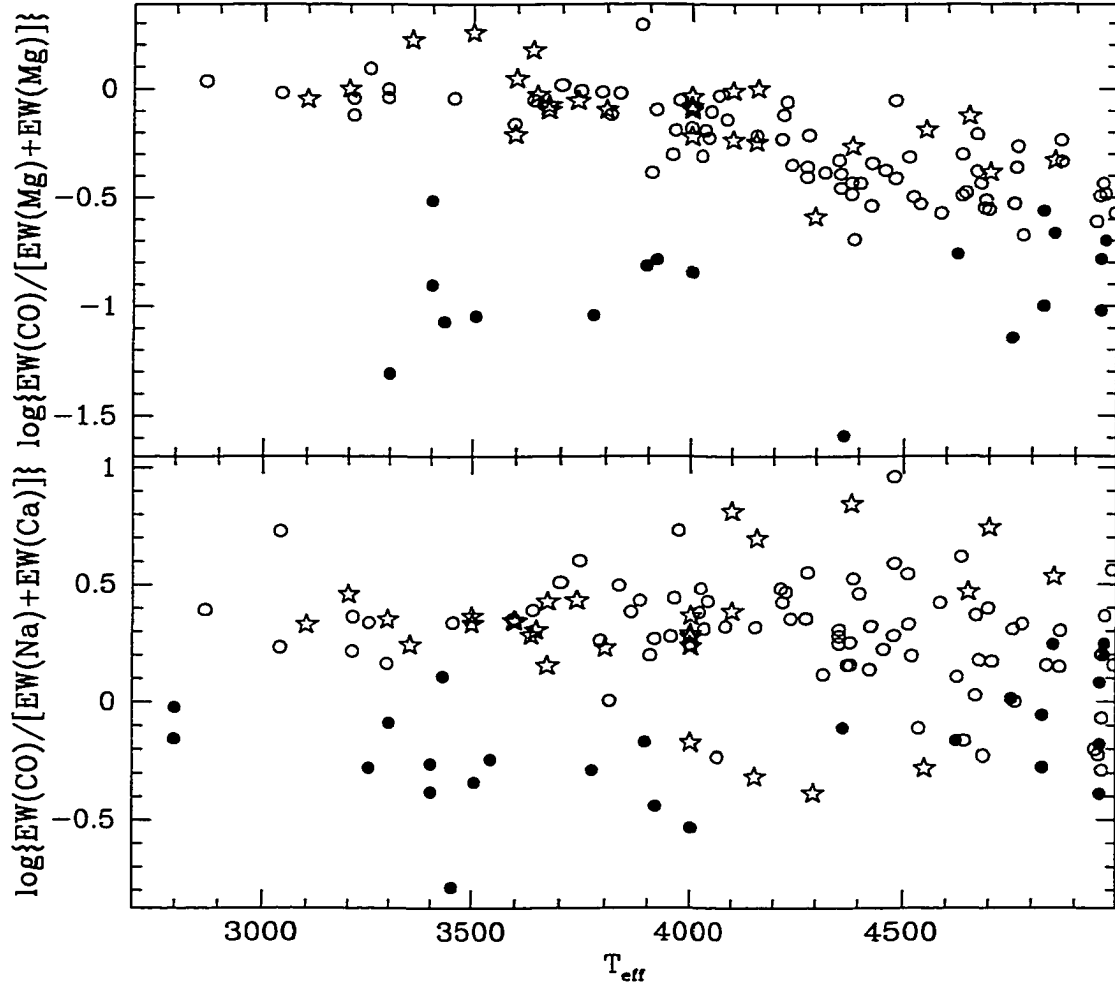


Figure 4.13 New spectral and luminosity class diagnostics. The top panel shows $\log\{\text{EW}(\text{CO}1.62)/[\text{EW}(\text{Mg}1.50)+\text{EW}(\text{Mg}1.71)]\}$ and the bottom $\log\{\text{EW}(\text{CO}2.29)/[\text{EW}(\text{Na}2.21)+\text{EW}(\text{Ca}2.26)]\}$ (following Ramírez et al. 1997) versus T_{eff} . Stars indicate supergiants, circles are giants, and dots are dwarf stars. Only stars with $[\text{Fe}/\text{H}] \geq -0.35$ are included.

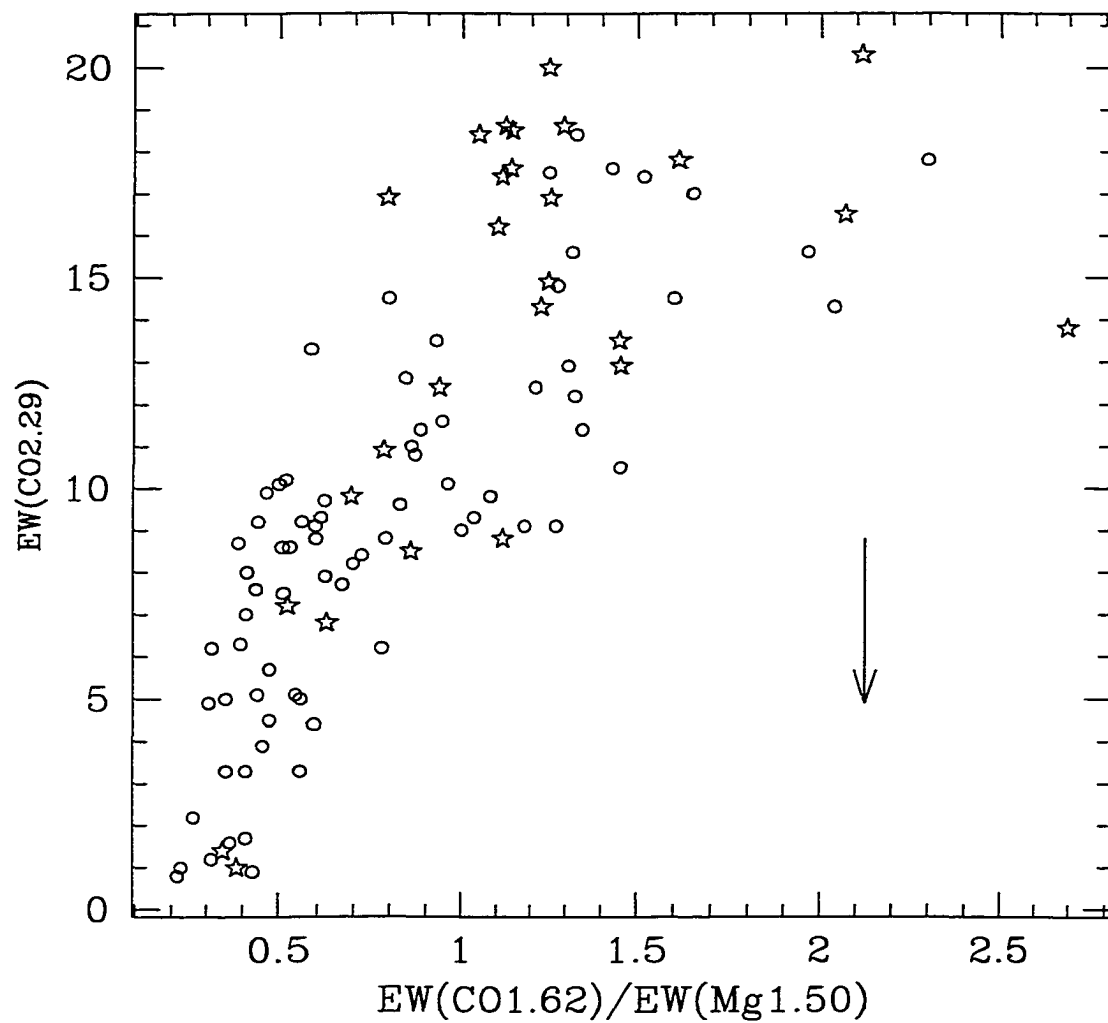


Figure 4.14 Dilution estimate technique, based on the dilution-sensitive CO $2.29\mu\text{m}$ versus the temperature sensitive $EW(CO1.62)/EW(Mg1.50)$ ratio. Stars are supergiants, and open circles are giants. The arrow indicates the effect of dilution by a featureless continuum source.

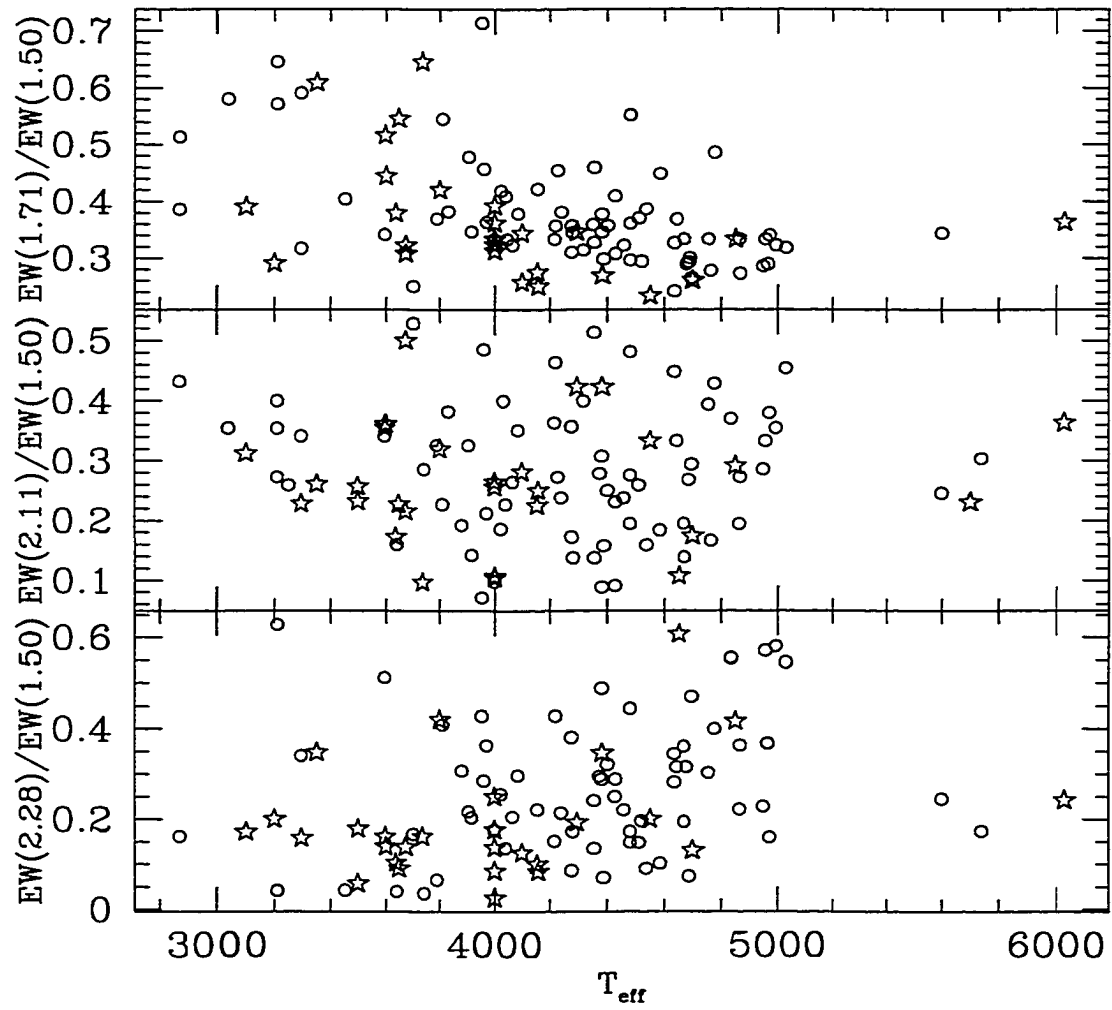


Figure 4.15 Behavior of the measured MgI line ratios. Stars are supergiants and open circles are giants.

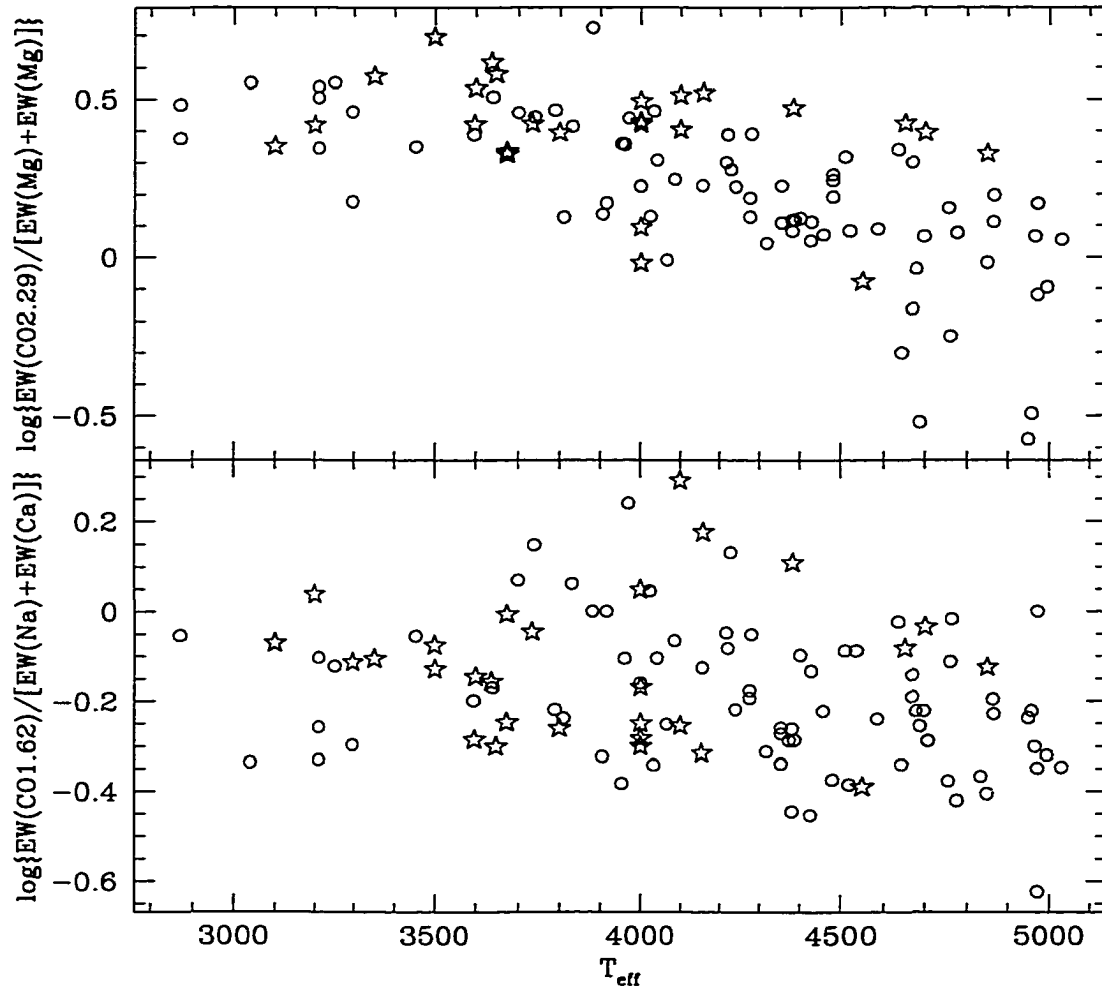


Figure 4.16 Behavior of the measured CO-to-metal line ratios. The top panel shows $\log\{EW(CO2.29)/[EW(Mg1.50)+EW(Mg1.71)]\}$ and the bottom panel shows $\log\{EW(CO1.62)/[EW(Na2.21)+EW(Ca2.26)]\}$. Stars are supergiants and open circles are giants.

5. NEAR-INFRARED EVOLUTIONARY POPULATION SYNTHESIS

5.1. Introduction

The spectral evolutionary population synthesis was turned into a powerful tool for stellar population studies over the last decade by the efforts of a number of authors (Bruzual & Charlot 1993; Worthey 1994; Vazdekis 1999; Leitherer et al. 1999, among others). This extensive work has produced a better understanding of the modeling limitations. It has been shown that the models can only answer specific and well defined questions.

There has been an extensive effort to expand the population synthesis to the near infrared region (e.g. Rieke et al. 1980). Attempts to incorporate the infrared region into the optical spectral models (e.g. Bruzual & Charlot 1993) have failed to achieve satisfactory results because the synthetic stellar atmospheres (usually from Kurucz 1994; see also Allard, Hauschildt & Schwenke 2000 and the references therein) lacked the difficult to model broad water molecule that accounts for most of the opacity in the near infrared. Besides less extinction and reddening, the infrared offered a number of useful stellar spectral features that could serve as reliable indicators of the parameters of unresolved stellar populations (Chapter 4).

The advantages of the infrared spectral region are most emphasized in starburst galaxies where the typical extinction is $A_V = 5$ mag, and can easily reach

and exceed $A_V = 20 - 30$ mag for ultra luminous infrared galaxies like Arp 220 (Murphy et al. 2000).

The first serious attempt to model the infrared wide filter bands and the CO spectral index, among other observables, specifically for this class of objects was carried out by Rieke et al. (1980), and was expanded later by Rieke et al. (1993), McLeod et al. (1993), Engelbracht et al. (1998), Alonso-Herrero et al. (2000), and Alonso-Herrero et al. (2001). The model was extremely successful in constraining the age of the stellar population, based on the number of ionizing photons, determined from the strength of the hydrogen recombination lines in emission. These works supported a hypothesis for top-heavy initial mass function in regions of active star formation. A similar model was produced also by Doyon, Joseph & Wright (1994a).

The spectral synthesis model of Lançon & Rocca-Volmerange (1996) was the first based on an empirical stellar library (Lançon & Rocca-Volmerange 1992), spanning the entire 1.4-2.5 μm wavelength range. However, their spectra suffered from a relatively low spectral resolution (only ~ 500) and signal-to-noise ratio, making it useful only for modeling of strong molecular bands.

Mayya (1997) investigated the utility of red supergiant spectral features as age indicators in starbursts by means of a population synthesis model based on 26 stellar spectra from Kleinmann & Hall (1986) library. However, this library includes only stars with near solar metallicity. Therefore, the metallicity effects in his CO index versus age plot has to be treated with caution, because they are due entirely to the differences in evolutionary tracks and not in the stellar atmospheres.

Origlia et al. (1999) and (Leitherer et al. 1999) included in the existing, starburst-oriented population model Starburst99 SiII at 1.59 μm , and CO bands at

1.62 and 2.29 μm . No other features were considered. The model used the synthetic stellar spectra calculated by Origlia, Moorwood & Oliva (1993), with spectral resolution $R \sim 1500$. The theoretical predictions failed to match the observations satisfactorily, probably because of the difficult treatment of the non-adiabatic convection that takes place in red supergiants. This problem results in wrong effective temperatures and lifetimes during the reddest phases of stellar evolution. To remedy this, the authors had to adjust the red supergiant parameters. A comparison with observations suggest that the temperature of the redmost stars has to be lower than 4000K, and their lifetime has to be extended by 30 – 50%. The near infrared population studies have proved a critical test for the post-main sequence stellar evolution - this wavelength range is dominated to a higher degree by the coolest stars than any bluer spectral region.

In the recent years the KPNO has undertaken a large effort to assemble a set of J, H, and K spectral libraries (Wallace et al. 2000, Meyer et al. 1998, and Wallace & Hinkle 1997, respectively). The goal was to provide high quality, uniform data. As soon as they became available, a number of teams incorporated them into various evolutionary population synthesis models. Gilbert & Graham (2000) simply convolved the H and K band spectra with the Starburst99 code output (Leitherer et al. 1999), and fitted the observed spectra of super star clusters in NGC 1569.

A similar approach was adopted by Schreiber (1998) to analyse 3D spectra of M 82. The evolutionary synthesis code STARS (Kovo, Sternberg & Alexander 2001) was used in this case. The emission line spectrum was added with CLOUDY (Ferland 1996). A special extension to the Geneva evolutionary tracks (e.g. Meynet et al. 1994) was necessary to include the thermally pulsating asymptotic giant branch stars. This addition is equivalent to the lowering of the effective stellar

temperature applied by Origlia et al. (1999). The model output was compared to the data, confirmed the top-heavy initial mass function (e.g. Rieke et al. 1993).

Both Gilbert & Graham (2000) and Schreiber (1998) can not address the question of the metal content of starburst galaxies by means of stellar metal absorption features, because of the sample selection of the KPNO libraries. The sample stars were selected to have no large deviations from the solar abundance.

We (Chapter 4) assembled the first near infrared spectral library to cover a range of metallicity, suitable for stellar population synthesis. The library includes H and K band spectra of 218 stars, with spectral resolution $R \sim 2000 - 3000$, and with typical signal-to-noise ratios $S/N = 50 - 100$. Our goal is to incorporate this library into the spectral synthesis code Starburst99 and to explore the parametric space, in particular trying to constrain directly the stellar abundance of starburst galaxies by means of metal absorption features.

5.2. Short Description of Starburst99

Typically the population models are divided into two large groups. The first one, both historically and logically, is the statistical population synthesis. It involves varying the relative contribution from a number of stellar types to match the observed color or spectra of stellar systems. The major difficulty of this technique is the multiplicity of the possible solutions. Fortunately, as the understanding of the physics of stellar interiors has improved, a number of additional constraints have become available. This led to the development of the so called evolutionary population synthesis. Unlike the other method, it uses the knowledge of the stellar evolution and stellar atmospheres, derived from first principles and tested on single age systems (open or globular clusters), and binary stars. Even though the

evolutionary population synthesis never completely solved the the non-uniqueness problem, it has helped greatly to understand the origin of the problem and the natural limitations of the population synthesis technique.

The first step of the evolutionary population synthesis is to create a synthetic Hertzsprung-Russell diagram (HRD, thereafter), using theoretical stellar evolutionary tracks, and adopting an initial mass function. The next step is to convolve this diagram with observable parameters - just colors, or spectra, or a combination of both. These observables can be either theoretically or observationally derived. Finally, we have to sum up the fluxes of the entire synthetic population to obtain the total parameters, and to compare them to the observed parameters of real objects.

Starburst99 belongs to the class of evolutionary population synthesis models. A grid of models calculated with the same code was reported in Leitherer & Heckman (1995) but the fast development of the stellar modeling and the pressure for a more convenient and user friendly distribution led to a new release (Leitherer et al. 1999) which made the code public.

The model is based on the latest stellar evolutionary track by the Geneva group, with standard and enhanced mass loss (Schaller et al. 1992; Schaerer et al. 1993a, 1993b; Charbonnel et al. 1993; Meynet et al. 1994). Binary evolution was not taken into account. The available metallicities are: $Z=0.040$, $0.020 (= Z_{\odot})$, 0.008 , 0.004 , and 0.001 . Here Z is the mass fraction of the metals, and all elements heavier than helium are considered "metals". The abundance ratios are fixed and independent of Z .

The possible star formation histories are limited to two cases - an instantaneous burst and a continuous star formation at a constant rate. The initial mass function

is a power law, governed by three parameters: slope, lower and upper mass limits.

The stellar atmosphere models for the optical spectral region were from Lejeune, Cuisinier, & Buser (1997). They are organized in a homogeneous equally spaced grid, covering the entire HRD. Some interpolation was required to cover all metallicities. The UV spectra were obtained from the *IUE* and *HST* archives.

The near infrared part of the stellar spectra includes only three stellar features: the CO bands at 1.62 and 2.29 μm and SiI line at 1.59 μm , based on stellar atmosphere models of Origlia, Moorwood & Oliva (1993) and incorporated in Starburst99 by Origlia et al. (1999).

The model starts by generating a stellar population distributed along the zero age main sequence according to the adopted initial mass function. Then the position of the star on the HRD is determined according the age of the burst and the evolutionary track for the given stellar mass. The tracks also provide the stellar surface gravity $\log g$ and effective temperature T_{eff} at any given moment. Together with the metal abundance, $\log g$ and T_{eff} are used to select the appropriate stellar atmosphere or UV spectrum. The contributions of all stars in the burst are added together, weighted by their intrinsic luminosities and the initial mass function. Finally, the nebular spectrum is calculated as case B recombination, given the stellar ionizing UV radiation.

The more important model outputs include the total UV, optical, and infrared spectra, the broad band colors (produced by convolving the spectra with the filter transmission curves), the number of ionizing photons, supernova rate, etc. The model could be evolved up to Hubble time but the post main sequence tracks and lifetimes become increasingly less reliable after 30 Myr, and the typical ages of powerful starbursts are 10-30 Myr. Additional reasons to confine the

model to shorter burst lifetimes is the lack of self-enrichment. The model is not self-consistent, i.e. the metallicity remains the same during a burst, even for the continuous bursts. A more detailed description of Starburst99 is given in Leitherer et al. (1999).

5.3. Modifying Starburst99

Our modifications to Starburst99 were concerned exclusively with the output of the code. We added a set of subroutines that took the metallicity, $\log g$, and T_{eff} of each star on the HRD and found the best matching star from the infrared spectral library. Unfortunately, the stellar library neither offers the convenience of orderly theoretical model atmospheres, equally spaced over the entire parametric space (Figure 5.1), nor does it cover completely the entire parametric space of interest. Also, not all stars have complete H and K band spectra. We tried a number of different algorithms to determine the closest star. The scarcity of the low metallicity stars proved to be the biggest obstacle.

The first step was to separate the library stars in metallicity bins, corresponding to the metal abundance of the stellar evolutionary tracks. The bins, their limits, and the number of H and K spectra in each one of them are given in Table 5.1. The $Z=0.004$ tracks have to be omitted for the lack of stellar spectra.

The second step was to calculate the deviations along both $\log g$ and T_{eff} axes between the point on the theoretical HRD and each star in the selected metallicity bin. However, the different units of these parameters would lead to a rather uneven representation into the total deviation. Therefore, we had to apply some renormalization, to weight the deviations along the two axis equally.

The stars in the library were selected to span a range of $\log g$ and a range of T_{eff}

that would correspond to variation from strongest spectral features in the infrared, to their almost complete disappearance. Indeed, the molecular and low-excitation atomic lines are stronger in the cool stars but become almost undetectable in G stars. Molecules are destroyed by the higher temperature and pressure in the atmospheres of hotter stars, and the dominant fraction of metals turn from neutral to higher ionization states. Similar change occurs along the surface gravity axis, where the supergiants with extended atmospheres have strongest features, and the main sequence stars have very weak features.

Therefore, we normalized the $\log g$ and T_{eff} deviations by the span of the library stars in $\log g$ and T_{eff} , so the maximum deviation in either parameter can not exceed unity. Then we added the two deviations in quadrature, and minimized the result to determine the "closest" library star. The normalization ensured that the surface gravity and effective temperature have equal weights in finding the best matching stellar spectra.

We experimented with changing the normalization by up to a factor of two, giving precedence of one or the other parameter, still keeping the search inside the corresponding metallicity bin boundaries. The final synthetic spectrum did not change significantly. In fact, for low metallicity ($Z=0.001$) it did not change at all, because the library stars are so few and the selected "closest" stellar spectra were the same, independent of the weighting.

For effective temperatures outside the library coverage (hotter than $T_{\text{eff}} = 8000$ K) we assumed that the stellar spectra are just black bodies with the corresponding temperature. While this is a good assumption for neutral metal and molecular features, it is not for the hydrogen lines. Therefore, we refrained from hydrogen line analysis.

Origlia et al. (1999) suggested modifications to the Geneva evolutionary tracks (see Section 5.1), to match better the observations. However, a more recent test (Origlia & Oliva 2000), with improved evolutionary tracks from Bertelli et al. (1994) clearly demonstrated that significant effects occur only after $\gtrsim 60$ Myr, well outside the age interval we consider.

5.4. Spectral Measurements

Starburst99 has built in tools to measure the strength of the spectral features. However, we preferred to keep the output spectra at the spectral resolution of the library, and then carry out the measurements within *IRAF*, using the *sband* task. Since the measurements of the observed galaxy spectra were made with *IRAF*, this minimized possible systematic errors.

We measured 17 indices of 12 spectral features, as summarized in Chapter 4. These were chosen after a visual inspection of the near infrared spectral atlas of starburst galaxies (Engelbracht 1997), and included only the most prominent features that can be measured reliably. There are multiple definitions for some of the features, to facilitate direct comparison with other works. We omitted the Br γ absorption since in starburst galaxies it is filled in with gas emission.

Finally, we derived velocity dispersion corrections for each spectral index to account for the rigid limits of the spectral index bandpasses, by smoothing the synthetic spectra and measuring the equivalent widths of the smoothed spectra. We fitted the same relation between the real equivalent width $EW_\lambda(\text{true})$ and the measured equivalent width $EW_\lambda(\text{observed})$ as Origlia & Oliva (2000 and the references therein):

$$EW_\lambda(\text{true}) \simeq EW_\lambda(\text{observed}) \times [1 + a \times (\sigma - 180)] \quad (5.1)$$

where σ is the intrinsic velocity dispersion in km s^{-1} . The fitting coefficient a for each index is given in Table 5.2.

5.5. Results

5.5.1. Evolution of the Stellar Absorption Features

Time and metallicity sequences of our synthesis infrared spectra are shown in Figure 5.2. The time evolution of the prominent infrared absorption features is shown in Figures 5.3 to 5.6. All models represent single bursts of star formation, with Salpeter initial mass function. The ages span a range from 1 to 30 Myr, with 1 Myr interval for 1-10 Myr ages, and 2 Myr interval for older bursts. We adopted for all models an intrinsic velocity dispersion of 200 km s^{-1} . The measurements are presented in Table 5.3.

Not surprisingly, the equivalent widths of all features are negligible during the first few Myr. Hot blue supergiants from the top of the main sequence dominate the total spectrum of the starburst at that time. Their effective temperature is too high to allow the presence of any neutral atoms or molecules. However, after only 4-6 Myr, the first red supergiants start to appear. The spectrum of the burst changes dramatically over the next 1-2 Myr. Neutral atoms and molecules are abundant in the extended atmospheres of cool stars, which emit most of their flux in the infrared. Consequently the total spectra become rich with features.

The indices in our more metal rich ($[\text{Fe}/\text{H}] = -0.4$ to 0.0) synthetic spectra show a well developed peak at 8-12 Myr, while the supergiants dominate the total spectra. The line or band strengths then slowly subside to more moderate values. Notably, the most metal poor model ($[\text{Fe}/\text{H}] = -1.3$) lacks the peak. We attribute this to the complete absence of metal poor supergiants in our library. Instead, we

substituted for them with giants. One way to estimate the degree of this effect is to increase the equivalent width during the supergiant dominated stage for the $[\text{Fe}/\text{H}] = -1.3$ model by a factor of 2 or 3. The differences between solar metallicity model, and the metal poor model predictions are so large, that even the increase of the indices associated with the red supergiant phase can not bring the metal poor model predictions up to the solar metallicity values.

Among the MgI features, MgI at $2.28\ \mu\text{m}$ proves to be the most difficult to model (Figures 5.3, and 5.6), both because of its smaller strength compared to the others, and because it lies very close to the CO band head at $2.29\ \mu\text{m}$, which influences the long wavelength continuum.

Comparison of the two systems of definitions for the NaI $2.21\ \mu\text{m}$ and Ca $2.26\ \mu\text{m}$ (Figures 5.4) suggests that the definition of Ramírez et al. (1997) is preferable. It produces a larger amplitude of the indices. The indices of Kleinmann & Hall (1986) use two continuum bands far apart across the K atmospheric window. Since the continuum normalization to a black body shape, adopted in our library (Chapter 4) effectively cancels out the broad water vapor bands, this might cause an additional problem because the true continuum would be affected by the H_2O absorption. In contrast, the continuum bands of Ramírez et al. (1997) are adjacent to the lines.

The various CO band indices we measured (Figures 5.5) show no major differences in their behavior, except for the $^{13}\text{CO}(2,0)$ at $2.35\ \mu\text{m}$. There are two major difficulties here. First, the index is placed closest to the red edge of the K window, where the thermal sky background is the highest. Second, this index is affected by the continuum extrapolation more than the others.

A common feature in the behavior of almost all indices is a gradual increase

of the strength after the quick post-supergiant phase. We attribute this to the movement of the main sequence turn off point towards lower luminosity stars. As it was discussed above, the main sequence stars are too hot to permit neutral metals and molecules. Their spectra in the near infrared are nearly flat, except for the hydrogen lines, and they dilute the absorption features created in the atmospheres of red stars. As the burst ages, the luminosity of the stars at the turn off point fades and their relative contribution in the total flux decreases.

Figure 5.7 shows the time evolution of the line ratios. The variations are largest at 4-8 Myr, because at this interval the rapidly changing red supergiants dominate the burst. These stars move to the red over a very short time interval, causing an abrupt change of the line ratios.

The ratios quickly stabilize after 8 Myr. The same-species ratios (e.g. Mg-to-Mg, CO-to-CO) demonstrate the best overall stability. Changes are larger for the ratios of features of different species, which suggests the possibility of constraining element abundance ratios in actively star forming galaxies as a function of time. Currently our model is ill-suited to perform such a test because it does not incorporate the chemical self enrichment process.

The stellar CO bands exhibit a combined temperature and surface gravity dependence, and they were thought to be good age indicators. However, Origlia & Oliva (2000) questioned this assumption, particularly for older systems ($\gtrsim 100$ Myr) where the asymptotic giant branch stars contribute most of the near infrared flux. This is not a problem for the interval of ages (≤ 30 Myr) we consider here.

Figures 5.8, 5.9, 5.10, and 5.11 plot the equivalent widths of various lines versus the equivalent widths of the two CO bands. Figures 5.12, 5.13, and 5.14 plot various metal indices against each other. On average, the indices are well

correlated, especially the stronger ones, with more reliable measurements.

Summarizing, all selected features are very weak during the first 5-6 Myr. After that they all peak for a short interval (2-4 Myr), and then quickly drop by about a factor of 2-3, to remain almost constant at that level for the next 15-20 Myr. Apparently the initial rise can serve as a good age indicator. However, the metallicity scales dramatically the peak value and reliable abundance estimates can be obtained only after the burst is older than $\sim 12 - 15$ Myr, unless an independent estimate of the burst age is available.

5.5.2. Dilution by Featureless Continuum

Attempts to study the nature of the stellar populations in galaxies with active nuclei have been carried mainly in the infrared, because of the strong dust extinction that occurs in the central regions of these galaxies (e.g. Chapter 2). However, these efforts have been hampered by the presence of a featureless continuum, most probably warm dust surrounding the central engine in Seyferts.

Oliva et al. (1995) pointed out that the diagrams of $EW(CO1.62)$ or $EW(CO2.29)$ versus $EW(CO1.62)/EW(Si1.59)$ or $EW(CO1.62)/EW(CO2.29)$ ratios can help to disentangle the stellar and non-stellar components. Figure 5.8 overlays the output of our model, for single instantaneous bursts of star formation with Salpeter initial mass function, for two extreme cases of metallicity: $[Fe/H] = 0.0$ (solid line) and $[Fe/H] = -1.3$ (dashed line). The ages of the bursts (in Myr) are shown. The measurements of various objects are from Oliva et al. (1995), with typical errors 0.3\AA for Si 1.59 and CO 1.62 μm , and 0.6\AA for CO 2.29 μm . Our solar metallicity model matches well the observations for non-diluted objects. Schreiber (2000) demonstrated that the $EW(CO2.29)/EW(Mg2.28)$ ratio

can be used as well.

We showed the same for $\text{EW}(\text{CO}1.62)/\text{EW}(\text{Mg}1.50)$ (Chapter 4). Figure 5.9 plots the $\text{EW}(\text{CO}2.29)$ versus $\text{EW}(\text{CO}1.62)/\text{EW}(\text{Mg}1.50)$. The notation is the same as on Figure 5.8. These techniques to derive the dilution have to be applied with caution only for galaxies with some abundance estimates, since the CO band at $2.29 \mu\text{m}$ is metallicity dependent. However, the inverse problem - determining the abundance of active galaxies, - will require an independent dilution estimate, for instance from the mid-infrared, or an optical metallicity estimate for the less obscured systems.

5.6. Discussion

The information, obtained from the metal absorption features in the near infrared spectra of starburst galaxies leads to powerful constraints on the stellar continuum. The time evolution of these indices depends strongly on the abundance, presenting an opportunity to estimate $[\text{Fe}/\text{H}]$ from the total starburst spectra, similarly to the well-established techniques in the optical. We will explore this possibility further in Chapter 6).

Potentially, these indices would allow to recover the star formation history, and even to answer the question if previous bursts had occurred in the host galaxy. This is crucial for understanding the present-day chemistry of starburst galaxies, because the time scales of the bursts are comparable to the time scale of α -element production in high mass stars, but the stellar evolution is much slower in building up the iron-peak elements, in low mass stars. The abundance ratios between these two groups of elements could probe the metal enrichment history.

The infrared absorption features alone can not constrain directly the age to

the starburst. In the optical, a simultaneous age and metallicity estimates are obtained by plotting the $H\beta$ versus a metal index. In the infrared we have many good analogs of the metal indices but the only hydrogen absorption line $Br\gamma$ is relatively weak, and is filled in with emission in gas-rich starburst galaxies.

However, this emission coupled with a starburst model can measure the burst age very well (e.g. Rieke et al. 1980; see also Section 5.1). The emission strength is strongly correlated to the number of ionizing photons, and therefore, to the number of high mass blue stars, which is directly related to the initial mass function slope, and the age of the last burst. The major difficulty with measuring accurately the emission line comes from the need to subtract properly the continuum (e.g. Engelbracht 2000). Our population synthesis model helps to build for the first time a self consistent continuum.

5.7. Summary

We present here an evolutionary population synthesis model for young stellar populations (10 – 30 Myr), aimed at application to starburst galaxies. The model uses the Starburst99 code (Leitherer et al. 1999) and our empirical library of near infrared spectra (Chapter 4). We have measured 19 indices of 12 prominent spectral features that are strong enough to be measured reliably in starburst galaxies. We concluded that:

The strength of the infrared absorption features depends strongly on the metallicity. The indices peak at 7-12 Myr, and the amplitudes of this peaks are scaled by the abundance. However, reliable metallicity estimates can be obtained only for systems older than ~ 15 Myr, when the strengths steady at about $1/3$ to $1/2$ of the peak level, unless the age is known independently. The hydrogen

recombination emission provides the means for such estimates. The metallicity determinations become problematic about 100 Myr after the burst, when the uncertain physics of the asymptotic giant branch stars makes the modeling unreliable.

The models suggest a strong degeneracy between low metallicity and dilution from a featureless continuum. Independent dilution estimate, e.g. from the mid-infrared, is needed to circumvent the problem.

Table 5.1 Metallicity bins.

Metallicity	Stellar Limits,[Fe/H]		# spectra	
Bin, Z	lower	upper	H	K
0.001		-1.00	7	10
0.004	-1.00	-0.65	1	0
0.008	-0.65	-0.20	24	27
0.020	-0.20	+0.15	95	90
0.040	+0.15		34	29

COMMENTS: Metallicity Z of the evolutionary tracks, corresponding iron abundance limits for selection of the library stars, and number of spectra per bin are given.

Table 5.2 Velocity dispersion corrections.

Index	a
Mg150V	1.2×10^{-3}
Fe158V	1.3×10^{-3}
Si159O	4.5×10^{-4}
CO162O	3.0×10^{-4}
Mg171V	1.8×10^{-3}
Mg211V	7.8×10^{-4}
Na221R	2.0×10^{-4}
Na221K	1.6×10^{-3}
Ca226R	3.3×10^{-4}
Ca226K	1.5×10^{-3}
Mg228V	1.8×10^{-3}
Mg228R	5.0×10^{-4}
CO229O	6.4×10^{-4}
2CO22K	7.5×10^{-4}
CO229V	2.4×10^{-4}
2CO23K	6.6×10^{-4}
3CO23K	7.2×10^{-4}
NOTE: See Section 5.4 for details.	

Table 5.3 Equivalent widths for $\sigma = 200 \text{ km s}^{-1}$ models.

t	Mg _v	Fe _v	Si _o	CO _o	Mg _v	Mg _v	Na _r	Na _k	Ca _r	Ca _k	Mg _v	Mg _r	CO _o	CO _k	CO _v	CO _k	CO _k
	1.50	1.58	1.59	1.62	1.71	2.11	2.21	2.21	2.26	2.26	2.28	2.28	2.29	2.30	2.30	2.32	2.36
[Fe/H] = 0.0																	
1	0.03	0.01	0.01	0.00	0.01	0.02	0.00	0.90	0.03	0.48	0.02	0.02	0.46	0.51	2.14	3.06	4.95
2	0.02	0.01	0.01	0.00	0.01	0.02	0.00	0.90	0.03	0.48	0.01	0.02	0.46	0.51	2.16	3.06	4.96
3	0.01	0.00	0.00	0.00	0.01	0.01	0.00	0.88	0.02	0.47	0.01	0.01	0.46	0.50	2.15	3.04	4.93
4	0.12	0.05	0.12	0.04	0.02	0.04	0.03	0.89	0.09	0.46	0.08	0.10	0.55	0.61	2.17	3.01	4.82
5	1.44	0.81	1.62	0.73	0.33	0.33	0.29	1.44	0.79	1.12	0.57	0.47	4.07	3.97	5.66	5.67	4.66
6	1.82	1.15	2.10	1.05	0.53	0.37	0.19	1.71	0.98	1.70	0.56	0.23	6.61	6.34	8.52	7.95	4.67
7	4.48	1.95	3.70	5.38	1.79	0.00	4.61	4.29	0.24	1.26	0.93	0.75	8.76	9.67	12.35	18.83	9.12
8	5.56	2.18	2.83	6.56	1.86	3.04	5.68	4.98	5.92	5.08	0.79	0.00	16.87	17.83	23.55	17.53	8.57
9	5.57	2.18	2.83	6.57	1.86	3.04	5.68	4.98	5.93	5.09	0.79	0.00	16.89	17.85	23.58	17.54	8.57
10	4.84	1.85	2.86	6.29	1.58	2.37	5.03	4.62	5.30	4.59	0.83	0.04	16.88	17.56	23.92	17.38	8.13
12	2.92	1.06	2.15	4.37	1.20	0.98	2.88	3.48	3.75	3.49	0.71	0.41	15.13	15.51	22.06	15.48	7.48
14	2.66	1.11	1.94	3.12	1.13	0.76	2.21	2.93	2.65	2.73	0.62	0.50	11.00	11.43	15.90	12.84	7.13
16	2.49	1.01	1.92	3.80	1.07	0.72	2.59	3.11	3.35	3.22	0.63	0.44	12.61	12.82	17.96	13.87	8.00

t	Mg _v	Fe _v	Si _o	CO _o	Mg _v	Mg _v	Na _r	Na _k	Ca _r	Ca _k	Mg _v	Mg _r	CO _o	CO _k	CO _v	CO _k	CO _k
	1.50	1.58	1.59	1.62	1.71	2.11	2.21	2.21	2.26	2.26	2.28	2.28	2.29	2.30	2.30	2.32	2.36
18	2.53	1.02	1.86	3.69	1.12	0.81	2.60	3.12	3.47	3.34	0.63	0.51	12.67	12.97	18.17	13.90	8.02
20	2.57	1.05	2.01	3.96	1.09	0.76	2.73	3.19	3.66	3.47	0.68	0.51	13.11	13.28	18.56	14.28	8.25
22	2.59	1.09	2.12	4.17	1.08	0.72	2.82	3.24	3.84	3.60	0.72	0.52	13.43	13.47	18.64	14.55	8.55
24	2.74	1.15	2.31	4.30	1.11	0.76	2.97	3.34	3.95	3.71	0.80	0.61	13.85	13.86	19.05	14.97	8.58
26	2.88	1.21	2.51	4.67	1.15	0.74	3.20	3.47	4.23	3.91	0.85	0.64	14.56	14.47	19.82	15.68	8.99
28	3.21	1.25	2.75	4.91	1.28	0.92	3.73	3.77	4.38	4.05	0.98	0.81	15.30	15.39	21.06	16.78	9.21
30	3.18	1.22	2.73	4.80	1.25	0.90	3.66	3.72	4.27	3.91	0.95	0.69	15.07	15.12	20.79	16.62	9.05
$[\text{Fe}/\text{H}] = -0.4$																	
1	0.06	0.01	0.04	0.01	0.02	0.03	0.00	0.91	0.05	0.50	0.02	0.01	0.48	0.53	2.19	3.07	4.96
2	0.05	0.01	0.03	0.01	0.02	0.02	0.00	0.90	0.04	0.50	0.01	0.01	0.48	0.53	2.19	3.07	4.97
3	0.02	0.00	0.01	0.01	0.01	0.01	0.00	0.87	0.03	0.47	0.01	0.01	0.46	0.51	2.15	3.02	4.90
4	0.31	0.12	0.36	0.19	0.12	0.15	0.19	0.98	0.24	0.57	0.10	0.09	1.10	1.17	2.85	3.63	4.87
5	1.22	0.48	1.44	0.75	0.46	0.58	0.76	1.39	0.86	0.88	0.40	0.43	2.89	3.06	4.89	5.45	4.92
6	1.08	0.47	1.21	0.97	0.40	0.42	0.72	1.29	0.76	0.83	0.28	0.22	2.79	2.94	4.82	5.20	4.96

t	Mg _v	Fe _v	Si _o	CO _o	Mg _v	Mg _v	Na _r	Na _k	Ca _r	Ca _k	Mg _v	Mg _r	CO _o	CO _k	CO _v	CO _k	CO _k
	1.50	1.58	1.59	1.62	1.71	2.11	2.21	2.21	2.26	2.26	2.28	2.28	2.29	2.30	2.30	2.32	2.36
7	2.83	1.29	2.51	3.48	1.10	0.46	2.70	2.99	2.63	2.36	0.84	0.33	10.51	10.99	14.84	12.20	7.65
8	3.59	1.67	3.15	4.51	1.40	0.52	3.46	3.61	3.34	2.91	1.05	0.39	13.35	13.96	18.51	14.79	8.58
9	3.39	1.71	2.63	4.92	1.43	0.84	3.61	4.02	3.55	3.13	0.72	0.43	15.08	15.75	21.19	15.77	8.74
10	3.18	1.71	2.22	5.08	1.42	1.09	3.60	4.21	3.58	3.19	0.46	0.45	15.83	16.50	22.43	16.04	8.67
12	3.29	1.75	2.36	5.16	1.45	1.08	3.65	4.21	3.62	3.20	0.51	0.46	15.87	16.55	22.44	16.14	8.70
14	3.63	1.82	2.81	5.24	1.52	0.84	3.83	4.20	3.75	3.30	0.80	0.44	15.90	16.59	22.24	16.52	9.04
16	2.75	1.24	2.61	2.97	1.07	0.78	2.39	2.80	2.41	2.10	0.78	0.56	9.35	9.79	13.30	11.15	6.88
18	3.22	1.55	2.63	4.39	1.31	0.55	3.37	3.68	3.28	2.93	0.87	0.36	13.57	14.19	19.02	14.74	8.63
20	3.39	1.62	2.81	4.57	1.36	0.53	3.51	3.76	3.40	3.02	0.94	0.36	13.98	14.61	19.50	15.16	8.80
22	3.54	1.67	3.01	4.56	1.40	0.59	3.51	3.76	3.42	3.01	1.02	0.46	13.86	14.49	19.29	15.15	8.70
24	3.74	1.78	3.16	4.79	1.46	0.57	3.70	3.85	3.55	3.10	1.03	0.37	14.39	15.04	19.88	15.68	8.89
26	3.85	1.83	3.24	5.07	1.52	0.52	3.88	4.02	3.74	3.27	1.10	0.39	15.18	15.86	20.99	16.35	9.23
28	3.83	1.82	3.22	5.04	1.51	0.52	3.85	4.00	3.71	3.25	1.09	0.39	15.09	15.77	20.87	16.26	9.20
30	3.82	1.81	3.21	5.01	1.51	0.52	3.83	3.98	3.70	3.24	1.09	0.39	15.01	15.69	20.77	16.19	9.17

t	Mg _v	Fe _v	Si _o	CO _o	Mg _v	Mg _v	Na _r	Na _k	Ca _r	Ca _k	Mg _v	Mg _r	CO _o	CO _k	CO _v	CO _k	CO _k
	1.50	1.58	1.59	1.62	1.71	2.11	2.21	2.21	2.26	2.26	2.28	2.28	2.29	2.30	2.30	2.32	2.36
30	3.82	1.81	3.21	5.01	1.51	0.52	3.83	3.98	3.70	3.24	1.09	0.39	15.01	15.69	20.77	16.19	9.17
$[\text{Fe}/\text{H}] = -1.3$																	
1	0.03	0.01	0.01	0.01	0.01	0.00	0.00	0.89	0.02	0.47	0.01	0.02	0.53	0.57	2.29	3.12	4.97
2	0.02	0.01	0.01	0.01	0.01	0.00	0.00	0.89	0.02	0.48	0.01	0.02	0.52	0.56	2.27	3.12	4.98
3	0.23	0.06	0.13	0.05	0.10	0.00	0.03	0.83	0.02	0.41	0.10	0.12	1.02	1.06	3.06	3.53	4.80
4	0.01	0.00	0.00	0.00	0.00	0.00	0.00	0.78	0.02	0.42	0.00	0.01	0.44	0.49	2.07	2.90	4.69
5	0.27	0.07	0.14	0.06	0.12	0.00	0.04	0.81	0.02	0.39	0.11	0.14	1.08	1.12	3.15	3.57	4.75
6	0.15	0.01	0.15	0.03	0.07	0.00	0.04	0.83	0.00	0.39	0.06	0.04	0.81	0.86	2.73	3.29	4.79
7	0.09	0.00	0.15	0.01	0.03	0.00	0.04	0.85	0.00	0.38	0.02	0.00	0.64	0.69	2.47	3.11	4.80
8	0.08	0.00	0.17	0.01	0.03	0.07	0.05	0.41	0.02	0.00	0.00	0.00	0.28	0.22	1.59	2.84	3.95
9	0.17	0.00	0.46	0.22	0.00	0.10	0.05	0.22	0.06	0.00	0.00	0.00	0.42	0.30	2.33	2.73	3.68
10	0.21	0.00	0.62	0.37	0.00	0.13	0.05	0.09	0.10	0.00	0.00	0.00	0.73	0.56	3.54	2.71	3.56
12	0.27	0.00	0.75	0.45	0.00	0.14	0.06	0.00	0.12	0.00	0.02	0.00	1.03	0.83	4.48	2.77	3.45
14	0.32	0.00	0.94	0.54	0.00	0.18	0.08	0.00	0.14	0.00	0.00	0.00	0.96	0.69	4.50	2.60	2.98

t	Mg _v	Fe _v	Si _o	CO _o	Mg _v	Mg _v	Na _r	Na _k	Ca _r	Ca _k	Mg _v	Mg _r	CO _o	CO _k	CO _v	CO _k	CO _k
	1.50	1.58	1.59	1.62	1.71	2.11	2.21	2.21	2.26	2.26	2.28	2.28	2.29	2.30	2.30	2.32	2.36
16	0.40	0.00	0.96	0.56	0.00	0.17	0.10	0.00	0.14	0.00	0.01	0.00	1.23	0.97	5.00	2.82	3.07
18	0.37	0.00	1.00	0.50	0.00	0.19	0.15	0.00	0.12	0.00	0.00	0.00	1.00	0.71	4.39	2.63	2.70
20	0.50	0.00	1.30	0.53	0.00	0.26	0.19	0.00	0.12	0.00	0.00	0.00	0.47	0.05	2.99	2.26	1.67
22	0.62	0.00	1.46	0.46	0.00	0.28	0.24	0.00	0.09	0.00	0.00	0.00	0.13	0.00	1.68	2.20	1.28
24	0.68	0.00	1.60	0.47	0.04	0.30	0.27	0.00	0.08	0.00	0.00	0.00	0.01	0.00	1.25	2.12	1.05
26	0.69	0.00	1.72	0.47	0.07	0.33	0.29	0.00	0.08	0.00	0.00	0.00	0.00	0.00	0.73	1.99	0.83
28	0.70	0.00	1.78	0.45	0.12	0.36	0.31	0.00	0.08	0.00	0.00	0.00	0.00	0.00	0.00	1.82	0.40
30	0.71	0.00	1.81	0.47	0.12	0.37	0.30	0.00	0.09	0.00	0.00	0.00	0.00	0.00	0.00	1.72	0.18
COMMENTS: Equivalent widths in Å. Age t in Myr. See Section 5.5.1 for details.																	

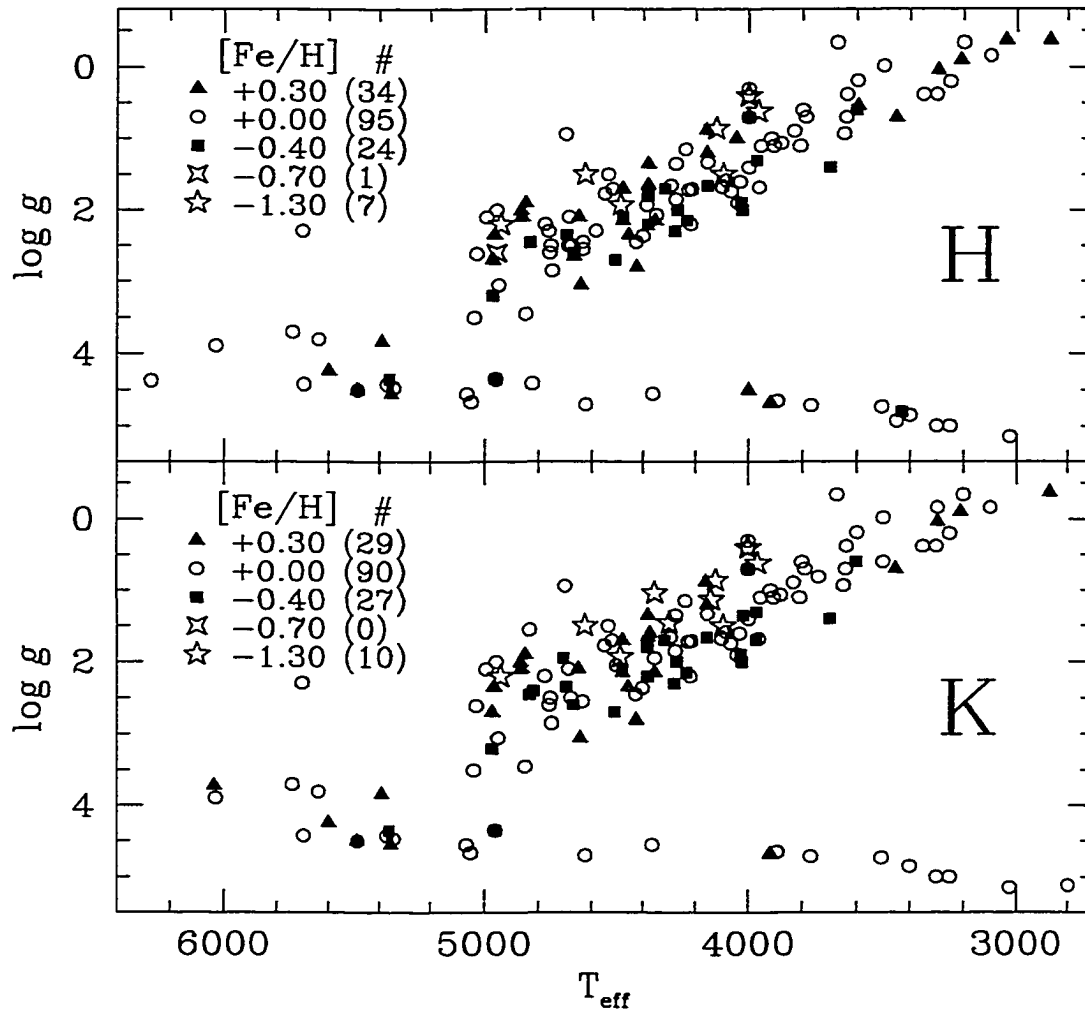
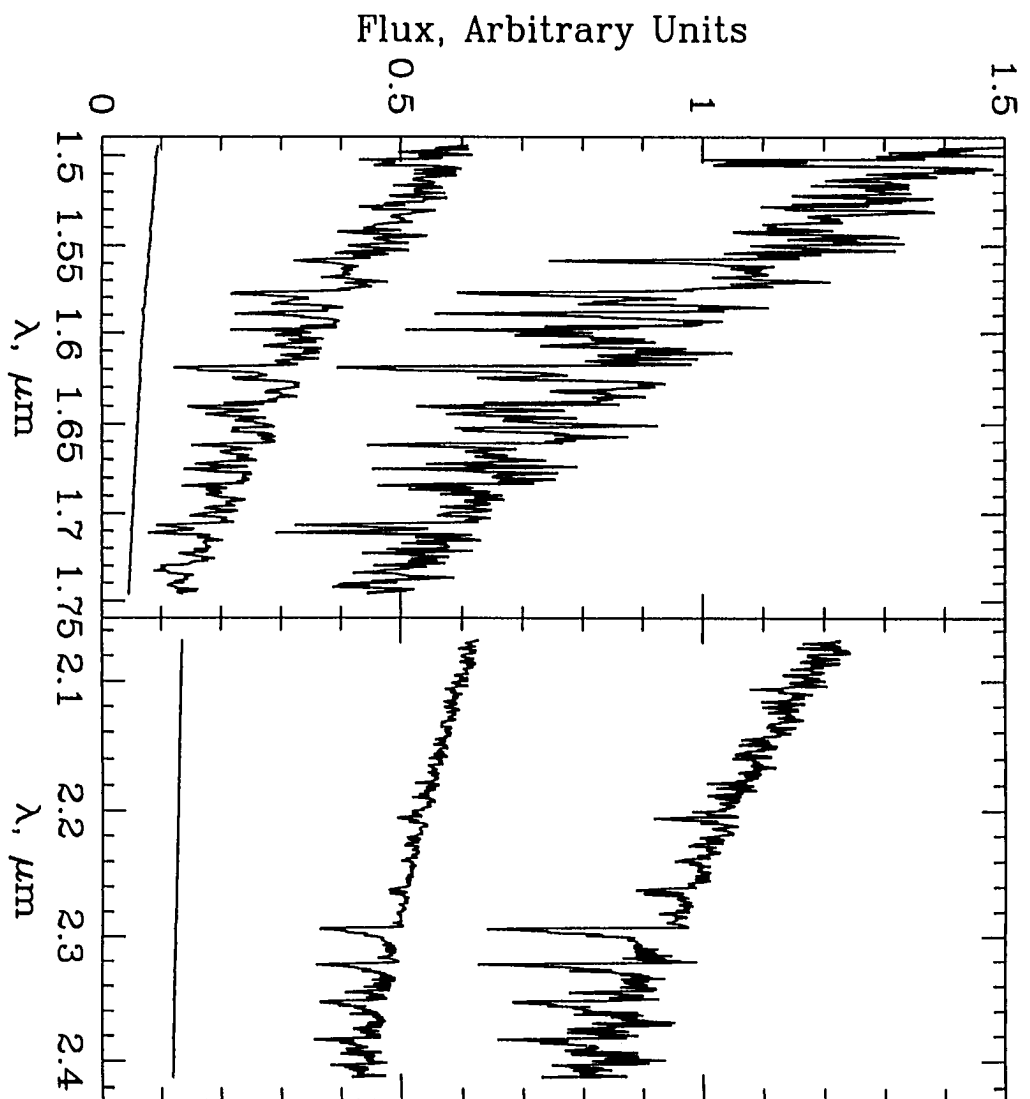
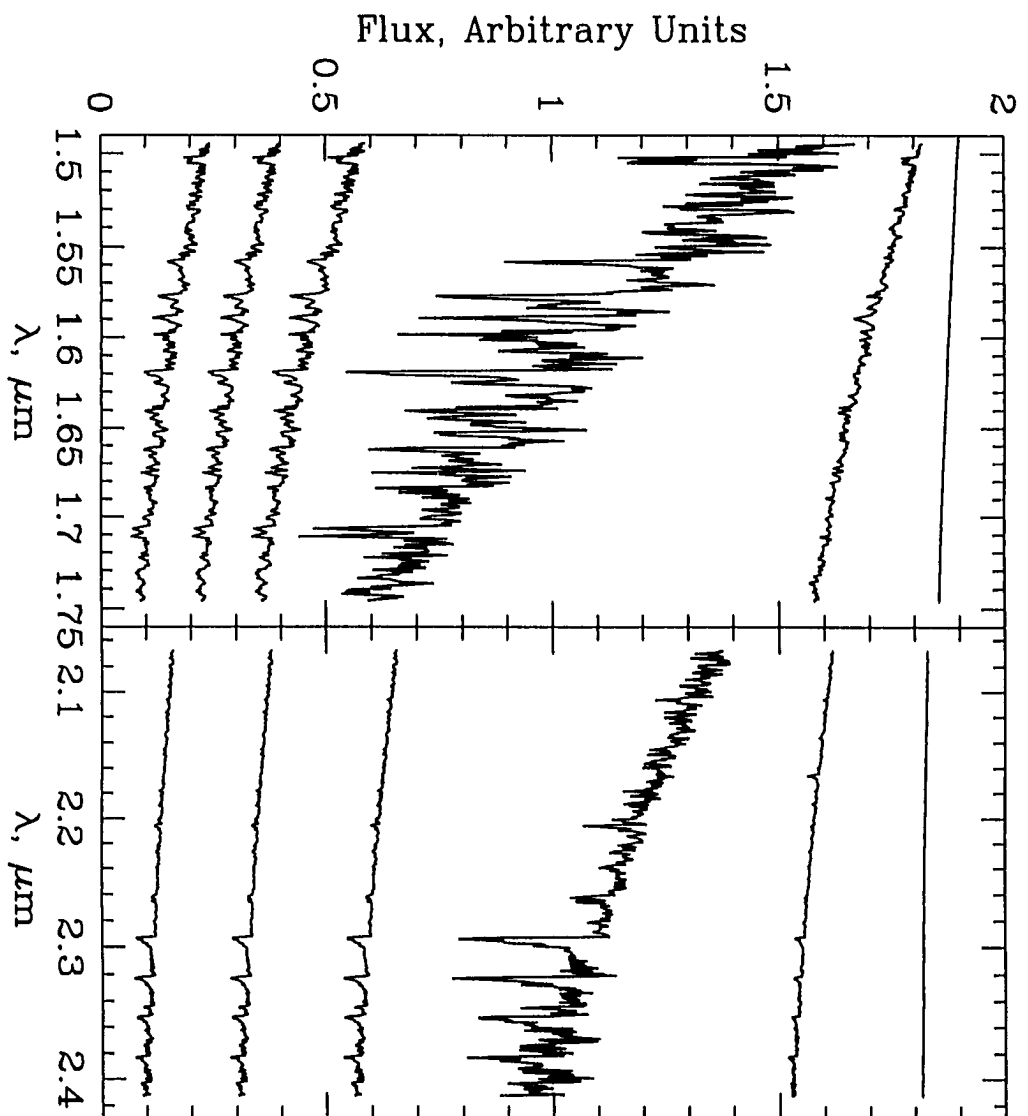


Figure 5.1 Distribution of the library stars in the $\log g$ versus T_{eff} plane for H and K-band (top and bottom, respectively). Different metallicity bins (Table 5.1) are indicated with different symbols, followed by the number of spectra included in the bin. See Section 5.3 for details.

Figure 5.2 Synthetic spectra of single bursts of star formation. (a) Metallicity sequence at 10 Myr: $[\text{Fe}/\text{H}] = 0.0, -0.4$ and -1.3 (from top to bottom) (b) Age sequence with $[\text{Fe}/\text{H}] = 0.0$: 1, 5, 10, 16, 22, and 30 Myr (from top to bottom).





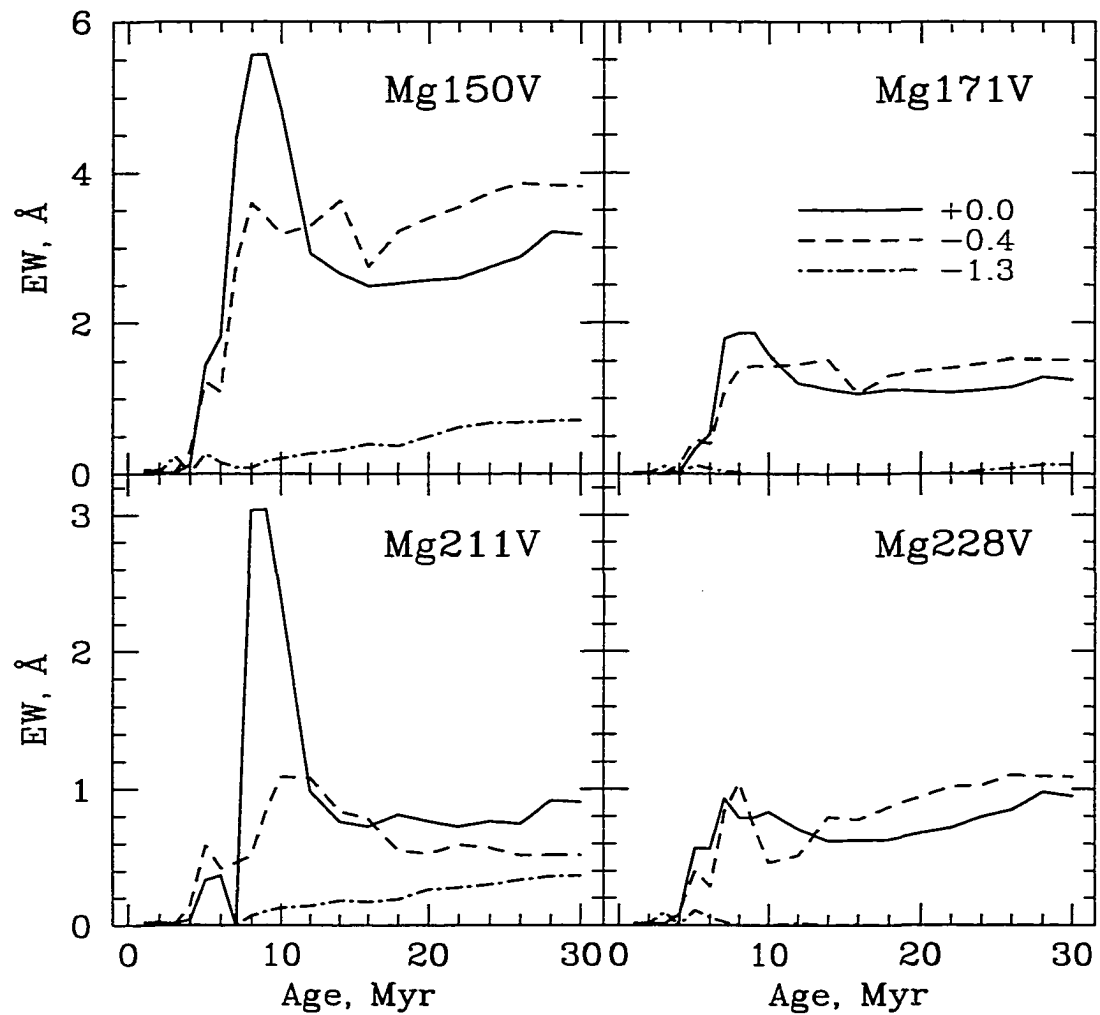


Figure 5.3 Time evolution of magnesium stellar absorption features. Indices are defined in Chapter 4. The metallicities of different models are indicated. See Section 5.5.1 for details.

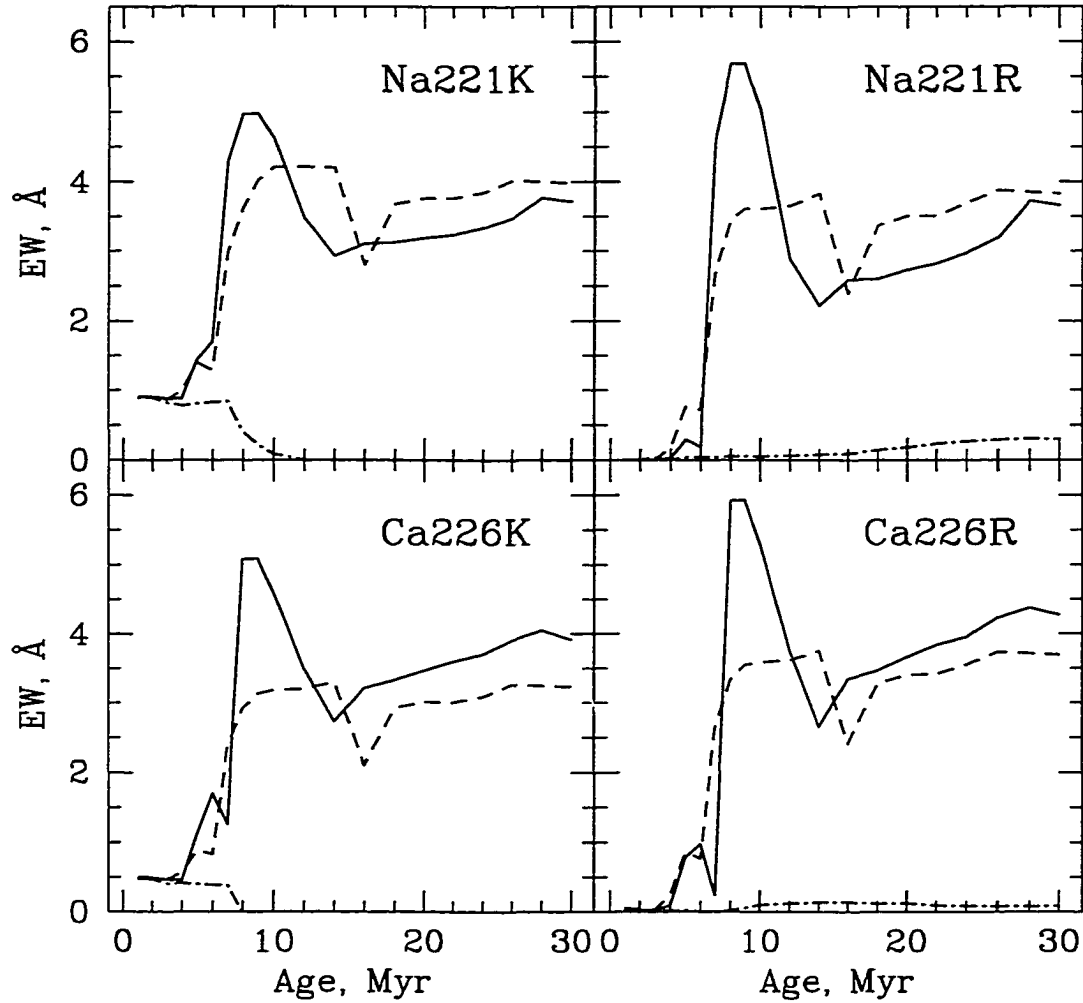


Figure 5.4 Time evolution of sodium and calcium stellar absorption features. Indices on the left according to Kleinmann & Hall (1986) and indices on the right according to Ramírez et al. (1997). The metallicities of different models are indicated as in Figure 5.3. See Section 5.5.1 for details.

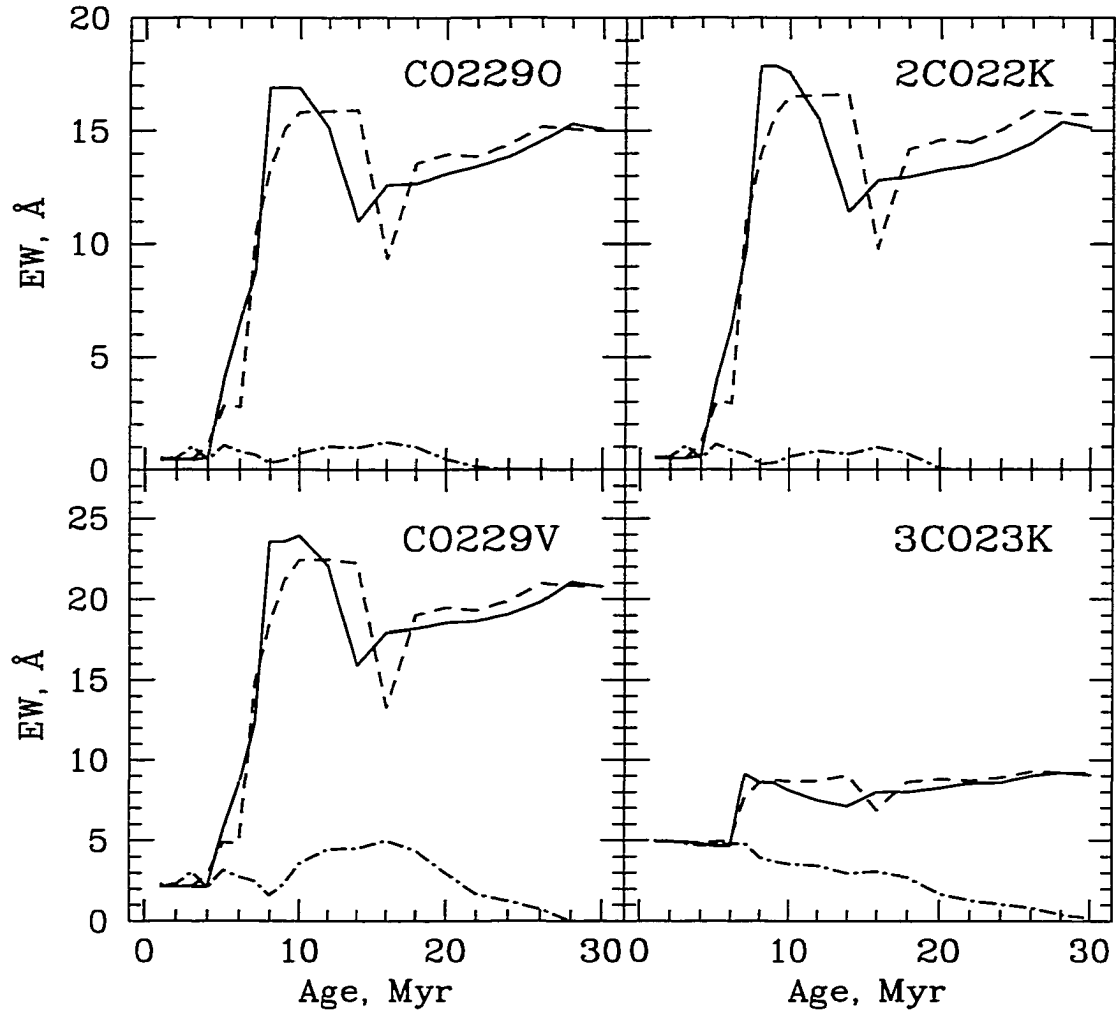


Figure 5.5 Time evolution of $2.29 \mu\text{m}$ CO bands. Index definitions: Origlia, Moorwood & Oliva (1993; top left), this work (Chapter 4; bottom left), Kleinmann & Hall (1986; right). The metallicities of different models are indicated as in Figure 5.3. See Section 5.5.1 for details.

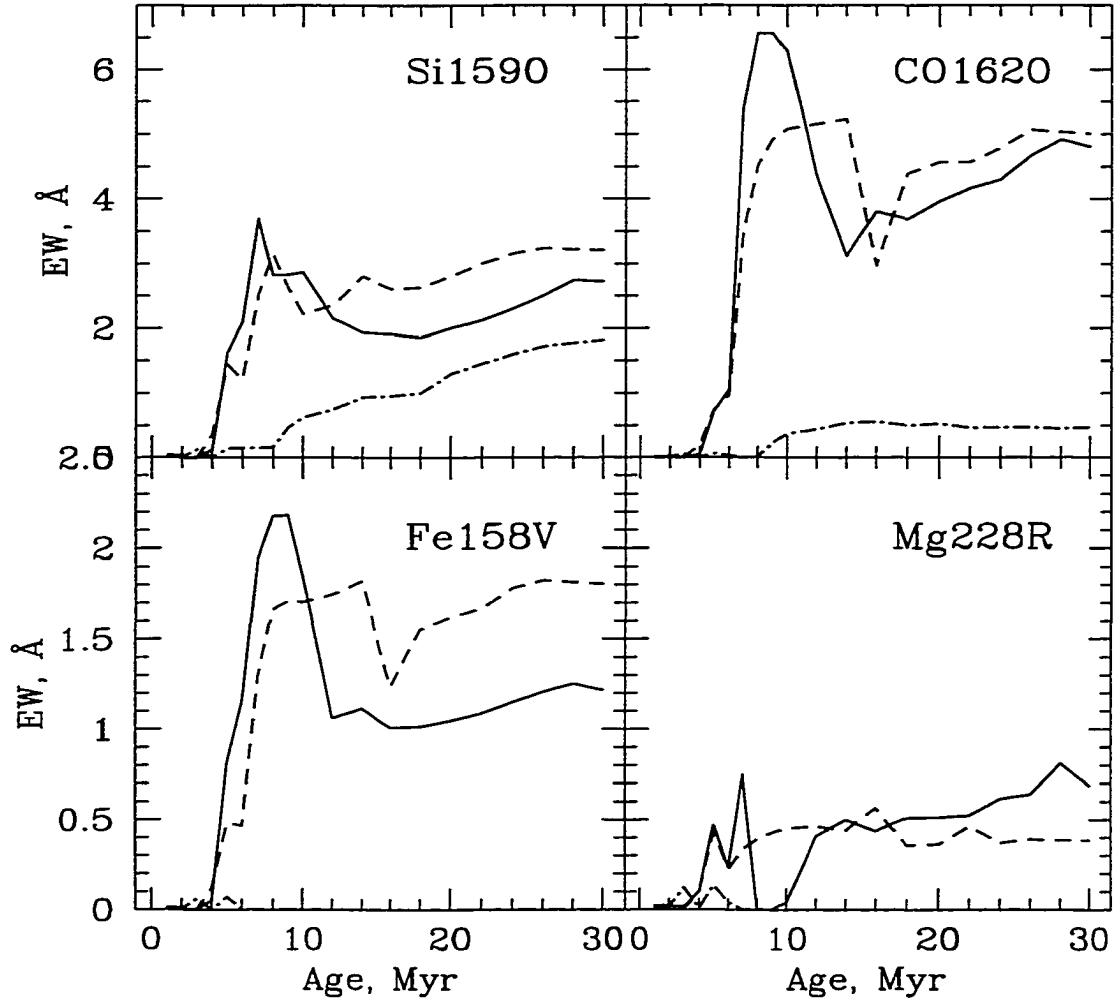


Figure 5.6 Time evolution of other indices: SiI at $1.59 \mu\text{m}$ and CO band at $1.62 \mu\text{m}$ (Origlia, Moorwood & Oliva 1993; top left and right, respectively), FeI at $1.58 \mu\text{m}$ (Chapter 4; bottom left), and MgI at $2.28 \mu\text{m}$ (Ramírez et al. 1997; bottom right). The metallicities of different models are indicated as in Figure 5.3. See Section 5.5.1 for details.

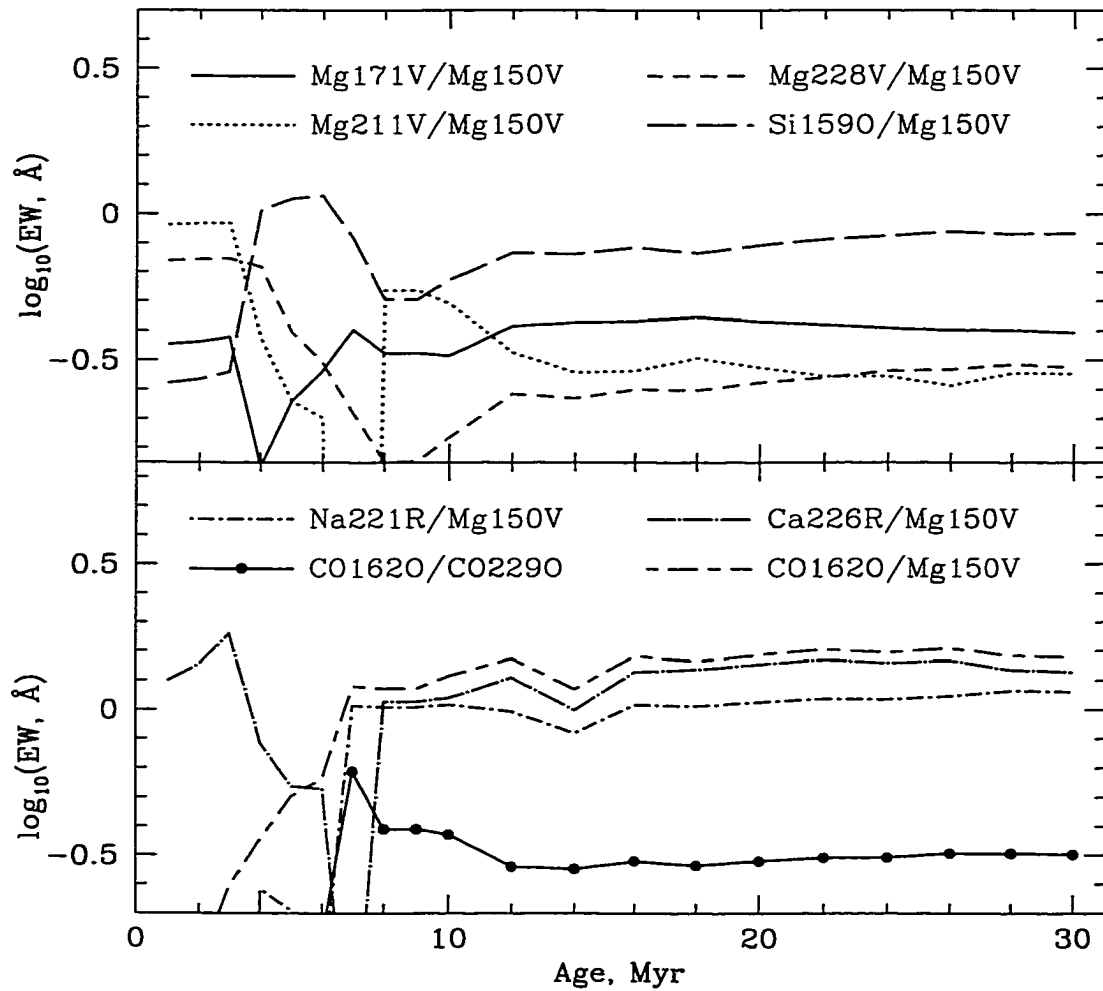


Figure 5.7 Time evolution of infrared line ratios for a solar metallicity burst. See Section 5.5.1 for details.

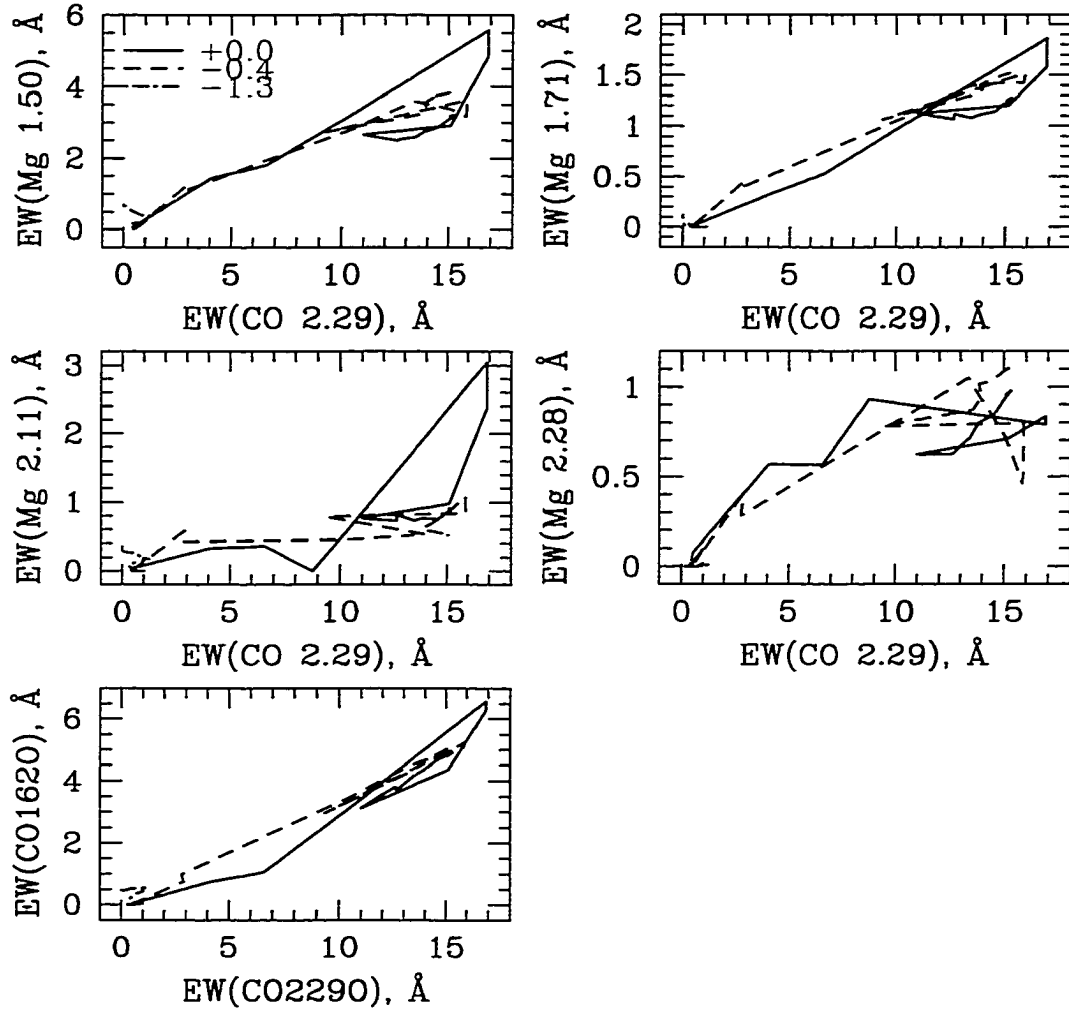


Figure 5.8 Magnesium line equivalent widths and CO 1.62 μm versus CO 2.29 μm equivalent width. The Mg lines are defined in Chapter 4 and the CO indices are defined by Origlia, Moorwood & Oliva (1993). The metallicities of different models are indicated. See Section 5.5.1 for details.

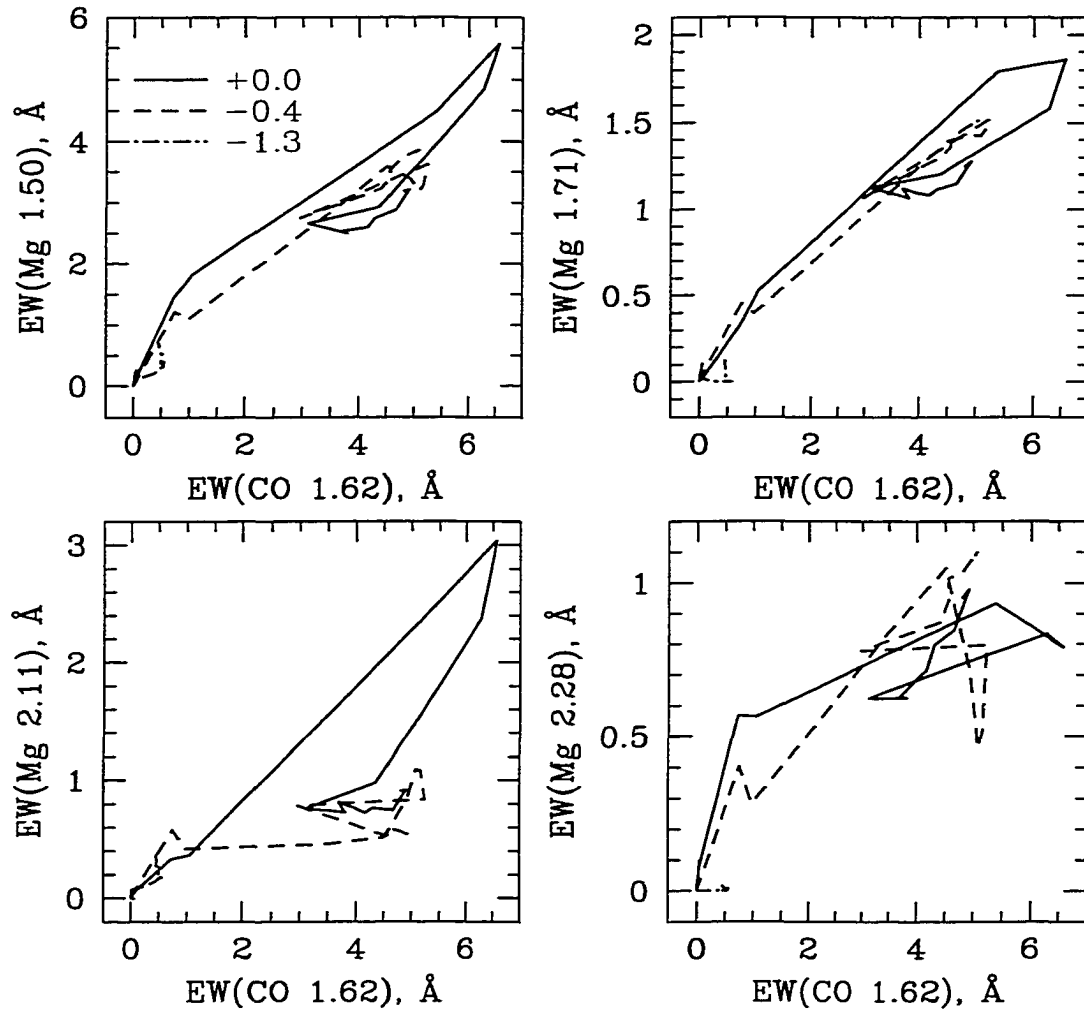


Figure 5.9 Magnesium line equivalent widths versus CO 1.62 μm equivalent width. The Mg lines are defined in Chapter 4 and the CO index is defined by Origlia, Moorwood & Oliva (1993). The metallicities of different models are indicated. See Section 5.5.1 for details.

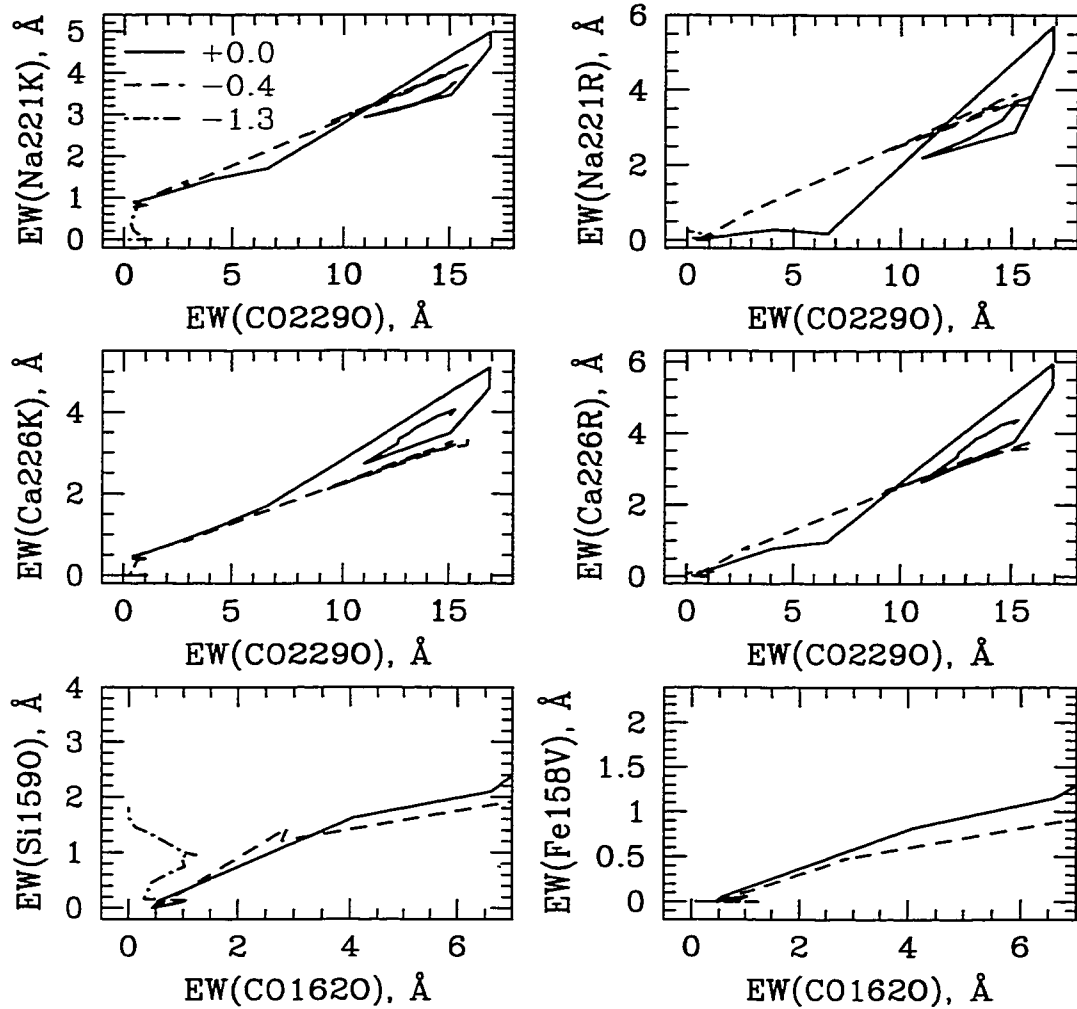


Figure 5.10 Sodium 2.21 μm (top panels), calcium 2.26 μm (both according to Kleinmann & Hall 1986 on the left, and Ramírez et al. 1997 on the right; middle panels), silicon 1.59 μm (Origlia, Moorwood & Oliva 1993; bottom left), and iron 1.58 μm (Chapter 4; bottom right) line equivalent widths versus CO 2.29 μm equivalent width (as defined by Origlia, Moorwood & Oliva 1993). The metallicities of different models are indicated. See Section 5.5.1 for details.

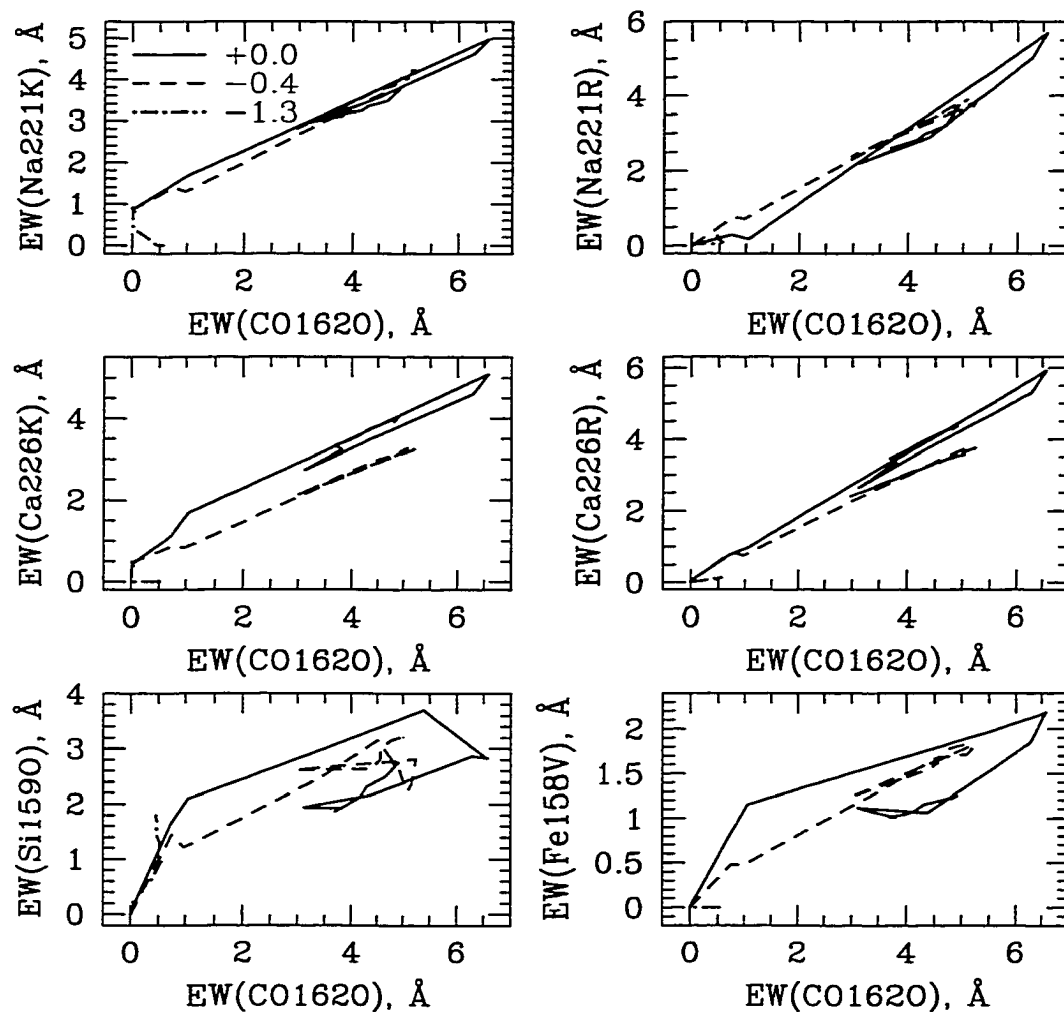


Figure 5.11 Sodium 2.21 μm (top panels), calcium 2.26 μm (both according to Kleinmann & Hall 1986 on the left, and Ramírez et al. 1997 on the right; middle panels), silicon 1.59 μm (Origlia, Moorwood & Oliva 1993; bottom left), and iron 1.58 μm (Chapter 4; bottom right) line equivalent widths versus CO 1.62 μm equivalent width (as defined by Origlia, Moorwood & Oliva 1993). The metallicities of different models are indicated. See Section 5.5.1 for details.

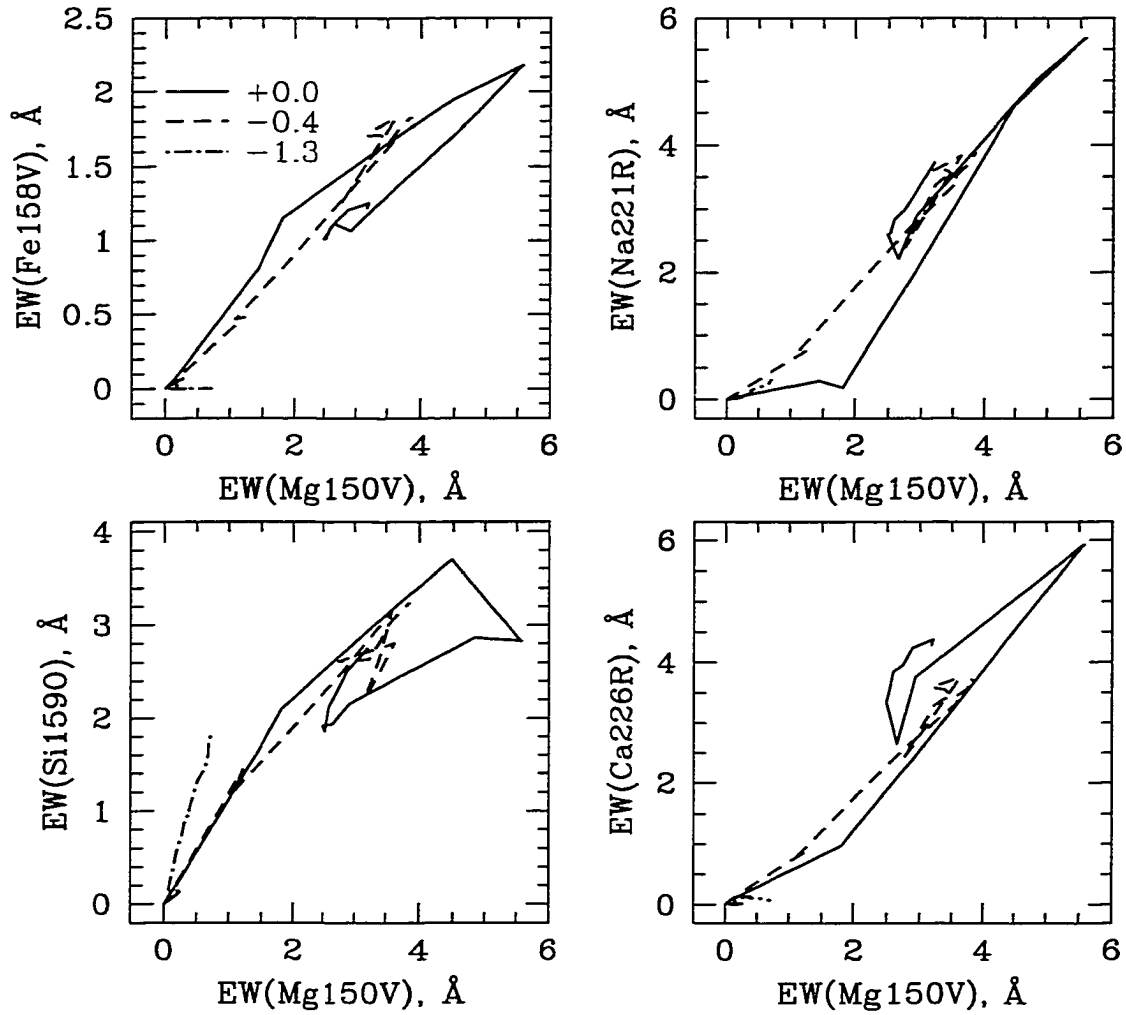


Figure 5.12 Iron 1.58 μm (Chapter 4; top left), silicon 1.59 μm (Origlia, Moorwood & Oliva 1993; bottom left), sodium 2.21 μm (Ramírez et al. 1997; top right), and calcium 2.26 μm (Ramírez et al. 1997; bottom right) equivalent widths versus magnesium 1.50 μm equivalent width (Chapter 4). The metallicities of different models are indicated. See Section 5.5.1 for details.

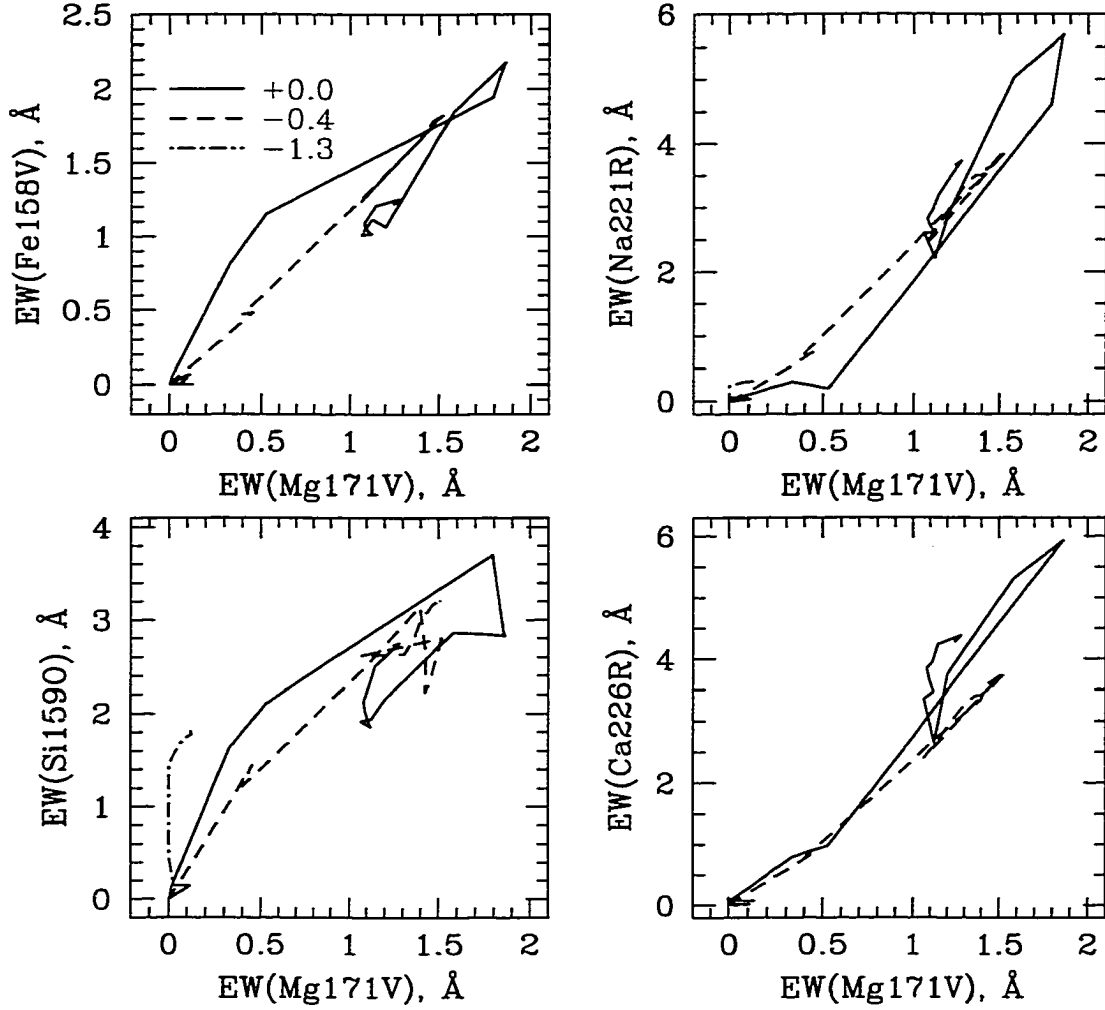


Figure 5.13 Iron 1.58 μm (Chapter 4; top left), silicon 1.59 μm (Origlia, Moorwood & Oliva 1993; bottom left), sodium 2.21 μm (Ramírez et al. 1997; top right), and calcium 2.26 μm (Ramírez et al. 1997; bottom right) equivalent widths versus magnesium 1.71 μm equivalent width (Chapter 4). The metallicities of different models are indicated. See Section 5.5.1 for details.

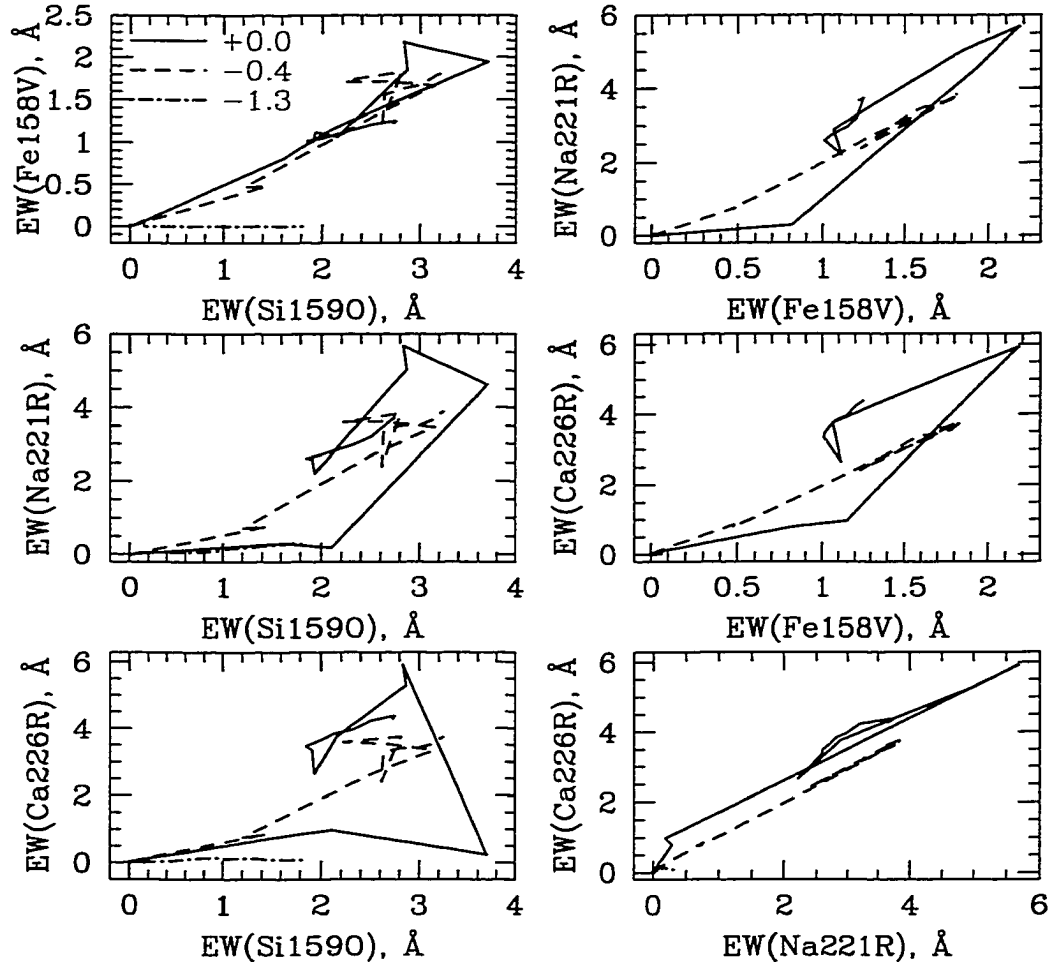


Figure 5.14 Iron 1.58 μm (Chapter 4; top left), sodium 2.21 μm (Ramírez et al. 1997; middle left), and calcium 2.26 μm (Ramírez et al. 1997; bottom left) versus silicon 1.59 μm (Origlia, Moorwood & Oliva 1993). sodium 2.21 μm (Ramírez et al. 1997; top right), and calcium 2.26 μm (Ramírez et al. 1997; middle right) versus iron 1.58 μm (Chapter 4). calcium 2.26 μm versus sodium 2.21 μm (both Ramírez et al. 1997; bottom right). The metallicities of different models are indicated. See Section 5.5.1 for details.

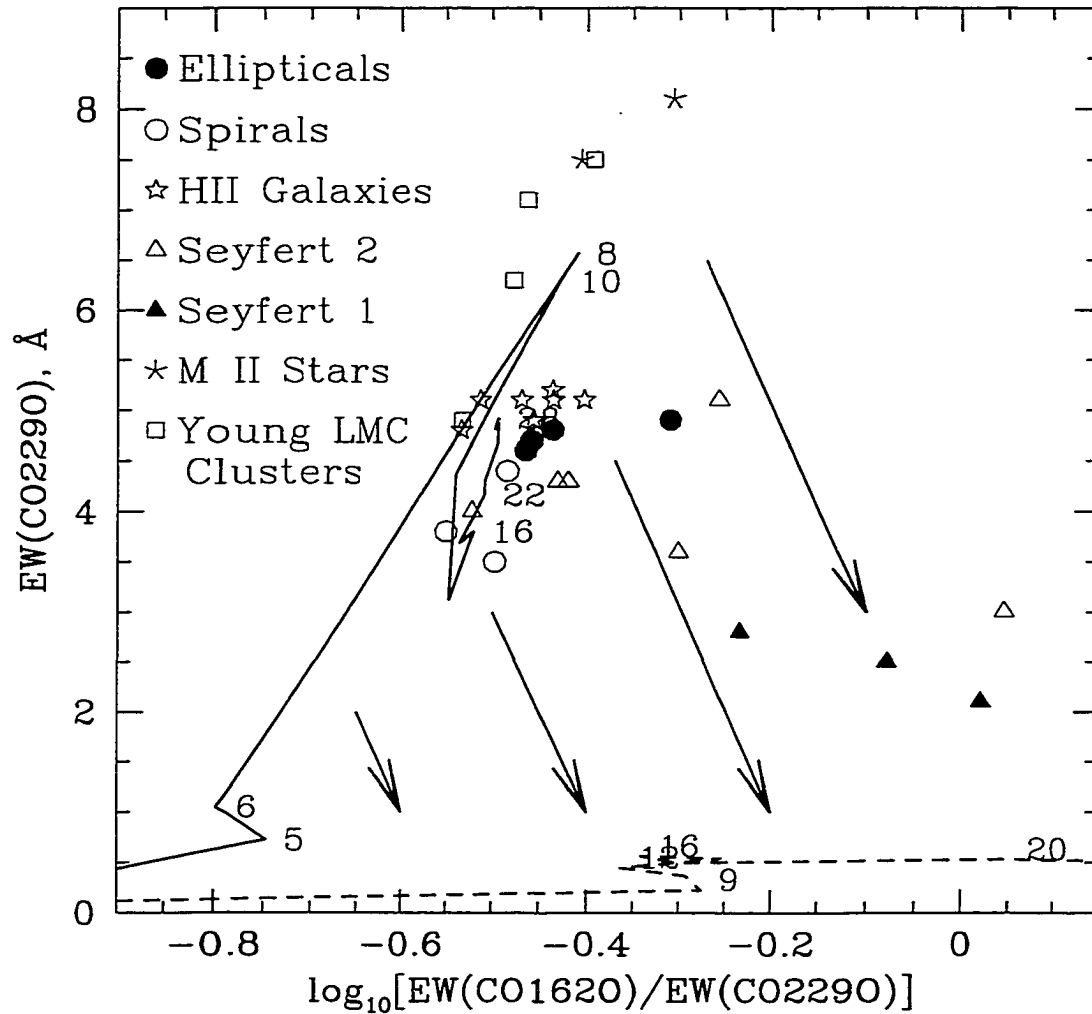


Figure 5.15 Dilution by featureless continuum spectrum: CO bands. The solid line represents a $[\text{Fe}/\text{H}] = 0.0$ single burst model with Salpeter initial mass function. The dashed line is for a similar model with $[\text{Fe}/\text{H}] = -1.3$. The numbers next to the tracks indicate the model age in Myr. Symbols are data taken from Oliva et al. (1995). The arrows represent the dilution vectors, and their slope depends on the shape of the dilution spectrum. See Section 5.5.2 for details.

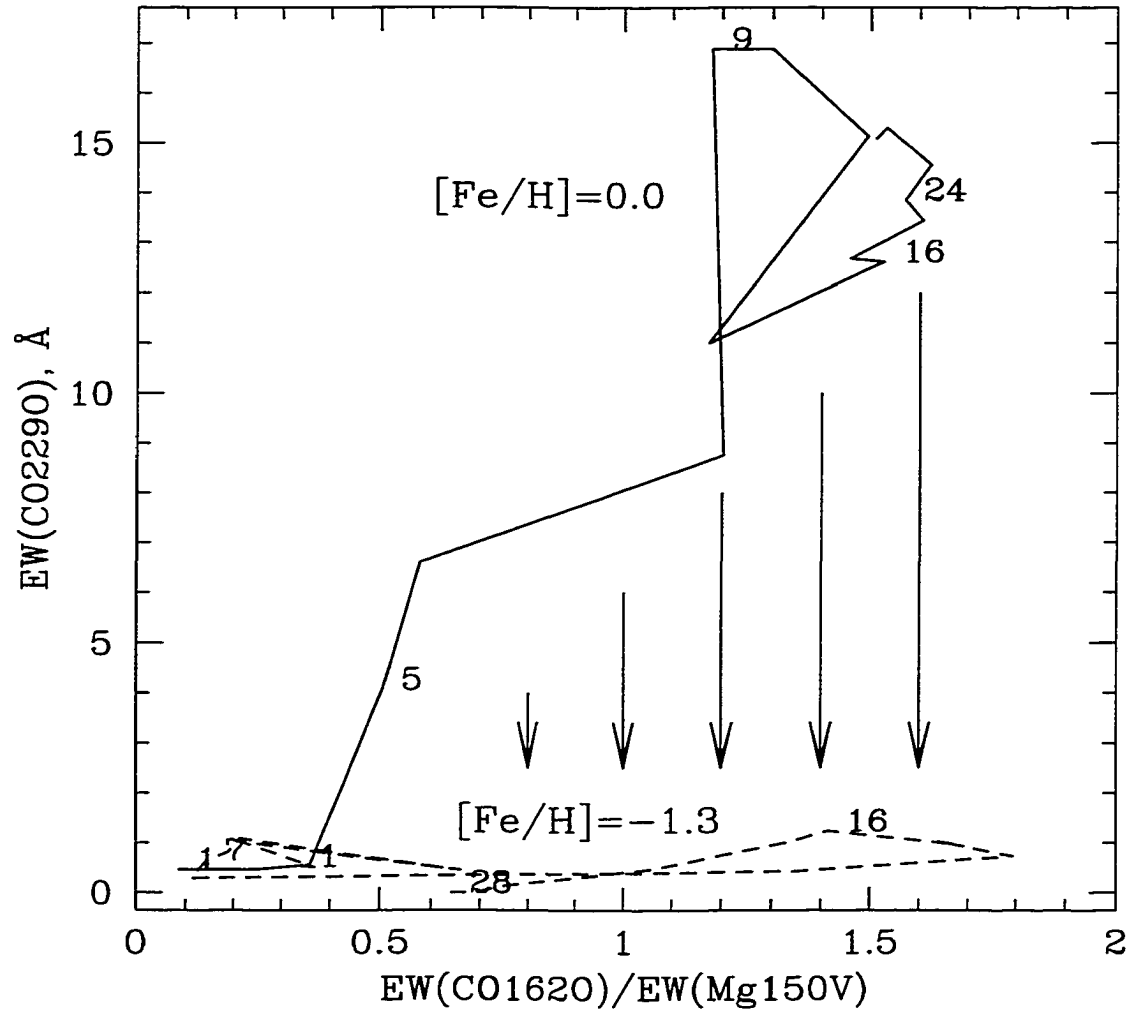


Figure 5.16 Dilution by featureless continuum spectrum: CO bands and magnesium. Models are the same as in Figure 5.15. The arrows represent the dilution vectors. See Section 5.5.2 for details.

6. METAL ABUNDANCES OF STARBURST GALAXIES

6.1. Introduction

Developing new tools for metallicity estimates of stellar systems is motivated by studies of the metal enrichment of the Universe. The abundance determinations are particularly difficult in obscured environments (e.g. starburst galaxies, circumnuclear regions of active galaxies), which may be similar to those where star formation at high redshift takes place. Recent sub-mm observations find evidence that much of the star formation at high redshift indeed occurred in dusty environments (e.g. Gear et al. 2000; Ivison et al. 2000). Optical methods are unsuitable for assessing the metallicity of stars hidden behind 20-30 mag of visual extinction, and infrared techniques remain the only viable alternative.

The existing metallicity indicators for distant, unresolved systems, can be divided in two general groups. First, the emission line based methods estimate the abundance of the gas in the galaxy, approximately equal to that of the latest generation of stars, formed out of that gas. Thus, they are intrinsically cumulative indicators, integrating the metal production over the entire star formation history of the stellar system. On the other hand, methods based on stellar absorption features offer a possibility to assess in detail the enrichment history, provided a number of different spectral indices are used, and each of them is dominated by

stars of different mass, respectively of different age. Therefore, the metallicity indicators, based on absorption features have intrinsically differential nature, if some prior knowledge of the stellar evolution is utilized. While undoubtedly both techniques should be pursued, and their results compared, here, we concentrate on the absorption indicators.

The optical wavelengths have been intensely explored for abundance sensitive features. The most comprehensive study up to date was carried out by the Lick group who provided a detailed analysis of a number of metal absorption lines in stellar spectra, calibrated them versus stellar atmospheric parameters (e.g. Gorgas et al. 1993; Worthey et al. 1994b), and produced a set of synthetic spectra (Worthey 1994a), to match the observed spectra of old systems, and to break the degeneracy between their age and metallicity.

Mould (1987) was the first to explore the metallicity dependence in the infrared spectroscopically, including Mg, Na, Ca, OH, and CO features. Bell & Briley (1991) modeled the infrared stellar spectra, including the metallicity effects. Terndrup, Frogel & Whitford (1991, and references therein) used a simple scaling relation to estimate the metallicity of bulge stars. Frogel et al. (1999) developed for the first time a red giant abundance scale based on Na, Ca and CO features in globular cluster stars, and Ramírez et al. (2000b) used it to estimate the metallicity of the red giants in the bulge. A more sophisticated technique involving stellar atmosphere modeling and high resolution spectroscopy ($R \sim 40,000$) was applied on the Galactic center supergiants by Carr, Sellgren & Balachandran (2000), and Ramírez et al. (2000a).

The only attempt to apply the knowledge of the effects of abundance on the stellar spectra to galaxies belongs to Origlia et al. (1997) who defined a metallicity

scale based on synthetic H-band stellar spectra. Their method utilizes the $1.62\ \mu\text{m}$ CO band, and depends strongly on the adopted microturbulent velocity and the carbon-to-iron ratio.

The main goal of this work is to develop a new tool for metallicity estimates in the infrared, that will connect with the optical indicators. Therefore, the Fe and Mg features are preferable because they can be compared directly to the traditional abundance probes.

6.2. Sample

6.2.1. Stars

The stellar sample includes over 200 high quality H and K spectra of red stars. Detailed overview of the spectral library is given in Chapter 4.

6.2.2. Galaxies

The bulk of our galaxy sample is comprised of starburst galaxies from Engelbracht (1997), who kindly provided us with a few more unpublished spectra observed with the same instruments and settings. A summary of the galaxy parameters is given in Table 6.1.

The sample is selected on the basis of high apparent $10\ \mu\text{m}$ flux, which constrained the members mainly to M 82 and NGC 253 like galaxies, and no blue compact dwarfs. A selection effect is present - the more distant galaxies tend to display brighter and more massive starbursts.

The optical-to-infrared flux ratio varies a lot across the sample: $-2 \leq \log(L_B/L_K) \leq 1$. It might be subject to aperture effects because the

B and K band photometries come from different sources (de Vaucouleurs et al. 1991 and the references therein, and Engelbracht 1997, respectively). However, most of the elevated star formation occurs in the central regions of the host galaxies. Together with the wide slit size (2.4x6 arcsec or larger), this ensures that the major fraction of the starburst light is included in the slit aperture.

Engelbracht (1997) derived ages of the last burst from 5 to 30 Myr, and in some cases demonstrated that a contribution from multiple bursts and an older red-giant dominated population is necessary to match the observations. The total starburst mass is often less than 10% of the dynamical mass of the central regions of the host.

Many of the galaxies have an obvious triggering mechanism - a bar or traces of a tidal interaction with a close companion. Some alternative mechanism is needed to explain how isolated galaxies like IC 342 were able to drive enough gas towards their centers, to feed a powerful starburst. Finally, this sample is not a complete one, and should be used for statistical comparisons with caution. However it demonstrates how broad ranges of starburst parameters can be. We also have some old systems, observed for calibration and comparison purposes.

6.3. Metallicity Indicators

We addressed in Chapter 4 the question which infrared lines are most sensitive to the metal abundance in a large sample of stars. Molecular CO bands, Ca and Na lines, used so far as metallicity indicators, indeed show metallicity effects. But they also exhibit complicated behavior, related to the surface gravity and effective temperature. On the contrary, Mg lines demonstrate a much weaker temperature dependence confirming our expectation that they are as good metallicity indicators

as their optical counterparts. Unfortunately, even the strongest iron line at $1.58\ \mu\text{m}$ is relatively weak, compared to the other features, and is placed close to stronger silicon and carbon monoxide absorptions that affect its strength, and made the continuum position uncertain. As Carr, Sellgren & Balachandran, (2000) and Ramírez et al. (2000a) demonstrated, better quality and higher resolution ($R \sim 40,000$) data are necessary to probe the iron abundance directly.

The strongest metal absorption lines in the infrared belong to magnesium. We measured four of them - at 1.50 , 1.71 , 2.11 , and $2.28\ \mu\text{m}$. The latter two are weaker, and the thermal sky background is stronger in K, making it more difficult to obtain spectra of comparable signal-to-noise to the H-band. They might be preferable for starbursts with $A_V \geq 40$ mag, when even the H band becomes opaque. For less obscured systems the first two features are preferable, and we will concentrate on them. They are both close to the edges of the atmospheric window, where the atmospheric absorption and some hydroxyle emission become problems. The redshift of extragalactic objects helps, moving the $1.50\ \mu\text{m}$ line towards a better wavelength region. It also shifts the $1.71\ \mu\text{m}$ line out of the atmospheric window, rendering it unobservable for galaxies with radial velocities greater than $8600\ \text{km s}^{-1}$. In addition, the $1.71\ \mu\text{m}$ line is contaminated by OH absorption in stars of spectral class M and later, as shown by Origlia, Moorwood & Oliva (1993, see their Figure 4a).

6.4. MgI $1.50\ \mu\text{m}$

6.4.1. Empirical Calibration

The considerations in Section 6.3 point at the best candidate for a metallicity calibrator - the MgI line at $1.50\ \mu\text{m}$. Chapter 4 defined and measured a spectral

index centered on this feature in over 200 stars, and produced multidimensional fits of the spectral index versus stellar parameters. However, spectral indices are not directly transferable from stars to galaxy spectra because the intrinsic velocity dispersion smooths the spectra and widens the feature. Therefore, we derived another fit, this time of the equivalent width versus stellar parameters. The equivalent width has the advantage of being independent from the velocity dispersion, provided a wide enough line passband is used, to encompass the entire spectral feature, and there are no other strong features nearby to contaminate the measurement. The fitting was subject to a number of constraints, emerging from the limitations of the empirical stellar library, which are discussed in detail in Chapter 4.

We followed a similar procedure as with the index fitting. The first step was to carry out a full three-dimensional fit of the effective width as function of $[\text{Fe}/\text{H}]$, temperature, and $\log g$ for giants only. We used second order terms for all independent variables, but omitted the cross terms. The last assumption effectively extrapolated the gradients over the entire parametric space, uncovered by stars.

For the purpose of this analysis we selected only stars with spectral types from K0 to M0, because the infrared spectra of most galaxies are well matched by K5 III. These stars contribute most of the near-infrared flux.

The results from this fit are shown in Figure 6.1. Obviously, the strength of MgI $1.50 \mu\text{m}$ is dominated by the metal abundance and not by any of the other two independent variables, at least over the selected range of stellar parameters.

The next step was to omit the temperature and surface gravity terms, because they are nearly constant, and to produce a more robust fit. It is shown in Figure 6.2. Again, we included the giant stars only, within the same temperature

limits. The best fit is:

$$\text{EW}(\text{MgI } 1.50\mu\text{m}) = (3.55 \pm 0.10) + (1.18 \pm 0.13) [\text{Fe}/\text{H}], \text{ \AA}. \quad (6.1)$$

We used 63 points, and the r.m.s. is 0.93 Å. Experiments with higher order polynomials did not improve the fit quality significantly.

Finally, we carried the same fit, but included the supergiants available in that temperature bin:

$$\text{EW}(\text{MgI } 1.50\mu\text{m}) = (3.45 \pm 0.09) + (1.19 \pm 0.12) [\text{Fe}/\text{H}], \text{ \AA}. \quad (6.2)$$

The number of measurements increased up to 75, with the same r.m.s. of 0.93 Å. Not surprisingly, the two equations are indistinguishable, within the errors, because the slope, in both cases, is dominated by globular cluster giants.

The inverted form of the last equation is:

$$[\text{Fe}/\text{H}] = -(2.90 \pm 0.30) + (0.84 \pm 0.08) \text{EW}(\text{MgI } 1.50\mu\text{m}). \quad (6.3)$$

6.4.2. Theoretical Calibration

The evolutionary stellar population model offers an alternative way to calibrate the strength of the MgI feature as a function of the metallicity. We followed the technique used by Origlia, et al. (1997) to produce a similar calibration for CO 1.62 μm, which includes generating a multitude of models spanning the entire feasible parametric space. They described the variations of the stellar population with three parameters - averaged effective temperature and surface gravity over the entire population, and microturbulent velocity. The later is a significant parameter only for saturated, or close to the saturation limit spectral features. This is the case with the CO bands in cool stars but not with the magnesium lines. Thus, we can simplify the parameterization by omitting the microturbulent velocity.

Next, we adopted a more direct approach, and instead of estimating the average stellar parameters, constrained our calibrations to the models with ages older than 15 Myr. This condition was additionally enforced by the limitations of the spectral library, implemented in the model. As it was discussed in Chapter 4, the library lacks metal poor supergiants, and therefore the predicted values of the spectral indices around the peak at 7-10 Myr are unreliable for low metallicities.

Figure 6.3 shows the synthetic calibration for MgI at $1.50 \mu\text{m}$. The solid line is a fit to all four available metallicities:

$$\text{EW}(\text{MgI } 1.50\mu\text{m}) = (3.30 \pm 0.13) + (1.85 \pm 0.19) [\text{Fe}/\text{H}], \text{ \AA}. \quad (6.4)$$

It uses 32 models, and has a r.m.s = 0.63 \AA . The inverse equation is:

$$[\text{Fe}/\text{H}] = -(1.78 \pm 0.19) + (0.54 \pm 0.05) \text{EW}(\text{MgI } 1.50\mu\text{m}). \quad (6.5)$$

For test purposes we calculated a similar calibration, omitting the $[\text{Fe}/\text{H}] = -0.4$ models, and obtained:

$$\text{EW}(\text{MgI } 1.50\mu\text{m}) = (3.00 \pm 0.06) + (1.89 \pm 0.08) [\text{Fe}/\text{H}], \text{ \AA}. \quad (6.6)$$

This relation has a r.m.s = 0.25 \AA , and is based on 24 model spectra. The two equations have the same slope, within the errors, but the zero-points differ by 0.3 \AA , which is about 2σ effect. We prefer using Equation 6.5 to the inverse of Equation 6.6, because it represents better the true model uncertainties. We also experimented with including models with ages down to 12 Myr into the fit, and found no significant differences.

The calibration, based on individual stars with K0-M0 spectral types is also shown in Figure 6.3 (dotted line). Apparently, they are virtually the same for

$[\text{Fe}/\text{H}] \geq -0.75$. The fits diverge for lower metallicities where the number of stars decreases, but the differences are never statistically significant.

Finally, we would like to point out, that although the calibrations in this section rely on theoretical stellar evolutionary tracks, derived from first principles, they are not purely theoretical, because the model uses an empirical stellar library.

6.4.3. Magnesium-based Metallicities of the Sample Galaxies

We measured the Mg line equivalent widths of our galaxy sample by hand, using the *splot* task in *IRAF*. We repeated the procedure multiple times, and estimated the variance. The uncertainties are dominated by the continuum placement. The measurements and the derived metallicities are given in Table 6.2. The $\sigma([\text{Fe}/\text{H}])$ reflects only the observational errors. Metallicities of starbursts younger than 12 Myr should be considered upper limits.

The histograms of magnesium-based abundances are shown on the left (observational calibration, Equation 6.3) and on the central panels (theoretical calibration, Equation 6.5) in Figure 6.4. Not surprisingly, the giant elliptical and S0's appear to be metal rich (bottom panel). The narrow span of their metallicities is encouraging, although more data are certainly necessary to test the quality of the new indicator. The starbursts show significant spread (top panels). This spread appears to be related with the age of the last epoch of star formation. Indeed, if we constrain the starbursts only to the ones older than 12 Myr, the spread is reduced greatly (middle panels), and the new distributions are centered near the solar abundance.

6.5. CO 1.62 μm

We applied to the same galaxy sample the CO 1.62 μm technique developed by Origlia et al. (1997). Table 6.3 summarizes our analysis. We measured the Si, and CO indices with the *IRAF* task *sband*, according to the definitions given in Origlia, Moorwood & Oliva (1993), and applied the velocity dispersion corrections from Oliva et al. (1995). Unlike the MgI 1.50 μm , which lies in a clear continuum region, these features are placed near other absorptions, and the indices can not be expanded freely to encompass the entire lines or bands. The corrections increase the measured indices by 10-15% depending on the intrinsic velocity dispersion σ , which was measured by Gaussian fits to 3-4 emission lines, usually including [FeII] 1.64 μm , Br γ , and H₂ at 2.16 μm and 2.12 μm . The velocity dispersion uncertainties cited in the table is the variance of these measurements, and has to be treated with caution because of the small number statistics.

To estimate the iron abundance [Fe/H] with this method, we adopted a microturbulent velocity $\xi = 3 \text{ km s}^{-1}$ and a "standard" carbon-to-iron ratio [C/Fe] = -0.3 (see Origlia et al. 1997 for discussion). Even after the velocity dispersion correction, the derived [Fe/H] are significantly lower than expected, particularly for the giant elliptical and S0 galaxies in our sample (Figure 6.4, the right panels).

Seeking to resolve the source of this difference, we compared the measure Si equivalent widths for the two galaxies we have in common with Oliva et al. (1995) - NGC 3379, and NGC 1614. In both cases our EW(Si1.58) are lower, and the average difference is 0.94 \AA . Even if we increase all our Si measurements by that amount, the E and S0 galaxies are still metal poor. This suggests that either the adopted microturbulent velocity ξ , or more probably, the carbon-to-iron ratio

[C/Fe] has to be modified. This agrees with the conclusion of Origlia et al. (1997), that very low [C/Fe] is needed in order to reproduce the optically derived metal abundance of their entire sample of galaxies and globular clusters.

6.6. Infrared Metallicities of the Sample Galaxies and Iron Abundance

A crucial test for the new magnesium-based metallicities is whether they correlate with the optical stellar metal absorption line strengths, especially with iron indices. The literature does not offer a comprehensive uniform set of optical absorption line measurements for starburst galaxies. The prominent emission lines are a lesser observational challenge. The strong dust extinction in the starbursts has discouraged such attempts even further.

For self-consistency, we selected only the galaxies with optical spectroscopy from Ho, Filippenko & Sargent (1997). The data correlate very well with our [Fe/H] estimates (Figure 6.5). The most notable exception is IC 342, but it has an extremely young starburst age (6.5 Myr, Engelbracht 1997), making our metallicity only an upper limit. The spectroscopy of Engelbracht (1997) suggests a significant internal extinction of $A_V \sim 7.5$ mag.

The other galaxy that deviates from the relation is NGC 2782, although the deviation from the correlation seems to diminish as more indices are averaged, as is the case with the combined calcium-iron index (bottom left panel). Engelbracht (1997) estimated that the starburst in this barred galaxy is subject to about 3 mag of visual extinction.

Trager et al. (1998) included in their survey NGC 2146, 3115, 3379, and 4339. Their measurements confirmed that the first of these galaxies exhibits very weak optical metal indices, in excellent agreement with the low metallicity derived by

our method.

Our result implies that the magnesium abundance follows very well the iron abundance, which can be explained only if all host galaxies have undergone significant star formation in the past, to produce enough iron-peak elements. In this context, the weak iron line of IC 342 might be a result from the specific star formation history, rather than a property of the most recent burst. Metallicity indicators, based on magnesium and other α -elements are preferable in studies of young stellar systems.

6.7. Metallicity and Parameters of the Sample Starburst Galaxies

We explored the correlations between the newly estimated metallicities, and the properties of the starbursts. More massive galaxies, with a larger gas reservoir can retain an elevated star formation rate for a longer time period, and their deeper potential well help to retain the produced metals, in comparison with less massive galaxies. This leads to the well known mass-metallicity relation in galaxies (e.g. Zaritsky 1993). Starbursts, occurring in larger galaxies will have to be more metal rich, because they start with already enriched material.

The new metallicity estimates are plotted versus the absolute B-band magnitude of the host galaxy in Figure 6.6 (top panel). The intrinsically brighter galaxies are indeed more metal rich. However, M_B is not the best galaxy mass indicator. It is affected by reddening, and by the presence of the starburst itself. That is why we also compared out $[\text{Fe}/\text{H}]$ with the intrinsic velocity dispersions. Contrary to the expected, less massive galaxies seem to harbor more metal rich bursts (dashed line). Careful inspection of the data reveal that the slope is dominated by the few galaxies with extremely young bursts (indicated with stars).

If they are removed, the correlation diminished greatly (solid line). The limited statistics prevents us from a more sophisticated analysis, and further study is necessary to verify this result. The lack of correlation may be related to the type of star formation triggering mechanisms, or to variation of the initial mass function from burst to burst.

We studied also the relation between the new metal estimates and the parameters of the starbursts themselves (Figure 6.7). Even though the sample is limited, some conclusions can be drawn from this comparison.

The quick self-enrichment with α -elements would lead to increase of the magnesium line strength with age, at least in older starbursts. Our data for starbursts with $t \geq 12$ Myr do show such a trend, albeit marginal (solid line, top panel). Younger bursts have a significant spread.

Surprisingly, starbursts brighter in K-band tend to be metal poor (middle panel). However, this trend is due mostly to the presence of NGC 2146, a very low metallicity galaxy with an extremely young burst. If we include only the bursts with age greater than 12 Myr, for which our calibrations work best, the trends disappear (solid lines). The K-band luminosity is related to the mass of the burst, which is determined, at least to first order, by efficiency of the star formation triggering mechanism, and the available gas, but not directly by the metal abundance. Similar situation exists with the dynamically estimated mass (Engelbracht 1997, bottom panel).

The one notable member of our sample is NGC 2146, the most metal poor member of the sample. It is a disturbed galaxy, with no apparent companion, and the irregular morphology could be related to the presence of prominent dust lanes. The HI radio observations produced a striking result - W20 and W50 differ by a

factor of 2.5 (de Vaucouleurs et al. 1991). Therefore, tidal interaction remains a possibility. The galaxy is nearly edge-on but the extinction (Engelbracht 1997) is not very different from that of other starbursts. However, his starburst modeling predicted a larger luminosity than observed. Engelbracht (1997) suggested that most of the flux probably escapes the galaxy perpendicularly to the disc.

Clearly, this object requires further attention. Its presence hints that the sample may indeed be too uniform, to represent the true metallicity range of starburst galaxies, even though the age and mass spreads are large.

Finally, we investigated the relation between the metal content and the dust temperature, represented by the *IRAS* flux ratios (Moshir et al. 1990). More metal rich starbursts seem to associate with galaxies in which the ratios F_{25}/F_{12} , F_{60}/F_{12} , and F_{100}/F_{12} are lower (Figure 6.8).

The dust emits as a black body, and it has a temperature of a few hundred degrees in a typical starburst environment. The dust spectrum peaks red-ward of 30-60 μm . The abundance can only change the total amount of dust, leaving the colors of the dust emission unchanged. More metal rich bursts produce more ultraviolet flux, increasing the dust temperature. Higher dust temperature moves the peak to the blue, increases the flux at 12 μm , and reduces F_{25}/F_{12} and the other ratios, just as the observations suggest. This result confirms independently our metallicity estimates.

6.8. Magnesium and the Iron Abundance in Starbursts

Optical magnesium lines are widely used to measure the iron abundance in galaxies. It is well known that the Mg-to-Fe ratio varies from galaxy to galaxy, depending on the specific star formation history. For instance, in the extreme case of giant

old ellipticals it is about 0.2-0.3 dex higher than in the metal rich Milky Way stars (Worthey, Faber & Gonzalez 1992). Starbursts represent the other extreme scenario, where a very recent burst of star formation is taking place. In this section we address the question if the magnesium abundance matches the iron abundance, and whether the enrichment history prior the burst is important for magnesium-based metallicity estimates.

6.8.1. Chemical Enrichment Toy-Model

We built a simple numerical model to simulate the star formation and chemical enrichment in galaxies. Similar models were pioneered by Talbot & Arnett (1971) and Tinsley (1975), among others. Recently, much more sophisticated chemical models were developed (e.g. Portinari, Chiosi, & Bressan 1998; Thomas, Greggio, & Bender 1998). The uncertain chemical yields prove to be a crucial obstacle to the interpretation of the results. A comparison between the Type II supernovae yields from different sources is particularly discouraging. For instance, the ^{24}Mg yield in a explosion of a 20 solar mass star, predicted by Woosley & Weaver (1995) and Thielemann, Nomoto, & Hashimoto (1996) differ by a factor of 4.7. The yields from Type I supernovae, and the mass loss rates during post-main sequence stages of low mass stars face similar problems.

These considerations prompted us to pursue a model, with just two generic elements, one representing the α -elements, and the other representing the heavy iron peak elements. We followed the outline of the model of Ferreras & Silk (2000) that went even further in the simplification, calculating only the total amount of heavy elements. The main assumption in that model is the instantaneous recycling of the material. The metallicity of the young stars follows closely that of the gas, helping to reduce the number of equations.

Our model has four components: total mass in gas M_g , the total mass in stars M_s , and masses M_{Z1} and M_{Z2} in elements Z1 and Z2, respectively.

The basic processes, taken into account are: (i) star formation with an efficiency C_{eff} , (ii) galactic superwind leading to a loss of a fraction B_{out} of the stellar ejecta, and (iii) an infall of a gas with mass A_{inf} at a moment τ_{lag} after the beginning of star formation, with a time scale τ_{inf} .

We assume that at time $t = 0$ yr, all of the material is in gaseous form, so $M_g(t = 0) = M_{total}$, $M_s(t = 0) = 0$, and masses of metals are determined by their initial mass fractions Z_{Z1}^0 and Z_{Z1}^0 . The same mass fractions determine the metallicities of the infalling material.

The four equations for the temporal evolution are:

$$\frac{dM_g}{dt} = -C_{sfr} M_g(t) + C_{sfr} (1 - B_{out}) M_E + \Theta(t - \tau_{lag}) A_{inf} e^{(t - \tau_{lag})/\tau_{inf}}, \quad (6.7)$$

$$\frac{dM_s}{dt} = C_{sfr} M_g(t) - C_{sfr} M_E. \quad (6.8)$$

$$\frac{dM_{Z1}}{dt} = -C_{sfr} M_{Z1}(t) + C_{sfr} (1 - B_{out}) M_E^{Z1} + \Theta(t - \tau_{lag}) Z_{Z1}^0 A_{inf} e^{(t - \tau_{lag})/\tau_{inf}}, \quad (6.9)$$

$$\frac{dM_{Z2}}{dt} = -C_{sfr} M_{Z2}(t) + C_{sfr} (1 - B_{out}) M_E^{Z2} + \Theta(t - \tau_{lag}) Z_{Z2}^0 A_{inf} e^{(t - \tau_{lag})/\tau_{inf}}, \quad (6.10)$$

where

$$M_E = \int_{m_t}^{m_{up}} dm \phi(m) \frac{(m - \omega_m)}{m} M_g(t - \tau_m) \quad (6.11)$$

is the ejected mass from stars that have reached the end of their lifetime τ_m , and have been formed at time $t - \tau_m$. The integration limits are the mass at the turn-off point m_t at time t , and the upper stellar mass limit $m_{up} = 120 M_\odot$. The mass loss is weighted by the initial mass function $\phi(m)$. We assumed a simple power law with Salpeter (1955) slope, normalized to a total mass of unity.

Here we adopted for τ_m a power law fit from Ferreras & Silk (2000), based on data from Tinsley (1980) and Schaller et al. (1992):

$$\left(\frac{\tau_m}{Gyr}\right) = \begin{cases} 9.694 \left(\frac{m}{M_\odot}\right)^{-2.762}, & m < 10M_\odot \\ 0.095 \left(\frac{m}{M_\odot}\right)^{-0.764}, & m > 10M_\odot \end{cases} \quad (6.12)$$

The model excludes from circulation the mass ω_m , locked out in stellar remnants. Again, we used the parameterization of Ferreras & Silk (2000):

$$\left(\frac{\omega_m}{M_\odot}\right) = \begin{cases} 0.1(m/M_\odot) + 0.45, & m/M_\odot < 10 \\ 1.5, & 10 < (m/M_\odot) \leq 25 \\ 0.61(m/M_\odot) - 13.75, & m/M_\odot > 25 \end{cases} \quad (6.13)$$

The three cases are based on, respectively: Iben & Tutukov (1984), Shapiro & Teukolsky (1983), and Woosley & Weaver (1995).

The metals Z1 and Z2, produced in stars and returned into the gas are described by:

$$M_E^{Z1,2} = \int_{m_t}^{m_{up}} dm \phi(m) \mathcal{Y}_{Z1,2} \frac{(m - \omega_m)}{m} M_g(t - \tau_m) \quad (6.14)$$

where $\mathcal{Y}_{Z1,2}$ is the fraction of the stellar mass, turned into metal Z1,2, i.e. the yield.

The step function $\Theta(t)$ is zero for $t < 0$ and one for $t \geq 0$. We integrated the system numerically, using a fourth order Runge-Kutta method (Press et al. 1992).

6.8.2. Discussion

The problem of magnesium and iron metallicity inconsistency reflects the different time scales of heavy element production. The α -elements, including Mg, are produced mostly in short lived massive stars. They are result of the CNO burning, and are made even in stars with zero initial metallicity. Therefore, they accumulate

within only a few tens of millions of years from the beginning of the star formation. The α -elements in our model are represented by Z1, formed only in stars with mass $m > 12M_{\odot}$, with a yield of $\mathcal{Y}_{Z1,2} = 10^{-2}$, based on the typical values from Woosley & Weaver (1995).

In contrast, the iron peak elements need higher temperatures, that generally happen during the late stages of stellar evolution. Such conditions occur in explosions. We consider two types. It is commonly accepted that Type II supernovae are core-collapse events in massive stars. They are present in spiral galaxies, but not in present day ellipticals. Low-mass binary stars produce Type I supernovae, which also contributes to the iron peak elements. These elements are represented in our model by Z2, which is being formed in all stars, with an yield $\mathcal{Y}_{Z1,2} = 10^{-3}$ (Woosley & Weaver 1995; Nomoto, Iwamoto, & Kishimoto 1997).

We also adopted for both elements Z1 and Z2 a solar abundance of $Z_{Z1,2\odot} = 5 \times 10^{-4}$, of the same order as the real solar iron and magnesium abundances. The initial metallicities are $Z_{Z1,2}^0 = 10^{-7}$.

Figure 6.9 (top panel) illustrates the evolution of a metallicity for a continuous star formation over the first 100 Myr. As expected, the α -elements build up quickly, and over the first 10-20 Myr. The ratio of the two abundances is determined only by the ratio of their yields, because at this time the massive stars are still present to enrich the galaxy with metals.

Introducing a previous burst may change the metallicity ratios drastically (Figure 6.9, bottom panel). A 15 Myr long burst, 4 Gyr ago, with twice the mass of the current burst, would enrich the material to about $Z_{Z1}^0 = 10^{-4}$, and $Z_{Z2}^0 = 10^{-5}$, respectively. It would also introduce an additional source of iron peak metals, coming from the low mass stars of the previous burst. The abundance ratio

Z_{Z1}/Z_{Z2} in this case is twice lower than the one produced by a "virgin" burst.

A similar problem is well known to exist in elliptical galaxies, but the shorter time scale of the starburst worsens it. This result calls for extra caution interpreting magnesium (this work) and carbon monoxide (Origlia et al. 1997) metallicity estimates of starbursts. The last burst of star formation completely dominates the spectrum of the galaxy, and the possibilities to constrain the preceding star formation history are limited. Only using a multiplicity of abundance indicators, related to different types of metals, can resolve this uncertainty. Most of the strong stellar absorption features in the infrared (CO, Si, Mg) belong to the α -elements. Sodium and aluminum, represented by a few weaker lines are mostly products of C and O burning in hot stars. However, as the stellar studies have demonstrated, there is a number of even weaker iron lines (Carr, Sellgren & Balachandran 2000, Ramírez et al. 2000a) that could be explored, given adequate data quality. Calcium, though an α -element, has been found to follow the iron abundance in elliptical galaxies and spheroid (Worthey 1998).

Infall of low metallicity gas can affect the metallicity of the stellar populations, although on a much longer time scale than a typical starburst. The loss of material through galactic superwind do not change our result to first order, because they only scale the total mass of the galaxy. Selective loss of metals, which can be thrown into the extragalactic space in the powerful supernova ejecta is a possibility but it falls outside of the scope of this work.

6.9. Summary

We defined a new metallicity indicator for obscured stellar systems in the infrared, based on MgI 1.50 μm line, and calibrated it (i) against [Fe/H] for the stars that

dominated the infrared flux in galaxies, and (ii) with an infrared evolutionary population model. The application of this indicator is limited to stellar systems older than 12-15 Myr, after the red supergiants have evolved and the stellar population is dominated by red giants.

The new technique was applied on a sample of starburst galaxies (Engelbracht 1997). The derived metallicities correlate very well with the strength of optical metal indices. We also compared our results with the abundance estimates based on the CO 1.62 μm (Origlia et al. 1997) and found that the latter underestimate the metallicities of galaxies.

Finally, we explored the variations of the abundance ratios in starbursts, by means of a simple chemical enrichment model. We demonstrated that the fraction of iron peak elements can be influenced significantly by the preceding star formation history. This poses a significant problem to metallicity estimates, based on α -element spectral features, but also opens up a possibility to explore the star formation history before the last burst had occurred. Our result underlines the importance of using abundance indicators based on elements of different types.

Table 6.1 Properties of the galaxy sample.

ID	Type	Dist.	B_T^0	W20	W50	Age
(1)	(2)	(3)	(4)	(5)	(6)	(7)
Starburst Galaxies						
IC 342	SAB(rs)cd	3.6(2)	5.58	175 ± 7	151 ± 6	6.5
Maffei 2	SAB(rs)bc?	3.6(2)		347 ± 7	305 ± 8	14.5
Mkn 331	S? HII Sy2	74.0(1)				13.0
NGC 253	SAB(s)c HII	2.6(6)	7.09	518 ± 5	410 ± 4	5.5
NGC 520	S?	11.0(1)	11.97			12.5
NGC 660	SB(s)a pec LINER	11.0(1)	11.44			11.5
NGC 1614	SB(s)c pec HII Sy2	64.0(1)	13.28			10.5
NGC 2146	SB(s)ab pec HII	12.0(3)	10.58	499 ± 6	194 ± 11	6.5
NGC 2782	Sb	34.0(1)	12.01	190 ± 4	145 ± 4	13.0
NGC 3079	SB(s)c LINER Sy2	15.0(3)	10.41	473 ± 7	435 ± 5	30.0
NGC 3628	Sb pec	11.0(1)	9.31	476 ± 3	449 ± 3	12.0
NGC 4102	SAB(s)b? LINER	11.0(1)	11.61	315 ± 8	283 ± 6	13.0
NGC 4194	IBm pec	33.0(1)	12.86	151 ± 5	87 ± 4	11.5
NGC 5990	(R')Sa pec?	51.0(1)		398 ± 5	398 ± 5	15.0
NGC 6000	SB(s)bc? HII	28.0(1)				12.0

ID	Type	Dist.	B_T^0	W20	W50	Age
(1)	(2)	(3)	(4)	(5)	(6)	(7)
NGC 6240 I0?	pec LINER Sy2	98.0(1)	13.17		172 ± 7	13.5
Comparison Galaxies						
NGC 3115 S0-		11.0(3)	9.74	254 ± 9		
NGC 3379 E1		11.5(4)	10.18			
NGC 4339 E0		17.0(3)	12.31			

COMMENTS: (1) Identifier; (2) Morphological type from NED; (3) Distances in Mpc, the reference number is given in brackets; (4) Total B-magnitude corrected for absorption and inclination from RC3 (de Vaucouleurs et al. 1991); (5), (6) W20, W50 - HI line widths in km s^{-1} from RC3; (7) starburst age estimate in Myr (Engelbracht 1997).

REFERENCES - Distances: (1) redshifts from Engelbracht (1997), and adopting $H_0 = 75 \text{ km s}^{-1} \text{ Mpc}^{-1}$; (2) Krishmer, Tully, & Giola (1995); (3) cz from NED, and adopting $H_0 = 75 \text{ km s}^{-1} \text{ Mpc}^{-1}$; (4) Sakai et al. (1997); (5) Elson (1997); (6) Puche & Carignan (1988).

Table 6.2 Magnesium line ($1.50 \mu\text{m}$) measurements and derived metallicities of the galaxies.

ID	EW(Mg1.50)	[Fe/H] _o	[Fe/H] _t
(1)	(2)	(3)	(4)
Starburst Galaxies			
IC 342	4.45 ± 0.12	0.84 ± 0.45	0.62 ± 0.29
Maffei 2	3.56 ± 0.20	0.09 ± 0.60	0.14 ± 0.38
Mkn 331			
NGC 253	4.14 ± 0.10	0.58 ± 0.35	0.46 ± 0.22
NGC 520			
NGC 660			
NGC 1614	3.80 ± 0.10	0.29 ± 0.32	0.27 ± 0.21
NGC 2146	1.57 ± 0.07	-1.58 ± 0.09	-0.93 ± 0.06
NGC 2782	3.60 ± 0.25	0.12 ± 0.76	0.16 ± 0.49
NGC 3079	3.29 ± 0.11	-0.14 ± 0.30	-0.00 ± 0.20
NGC 3628	3.22 ± 0.18	-0.20 ± 0.49	-0.04 ± 0.31
NGC 4102	2.60 ± 0.13	-0.72 ± 0.28	-0.38 ± 0.18
NGC 4194	4.26 ± 0.17	0.68 ± 0.61	0.52 ± 0.39
NGC 5990	3.49 ± 0.21	0.03 ± 0.62	0.10 ± 0.40
NGC 6000	3.28 ± 0.34	-0.14 ± 0.94	-0.01 ± 0.60
NGC 6240	3.02 ± 0.19	-0.36 ± 0.48	-0.15 ± 0.31

ID	EW(Mg1.50)	[Fe/H] _o	[Fe/H] _t
(1)	(2)	(3)	(4)
Comparison Galaxies			
NGC3115	4.10 ± 0.13	0.54 ± 0.45	0.43 ± 0.29
NGC3379	3.98 ± 0.15	0.44 ± 0.50	0.37 ± 0.32
NGC4339	3.79 ± 0.12	0.28 ± 0.38	0.27 ± 0.25

COMMENTS: (1) Identifier; (2) MgI 1.50 μ m
equivalent width in Å; (3) [Fe/H] estimate using
the observational calibration (Eqn. 6.3); (4) [Fe/H]
estimate the theoretical calibration (Eqn. 6.5).

Table 6.3 Measurements and derived parameters of the galaxies.

ID	Measured EW			σ	σ -corrected EW ^a			[Fe/H]	[Fe/H]
	Si	CO _H	CO _K	km s ⁻¹	Si	CO _H	CO _K		corr.
(1)	(2)	(3)	(4)	(5)	(6)	(7)	(8)	(9)	(10)
Starburst Galaxies									
IC 342	1.56	4.83	15.8	173 ± 28	1.71	5.22	17.4	-0.34	-0.14
Maffei 2	3.58	4.45	13.6	208 ± 6	4.04	4.92	15.4	-0.40	-0.21
Mkn 331	0.81	1.67	11.2	443 ± 59	1.08	2.12	14.8	-0.98	-0.78
NGC 253	1.69	3.96	12.5	224 ± 16	1.93	4.42	14.3	-0.51	-0.31
NGC 520				326 ± 19					
NGC 660	0.89	3.04	10.7	343 ± 6	1.11	3.65	13.3	-0.67	-0.47
NGC 1614	1.68	4.64	14.6	331 ± 9	2.08	5.53	18.1	-0.28	-0.08
NGC 2146	1.35	3.54	11.0	249 ± 12	1.57	4.02	12.8	-0.59	-0.39
NGC 2782	1.63	4.00	9.4	309 ± 16	1.98	4.71	11.4	-0.45	-0.25
NGC 3079	2.12	3.65	10.7	345 ± 20	2.65	4.39	13.4	-0.51	-0.32
NGC 3628	1.98	3.48	11.2	265 ± 12 ^b	2.33	3.99	13.2	-0.60	-0.40
NGC 4102	1.82	3.69	11.1	342 ± 13	2.27	4.43	13.8	-0.50	-0.31
NGC 4194	4.29	4.72	10.7	177 ± 17	4.73	5.11	11.8	-0.36	-0.17
NGC 5990	1.21	3.22	5.7	409 ± 39	1.58	4.02	7.4	-0.59	-0.39
NGC 6000	0.52	2.97	12.3	423 ± 20	0.68	3.74	16.2	-0.65	-0.45
NGC 6240	1.53	2.56	7.5	716 ± 45	2.40	3.75	11.8	-0.65	-0.45

ID	Measured EW			σ	σ -corrected EW ^a			[Fe/H]	[Fe/H]
	Si	CO _H	CO _K	km s ⁻¹	Si	CO _H	CO _K		corr.
(1)	(2)	(3)	(4)	(5)	(6)	(7)	(8)	(9)	(10)
Comparison Galaxies									
NGC 3115	1.84	3.08	10.1	247 ^c	2.14	3.49	11.8	-0.70	-0.50
NGC 3379	1.70	3.38	9.3	218 ^c	1.93	3.76	10.6	-0.64	-0.45
NGC 4339	2.94	3.27	8.0	135 ^c	3.13	3.44	8.5	-0.71	-0.51

^a see Oliva et al. (1995)

^b Whitmore, McElroy & Tonry (1985) measured 173 km s⁻¹

^c from Whitmore, McElroy & Tonry (1985)

COMMENTS: (1) Identifier; (2,6) SiI 1.58 μm equivalent width in \AA ; (3,7) CO 1.62 μm equivalent width in \AA ; (4,8) CO 2.29 μm equivalent width in \AA ; (5) velocity dispersion σ , measured from the infrared emission lines, in km s⁻¹; (9) CO 1.62 μm based iron abundance (Origlia et al. 1997); (10) iron abundance, corrected for the systematic difference of EW with Origlia et al. (1997).

See Section 6.7 for details.

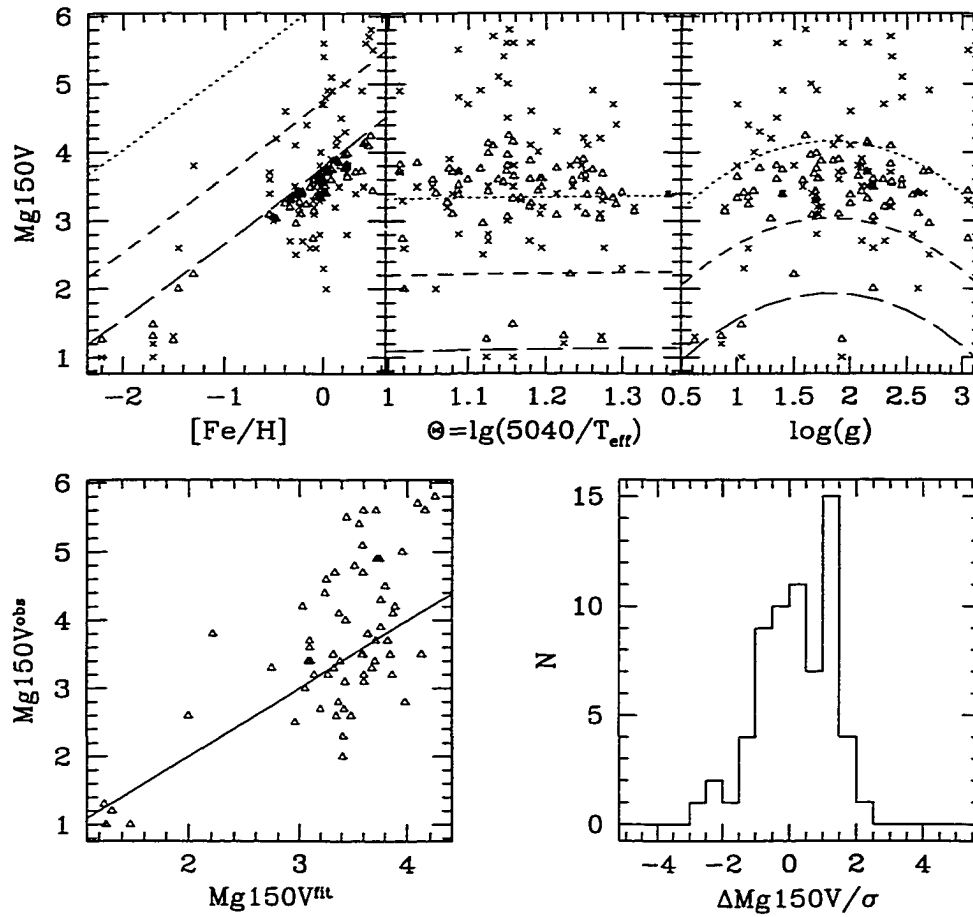


Figure 6.1 Tree-dimensional fit for MgI $1.50 \mu\text{m}$ equivalent width (in \AA). Only K0-M0 III are included. The top panels show the behavior of the index as function of $[\text{Fe}/\text{H}]$, V-K, and $\log g$. Crosses are measurements, and triangles are corresponding fit values. The lines on the top left are fits for V-K=7 (dots), 5 (short dashes), and 3 mag (long dashes), and $\log g=1.0$. The lines in the top middle are fits for $[\text{Fe}/\text{H}]=0$ (dots), -1 (short dashes), and -2 (long dashes), and $\log g=1.0$. The lines in the top right are fits for $[\text{Fe}/\text{H}]=0$ (dots), -1 (short dashes), and -2 (long dashes), and V-K=3.0 mag. The bottom left shows the observed versus fitted values, and the bottom right shows the residuals to the fit normalized to the measurement errors σ .

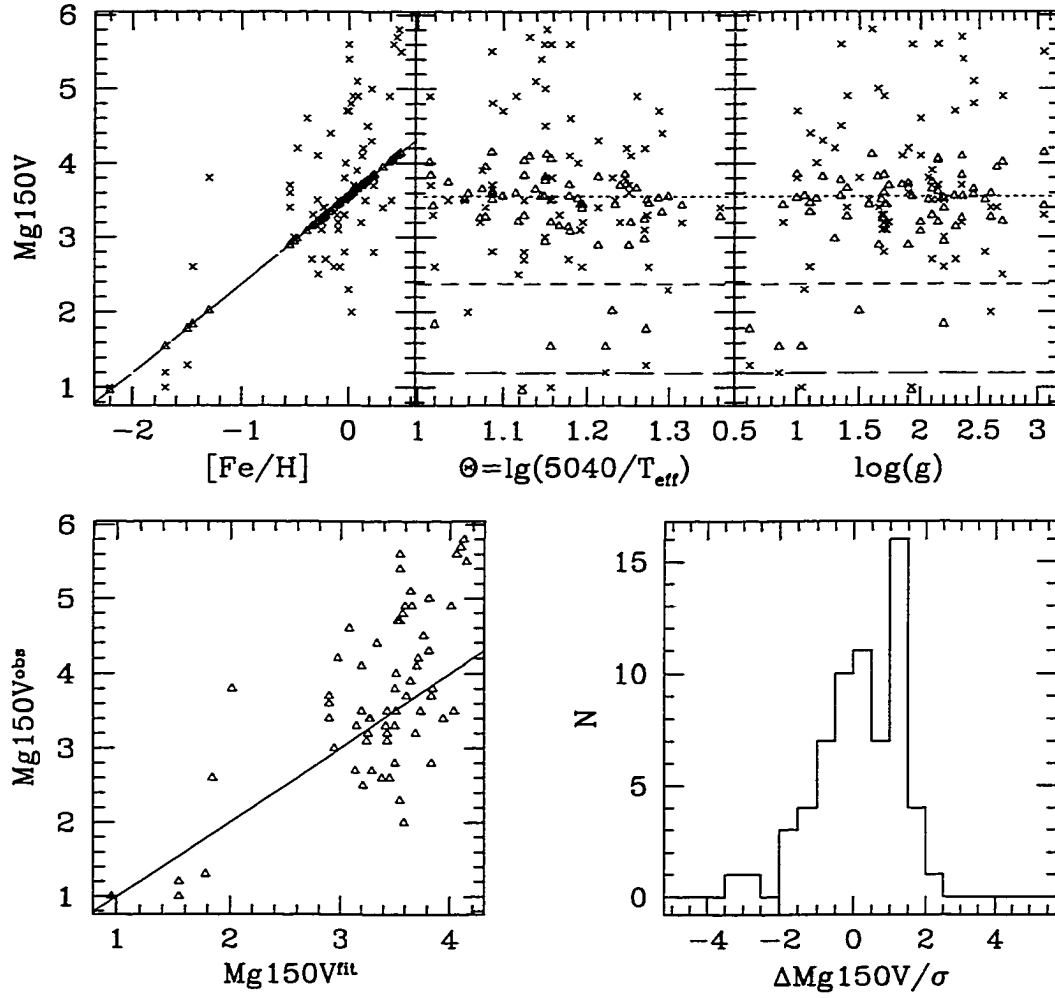


Figure 6.2 One-dimensional fit for MgI $1.50 \mu\text{m}$ equivalent width (in \AA). Only K0-M0 giants are included. For the basic description see Figure 6.1.

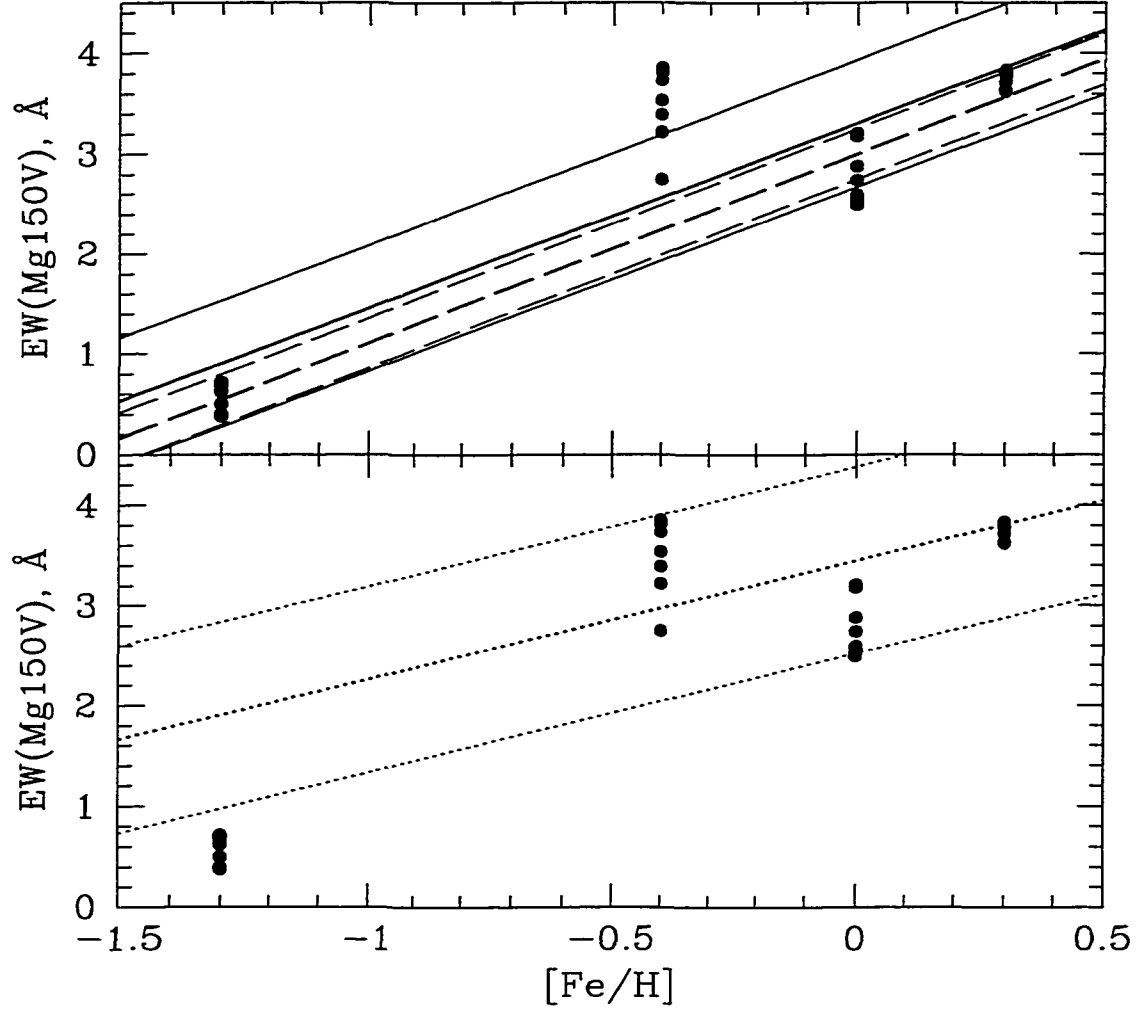


Figure 6.3 Theoretical calibration of MgI $1.50\ \mu\text{m}$ equivalent width (in \AA) versus $[Fe/H]$ (top panel), and observational calibration (bottom panel). The solid lines are a fit to models with all available metallicities, the dashed lines omit the $[Fe/H] = -0.4$ model, and the dotted lines are the calibration based directly on K0-M0 stars from the spectra library. In all cases the thicker central line is the fit, and the two side lines represent the fit $\pm 1\sigma$.

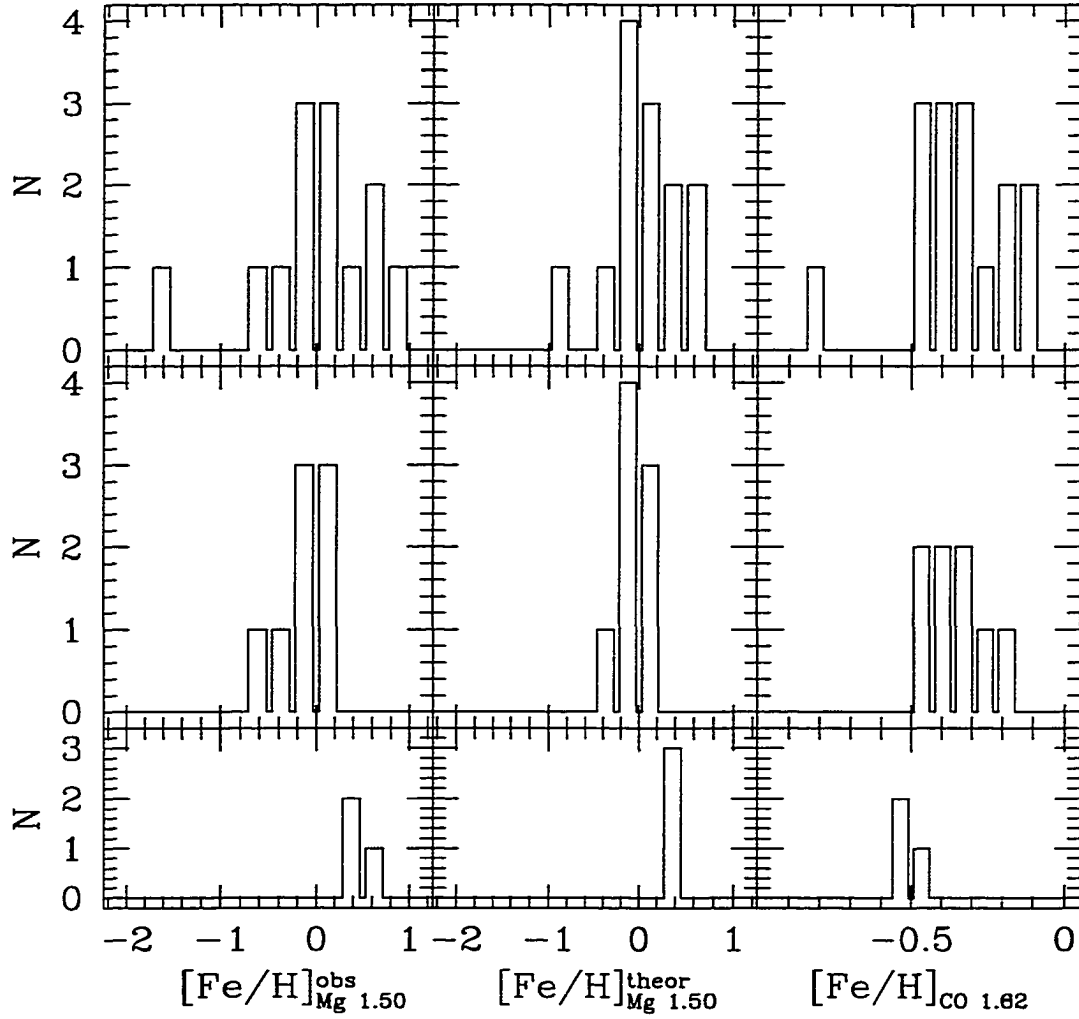


Figure 6.4 Histograms of the derived metallicities from MgI 1.50 μm (observational - Equation 6.3 on the left panels; theoretical - Equation 6.5 on the central panels; this work) and CO 1.62 μm (right panels; Origlia et al. 1997). The top panels show all starbursts, magnesium-based estimates for the starbursts older than 12 Myr are shown on the middle row, and elliptical and S0 galaxies are shown on the bottom.

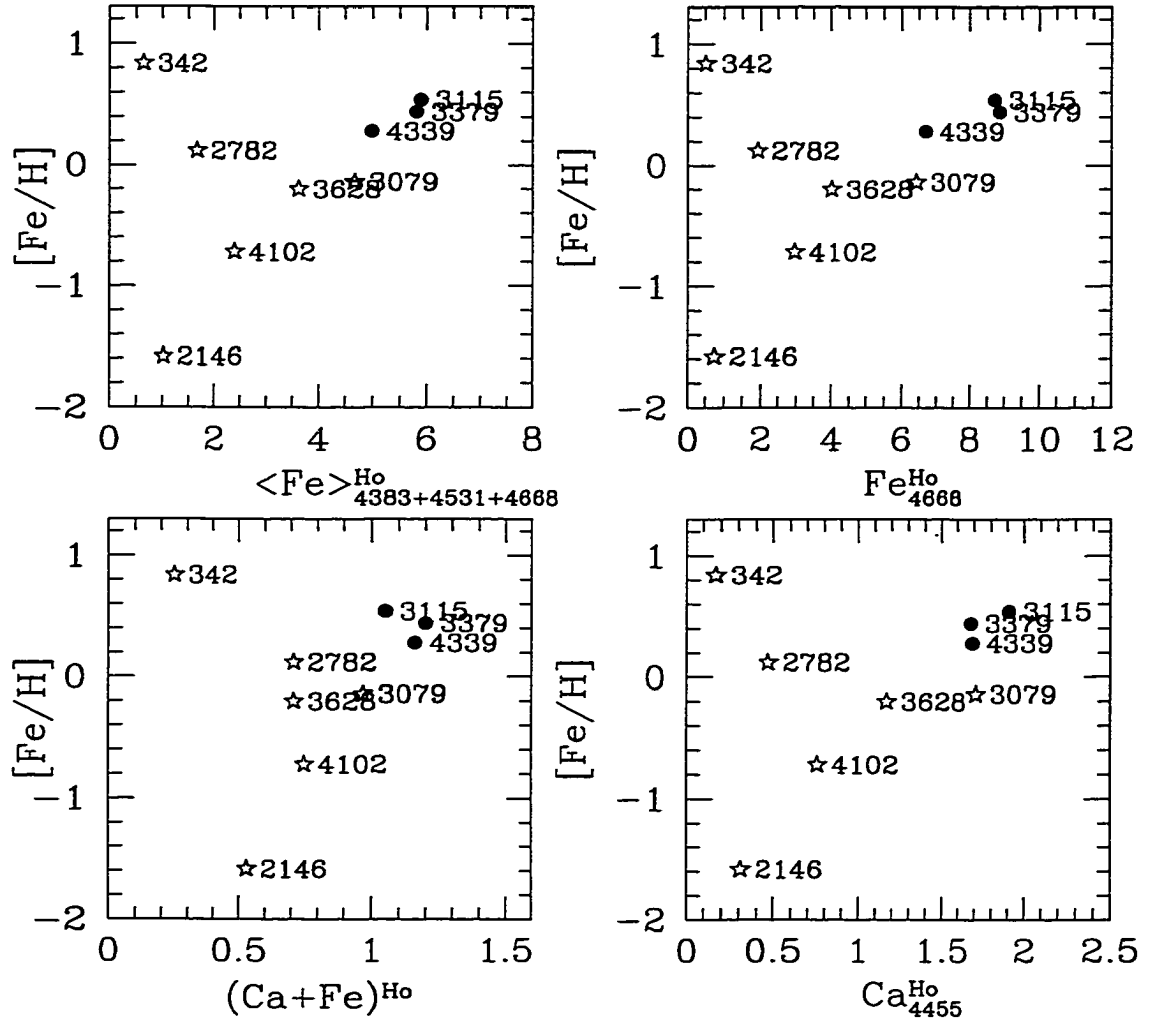


Figure 6.5 Magnesium-based iron abundance versus optical metal indices from H α , Filippenko & Sargent (1997). Stars are starburst and solid dots are elliptical and S0 galaxies. IC and NGC numbers are indicated.

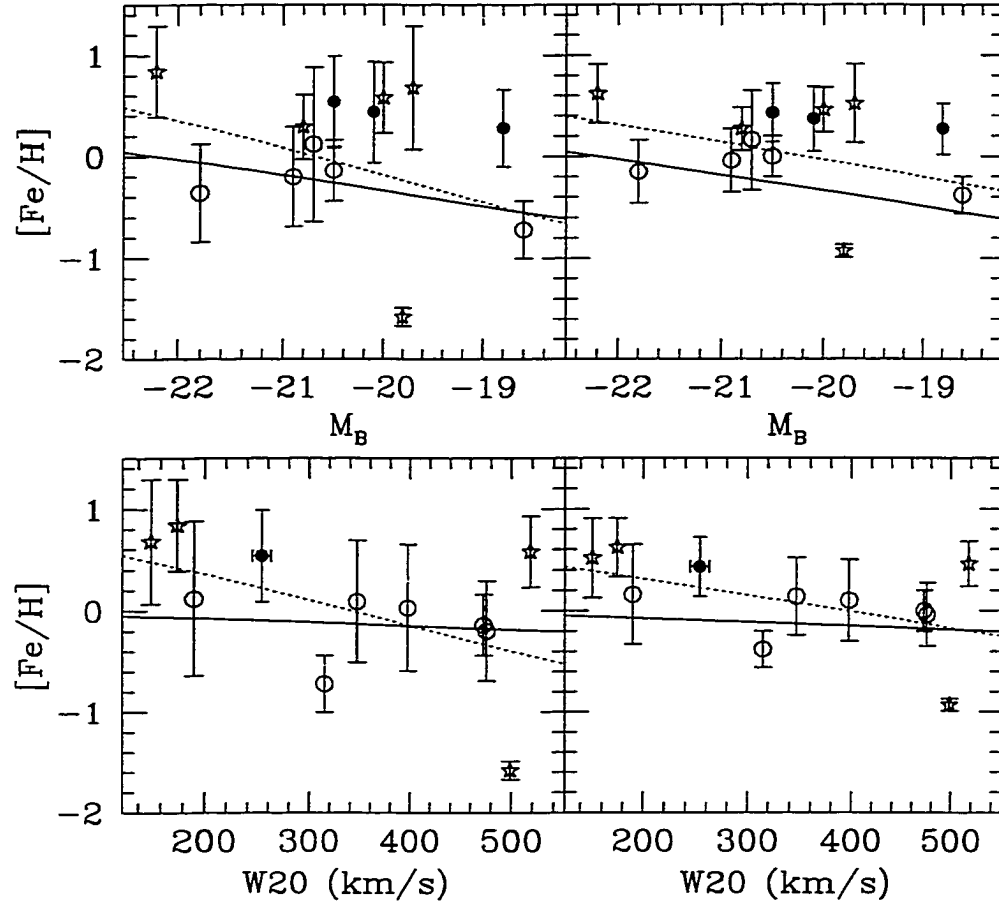


Figure 6.6 Magnesium-based iron abundance versus parameters of the starburst host galaxies. The observational calibration (Equation 6.3) is used on the left, and the theoretical calibration (Equation 6.5) on the right. Stars are young bursts ($t < 12$ Myr), circles are old bursts ($t \geq 12$ Myr), and solid dots are elliptical/S0 galaxies. Only the observational component of $[\text{Fe}/\text{H}]$ errors is indicated. The solid lines are fits to old starbursts, and the dashed lines are fits to all starbursts. Top panels: total B-band magnitude of the host, corrected for absorption and inclination, from RC3 (de Vaucouleurs et al. 1991). Bottom panels: rotational velocity at 20 and 50% level, from RC3 (de Vaucouleurs et al. 1991).

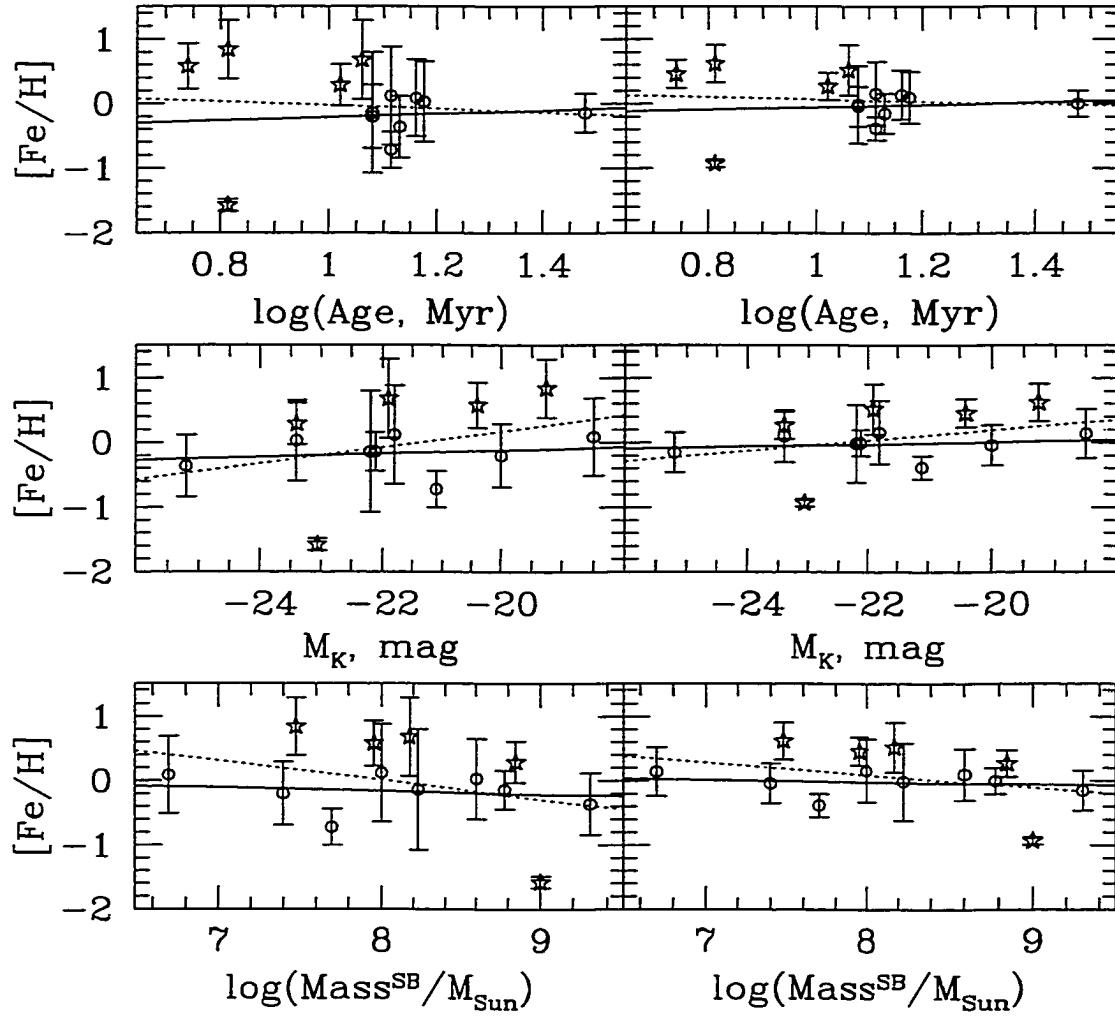


Figure 6.7 Magnesium-based iron abundance versus properties of the starbursts from Engelbracht (1997): age (top), absolute K-band magnitude within the slit aperture (middle), and total starburst mass (bottom). For basic description see Figure 6.6.

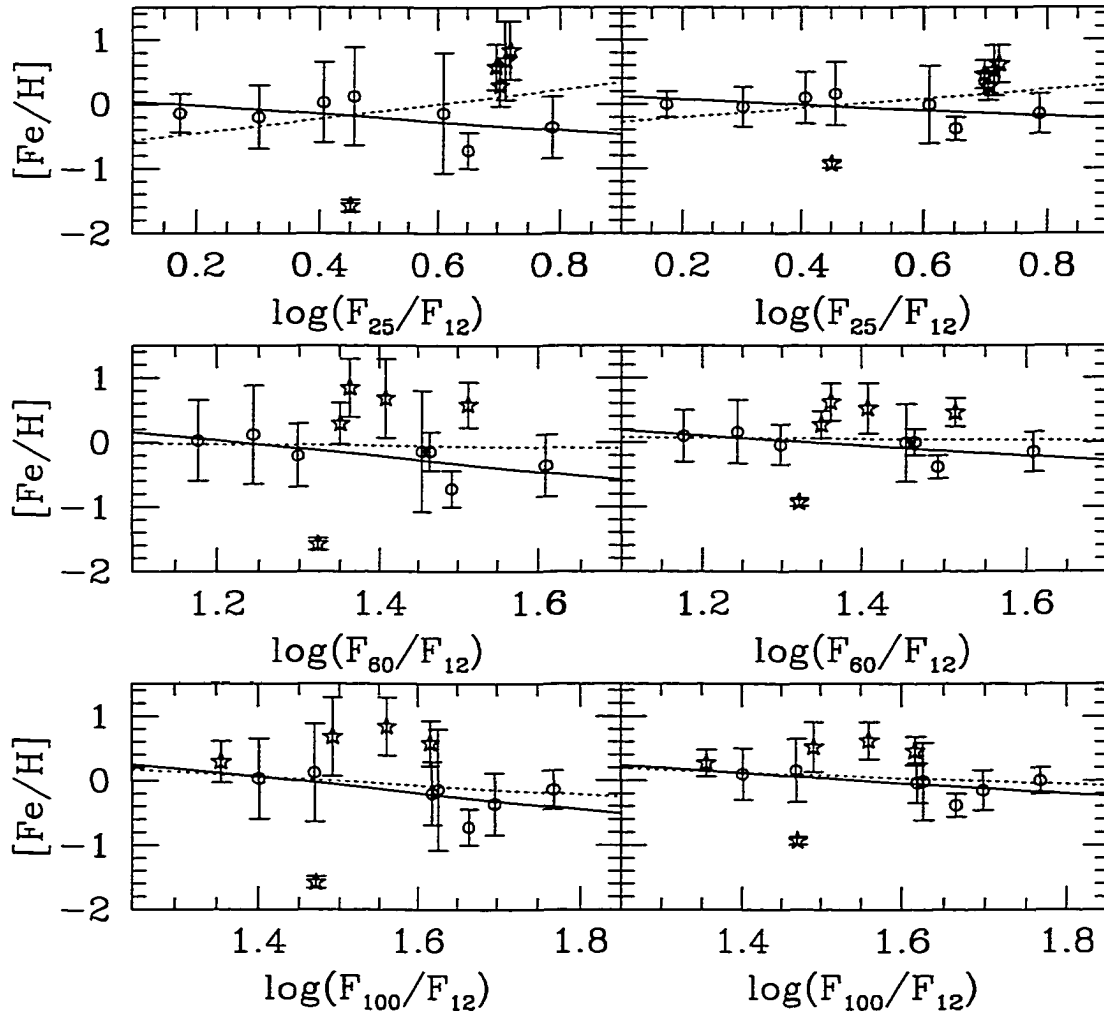


Figure 6.8 Magnesium-based iron abundance versus mid-infrared *IRAS* colors. For basic description see Figure 6.6.

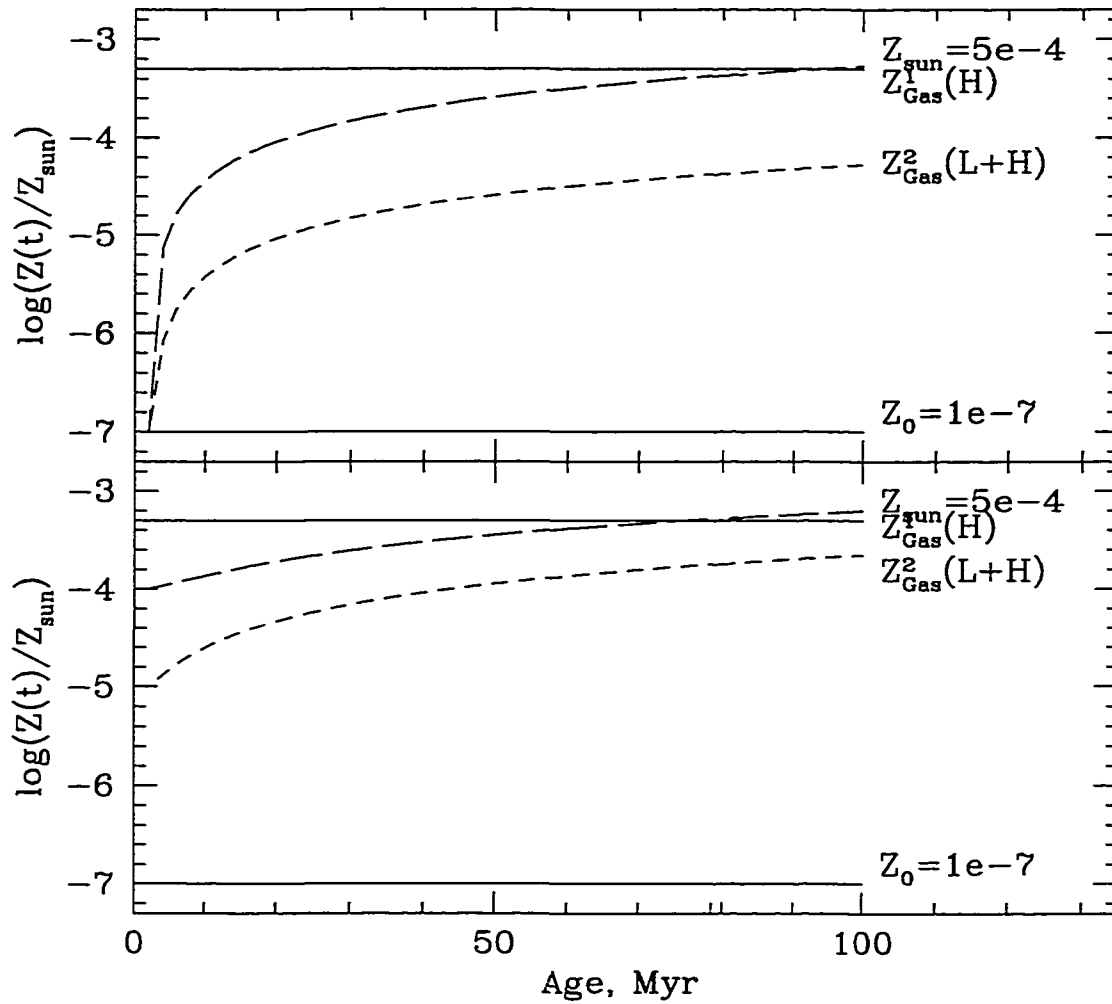


Figure 6.9 Metallicity evolution of Z1 (produced in high mass stars only) and Z2 (produced in both low and high mass stars). The initial metallicity, and the solar metallicity are indicated. The top panel shows a continuous burst in a system with no previous star formation. The burst on the bottom panel was preceded by a 4 Gyr old burst of duration 15 Myr. See Section 6.8.2 for details.

7. CONCLUDING REMARKS

7.1. Summary of the Main Results

7.1.1. Seyfert Galaxies

We used new infrared spectroscopy of the CO band at $2.3\ \mu\text{m}$, of 46 Seyfert galaxies from the CfA sample, to constrain the populations of young stars in the central regions of Seyfert galaxies. This is the first set of infrared spectra of a complete sample of Seyferts.

The CO band appears diluted by a non-stellar featureless component - most likely, warm dust near the central engine. We devised a technique, based on JHK colors, to separate the stellar and non-stellar components at $2.3\ \mu\text{m}$. We successfully carried out the dilution correction for 16 Seyfert galaxies from our sample. A comparison with the CO indices of ellipticals and pure starburst galaxies led us to the conclusion that no red supergiant phase starbursts occur in the majority of Seyfert galaxies currently.

We utilized the spectra to search for the best Seyfert-starburst separator, and concluded that the $[\text{FeII}]^{1.26\mu\text{m}}/\text{Pa}\beta^{1.28\mu\text{m}}$ versus $\text{H}_2^{2.121\mu\text{m}}/\text{Br}\gamma^{2.16\mu\text{m}}$ diagram is the most promising one.

The narrow emission line properties of our sample are significantly different

from those of ultraluminous infrared galaxies (ULIRG) from the sample of Murphy et al. (2000). Therefore, at least $\sim 2/3$ of the ULIRGs can not contain hidden active nuclei. The other $\sim 1/3$ can still harbor completely obscured AGNs, invisible even in the K-band.

7.1.2. Starburst

We have compiled moderately high resolution ($R \approx 2000-3000$) H ($1.6 \mu\text{m}$) and K band ($2.2 \mu\text{m}$) spectral atlas containing 218 stars. The atlas spans most of the ranges of effective temperature, surface gravity and metallicity, relevant for modeling starburst galaxies. We report the indices for 19 spectral features, and developed new diagnostic techniques for estimates of stellar parameters.

Magnesium indices are the best near infrared metallicity indicators because they are less sensitive to the effective stellar temperature than other lines, particularly for cool K-M giants. Because these are the stars that contribute a significant fraction of the near infrared radiation in many galaxies, we conclude that the H and K band MgI indices are just as good indicators for the abundance in composite systems, as their optical counterparts. We have calibrated the strength of MgI at $1.50 \mu\text{m}$ as function of the stellar metallicity.

We also calibrated a number of line ratios as temperature indicators [EW(CO1.62)/EW(Si1.59), EW(CO1.62)/EW(Mg1.50), EW(Mg1.50)/EW(Ca2.26), and EW(Mg1.50)/EW(Na2.21)] and giant/supergiant versus dwarf separators [EW(CO1.62)/(EW(Mg1.50)+EW(Mg1.71)), and EW(CO2.29)/(EW(Na2.21)+EW(Ca2.26))].

Despite the lack of suitable iron lines, the light-to-heavy element abundance ratio can be estimated in the infrared by using the CaI line at $2.26 \mu\text{m}$, because it

has been shown from the optical observations that the calcium abundance follows the iron abundance.

The spectral library was incorporated into an evolutionary population synthesis model for young stellar populations (10 – 30 Myr), aimed specifically at starbursts. The model is based on the Starburst99, developed by Leitherer et al. (1999).

The model predicts the time evolution of near infrared features for single bursts of star formation. They all are very weak during the first $\sim 5 - 7$ Myr while most of the flux in the burst comes from hot blue supergiants. The indices become stronger as the red supergiants begin to develop at 7-10 Myr. The peak values are scaled by the metal abundance. The indices weaken as the supergiants explode as supernovae at 12-15 Myr, and stabilize at $1/3$ to $1/2$ of the peak values after that. Our models, if combined with age estimates from hydrogen recombination emission lines, can be used to probe directly the abundance of the starbursts.

We explored the effects from abundance ratios variations in starbursts, by means of a simple chemical enrichment model. We demonstrated that the fraction of iron peak elements can be influenced significantly by the preceding star formation history, particularly in galaxies that have not undergone an extensive star formation before the last burst. This poses a significant problem to metallicity estimates, based on α -element spectral features, but also opens up a possibility to explore the previous star formation history. Our result underlines the importance of using abundance indicators based on elements of different types.

Finally, we determined the metallicity of the starbursts and "normal" (mostly giant ellipticals) galaxies from the sample of Engelbracht (1997), and found that our $[\text{Fe}/\text{H}]$ estimates correlate very well with the optical iron indices and some starburst properties.

7.2. Future Work

An intrinsic drawback of a purely observational spectral atlas is the lack a variety among the abundances of youngest red supergiants. Apart from incorporating somewhat uncertain theoretical models of stellar atmospheres, the only possibility to alleviate the problem is to obtain spectra of Magellanic Cloud stars. With metallicities at $1/5$ and $1/20$ of the solar, they would provide an observational stepping stone towards lower metallicity models. These stars have apparent K magnitudes 8-10 mag, and are easily observable with 2-4 meter class telescopes.

The Magellanic Clouds might prove to be an useful targets for further observations in more than one way. Young LMC and SMC clusters with reliable optical spectroscopy and even resolved stellar photometry are invaluable calibrators for any evolutionary population model.

The most important avenue of pursuit involves building a redshift limited complete sample of starburst galaxies. The traditional selection techniques invariably involve some biases. Recent surveys provided optical spectra of most galaxies within 100 Mpc but they select against highly obscured Arp 220-like galaxies. Future, sensitive space-based mid-infrared surveys (e.g. with *SIRTF*) may be the answer to this problem.

APPENDIX

CALIBRATIONS FOR THE INFRARED SPECTRAL INDICES - FIGURES

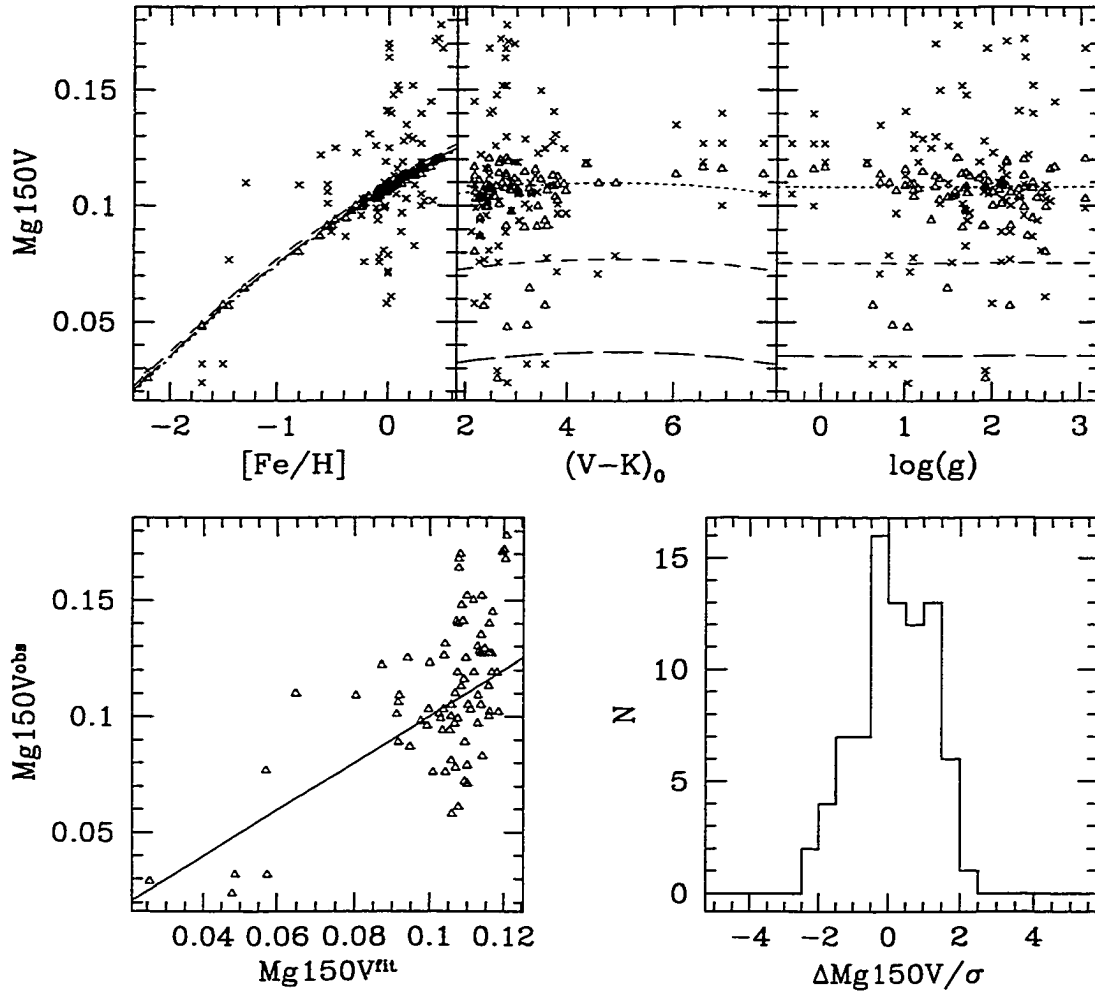


Figure A.1 Calibration of MgI 1.50 μ m index. The top three panels show the behavior of the index as function of [Fe/H], V-K and log g . Crosses are the measurements, and triangles are the corresponding fit values. The lines on the left top panel are fits for V-K=7 (dots), 5 (short dashes), and 3 mag (long dashes), and log g =1.0. The lines in the middle top panel are fits for [Fe/H]=0 (dots), -1 (short dashes), and -2 (long dashes), and log g =1.0. The lines in the right top panel are fits for [Fe/H]=0 (dots), -1 (short dashes), and -2 (long dashes), and V-K=3.0 mag. The bottom left panel shows the observed versus fitted values, and the bottom right panel shows the residuals to the fit, normalized to the measurement errors σ .

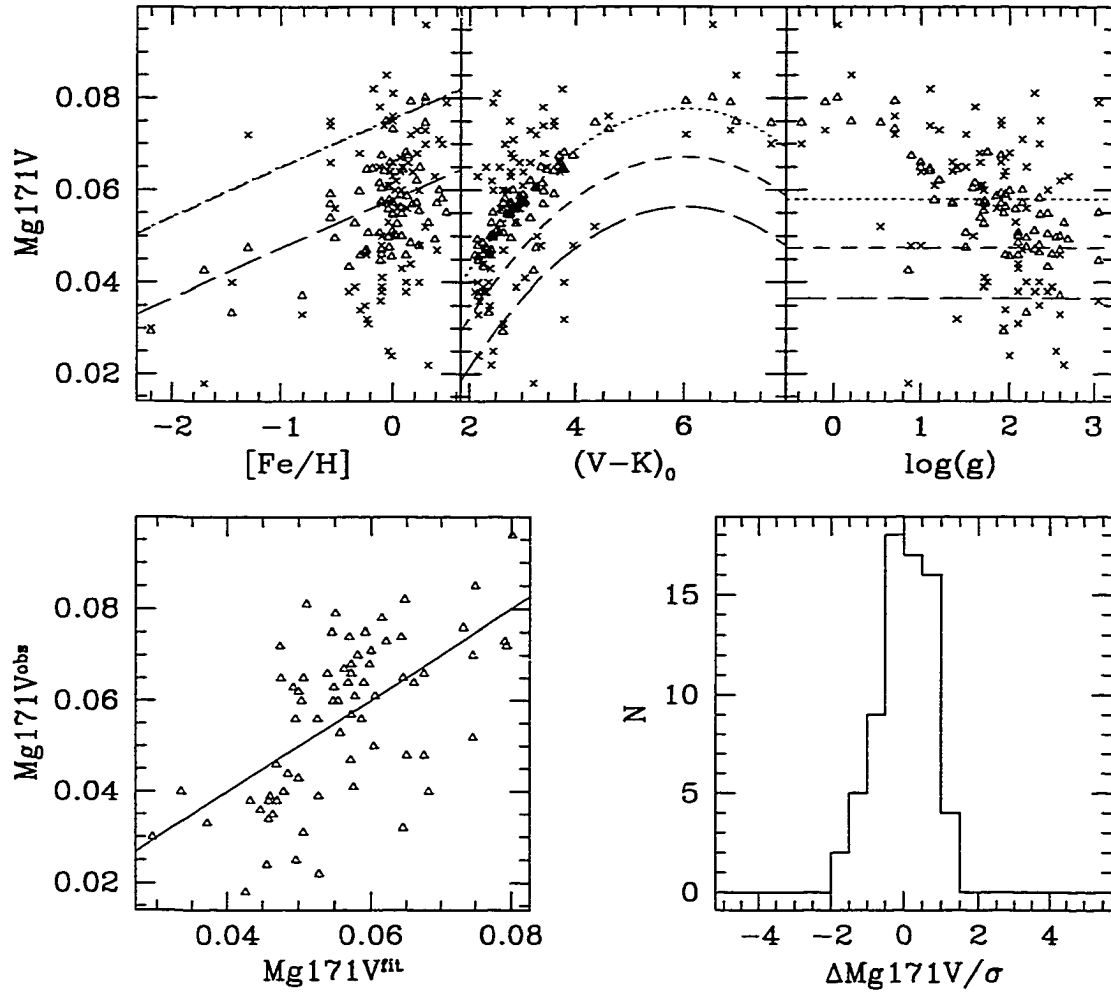


Figure A.2 Calibration of MgI 1.71μm index. For description see Figure A.1.

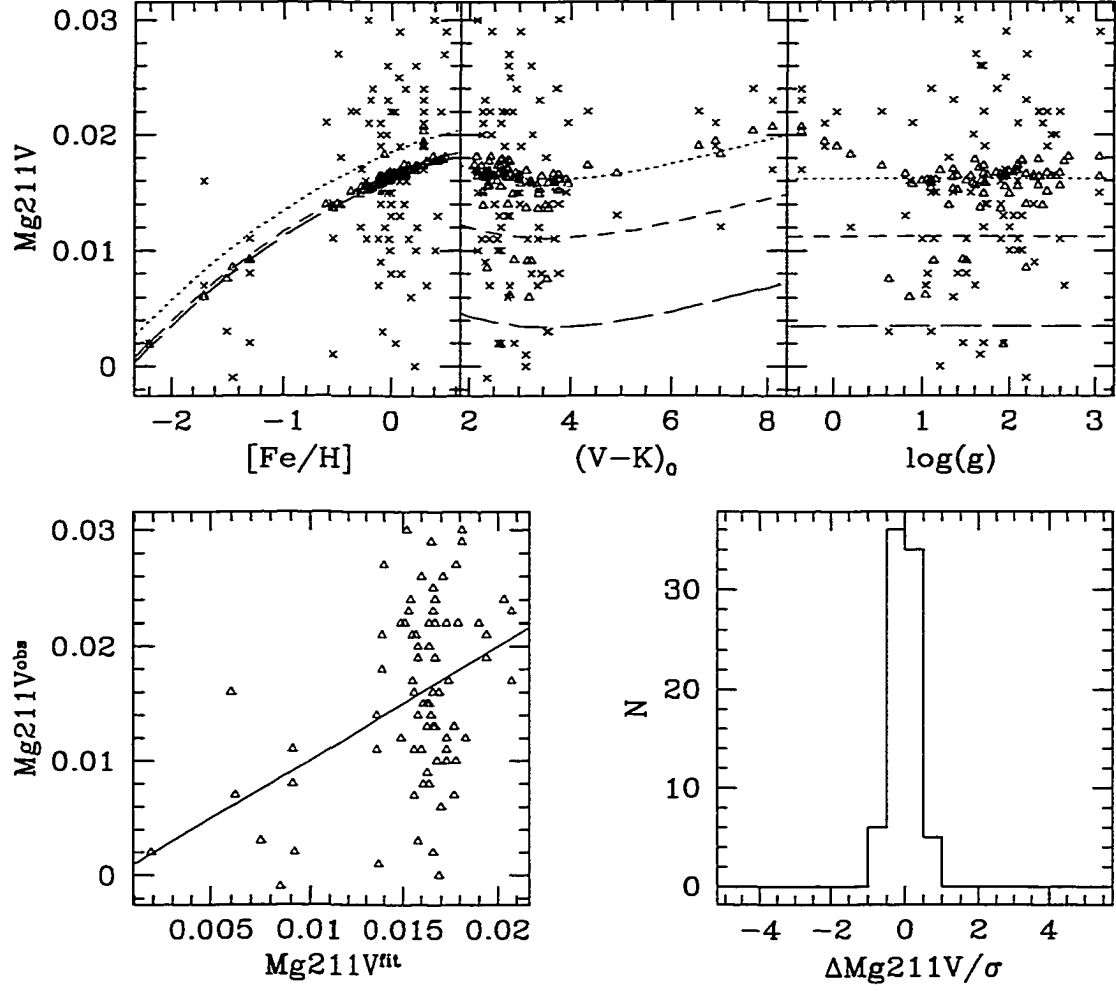


Figure A.3 Calibration of MgI 2.11 μ m index. For description see Figure A.1.

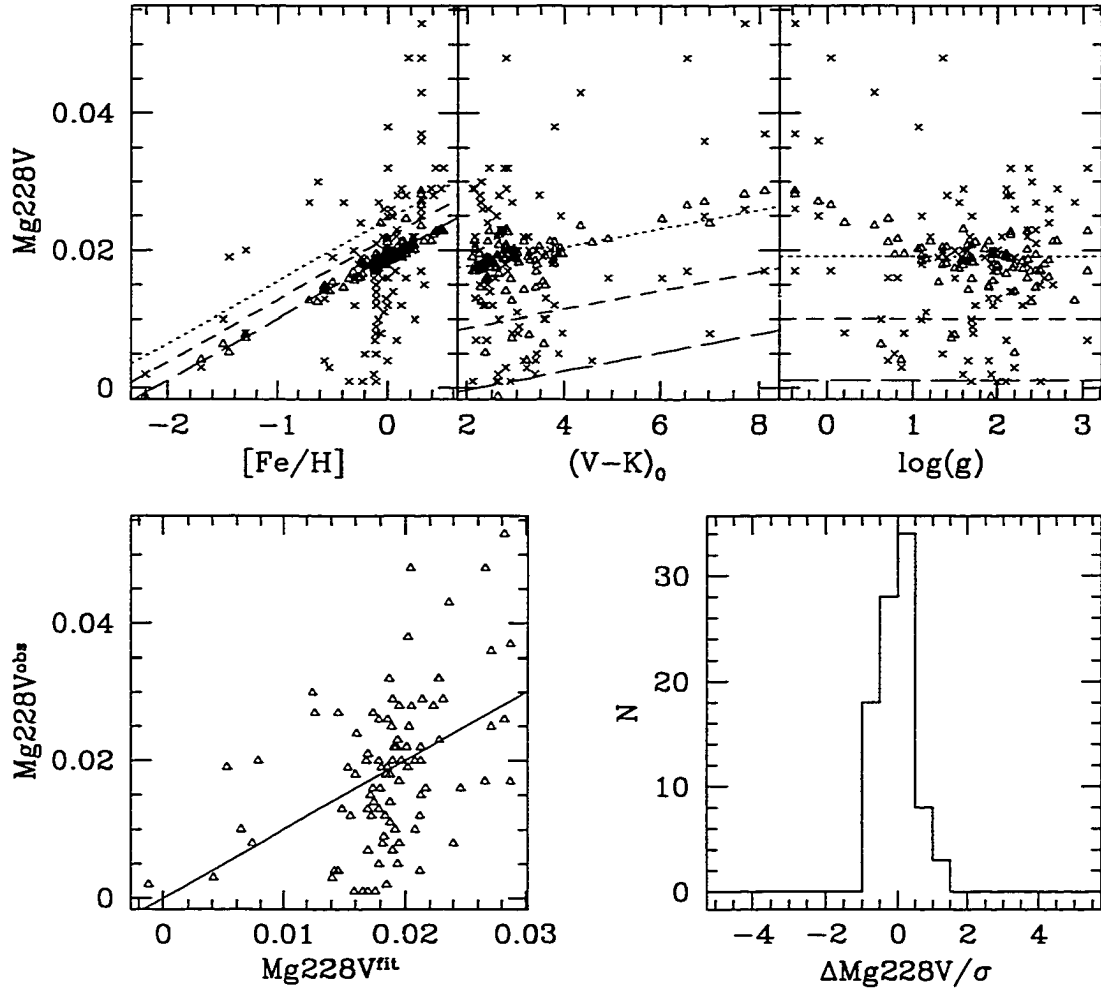


Figure A.4 Calibration of MgI 2.28 μ m index, as defined in this work. For description see Figure A.1.

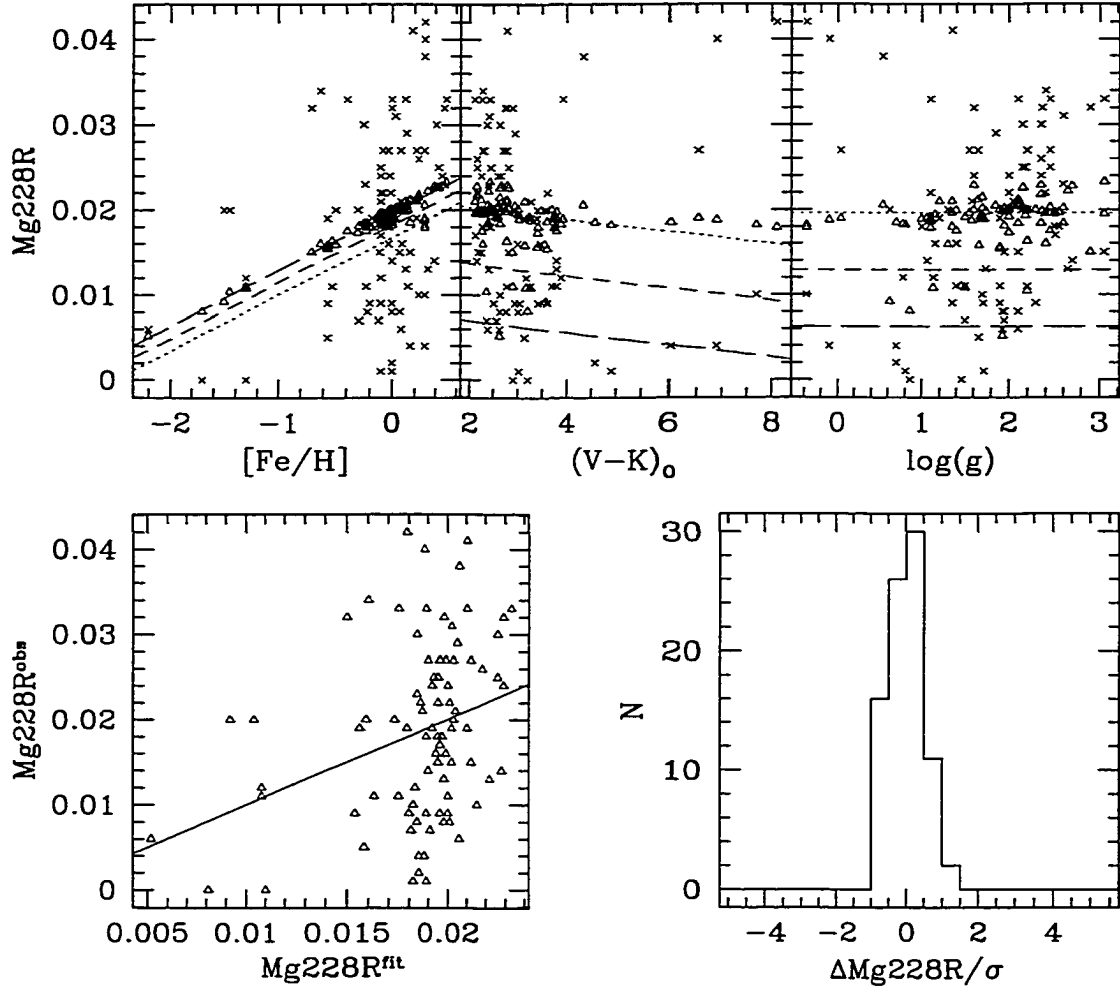


Figure A.5 Calibration of MgI 2.28μm index, as defined by Ramírez et al. (1997).
For description see Figure A.1.

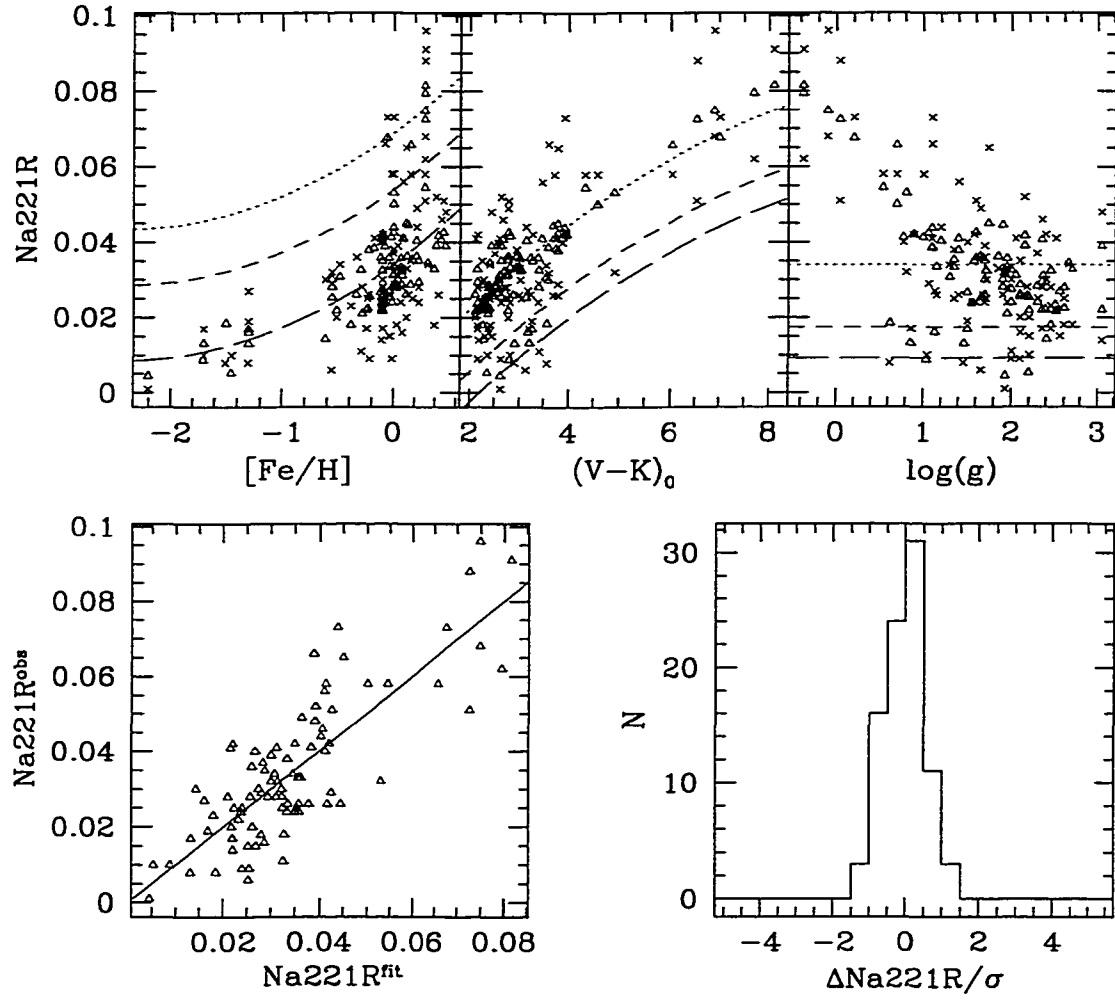


Figure A.6 Calibration of NaI 2.21 μm index, as defined by Ramírez et al. (1997).
For description see Figure A.1.

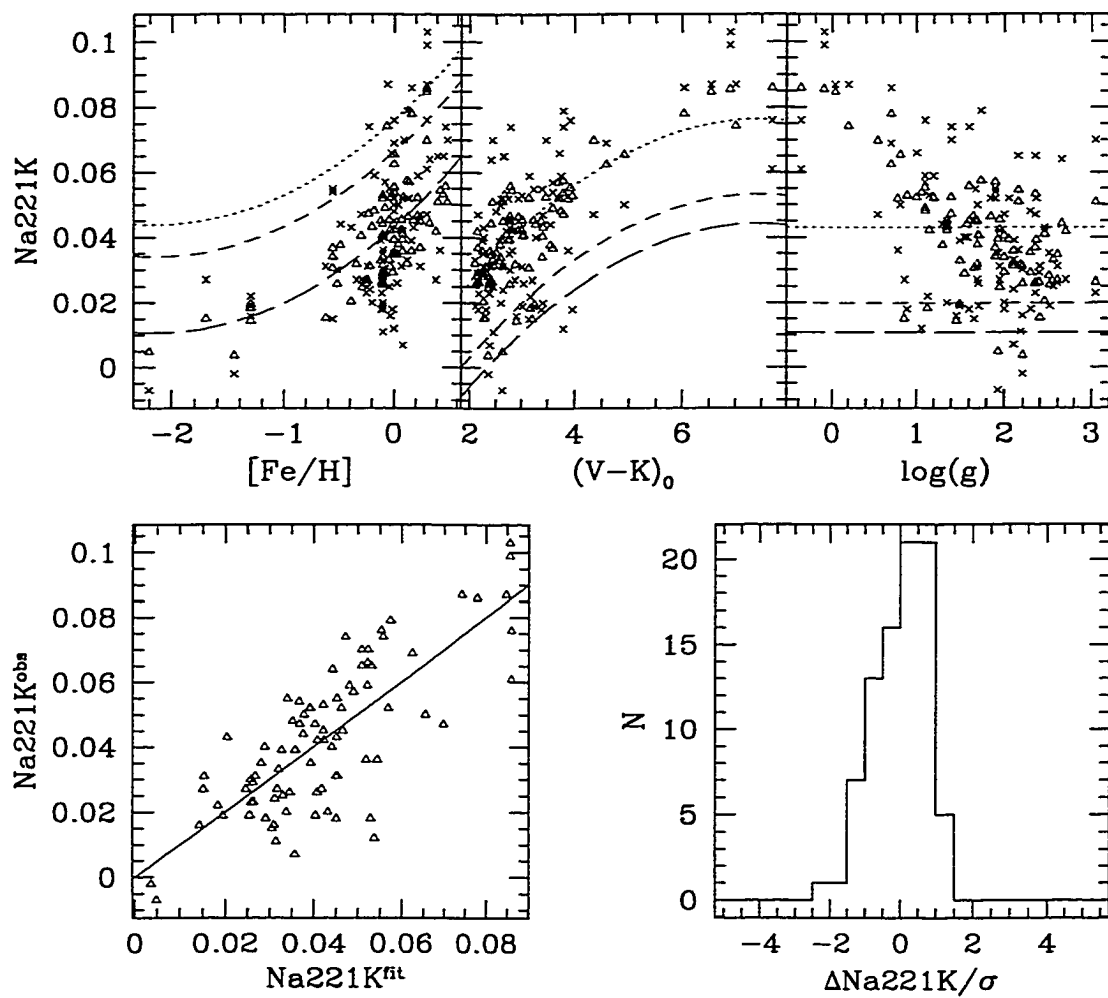


Figure A.7 Calibration of NaI 2.21 μm index, as defined by Kleinmann & Hall (1986).

For description see Figure A.1.

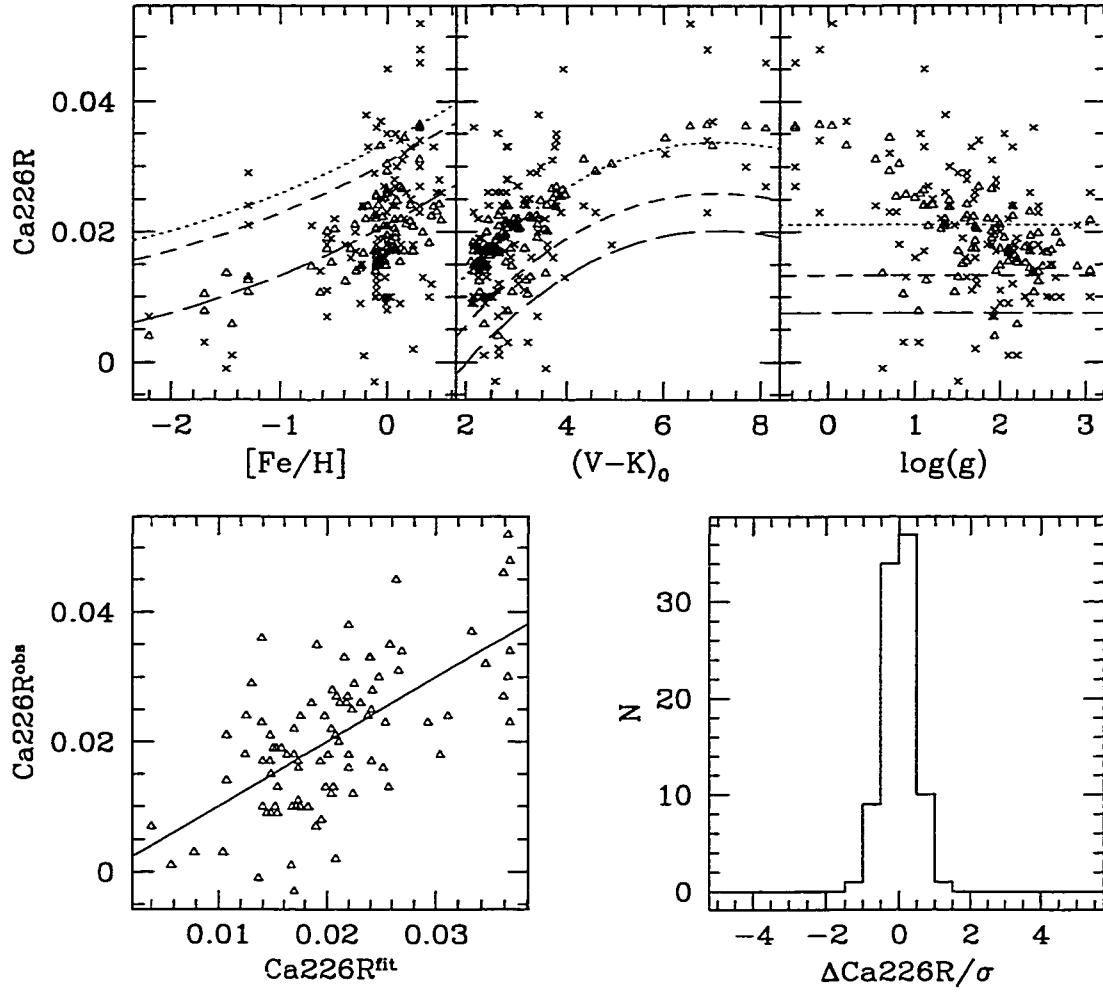


Figure A.8 Calibration of CaI $2.26\mu\text{m}$ index, as defined by Ramírez et al. (1997).
For description see Figure A.1.

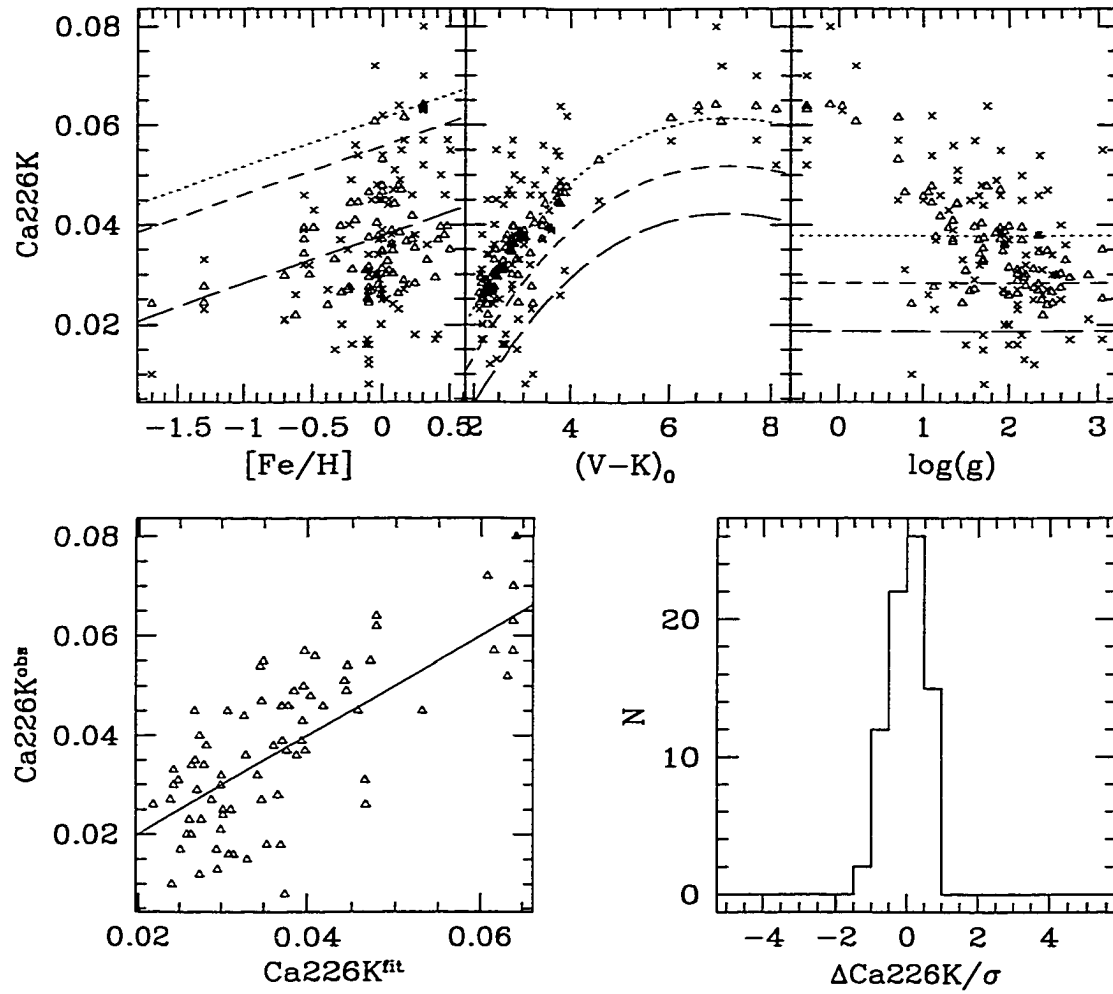


Figure A.9 Calibration of for CaI 2.26 μ m index, as defined by Kleinmann & Hall (1986). For description see Figure A.1.

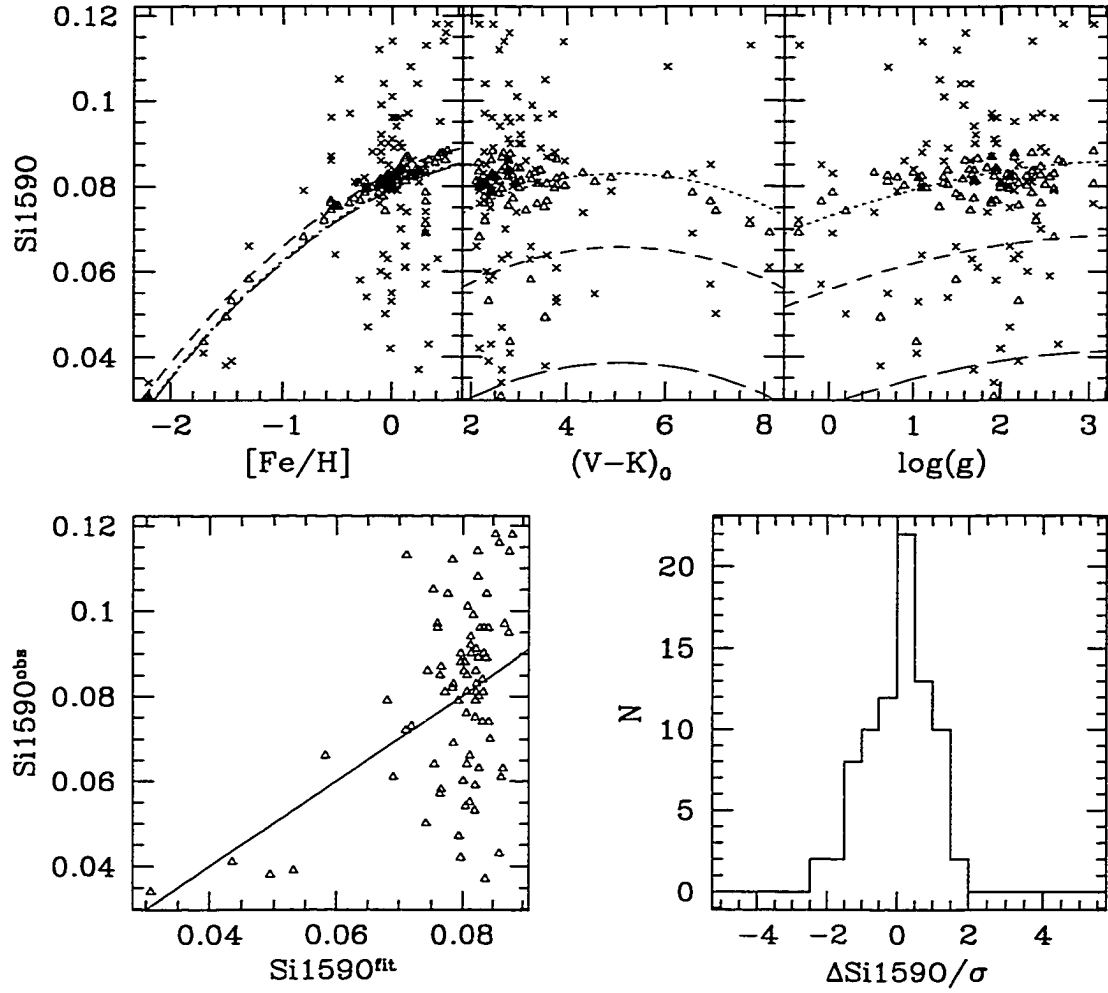


Figure A.10 Calibration of SiI 1.59 μm index, as defined by Origlia, Moorwood & Oliva (1993). For description see Figure A.1.

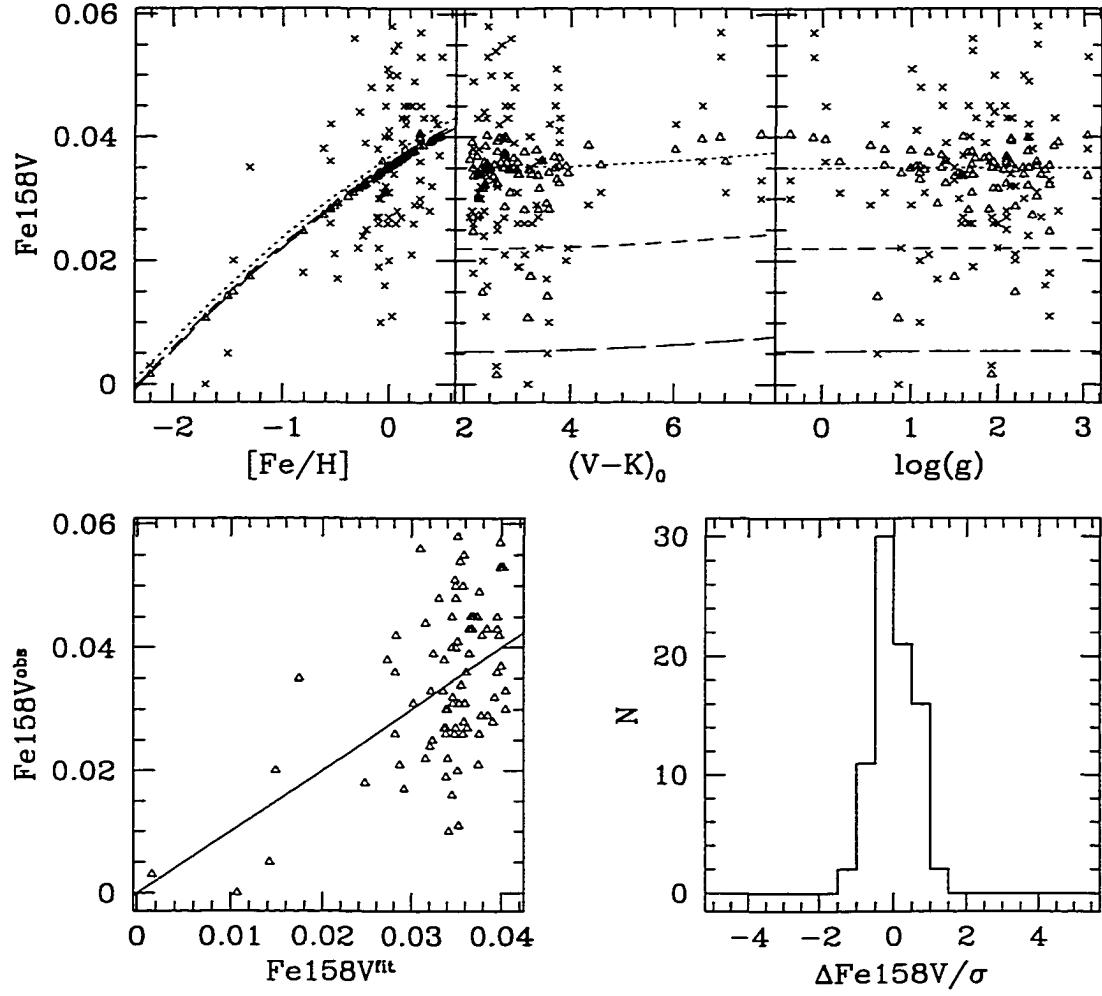


Figure A.11 Calibration of FeI 1.58 μm index, as defined in this work. For description see Figure A.1.

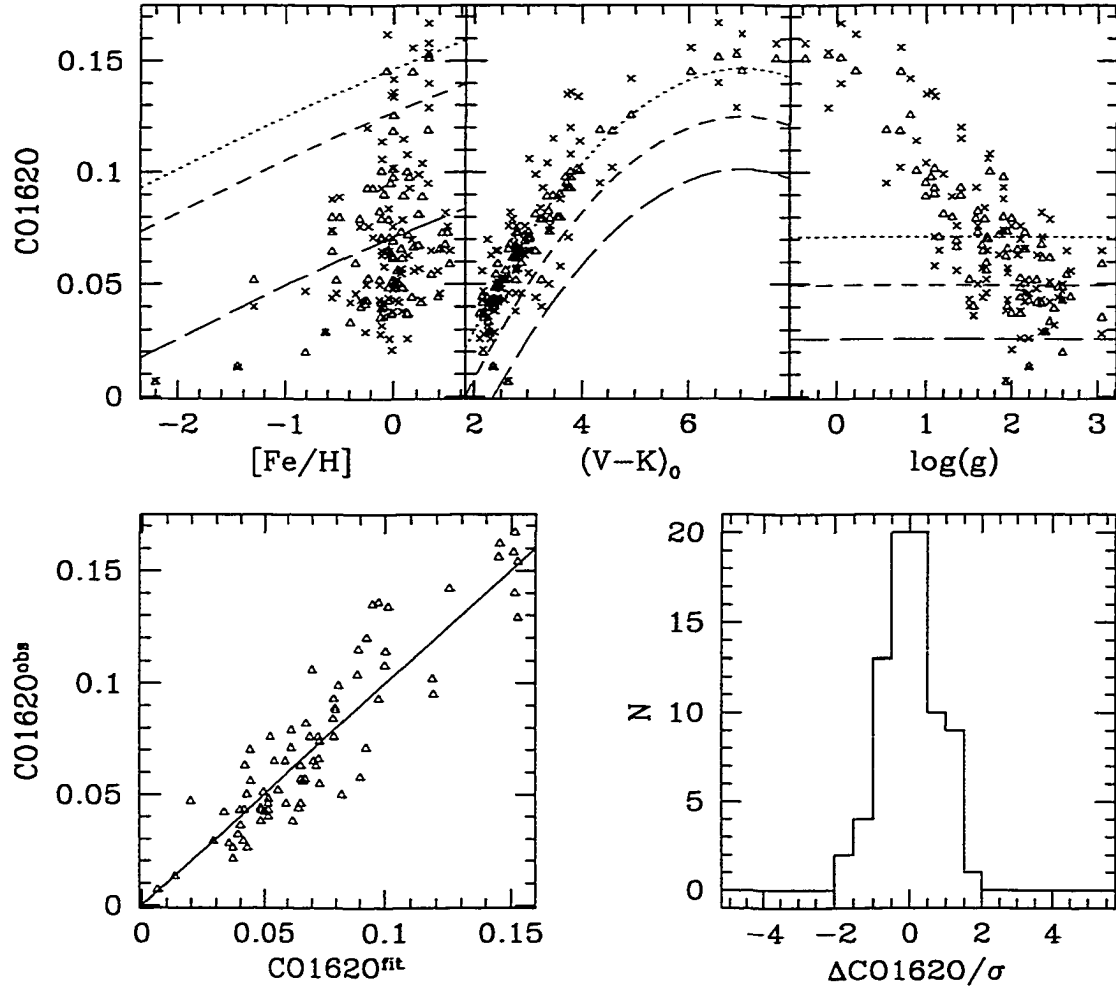


Figure A.12 Calibration of CO 1.62 μm index, as defined by Origlia, Moorwood & Oliva (1993). For the basic description see Figure A.1.

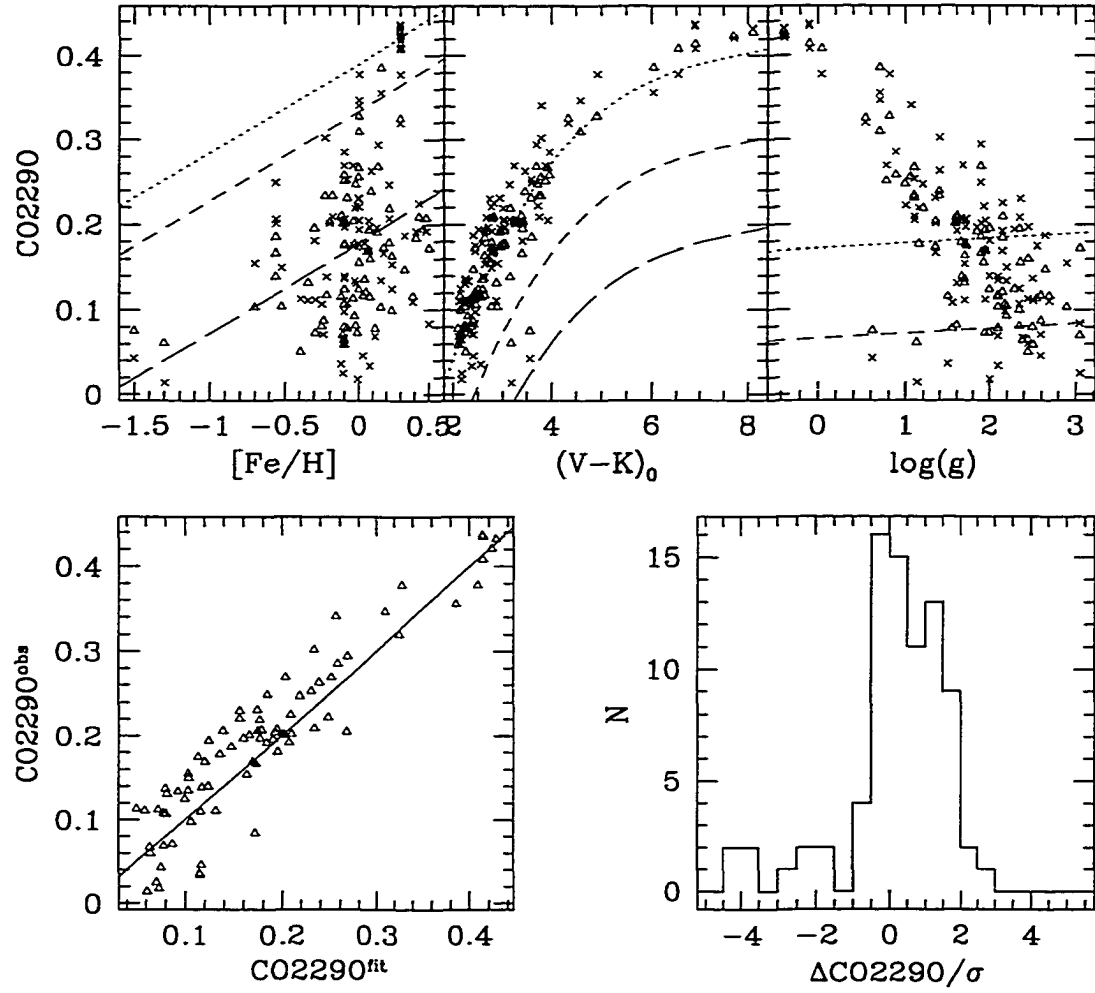


Figure A.13 Calibration of CO 2.29 μm index, as defined by Origlia, Moorwood & Oliva (1993). For description see Figure A.1.

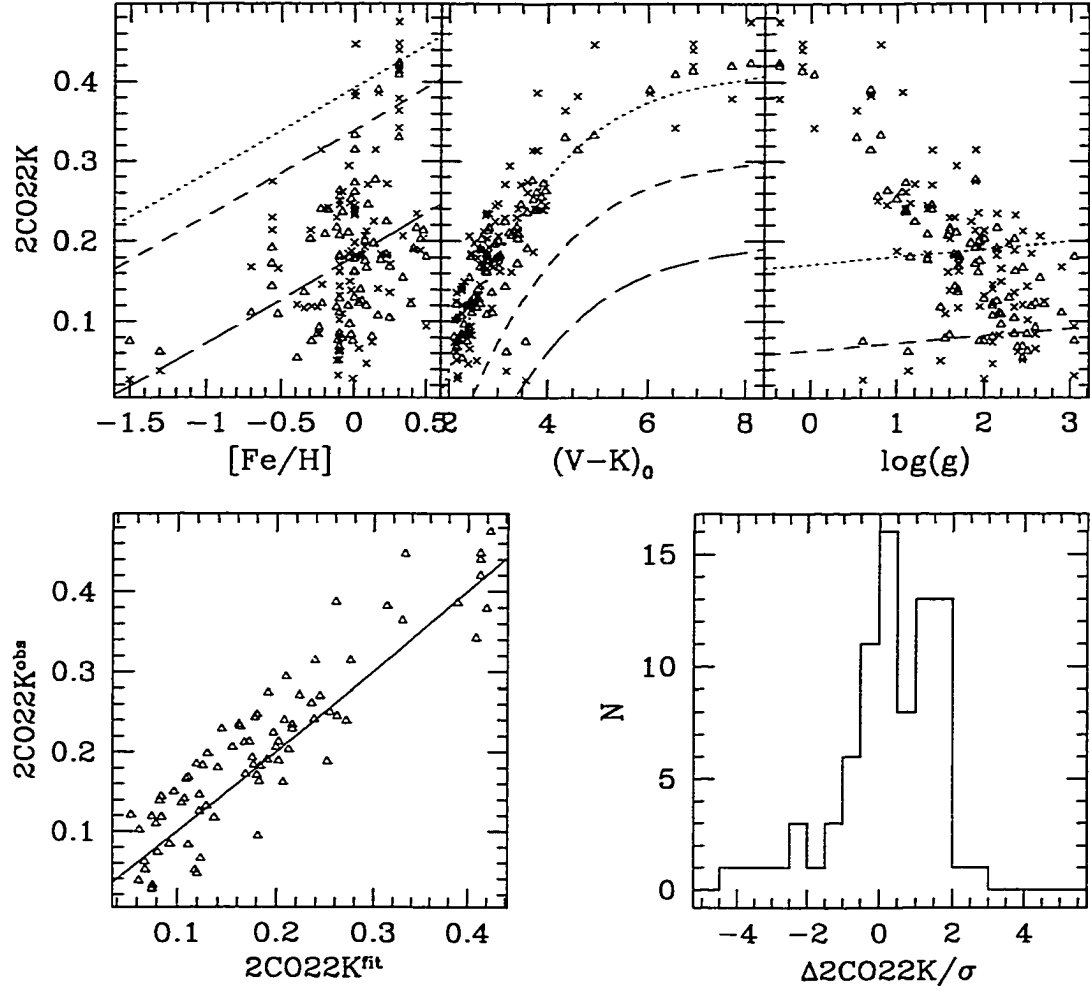


Figure A.14 Calibration of $^{12}\text{CO}(2,0)$ 2.29 μm index, as defined by Kleinmann & Hall (1986). For description see Figure A.1.

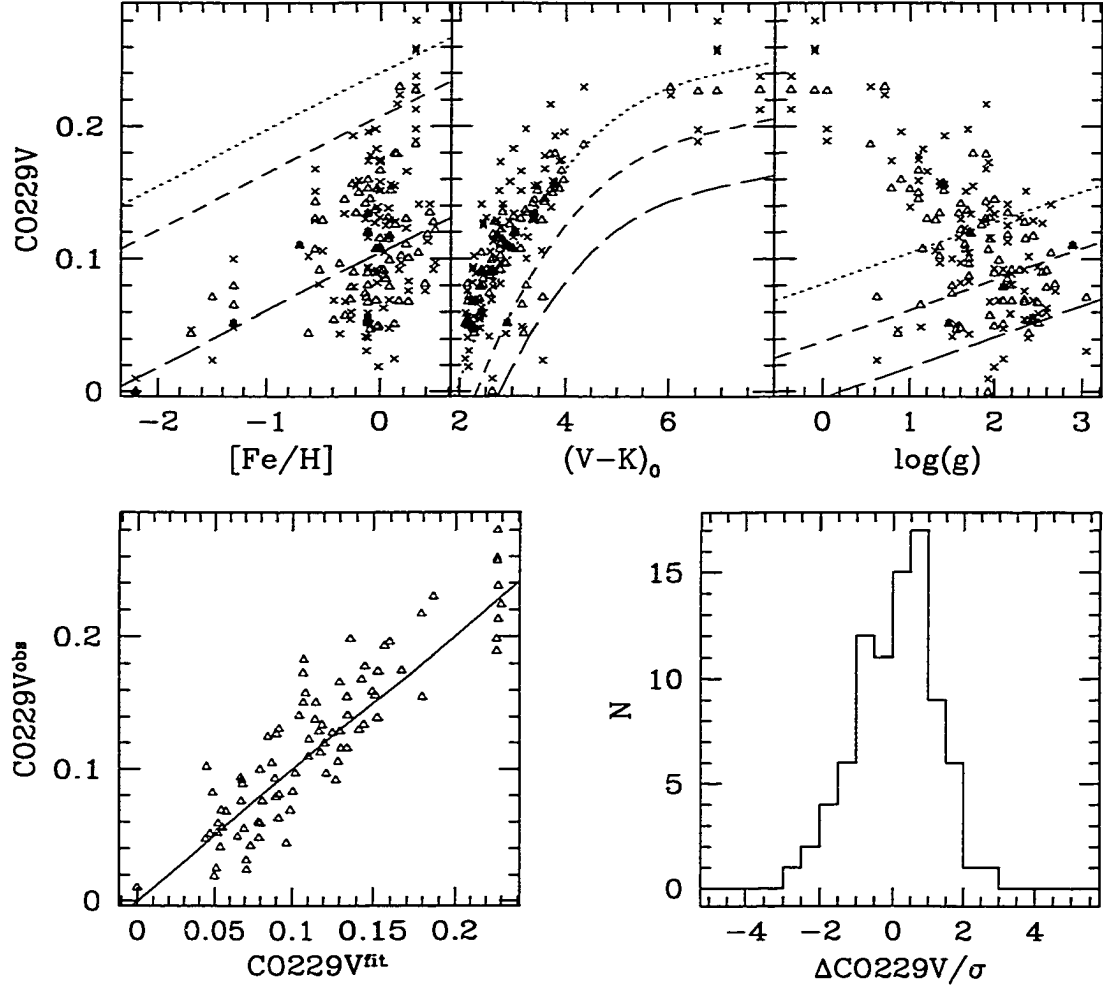


Figure A.15 Calibration of CO 2.29 μm index, as defined by Ivanov et al. (2000). For description see Figure A.1.

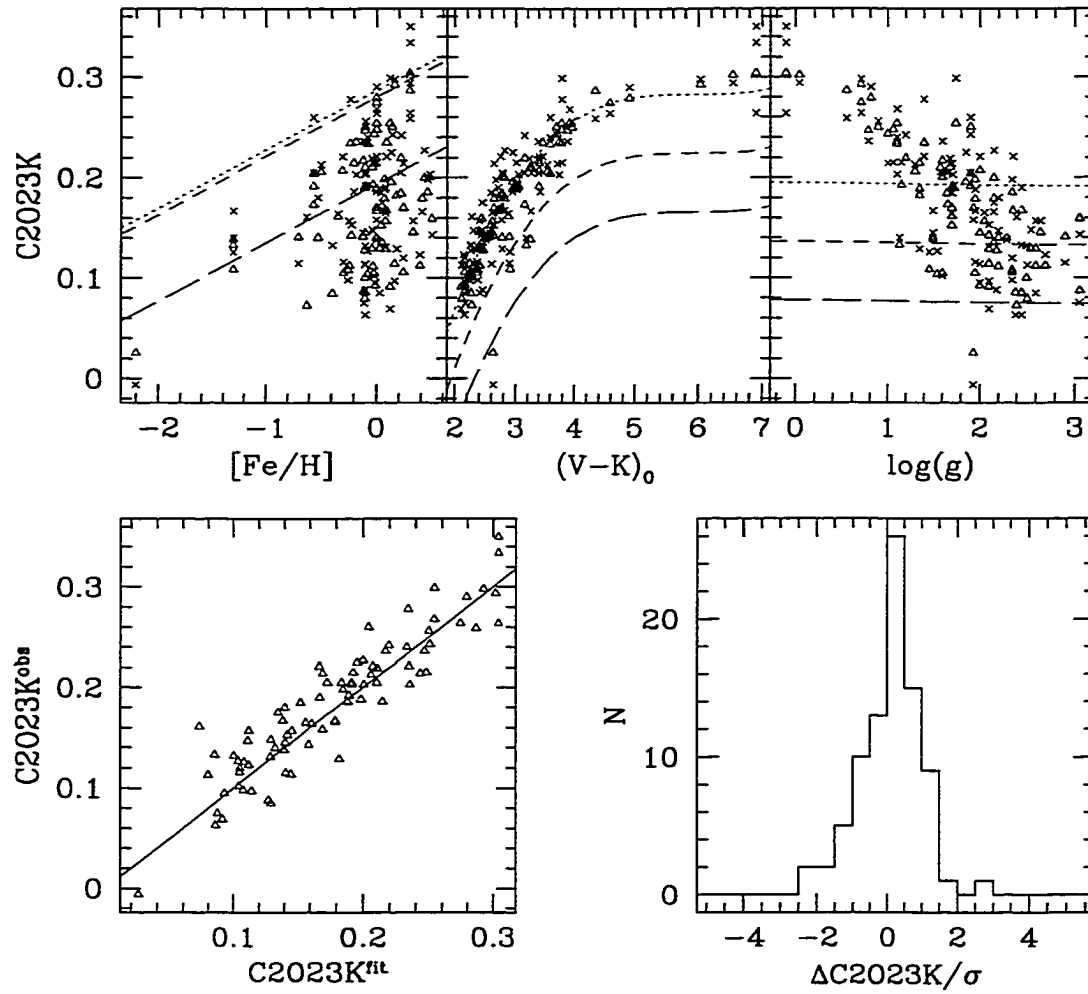


Figure A.16 Calibration of $^{12}\text{CO}(3,1)$ 2.29 μm index, as defined by Kleinmann & Hall (1986). For description see Figure A.1.

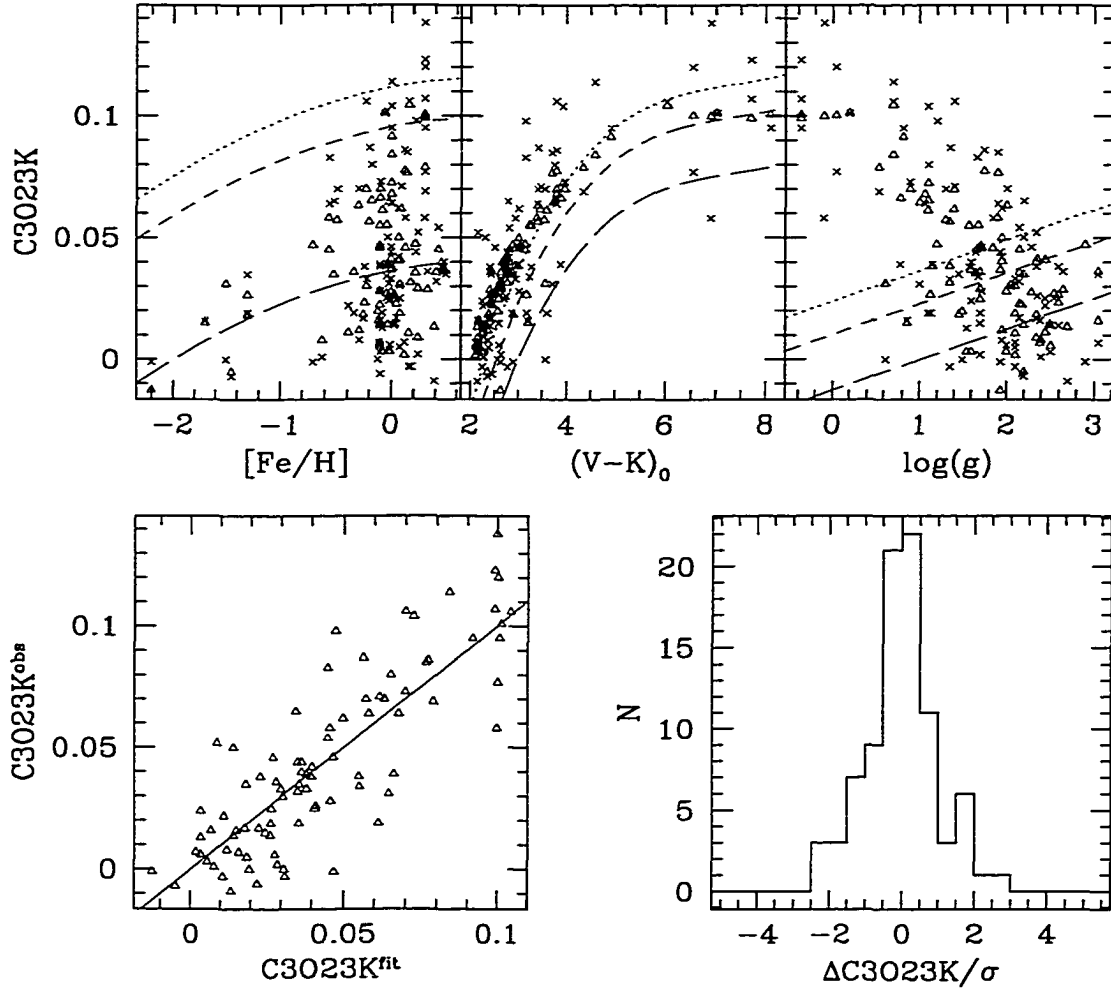


Figure A.17 Calibration of $^{13}\text{CO}(2,0)$ 2.29 μm index, as defined by Kleinmann & Hall (1986). For description see Figure A.1.

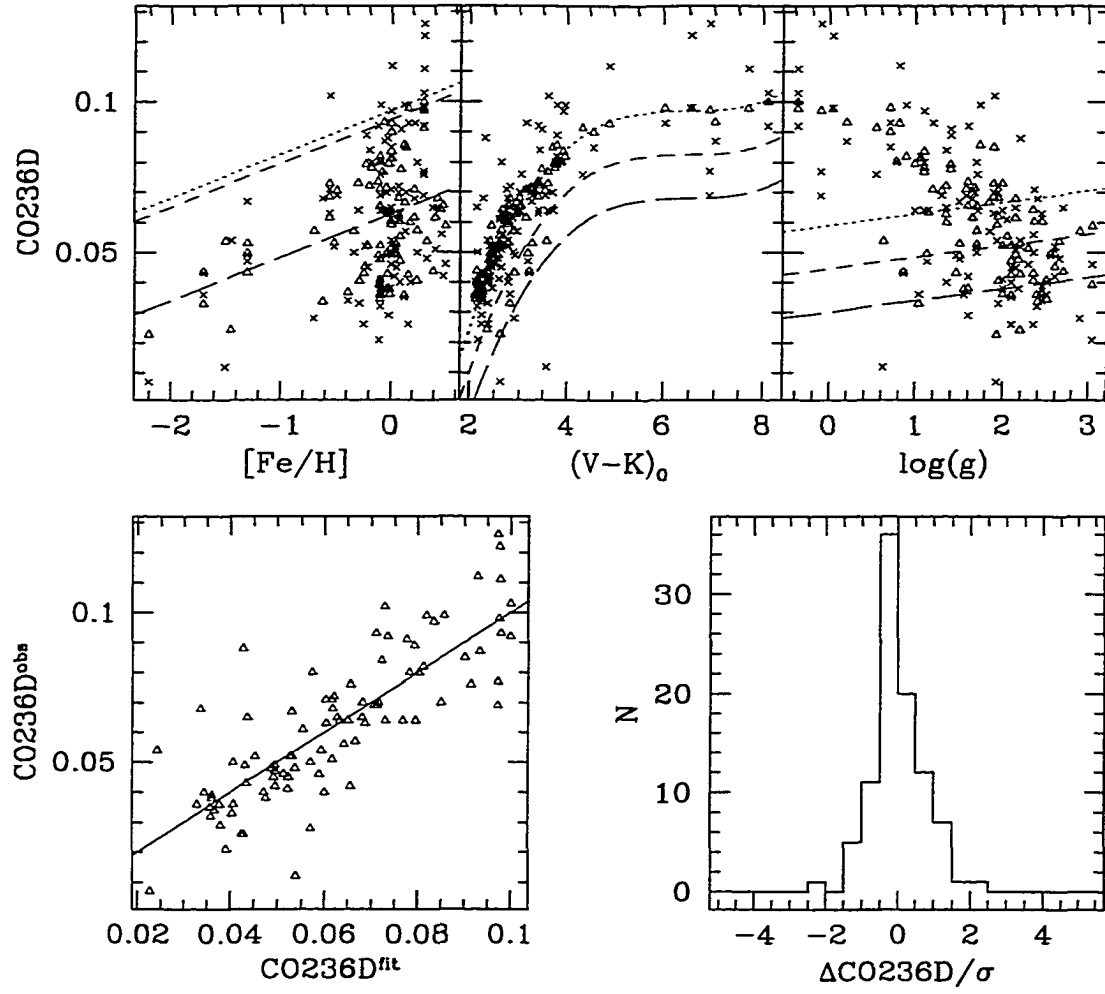


Figure A.18 Calibration of CO 2.29 μm index, as defined by Doyon, Joseph & Wright (1994). For description see Figure A.1.

REFERENCES

- Aaronson, M, 1977, Ph.D. Thesis, Harvard University
- Ali, B., Carr, J.S., Depoy, D.L., Frogel, J.A., Sellgren, K., 1995, AJ, 110, 2415
- llard, F., Hauschildt, P.H., & Schwenke, D., 2000, ApJ, 540, 1005
- Allen, D.A., 1976, ApJ, 207, 367
- Alonso, A., Arribas, S., & Martinez-Roger, C., 1994, A&AS, 107, 365
- Alonso-Herrero, A., Engelbracht, C.W., Rieke, M.J., Rieke, G.H., & Quillen, A.C.,
2000, ApJ, 546, 952
- Alonso-Herrero, A., Rieke, G.H., Rieke, M.J., & Scoville, N.Z., 2000, ApJ, 532, 845
- Alonso-Herrero, A., Rieke, M.J., Rieke, G.H., & Ruiz, M., 1997, ApJ, 482, 747
- Alonso-Herrero, A., Rieke, M.J., Rieke, G.H., & Shields, J.C., 1999, ApJ, 530, 688
- Alonso-Herrero, A., Simpson, C., Ward, M.J., Wilson, A.S., 1998, ApJ, 495, 196
- Alonso-Herrero, A., Ward, M.J., & Kotilainen, J.K., 1996, MNRAS, 278, 902
- Alvarez, R., Lançon, A., Plez, B., Wood, P.R., 2000, A&A, 353, 322
- Antonucci, R.R.J., 1983,
at, 303, 158
- Antonucci, R.R.J., & Miller, J.S, 1985, ApJ, 297, 621
- Appenzeller, I.sch0067, PASP, 79, 102
- Applegate, J. H., & Terman, J. L. 1989, ApJ, **340**, 380

- Ardeberg, A., Sarg, K., & Wramdemark, S., 1973, A&AS, 9, 163
- Argue, A.N., 1963, MNRAS, 125, 557
- Argue, A.N., 1966, MNRAS, 133, 475
- Bailey, M.E., 1980, MNRAS, 191, 195
- Barbier, M., 1963, Publ. Obs. Haute-Provence, 6, 36
- Barger, A.J., Cowie, L.L., Mushotzky, R.F., Richards, E.A., AJ, 2001, 121, 662
- Becklin, E.E., Gatley, I., Matthews, K., Neugebauer, G., Sellgren, K., Werner, M.W., Winn-Williams, C.G., 1980, ApJ, 236, 441
- Bell, R.A., & Briley, M.M., 1991, AJ, 102, 763
- Bell, R.A., & Gustafsson, B., 1989, MNRAS, 236, 653
- Bertelli, G., Bressan, A., Chiosi, C., Fagotto, F., Nasi, E., 1994, A&AS, 106, 275
- Bessel, M.S., 1990, A&AS, 83, 357
- Blanco, P.R., Ward, M.J., & Writgh, G.S., 1990, MNRAS, 242, P4
- Blietz, M., Cameron, M., Drapatz, S., Genzel, R., Krabbe, A., van der Werf, P., Sternberg, A., & Ward, M., 1994, ApJ, 421, 92
- Brindle, C., Hough, J.H., Bailey, J.A., Axon, D.J., Sparks, W.B., 1991, MNRAS, 252, 288
- Bruzual, G.A., & Charlot, S., 1993, ApJ, 405, 538
- Bushouse, H.A., & Stanford, S.A., 1992, ApJS, 79, 213
- Campins, H., Rieke, G.H., & Lebofsky, M.J., 1985, AJ, 90, 896

- Carico, D.P., Sanders, D.B., Soifer, B.T., Elias, J.H., Matthews, K., & Neugebauer, G., 1988, AJ, 95, 365
- Carr, J.S., Sellgren, K., & Balachandran, S.C., 2000, ApJ, 530, 307
- Cayrel de Strobel, G., Soubiran, C., Friel, E.D., Ralite, N., François, P., 1997, A&AS, 124, 299
- Charbonnel, D., Meynet, G., Maeder, A., Schaller, G., & Schaerer, D. 1993, A&AS, 101, 415
- Charlot, S., Worthey, G., Bressan, A., 1996, ApJ, 457, 625
- Cid Fernandes, R., 1997, in Starburst Activity in Galaxies, eds. Franco J., Terlevich, R.J., Serrano, A., Rev. Mex. A. A. Conf. Ser., 6, 201
- Cimatti, A., Daddi, E., di Sergio Alighieri, S., Pozzetti, S., Mannuchi, F., Renzini, A., Oliva, E., Zamorani, G., Andreani, P., Röttgering, H.J.A., 1999, A&A, 352, L45
- Conselice, C.J., Bershady, M.A., & Gallagher, J.S., III, 2000, A&A, 354, L21
- Corbin, M.R., Baldwin, J.A., & Wilson, A.S., 1988, ApJ, 334, 584
- Cowley, A., Cowley, C., Jaschek, M., & Jaschek, C., 1969, AJ, 74, 375
- Cowley, A.P., Hiltner, W.A., & Witt, A.N., 1967, AJ, 72, 1334
- Cutri, R.M., & McAlary, C.W., 1985, ApJ, 296, 90
- Dallier, R., Boisson, C. & Joly, M., 1996, A&AS, 116, 239
- David, L.P., Durstein, R.H., & Cohn, H.N., 1987a, ApJ, 313, 556
- David, L.P., 1987b, ApJ, 316, 505

- de Vaucouleurs, G., de Vaucouleurs, A., Corwin, H.G., Jr., Buta, R.J., Paturel, G., Fouque, P., 1991, Third Reference Catalog of Bright Galaxies, Springer-Verlag Berlin Heidelberg New York
- Dey, A., Breugel, W., Vacca, W.D., & Antonucci, R., 1997, ApJ, 490, 698
- Dey, A., Graham, J.R., Ivison, R.J., Smail, I., Wright, G.S., & Liu, M.C., 1999, ApJ, 519, 610
- Di Benedetto, G.P., 1998, A&A, 339, 858
- Diaz, A.I., Terlevich, E., & Terlevich, R., 1989, MNRAS, 239, 325
- Doyon, R., Joseph, R.D., & Wright, G.S., 1994a ApJ, 421, 101
- Doyon, R., Joseph, R.D., & Wright, G.S., 1994b, ApJ, 421, 115
- Dumm, T., & Schild, H., 1998, NewA, 3, 137
- Dyck, H.M., van Belle, G.T. & Thompson, R.R., 1998, AJ, 116, 981
- Edelson, R.A., Malkan, M.A., & Rieke, G.H., 1987, ApJ, 321, 233
- Eggen, O.J., 1964, AJ, 69, 570
- Eggen, O.J., 1996, AJ, 111, 466
- Eggen, O.J., 1998, AJ, 115, 2397
- Eggen, O.J., & Greenstein, J.L., 1965, ApJ, 142, 925
- Eggleton, P. P. 1983, ApJ, **268**, 368
- Elias, J.H., Frogel, J.A., Matthews, K., & Neugebauer, G., 1982, AJ, 87, 1029
- Elias, J.H., Frogel, J.A., & Humphreys, R.M., 1985, ApJS, 57, 91

- Elson, R.A.W., 1997, MNRAS, 286, 771
- Engelbracht, C.W., 1997, Ph.D. Thesis, The University of Arizona, Tucson
- Engelbracht, C.W., 1999, private communication
- Engelbracht, C.W., 2000, private communication
- Engelbracht, C.,W., Rieke, M.J., Rieke, G.H., Kelly, D.M., 1998, ApJ, 505, 639
- Erro, B.I., 1971, Bol., Inst. Tonantz., 6, 143
- Faber, S.M., Friel, E.D., Burstein, D., & Gaskell, C.M., 1985, ApJS, 57, 711
- Feltzing S. & Gustafsson, B., 1998, A&A, 129, 237
- Ferland, G., 1996, *Hazy, a Brief Introduction to Cloudy*, University of Kentucky,
Department of Physics and Astronomy Internal Report
- Fernie, J.D., 1959, ApJ, 130, 610
- Fernie, J.D., 1983, ApJS, 52, 7
- Ferreras, I. & Silk, J., 2000, ApJ, 532, 193
- Filippenko, A. V. 1997, ARA&A, **35**, 309
- Fischer, J., Geballe, T.R., Smith, H.A., Simon, M., & Storey, J.W.V., 1987, ApJ,
320, 667
- Forbes, D.A., Boisson, C., Ward, M.J., 1992, MNRAS, 259, 293
- Förster-Schreiber, N.M., 2000, AJ, 120, 2089
- Frogel, J. A., 1985, ApJ, 298, 528

- Frogel, J.A., Persson, S.E., Aaronson, M., & Matthews, K., 1978, ApJ, 220, 75
- Frogel, J.A., Stephens, A.W., Ramírez, S., DePoy, D.L., 1999, AAS, 195.0314
- Frogel, J.A., & Whitford, A.E., 1987, ApJ, 320, 199
- Fryxell, B. A., & Arnett, W. D. 1981, ApJ, **243**, 994
- Garmany, C.D., & Stencel, R.E., 1992, A&AS, 94, 211
- Gear, W.K., Lilly, S.J., Stevens, J.A., Clements, D.L., Webb, T.M., Eales, S.A.,
Dunne, L., 2000, MNRAS, 316 L51
- Genzel, R., Lutz, D., Sturm, E., Egami, E., Kunze, D., Moorwood, A.F.M.,
Rigopoulou, D., Spoon, H. W. W., Sternberg, A.,
- Genzel, R., Weitzel, L.E., Tacconi-Garman, L.E., Blietz, M., Cameron, M., Krabbe,
A., & Lutz, D., 1995, ApJ, 444, 129 Tacconi-Garman, L. E., Tacconi, L.,
Thatte, N., 1998, ApJ, 498, 597
- Gilbert, A.M., & Graham, J.R., 2000, preprint (astro-ph/0012089)
- Glass, I.S., 1992, MNRAS, 256, 23
- Glass, I.S., 1997, MNRAS, 292, L50
- Glass, I.S., 1998, MNRAS, 297, 18
- Glass, I.S., & Moorwood, A.F.M., 1985, MNRAS, 214, 429
- Goldader, J.D., Joseph, R.D., Doyon, R., & Sanders, D.B., ApJ, 444, 97
- Goldader, J.D., Joseph, R.D., Doyon, R., & Sanders, D.B., ApJS, 108, 449
- Goldader, J.D., Joseph, R.D., Doyon, R., & Sanders, D.B., ApJ, 474, 104

- Gonzalez-Delgado, R.M., Heckman, T., Leitherer, C., Meurer, G., Krolik, J.,
Wilson, A.S., Kinney, A., Koratkar, A., 1998, *ApJ*, 505, 174
- Gorgas, J., Faber, S.M., Burstein, D., Gonzalez, J.J., Courteau, S., & Prosser, C.,
1993, *ApJ*, 86, 153
- Grebel, E.K., 1996, *PASP*, 108, 1141
- Groppi, C., Ivanov, V.D., & Rieke, G.H., 2001, in preparation
- Gunn, J.E., & Stryker, L.L., 1983, *ApJS*, 52, 121
- Haggkvist, L., & Oja, T., 1969, *Arkiv for Astron.*, 5, 125
- Hall, D.N.B., 1970, Ph.D. Thesis, Harvard University
- Hanson, M.M., Conti, P.S., Rieke, M.J., 1996, *ApJS*, 107, 281
- Harlan, E.A., 1974a, *AJ*, 74, 916
- Harlan, E.A., 1974b, *AJ*, 79, 682
- Hicks, E.K., Malkan, M.A., Teplitz, H.I., Sugai, H., Guichard, J., 2000, *AAS*,
197.4408
- Heckman, T.M., Gonzalez-Delgado, R., Leitherer, C., Meurer, G.R., Krolik, J.,
Wilson, A.S., Koratkar, A., & Kinney, A., 1997, *ApJ*, 482, 114
- Heckman, T.M., 1999, preprint (astro-ph/9912029)
- Henry, R.B.C., & Worthey, G., 1999, *PASP*, 111, 919
- Henry, T.J., Kirkpartick, J.D., & Simons, D.A., 1994, *AJ*, 108, 1437
- Hill, V., 1999a, *A&A*, 345, 430

- Hill, T.L., Heisler, C.A., Norris, R.P., Reynolds, J.E., Hunstead, R.W., 2000, preprint (astro-ph/0009260)
- Hill, T.L., Heisler, C.A., Sutherland, R., Hunstead, R.W., 1999b, AJ, 117, 111
- Hines, D.C., 1991, ApJ, 374, L9
- Ho, L.C., Filippenko, A.V., Sargent, W.L.W., 1997, ApJS, 112, 315
- Hodge, P., 1989, ARA&A, 27, 139
- Houdashelt, M.L., Bell, R.A., Sweigart, A.V., & Wing, R.F., 2000, AJ, 119, 1424
- Houk, N. & Smith-Moore, M., 1988, Michigan Spectral Survey, Ann Arbor, Univ. of Michigan, No. 4
- Huchra, J., & Burg, R., 1992, ApJ, 393, 90
- Huchra, J., & Sargent, W.L.W., 1973, ApJ, 186, 433
- Humphreys, R.M., 1970, AJ, 75, 602
- Hunt, L.K., & Giovanardi, C., 1992, AJ, 104, 1018
- Iben, I. & Tutukov, A. 1984, ApJS, 54, 335
- Impey, C.D., Winn-Williams, C.G., & Becklin, E.E., 1986, ApJ, 309, 572
- Ivanov, V.D., Rieke, G.H., Groppi, C.E., Alonso-Herrero, A., Rieke, M.J., & Engelbracht, C.W., 2000, ApJ, 545, 190
- Ivanov, V.D., et al., 2001, in preparation
- Ivison, R.J., Smail, I., Barger, A.J., Kneib, J.-P., Blain, A.W., Owen, F.N., Kerr, T.H., Cowie, L.L., 2000, MNRAS, 315, 209

- Jennens, P.A., & Helfer, H.L., 1975, MNRAS, 172, 667
- Johnson, H.L., 1966, ARA&A, 4, 193
- Johnson, H.L., Iriarte, B., Mitchell, R.I., & Wisniewski, W.Z., 1966, Comm. Lunar Plan. Ab., 4, 99
- Johnson, H.L. & Morgan, W.W., 1953, ApJ, 117, 313
- Johnosn, H.J. & Mèndez, M.E., 1970, AJ, 75, 785
- Joy, A.H. & Abt, H.A., 1974, ApJS, 28, 1
- Joy, M., & Ghigo, F.D., 1988, ApJ, 332, 179
- Joyce, R.R., 1998, AJ, 115, 2059
- Kawara, K., Nishida, M., & Gregory, B., 1990, ApJ, 352, 433
- Keenan, P.C., & McNail, R.C., 1989, ApJS, 71, 245
- Kerschbaum, F., & Hron, J., 1994, A&AS, 106, 397
- Kirkpatrick, J.D., Kelly, D.M., Rieke, G.H., Liebert, J., Allard, F., Wehrse, R., 1993, ApJ, 402, 643
- Kleinmann, S.G., & Hall, D.N.B., 1986, ApJS, 62, 501
- Knapen, J.H., Shlosman, I., & Peletier, R.F., 1999, preprint
- Knop, R.A., 1997, Ph.D. Thesis, Cal. Tech., Pasadena, CA
- Königl, A., & Kartje, J.F., 1994, ApJ, 434, 446
- Koski, A.T., 1978, ApJ, 223, 56

- Kovo, O., Sternberg, A., & Alexander, T., in preparation
- Krabbe, A., Colina, L., Thatte, N., & Kroker, H., 1997, *ApJ*, 104, 476
- Krabbe, A., Sams III, B.J., Genzel, R., Thatte, N., & Pradda, F., 2000, *A&A*, 354, 439
- Krishmer, M., Tully, B.R., & Giola, I.M., 1995, *AJ*, 110, 1584
- Kunth, D., & Contini, T., 1999, in *Wolf-Rayet Phenomena in Massive Stars and Starburst Galaxies*, 193th Symp. of IAU, eds. van der Hucht, K., Koenigsberger, G., & Eenens, P.R.J., p. 725
- Kurucz, R., 1994, Solar abundance model atmospheres for 0,1,2,4,8 km/s.
Kurucz CD-ROM No. 19. Cambridge, Mass.: Smithsonian Astrophysical Observatory, 1994.
- Lançon, A. & Rocca-Volmerange, B., 1992, *A&AS*, 96, 593
- Lançon, A. & Rocca-Volmerange, B., 1996, *New Astr.*, 1, 215
- Lançon, A. & Wood, P.R., 2000, *A&AS*, 146, 217
- Larkin, J.E., Armus, L., Knop, R.A., Soifer, B.T., & Mattheus, K., 1998, *ApJS*, 114, 59
- Lawrence, A., Ward, M., Elvis, M., Fabbiano, G., Willner, S.P., Carleton, N.P., Longmore, A., 1985, *ApJ*, 291, 117
- Lee, T.A., 1970, *ApJ*, 162, 217
- Leggett, S.K., 1992, *ApJS*, 82, 351

- Leggett, S.K., Allard, F., Berriman, G., Dahn, C.C., & Hauschildt, P.H., 1996, *ApJS*, 104, 117
- Leggett, S.K., Allard, F., Dahn, C., Hauschildt, P.H., Kerr, T.H., & Rayner, J., 2000, *ApJ*, 535, 965
- Leitherer, C., & Heckman, T., 1995, *ApJS*, 96, 9
- Leitherer, C., Schaerer, D., Goldader, J.D., Delgado, R.M.G., Robert, C., Kune, D.F., de Melo, D.F., Devost, D. & Heckman, T., 1999, *ApJS*, 123, 3
- Lejeune, Th., Cuisinier, F., & Buser, R., 1997, *A&AS*, 125, 229
- Livingston, W. & Wallace, L., 1991, *An Atlas of the Solar Spectrum in the Infrared from 1850 to 9000 cm^{-1} (1.1 to 5.4 μm)*, N.S.O., Technical Report # 91-001, National Solar Observatory, National Optical Astronomical Observatories, Tucson, AZ, U.S.A.
- Ljunggren, B., & Oja, T., 1964, *Arkiv for Astron.*, 3, 439
- Luck, R.E. & Bond, H.E., 1989, *ApJS*, 71, 559
- Luck, R.E., Moffet, T.J., Barnes, T.G. III, Gieren, W.P., 1998, *AJ*, 115, 605
- Luhman, M.L., Jaffe, D.T., Keller, L.D., & Pak, S., 1994, *ApJ*, 436, L185
- Lutz, D., Spoon, H.W.W., Rigopoulou, D., Moorwood, A.F.M., & Genzel, R., 1998, *ApJ*, 505, L103
- Maiolino, R., Alonso-Herrero, A., Anders, S., Quillen, A., Rieke, M.J., Rieke G.H., & Tacconi-Garman, L.E., 2000, *ApJ*, 531, 219
- Maiolino, R., & Rieke, G.H., 1995, *ApJ*, 454, 95

- Maiolino, R., Rieke, G.H., & Rieke, M.J., 1996, AJ, 111, 537
- Maiolino, R., Ruiz, M., Rieke G.H., & Papadopoulos, P., 1997, ApJ, 485, 552
- Mauder, W., Weigelt, G., Appenzeller, I., Wagner, S.J., 1994, A&A, 285, 44
- Mayya, Y.D., 1997, ApJ, 482, L149
- McAlary, C.W., McLaren, R.A., & Crabtree, D.R., 1979, ApJ, 234, 471
- McAlary, C.W., & Rieke, G.H., 1988, ApJ, 333, 1
- McClure, R.D., 1970, AJ, 75, 41
- McLeod, K.K., & Rieke G.H., 1995, ApJ, 441, 96
- McLeod, K.K., Rieke G.H., Rieke, M.J., & Kelly, D.M., 1993, ApJ, 412, 111
- McWilliam, A. & Lambert, D.L., 1984, PASP, 96, 882
- McWilliam, A. & Rich, R.M., 1994, ApJS, 91, 749
- McLeod, K.K., & Rieke, G.H., 1995, ApJ, 441, 96
- Mendoza V., E.E., 1967, Bo. Obs. Tonantz. Tacub., 4, 149
- Mendoza V., E.E., & Johnson, L.H., 1965, ApJ, 141, 161
- Mermilliod, J.-C., 1986, Compilation of Eggen's UBV data, transformed to UBV
(unpublished)
- Merrill, K.M., & Ridgway, S.T., 1979, ARA&A, 17, 9
- Meyer, M.R., Edwards, S., Hinkle, K.H., & Strom, S.E., 1998, ApJ, 508, 397
- Meynet, G., Mader, A., Schaller, G., Schaerer, D., & Charbonnel, C., 1994, A&AS,
103, 97

- Mihos, J.C., & Hernquist, L., 1994, *ApJ*, 425, L13
- Moorwood, A.F.M., & Oliva, E., 1990, *A&A*, 203, 278
- Moorwood, A.F.M., & Oliva, E., 1990, *ApJ*, 429, 602
- Morgan, W.W., & Keenan, P.C., 1973, *ARA&A*, 11, 29
- Moshir, M., Kopan, G., Conrow, T., Mccallon, H., Hacking, P., Gregorich, D., Rohrbach, G., Melnyk, M., Rice, W., Fullmer, L., et al. Infrared Astronomical Satellite Catalogs, 1990, The Faint Source Catalog, Version 2.0
- Mould, J.R., 1978, *ApJ*, 226, 923
- Murphy, T.W., Jr., Soifer, B.T., Matthews, K., Kiger, J.R., Armus, L., 1999, *ApJ*, 525, L85
- Murphy, T.W., Jr., Soifer, B.T., Matthews, K., Armus, L., Kiger, J.R., 2000, preprint (astro-ph/0010077)
- Nakajima, T., Carleton, N.P., & Nishinda, M., 1991, *ApJ*, 375, L1
- Nassau, J.J., & van Albada, G.B., 1947, *ApJ*, 106, 20
- Neckel, H., 1974, *A&AS*, 18, 169
- Nelson, C., & Whittle, M., 1998, in The AGN/Host Galaxy Connection as part of the Scientific Assembly of COSPAR (astro-ph/9811035)
- Nomoto, K., Iwamoto, K., & Kishimoto, N., 1997, *Science*, 276, 1378
- Norman, C., & Scoville, N., 1988, *ApJ*, 332, 124
- Ohsuga, K., & Umemura, M., 1999, *ApJ*, 521, L13

- Oja, T., 1987, A&AS, 68, 211
- Oliva, E., & Origlia, L. 1992, A&A, 254, 466
- Oliva, E., Origlia, L., Kotilainen, J.K., & Moorwood, A.F.M., 1995, A&A, 301, 55
- Oliva, E., Origlia, L., Maiolino, R., & Moorwood, A.F.M., 1999, A&A, 350, 9
- Origlia, L., Ferraro, F.R., Fusi Pecci, F., & Oliva, E., 1997, A&A, 321, 859
- Origlia, L., Goldader, J.D., Leitherer, C., Shaerer, D., Oliva, E., 1999, ApJ, 514, 96
- Origlia, L., Moorwood, A.F.M., & Oliva, E., 1993, A&A, 280, 536
- Origlia, L., & Oliva, E., 2000, A&A, 357, 61
- Osawa, K., 1959, ApJ, 130, 159
- Parsons, S.B., & Montemayor, T.J., 1982, ApJS, 49, 175
- Perry, J.J., 1992, in Relationships between Active Galactic Nuclei and Starburst Galaxies, ed. Filippenko, A.V., ASP Conf. Ser., 31, 169
- Perry, J.J., & Dyson, J.E., 1985, MNRAS, 235, 665
- Persson, S.E., 1988, ApJ, 330, 751
- Portinari, L., Chiosi, C., & Bressan, A., 1998, A&A, 334, 505
- Press, W. H., Teukolsky, S. A., Vetterling, W. T. & Flannery, B. P. 1992, *Numerical Recipes in C*, Cambridge University Press
- Puche, D., & Carignan, C., 1988, AJ, 95, 1025
- Quillen, A.C., Shaked, S., Alonso-Herrero, A., McDonald, C., Lee, A., Rieke, M.J., Rieke, G.H., 2000, ApJ, 532, L17

- Ramírez, S.V., DePoy, D.L., Frogel, J.A., Sellgren, K., & Blum, R.D., 1997, AJ, 113, 1411
- Ramírez, S.V., Sellgren, K., Carr, J.S., Balachandran, S.C., Blum, R.D., Terndrup, D.M., & Steed, A., 2000a, ApJ, 537, 205
- Ramírez, S.V., Stephens, A., Frogel, J.A., DePoy, D.L., 2000b, AJ, 120, 833
- Rhee, J.H., & Larkin, J.E., 2000, ApJ, 538, 98
- Ridgway, S.E., Winn-Williams, C.G., & Becklin, E.E., 1994, ApJ, 428, 609
- Rieke, G.H., 1978, ApJ, 226, 550
- Rieke, G.H., & Lebofsky, M.J., 1979, ApJ, 229, L111
- Rieke, G.H., & Lebofsky, M.J., 1981, ApJ, 250, 87
- Rieke, G.H., & Lebofsky, M.J., 1985, ApJ, 288, 618
- Rieke, G.H., Lebofsky, M.J., Thompson, R.I., Low, F.J., & Tokunaga, A.T., 1980, ApJ, 238, 24
- Rieke, G.H., Locken, K., Rieke, M.J., & Tamblyn, P., 1993, ApJ, 412, 99
- Rieke, G.H., & Low, F.J., 1975, ApJ, 197, 17
- Risaliti, G., Gilli, R., Maiolino, R., & Salvati, M., 2000, A&A, 357, 13
- Roche, P.F., Aitken, D.K., Smith, C.H., Ward, M.J., 1991, MNRAS, 248, 606
- Sakai, S., Madore, B.F., Freedman, W.L., Lauer, T.R., Ajhar, E.A., Baum, W.A., 1997, ApJ, 478, 49
- Salpeter, E.E., 1955, ApJ, 121, 161

- Sandage, A., 1997, PASP, 109, 1193
- Schaerer, D., Charbonnel, C., Meynet, G., Maeder, A., & Schaller, G. 1993a, A&AS, 102, 339
- Schaerer, D., Meynet, G., Maeder, A., & Schaller, G. 1993b, A&AS, 98, 523
- Schaller, G., Schaerer, D., Maeder, A., & Meynet, G., 1992, A&A, 96, 269
- Schild, R.E., 1973, AJ, 78, 37
- Shinnerer, E., Eckart, A., & Boller, Th., 2000a, preprint (astro-ph/0007461)
- Shinnerer, E., Eckart, A., & Tacconi, L.J., 2000b, preprint (astro-ph/0010317)
- Schmitt, J.L., 1971, ApJ, 163, 75
- Schreiber, N.M., 1998, Ph.D. Thesis, Ludwig – Maximilians – Universität, München, 1998
- Scoville N., et al., 2001, in press
- Shapiro, S.L. & Teukolsky, S.A. 1983, *Black Holes, White Dwarfs and Neutron Stars*, New York, Wiley-Interscience
- Shlosman, I., Begelman, M.C., & Frank, J., 1990, Nature, 345, 679
- Shlosman, I., Frank, J., & Begelman, M.C., 1989, Nature, 338, 45
- Siogren, U., 1964, Arkiv for Astron., 3, 339
- Smith, H.E., Lonsdale, C.J., & Lonsdale, C.J., 1998, ApJ, 492, 137
- Soifer, B.T., Neugebauer, G., Matthews, K., Egami, E., Becklin, E. E., Weinberger, A. J., Ressler, M., Werner, M. W., Evans, A. S., Scoville, N. Z., Surace, J. A., Condon, J., 2000, AJ, 119, 509

- Spinoglio, L., Malkan, M.A., Rush, B., Carrasco, L., & Recillas-Cruz, 1995, *ApJ*, 453, 616
- Storchi-Bergmann, T., Winge, C., Ward, M.,J., & Wilson, A.S., 1999, *MNRAS*, 304, 35
- Straizys, V., 1992, *Multicolor Stellar Photometry*, Pachart Pub., Tucson, Arizona, U.S.A.
- Strauss, M.A., Davis, M., Yahil, A., & Huchra, J.P., 1990, *ApJ*, 361, 49
- Surace, J.A., Sanders, D.B., & Evans, A.S., 2000, *ApJ*, 529, 170
- Talbot, Jr., R.J., & Arnett, W.D., 1971, *ApJ*, 170, 409
- Taylor, B.J., 1991, *ApJS*, 76, 715
- Taylor, B.J., 1999, *A&A*, 134, 523
- Taylor, B.J., Spinrad, H., & Schweizer, F., 1972, *ApJ*, 173, 619
- Terlevich, E., Diaz, A.I., & Terlevich, R., 1989, *ApJS*, 157, 15
- Terlevich, E., Diaz, A.I., & Terlevich, R., 1990, *MNRAS*, 242, 284
- Terlevich, R., & Melnick, J., 1985, *MNRAS*, 213, 841
- Terlevich, R., Tenorio-Tagle, G., Franco, J., & Melnick, J., 1992, *MNRAS*, 255, 713
- Terndrup, D.M., Frogel, J.A., & Whitford, A.E., 1991, *ApJ*, 378, 742
- Thielemann, F.-K., Nomoto, K., & Hashimoto, M., 1996, *ApJ*, 460, 408
- Thomas, D., Greggio, L., & Bender, R., 1998, *MNRAS*, 296, 119
- Teinsley, B.M., 1975, *ApJ*, 198, 145

- Teinsley, B.M., 1980, *Fundam. Cosm. Phys.*, 5, 287
- Trager, S.C., Worthey, G., Faber, S.M., Burstein, D., Gonzalez, J.J., 1998, *ApJS*, 116, 1
- Usuda, T., Sugai, H., Kawbata, H., Inoue, M.Y., Kataza, H., & Tanaka, M., 1996, *ApJ*, 464, 818
- van Belle, G.T., Lane, B.F., Thompson, R.R., Boden, A.F., Colavita, M.M., Dumont, P.J., Mobley, D.W., Palmer, D., Shao, M., Vasisht, G.X., Wallace, J.K., Creech-Eakman, M.J., Koresko, C.D., Kulkarni, S.R., Pan, X.P., & Gubler, J., 1999, *AJ*, 117, 521
- van Breugel, W.J.M., & Dey, A., 1993, *ApJ*, 414, 563
- van Breugel, W., Filippenko, A.V., Heckman, T., & Miley, G., 1985, *ApJ*, 293, 83
- Vanzi, L., & Rieke, G.H., 1997, *ApJ*, 479, 694
- Vanzi, L., Rieke, G.H., Martin, C.I., & Sields, J.C., 1996, *ApJ*, 466, 150
- Vazdekis, A., 1999, *ApJ*, 513, 224
- Vazdekis, A., Salaris, M., Arimoto, N., Rose, J.A., 2001, *ApJ*, 549, 274
- Veeder, G.J., 1974, *AJ*, 79, 1056
- Veilleux, S., Goodrich, R.W., & Hill, G.H., 1997, *ApJ*, 477, 631
- Veilleux, S., & Osterbrock, D.E., 1987, *ApJS*, 63, 295
- Veilleux, S., Sanders, D.B., & Kim, D.C., 1999, *ApJ*, 522, 139
- von Linden, S., Biermann, P.L., Duschl, W.J., Lesch, H., & Schmutzler, T., 1993, *A&A*, 280, 468

- Wallace, L., Meyer, M.P., Hinkle, K., Edwards, S., 2000, *ApJ*, 535, 325
- Wallace, L. & Hinkle, K., 1996, *ApJS*, 107, 312
- Wallace, L. & Hinkle, K., 1997, *ApJS*, 111, 445
- Weaver, W.B., & Torres-Dogen, A.V., 1997, *ApJ*, 487, 847
- Weedman, D.W., 1983, *ApJ*, 266, 479
- Weistrop, D., 1977, *ApJ*, 215, 845
- White, N.M. & Wing, R.F., 1978, *ApJ*, 222, 209
- Whitmore, B.C., McElroy, D.B., & Tonry, J.L., 1985, *ApJS*, 59, 1
- Whittle, M., Pedlar, A., Meurs, E.J.A., Unger, S.W., Axon, D.J., Ward, M.J.,
1988, *ApJ*, 326, 125
- Williams, R.J.R., Baker, A.C., & Perry, J.J., 1999, *MNRAS*, 310, 913
- Williams, D.M., Thompson, C.L., Rieke, G.H., & Montgomery, E.F., 1993, *S.P.I.E.*,
1946, 482
- Winge, C., Storchi-Bergmann, T., Ward, M.,J., & Wilson, A.S., 2000, preprint
(astro-ph/0001206)
- Woosley, S.E., & Weaver, T.A., 1995, *ApJS*, 101, 181
- Worthey, G., 1994a, *ApJS*, 95, 107
- Worthey, G., 1998, *PASP*, 110, 888
- Worthey, G., Faber, S.M., & Gonzalez, J.J., 1992, *ApJ*, 398, 69
- Worthey, G., Faber, S.M., Gonzalez, J.J. & Burstein, D., 1994b, *ApJS*, 94, 687

Zakhozhaĭ V.A., & Shaparenko E.F., 1996, *Kin. Fiz. Nebesn. Tel.*, 12, No, 2, 20

Zaritsky, D., *PASP*, 105, 1006

Zhou Xu, 1991, *A&A*, 248, 367